Aspects of Improvement in the Sensitivity of Long-Baseline Laser Interferometric Gravitational Wave Detectors

Kenneth David Skeldon

Presented for the Degree of PhD, Department of Physics and Astronomy,
University of Glasgow, University Avenue, G12 8QQ.

July 4, 1996

ProQuest LLC.
789 East Eisenhower Parkway
P.O. Box 1346
Ann Arbor, MI 48106 – 1346

Acknowledgements

I would like to thank my supervisors Jim Hough and Norna Robertson for their help and guidance throughout the entire course of my studies, but particularly for their understanding during my final year.

Financial support came primarily from a University of Glasgow Research Scholarship. I also acknowledge the assistance of the Particle Physics and Astronomy Research Council for the industrial support grant which funded some of my work.

Technical support was very competently provided by Colin Craig, Dave Edwards, Allan Latta and Angus McKellar. My thanks go also to other members of the Glasgow group; Alison McLaren, Gavin Newton, David Robertson, Sheila Rowan, Sharon Twyford and Harry Ward, with whom I have had many useful discussions.

I would especially like to acknowledge the help and advice of Kenneth Strain, particularly throughout the development of the resonant modecleaner system. I am also grateful to Alastair Grant for lending his technical skills to my work on several occasions. The other inhabitants of my office deserve a special mention for putting up with my moods and general untidiness throughout my thesis writing; Stuart Killbourn, whose constructive sarcasm kept me going at times, and Paul McNamara whose knowledge and advice on the ESA space mission project were gratefully received.

Some of my work was carried out with people no longer with the group. Part of the infra-red laser work, concerned with intensity servo performance, was done with Anne Campbell. I would like to acknowledge the early help and encouragement given to me by Brian Meers, whose death back in 1992 was a tragedy felt across the entire breadth of our field.

I am indebted to Rebecca Crawford for her help and encouragement in allowing me to continue some of my public understanding of science activities, whilst not letting my thesis writing get behind schedule.

My thanks must also go to my family and friends, both in Britain and overseas, for their much needed support and encouragement particularly during 1995.

Lastly, I owe a special debt of gratitude to my mother for her continuing bravery throughout all the darkness. Her love and support have made the completion of this thesis possible.

This work is lovingly dedicated to my father, to whom I owe much.

David Skeldon 1928 - 1995

Contents

List of Figures

List of Tables

Preface

The work presented in chapter 1 on gravitational wave astrophysics, especially on the nature and variety of sources, is derived from numerous articles and papers, some of which are very recent. The chapter represents a summary of current beliefs regarding source strengths and event rates for the long baseline laser interferometers being developed around the world.

The subject matter of chapter 2 is mainly review material, demonstrating the various noise barriers that have to be overcome both in the development of resonant bar antennae and long baseline interferometer detectors. Chapter 3 contains a brief review of the properties of Fabry-Perot optical cavities.

The content of chapter 4 describes experimental techniques used to measure both the total loss, and absorptance loss, of very high quality mirrors. The equipment and clean tent was set up initially by the author and then subsequent modifications to provide the absorptance test apparatus were made by K.A. Strain. The automatic mirror loss meter was developed by the author in conjunction with K.A. Strain and our technical staff. Software for the project was written by the author. The contact person for the OMITEC company was N.A. Robertson.

Chapter 5 provides an overview of beam geometry fluctuations and how they can be modelled as additions to the fundamental laser mode of higher order transverse modes. The instruments designed to measure the levels of beam geometry noise were designed and built by the author, with input from our technical staff on the constructional side. Precision low noise differential amplifiers were designed and constructed by our senior technician A. McKellar. The experimental results presented are derived from a set of measurements taken and analysed by the author.

The intensity stabilisation servo of chapter 6 was developed by S. Rowan, A.M. Campbell and J. Hough. The measurements of beam jitter at the relaxation oscillation frequency of the Nd:YAG laser were performed by the author working with S. Rowan. Subsequent performance diagnostics regarding the broadband servo were conducted by the author and A.M. Campbell.

The coupling mechansims for beam geometry noise and detector sensitivity in chapter 7 are analysed and the theory behind the operation of a resonant modecleaner to suppress beam geometry noise is shown in chapter 8. The author puts forward that two modecleaners should provide the necessary level of beam geometry noise suppression to safeguard interferometer sensitivity, in view of the results of chapter 7.

The design and construction of a prototype modecleaner is described in chapter 9. The system was constructed primarily by the author with occasional help from other colleagues. Aspects of the various locking circuits were studied by H. Ward and K.A. Strain alongside the author.

In chapter 10 conclusions are drawn and the modecleaner scheme for GEO 600 is shown using a scale diagram produced by our German colleagues.

Appendix A contains a review of Gaussian beam propagation through various optical systems and in particular the equations that determine the existence of a stable cavity eigenmode. Appendix B contains a description of software written by the author to chart the progress of a Gaussian beam throughout optical systems, including those of the GEO 600 interferometer.

Summary

It is now widely believed that the direct detection of gravitational waves will begin a new chapter in observational astronomy. Yet for many years, their very physical existence was in doubt and they were regarded by many to be merely a mathematical artifact of the general theory of relativity. However recently, Russell Hulse and Joseph Taylor were given Nobel recognition for their discovery, and subsequent study, of the binary star system PSR1913. They have shown, using twenty years of carefully taken data, that the decay in the orbital period of the stars exactly matches the predicted rate through loss of energy by gravitational radiation emmision. Gravitational waves have been detected, albeit indirectly.

There has never been a greater level of interest and activity in the field of experimental gravitational wave research. Now that large detectors with astrophysically useful sensitivities seem likely to be completed by the turn of the century, there is an intensive worldwide effort to combat the various experimental challenges associated with their successful operation. The first phase of detectors will come on-line during or soon after the turn of the century. These should not only detect gravitational waves conclusively, but should initiate an unprecedented dependence on them, to reveal what goes on at the heart of some of the most interesting and exotic events the universe has to offer.

There are two types of detector under development today. These are *long-baseline laser interferometers* and *cryogenic resonant-bars*. The first resonant-bar detectors were built at the University of Maryland in the 1960s by Joseph Weber. The primary motivation was to detect bursts from supernova explosions - a fact difficult to forget in view of Weber's now infamous report of detections. The 'false alarm' publications

of Weber demonstrate something that many experimental physicists know only too well - that when looking for signals in a background of noise, it is only too easy to think you have seen something. The signal to noise ratios of the early bar detectors were too small to make them astrophysically useful. It is interesting, although some might argue frustrating, that even with present technology, projected detector sensitivity has only recently become comparable with theoretical calculations of source strengths. It is a fascinating scenario, whereby relativistic physics (of the universe) and classical physics (of detectors) have provided two scales (signal strengths on the one hand, and signal sensitivity on the other) which have taken twenty years of research and perseverance to make overlap, and even then, by a satisfactory if not satisfying margin.

Chapter 1 deals with the astrophysics of gravitational radiation, beginning with a brief review of relativity and introducing the equations that describe gravitational waves. The chapter then covers the most potentially exciting sources that the new generation of long baseline interferometers will search for. For completeness, the proposed ESA-funded mission to have an interferometer in space is mentioned, together with its role relative to ground based detectors.

Chapter 2 describes gravitational wave detectors, and particularly their design aspects in view of the extremely small displacements they are required to measure. Resonant-bars and then laser interferometers are discussed, with consideration given to the various sources of noise that each type of detector has to overcome. The chapter ends by introducing the German-British GEO 600 project which is a 600 m arm length advanced interferometer being built in Hannover.

Chapter 3 reviews the properties of Fabry-Perot optical cavities. Concepts such as finesse, power throughput and visibility are all used in later chapters and the formulae presented will prove very useful. The role of a Fabry-Perot cavity as a frequency discriminator using RF-reflection locking is outlined at the end of the chapter.

Chapter 4 examines the losses associated with optical components used in laser interferometer systems. Experimental techniques for measuring both scatter loss and

absorptance loss are described and results for various state-of-the-art supermirrors are presented. The chapter ends with an overview of a project currently being undertaken to build an automatic loss meter for use in industry.

Chapter 5 focuses on one particular form of laser noise - fluctuations in the geometry of the laser beam. The various types of geometry fluctations are introduced along with techniques for modelling their behaviour. Sensitive instruments for measuring their magnitude are described and levels of beam positional fluctuations and beam diameter fluctuations from two commonly used types of laser are presented.

Chapter 6 describes an application of the measuring systems introduced in Chapter 5 to set a limit to the beam jitter levels that may be present at the relaxation oscillation frequency of a Nd:YAG monolithic ring laser. A second investigation of the same laser is presented which deals with limitations to the performance of an intensity servo, found to be caused by beam geometry noise.

Chapter 7 is a brief summary of the possible coupling mechanisms in a laser interferometer between beam geometry noise and displacement sensitivity. The primary example is that of a misalignment of the beam splitter from perfect symmetry with respect to each arm. Other mechanisms are also discussed.

Chapter 8 introduces the resonant modecleaner as a scheme for suppressing beam geometry noise. The principles behind the modecleaner action are explained with reference to transverse mode frequencies in a two mirror optical cavity. Design aspects of a modecleaner system suitable for long baseline interferometers are outlined and conclusions are made regarding the specifications of such a system.

Chapter 9 describes the design, development and performance of a prototype modecleaner developed at Glasgow. The modecleaner is based around a four mirror suspended Fabry-Perot ring cavity. Details of the electronic locking schemes used to keep the modecleaner on resonance with the light are presented, along with results of the power throughput, noise suppression characteristics and other relevant properties of the system.

Chapter 10 uses the results and experience developed from the work described in previous chapters, but particularly chapters 5, 7, 8 and 9 to present the implications and conclusions for a full scale gravitational wave detector. The modecleaner

system for the German-British detector GEO 600 will be outlined, and the expected performance of this scheme is discussed.

Appendix A reviews some fundamental results in Gaussian beam propagation which are important in designing optical cavities. In Appendix B, a software package is described that manipulates Gaussian beams through optical systems, in particular acting as a database of the beam parameters at various locations in the GEO 600 interferometer.

Chapter 1

Gravitational Wave Astrophysics

1.1 Introduction

The existence of gravitational waves was first predicted in Albert Einstein's General Theory of Relativity [1] where it is apparent that certain equations have periodic, or wave-like, solutions. Gravitational waves, unlike other forms of radiation, should relay direct information about the intrinsic physics of the astronomical events that generate them. It is this encoding of dynamical information onto the waves that makes the physics associated with their detection so exciting. Einstein's theory has survived a near comprehensive selection of tests and checks, both experimental and theoretical in nature, since its inception in 1916. The detection and subsequent analysis of gravitational wave signals will form another experimental check of Einstein's theory, as well as providing an exciting new field of astronomy.

The following sections will present a summary of the ideas of relativity. In section 1.2 special relativity will be reviewed, including its limitations for describing gravity. The rest of the section is spent outlining the important results in the general theory. In section 1.3 the existence and nature of gravitational waves is introduced. The chapter closes with a section devoted to the various astrophysical sources that ground-based detectors will explore, and also a class of sources characterised by

lower frequencies that a space-borne detector might hope to observe.

1.2 Brief Review of Relativity

The General Theory of Relativity is usually introduced by first describing the results of the *special theory.* The original set of papers that make up the special theory can be found in [2]. Here, a brief summary of the important results will suffice and then the expansion to general relativity will be outlined.

1.2.1 Special Relativity

Eintein's major insight into resolving the problem of measuring *absolute velocity* was to suggest that such a concept has no physical meaning. Velocities can only be measured *relative* to a reference system. The reference systems of special relativity (SR) are non-accelerating coordinate axes called *inertial frames.* All inertial frames assume equal importance and the laws of physics reported by an observer in one frame will be the same as those defined in any other frame. This is a one way of expressing the *principle of relativity.* There is only one other input to the theory that is required to establish all the laws of SR – the *universality of the speed of light.* This postulates that any observer will measure the same value for the speed of light regardless of the relative motion of the observer and the source of the light. The consequences of these two postulates lead naturally to a geometrical description, first suggested by Minkowski, in which three spatial coordinates and a time coordinate (t, x, y, z) are used to describe events. These coordinates form a four-dimensional *spacetime* that is convenient in the special theory and crucial for expressing the results of the general theory.

Given two events (t, x, y, z) and $(t + \Delta t, x + \Delta x, y + \Delta y, z + \Delta z)$, the *interval* between the events is defined as

$$\Delta s^2 = \Delta x^2 + \Delta y^2 + \Delta z^2 - c^2 \Delta t^2. \tag{1.1}$$

This quantity is invariant under a change of inertial frame and is something that all inertial observers will agree on. Since the inertial frames of SR are by definition

non-accelerating frames, there is no scope for introducing gravitational forces into the theory, since these cause an observer to accelerate. A more general theory is required, but which must have two important properties. Firstly it has to agree with the results of SR in regions where the gravitational field is very weak. Secondly it has to possess a coordinate frame *invariance* so that the laws of physics are the same for all observers regardless of their local gravitational environment. These demands can be met, and the mathematical tools required for the resulting theory are *differential geometry* and *tensor calculus.*

1.2.2 General Relativity

At any point in spacetime it is possible to define a tensor function called a *metric* which locally defines the structure or *curvature* of spacetime. Given two neighbouring points (x^1, x^2, x^3, x^4) and $(x^1 + \mathrm{d}x^1, x^2 + \mathrm{d}x^2, x^3 + \mathrm{d}x^3, x^4 + \mathrm{d}x^4)$, the *proper distance* $\mathrm{d}s^2$ between these points can be expressed in terms of the metric as

$$\mathrm{d}s^2 = g_{\alpha\beta} dx^\alpha dx^\beta. \tag{1.2}$$

For example in SR the metric tensor components are $g_{11} = -c^2$, $g_{22} = 1$, $g_{33} = 1$, $g_{44} = 1$ and $g_{\alpha\beta} = 0$ for all $\alpha \neq \beta$. If we choose cartesian coordinates so that $\mathrm{d}x^1 = \mathrm{d}t$, $\mathrm{d}x^2 = \mathrm{d}x$, $\mathrm{d}x^3 = \mathrm{d}y$ and $\mathrm{d}x^4 = \mathrm{d}z$, then in the case of SR Eqn.(1.2) becomes

$$\mathrm{d}s^2 = \mathrm{d}x^2 + \mathrm{d}y^2 + \mathrm{d}z^2 - c^2\mathrm{d}t^2. \tag{1.3}$$

In SR, Eqn.(1.3) applies *globally* to all points in spacetime - sometimes this is expressed by stating that the four-dimensional spacetime of SR has no curvature, or is *flat.* However SR is not an accurate description of the universe since the effects of gravitational forces will distort the metric from point to point. In general relativity (GR), Eqn.(1.3) only applies locally[1] and in general there is a more complex relationship between the metric and the proper distances it describes. The new metric form can be written as

$$g_{\alpha\beta} = \eta_{\alpha\beta} + \mathrm{O}[(x^\gamma)^2] \tag{1.4}$$

[1] the details regarding the confines of such a local region will not be discussed except to note that Eqn.(1.3) will be valid over larger domains for weaker local gravitational fields.

where $g_{\alpha\beta}$ is the metric associated with some point in spacetime and $\eta_{\alpha\beta}$ is the metric of SR. Eqn.(1.4) expresses a dependence of the metric on terms of second order in the coordinates. This can be re-expressed

$$\frac{\partial^2}{\partial x^\gamma \partial x^\zeta} g_{\alpha\beta} \neq 0 \tag{1.5}$$

for some of the values of α, β, γ and ζ. If the mathematics is checked in detail [3] then it is found that twenty of these components generally do not vanish and contain the necessary information about the curvature of spacetime. To express the relation between the metric tensor and curvature less vaguely consider the tensor whose components represent all possible basis vector derivatives with respect to the coordinates

$$\frac{\partial \vec{e}_\alpha}{\partial x^\beta} = \Gamma^\gamma{}_{\alpha\beta} \vec{e}_\gamma. \tag{1.6}$$

The tensor components $\Gamma^\gamma{}_{\alpha\beta}$ are known as the *Christoffel symbols* and it turns out that they are related to the metric tensor via its first order partial derivatives with respect to the coordinates

$$\Gamma^\alpha{}_{\gamma\zeta} = \frac{1}{2} g^{\alpha\beta} \left(\frac{\partial g_{\beta\gamma}}{\partial x^\zeta} + \frac{\partial g_{\beta\zeta}}{\partial x^\gamma} + \frac{\partial g_{\gamma\zeta}}{\partial x^\beta} \right). \tag{1.7}$$

In the case of curved spacetime it has already been pointed out that only the second partial derivatives of the metric tensor components with respect to any coordinate are non-zero, and we would expect the Christoffel symbols in Eqn.(1.7) to vanish in a coordinate frame that is locally inertial. This is indeed true, and it is only in the derivatives of the Christoffel symbols that the local curvature can be revealed. A curvature tensor, whatever may be its form, must therefore depend only on the derivatives of the Christoffel symbols. The method of identifying the form of such a curvature tensor is rather complex and cannot be described fully here, but it relies upon the idea of *parallel-transport* around a closed loop in spacetime. If a vector $\vec{x}$ is moved from point to point in a flat spacetime so that during each infinitesimal step it remains parallel to itself, then we can deduce that over a closed loop the initial and final states $\vec{x}_{initial}$ and $\vec{x}_{final}$ will be identical. However in a curved spacetime this is no longer true, and there will be a discrepancy between the initial and final

vectors $\delta\vec{x} = \vec{x}_{final} - \vec{x}_{initial}$. The tensor that describes this difference vector is called the *Riemann-Christoffel curvature tensor* defined by

$$R^{\alpha}{}_{\beta\gamma\zeta} = \frac{\partial\Gamma^{\alpha}{}_{\beta\zeta}}{\partial x^{\gamma}} - \frac{\partial\Gamma^{\alpha}{}_{\beta\gamma}}{\partial x^{\zeta}} + \Gamma^{\alpha}{}_{\eta\nu}\Gamma^{\eta}{}_{\beta\zeta} - \Gamma^{\alpha}{}_{\eta\zeta}\Gamma^{\eta}{}_{\beta\nu}. \tag{1.8}$$

The curvature tensor can be expressed in terms of the metric components alone by substituting Eqn.(1.7) into Eqn.(1.8) to give

$$R^{\alpha}{}_{\beta\gamma\zeta} = \frac{1}{2}g^{\alpha\eta}\left(\frac{\partial g_{\eta\zeta}}{\partial x^{\beta}\partial x^{\gamma}} - \frac{\partial g_{\eta\gamma}}{\partial x^{\beta}\partial x^{\gamma}} + \frac{\partial g_{\beta\gamma}}{\partial x^{\eta}\partial x^{\gamma}} - \frac{\partial g_{\beta\zeta}}{\partial x^{\eta}\partial x^{\gamma}}\right). \tag{1.9}$$

which can be seen to depend on the twenty terms involved in Eqn.(1.5). Ultimately there has to be a set of equations that describes how bodies behave in the presence of an arbitrary gravitational field. Einstein's progression to these *field equations* was to introduce another tensor which is a *contraction* of the general curvature tensor

$$R_{\eta\zeta} = R^{\alpha}{}_{\eta\zeta\alpha} \tag{1.10}$$

called the *Ricci tensor*. Acting on the Ricci tensor by the metric generates a number R which Einstein recognised to have physical significance in the curved spacetime of GR. In fact, the field equations can be written

$$R_{\alpha\beta} - \left(\frac{1}{2}R + \Lambda\right)g_{\alpha\beta} = \frac{8\pi G}{c^4}T_{\alpha\beta} \tag{1.11}$$

where Λ is the so-called *cosmological constant*, G is the universal gravitational constant and $T_{\alpha\beta}$ is the *energy-momentum tensor* for the local region to which Eqn.(1.11) applies. Eqn.(1.11) is really a set of equations[2] that are arrived at by generalising the familiar law of Newtonian gravity $\nabla^2\phi = 4\pi G\rho$ where ϕ is the gravitational field and ρ is the mass density. The tensorial nature of the law is required to keep it coordinate frame invariant. The constant Λ was added by Einstein years after the initial publication of GR in order to allow solutions of Eqn.(1.11) that would apply to a static universe. It is usually set to zero except for certain cosmological applications when it assumes a non-zero value.

[2] in this case ten coupled differential equations, not sixteen due to the symmetric nature of $R_{\alpha\beta}$ and $T_{\alpha\beta}$

1.3 Existence of Gravitational Waves

From now on the value of the cosmological constant Λ is taken to be zero. In a region of spacetime where the gravitational field is weak we can express the general metric $g_{\alpha\beta}$ as

$$g_{\alpha\beta} = \eta_{\alpha\beta} + h_{\alpha\beta} \tag{1.12}$$

where $h_{\alpha\beta}$ can be regarded as a small perturbation to the simple metric of SR $\eta_{\alpha\beta}$. There is an entire class of objects $h_{\alpha\beta}$ that will work in Eqn.(1.12) each related to the next by *gauge transformations* - coordinate changes of very small magnitude. This justifies using a particular form for $h_{\alpha\beta}$ which is defined in terms of the trace $h = h^{\alpha}{}_{\alpha}$ of $h_{\alpha\beta}$ by

$$\bar{h}^{\alpha\beta} = h^{\alpha\beta} - \frac{1}{2}\eta^{\alpha\beta}h \tag{1.13}$$

and which allows the Einstein field equations to be written in the particularly simple form

$$\left(\nabla^2 - \frac{1}{c^2}\frac{\partial^2}{\partial t^2}\right)\bar{h}^{\alpha\beta} = \frac{-16\pi G}{c^4}T^{\alpha\beta}. \tag{1.14}$$

In vacuum ($T^{\alpha\beta} = 0$) the field equations of Eqn.(1.14) can be written

$$\left(\nabla^2 - \frac{1}{c^2}\frac{\partial^2}{\partial t^2}\right)\bar{h}^{\alpha\beta} = 0 \tag{1.15}$$

which have periodic or wave-like solutions that propagate with velocity c. The problem of analysing gravitational waves can be simplified somewhat further by taking advantage of the coordinate freedom which underpins the field equations. By choosing a system in which we define there to be a *transverse traceless* gauge we can write the $h_{\alpha\beta}$ tensor for a gravitational wave propagating along the z-axis as

$$h^{\mathrm{TT}}_{\alpha\beta} = \begin{bmatrix} 0 & 0 & 0 & 0 \\ 0 & h_{xx} & h_{xy} & 0 \\ 0 & h_{yx} & h_{yy} & 0 \\ 0 & 0 & 0 & 0 \end{bmatrix} \tag{1.16}$$

where $h_{xy} = h_{yx}$ and the trace of $h_{\alpha\beta}$ is zero implying $h_{xx} = -h_{yy}$. Eqn.(1.16) represents a gravitational wave of two distinct polarisations which influence the proper separation of two orthogonal dimensions in space. This can be realised by

applying the metric of Eqn.(1.12) with $h_{\alpha\beta}$ as defined in Eqn.(1.16) to the proper distance formula of Eqn.(1.2) giving

$$\Delta s^2 = (1 + h_+)\Delta x^2 + 2(1 + h_\times)\Delta x \Delta y + (1 - h_+)\Delta y^2 - c^2\Delta t^2 \tag{1.17}$$

where $h_+ = h_{xx}$ and $h_\times = h_{xy}$. Applying Eqn.(1.17) to the worldline of a light ray travelling along the $x-$axis ($\Delta y^2 = 0$) gives

$$(1 + h_+)\Delta x^2 - c^2\Delta t^2 = 0 \tag{1.18}$$

since $\Delta s^2 = 0$ for photons. Eqn.(1.18) can be written in the form

$$\frac{dx}{dt} = \frac{c}{\sqrt{1 + h_+}} \tag{1.19}$$

which shows the relationship between the speed of light along the $x-$axis and the gravitational wave term h_+. Although Eqn.(1.19) suggests that the speed of light is being modulated by the gravitational wave, it is more correct to consider the metric of spacetime as undergoing the modulation. The terms h_+ and $h_\times$ are often referred to as the *strain amplitudes* of the polarisations and in general, the strain amplitude h of a wave can be calculated as $\sqrt{(h_+^2 + h_\times^2)}$. Consideration of Eqn.(1.17) will show that light travelling along the $y-$axis can be described by a similar expression to Eqn.(1.19) with denominator $\sqrt{1 - h_+}$. The cross term can be seen to be involved in neither of these two examples, and represents a second polarisation characterised by setting $\Delta x = \Delta y$. The classic example is the effect of a gravitational wave passing perpendicularly to the plane of a circular ring of test particles as shown in Fig.1.1. An important observation in passing is that, while the h_+ polarisation causes a *differential* motion of the particles in the x- and y-axes, the $h_\times$ polarisation produces no differential motion in these axes (compare the distance from the origin to a particle along the x- and y-axes as the motion evolves). This important property is the reason that laser interferometers (which measure the differential length change along two perpendicular paths) are so suited to detecting gravitational waves. To gain a physical understanding of what the strain amplitude actually means consider a length interval L, say, lying along the x-axis, being traversed by a light ray. In the absence of any gravitational waves, the length is related to the time τ for the

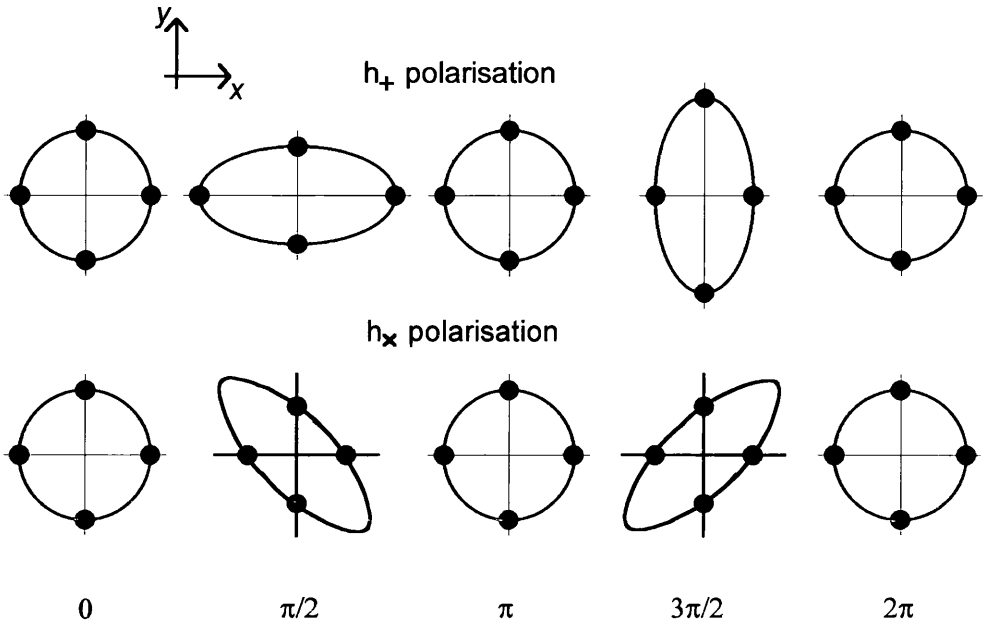

Figure 1.1: *Influence on a ring of particles by the two polarisations of gravitational waves*

journey simply by $L = c\tau$. However in the presence of a gravitational wave, the length is altered and is best described by

$$L' = \int_0^\tau \frac{dx}{dt} dt. \tag{1.20}$$

Using Eqn.(1.19) in Eqn.(1.20) and expanding to consider only first order terms in h_+ gives

$$L' = c\tau + \frac{c}{2}\int_0^\tau h_+(t)dt. \tag{1.21}$$

By letting $\delta L = L' - L$ and choosing a small integration time τ over which $h_+(t)$ is constant, Eqn.(1.21) simplifies to

$$\delta L = \frac{h_+}{2} c\tau \tag{1.22}$$

which can be written

$$\frac{\delta L}{L} = \frac{h_+}{2}. \tag{1.23}$$

This last expression demonstrates the justification for terming h_+ a *strain* in space.

A gravitational wave force field is often referred to as being a *quadrupole field*, in contrast with a magnetic field which can be regarded as dipole in nature, or an

electric field which can be monopole. The distinction between these force fields is shown in Fig.1.2. It is always the case that the gravitational force field appears to be subtending to four poles (the lines of force for each polarisation can be obtained by charting the motion of the test particles in Fig1.1). The nature of the waves lends insight into potential sources, which might be expected also to exhibit quadrupole form. To investigate the form that a gravitational wave source might have, Eqn.(1.14) is used where in general there will be non-zero components of the energy-momentum tensor $T_{\alpha\beta}$. Exact solutions can be found that depend on the second time derivative of the quadrupole moment of the source mass distribution. The strain amplitude can then be written [4]

$$\bar{h}^{\alpha\beta} = \frac{1}{r}\frac{G}{c^4}\frac{\partial^2}{\partial t^2}\left[D_{\alpha\beta}(t - r/c)\right] \tag{1.24}$$

which can be seen to have a $1/r$ dependence in common with magnetic and electric fields. The term $D_{\alpha\beta}$ is the quadrupole moment in the transverse traceless gauge, defined for weak fields in terms of the mass density ρ by

$$D_{\alpha\beta}(t) = \int \rho(t)\left[x^\alpha x^\beta - \frac{1}{3}x^2\delta^{\alpha\beta}\right] \mathrm{d}^3x. \tag{1.25}$$

Eqn.(1.24) is valid for sources generating waves that satisfy the criterion that the reduced wavelength of the radiation ($\lambda/2\pi$) is greater that the source dimensions. This is certainly true for some systems, but not all. In the following sections, the detectability of various sources will be examined.

1.4 Astrophysical Sources

The nature of the gravitational wave production mechanism is such that any potential source must possess some degree of dynamical asymmetry. Several classes of sources have emerged having this property in common, but each having different strain amplitude and frequency characteristics. These include *pulsars* (rotating neutron stars), *coalescing binary star systems*, stellar *gravitational collapse* events, *supernovae explosions* and other exotic sources such as black hole collisions. Traditionally, the categorisation of sources has largely been defined by the anticipated

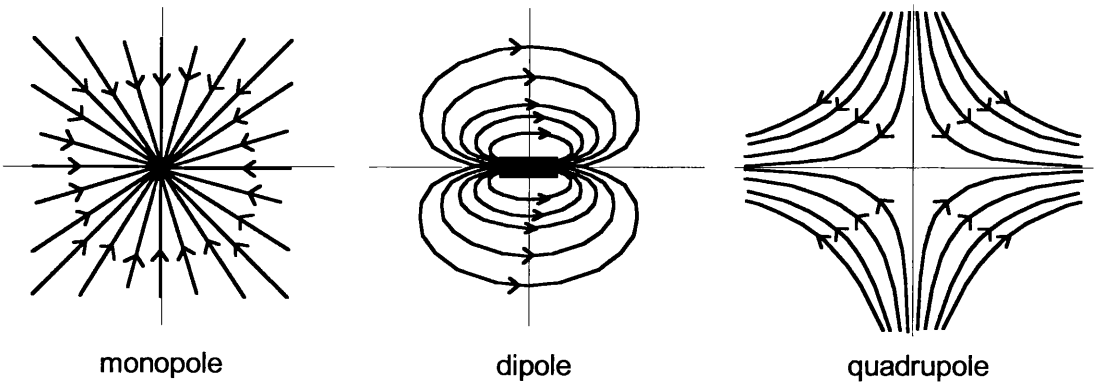

Figure 1.2: *Comparsion of the force fields due to an electrostatic monopole, a magnetic dipole and a gravitational wave.*

frequency sensitivity windows of detector designs. Ground based detectors are subject to a seismic noise barrier that prevents useful sensitivity at low frequency (below a few Hz). However, now that there is the possibility of a future space based detector having a sensitivity window covering much lower frequencies (down to 10^{-4} Hz) the range of interesting sources to be considered has increased. Sections 1.4.1, 1.4.2 and 1.4.3 will introduce sources with frequency characteristics of primary interest to ground based detectors. Following this, section 1.4.4 will describe some of the low frequency sources that are of interest to a space-borne detector.

1.4.1 Pulsars

Pulsars have always been interesting candidates for gravitational wave production. In determining whether a given pulsar is observable to a ground based detector, we have to consider its proximity to earth, level of spherical asymmetry, spin rate and spindown rate. Pulsars with high spin rates are preferred sources since they radiate at frequencies where the sensitivity of laser interferometers is likely to be optimal. The spindown rate of the pulsar gives a measure of how quickly the star is losing energy, be it via gravitational radiation emission or otherwise. In general, pulsars with high spindown rates will make for more interesting sources.

To investigate the gravitational wave signal strength of a pulsar consider again Eqn.(1.24). This equation can be expressed in a more revealing manner by using the

fact that the second time derivative of $D_{\alpha\beta}$ is directly related to the kinetic energy of the nonspherical component of the motion E_{ns}. To see this, consider that a highly nonspherical object of size L will have quadrupole moment $D \simeq ML^2$. The second time derivative of D is then approximately $2Mv^2$ where v is the internal velocity of the object. This can be written $4E_{ns}$ giving for the strain amplitude

$$h \approx \frac{G}{c^4}\frac{4E_{ns}}{r} \tag{1.26}$$

where r is the distance to the source. The E_{ns} term will contain components due to the ellipticity of the star and perhaps a misalignment of the principal and spin axis too. By normalising to typical pulsar parameters, the strain amplitude may be written [5]

$$h \approx 6 \times 10^{-25} \left(\frac{f_{rot}}{500\,\mathrm{Hz}}\right)\left(\frac{1\,\mathrm{kpc}}{r}\right)\left(\frac{\epsilon}{10^{-6}}\right) \tag{1.27}$$

where f_{rot} is the frequency of rotation of the pulsar[3], r is the distance to the source and ϵ is the ellipticity of the star. Current models of neutron stars suggest maximum ellipticities in the order of 10^{-4} to 10^{-6}.

As shown above, in assessing the strength of a specific source, several aspects must be considered. For example the recently discovered PSR J0437-4715 is a pulsar rotating at a frequency of 173 Hz whose close proximity to earth (about 100 pc) makes it a viable source, even although its low spindown rate would normally render it undetectable. Another interesting candidate is the optical pulsar in the supernovae remnant SN1987A which is much further away (about 50 kpc) but is reported to have a higher spindown rate[4]. The rotation rate of this pulsar is reported to be 467 Hz. In the absence of a reliable neutron star model it is difficult to give concrete estimates for the strength of these sources, but it is expected that values of h in the order of 10^{-26} are not unlikely. In practice, a long integration period would be involved in order to search for a pulsar signal whereby the sensitivity is increased by the square root of the number of cycles averaged over[5]. For example a detector observing a pulsar producing signals at 500 Hz can be increased in sensitivity by a factor of

[3] note that the gravitational wave frequency will be twice the dynamical rotation frequency

[4] at the time of writing, the data regarding this pulsar are as yet unpublished.

[5] this is true for any continuous source being observed by a broadband detector

around 4×10^4 by integrating the signal over a period of one month. It will become evident in chapter 2 that this brings some pulsars within the sensitivity capabilities of the proposed long baseline interferometers.

Until recently the mean spatial velocity of pulsars was thought to be around $150\,\mathrm{kms}^{-1}$. However this result is now thought to be artificially low since it originates by measuring too many older pulsars with low birth velocities (which accumulate in the galactic plane). The new result is thought to be nearer $450\,\mathrm{kms}^{-1}$, perhaps even as high as $1000\,\mathrm{kms}^{-1}$, which is greater than the escape velocity from the galactic disc and perhaps even the entire galaxy [6]. The implications of this are numerous. For example, there may exist a halo of old pulsars around the galaxy, isotropic in the sky. This pulsar population may be the sites of some of the gamma-ray bursters that BATSE[6] mounted on the CGRO[7] has been studying since 1991 [7]. Gamma-ray bursters have the property that their source distribution is isotropic in the sky suggesting that they originate outside the galaxy. Most isotropic models for sources will therefore imply cosmological distances out to the burst sources. This immediately raises questions about the extremely high energies that would have to be involved to account for the signal strengths that BATSE detects. A local isotropic pulsar population is therefore certainly of interest to teams working on the BATSE results, and if gamma-ray bursts are accompanied by gravitational wave bursts, there may be broader implications for coincidence experiments.

Unfortunately very little is known about the number of pulsars which may be detectable. It could be said with reference to Eqn.(1.27) that all pulsars with ellipticity satisfying

$$\epsilon > 3 \times 10^{-10} \left(\frac{500\,\mathrm{Hz}}{f_{rot}} \right)^2 \left(\frac{r}{1\,\mathrm{kpc}} \right)^2 \tag{1.28}$$

will be detectable with a long baseline interferometer fitted with signal recycling. Exactly how many pulsars in the galaxy satisfy condition (1.28) is simply unknown at present. This may be one field of data that gravitational wave observatories will feed back to existing astronomy.

[6] Burst And Transient Source Experiment

[7] Compton Gamma-Ray Observatory launched by NASA in 1991

1.4.2 Coalescing Binary Star Systems

In 1993, Russell Hulse and Joseph Taylor received the Nobel Prize for physics for their observational work concerning the pulsar PSR1913+16. For the past two decades, they have been measuring the orbital period of this system, and have found that the spin-down fits exactly with that predicted due to gravitational radiation loss [8, 9]. This indirect evidence for gravitational waves may boost the moral of experimentalists in the field, but such radiation is too weak to be detected directly by ground based instruments. Only in the last few seconds of the life of a binary system do the stars become close enough to produce detectable amounts of radiation. During these last moments the stars produce a distinctive chirp signal of gravitational radiation where the signal frequency sweeps through the detector sensitivity window, up to a few kHz, with increasing signal amplitude. The stars must be small and dense, and so only binary systems containing neutron stars or black holes are of interest, often called *compact binaries.* The strain amplitude produced at a distance r from a binary star system can be expressed in terms of the orbital frequency and masses of the system by

$$h \approx 2.6 \times 10^{-23} \left(\frac{M_c}{M_\odot}\right)^{\frac{5}{3}} \left(\frac{f}{100\,\mathrm{Hz}}\right)^{\frac{2}{3}} \left(\frac{100\,\mathrm{Mpc}}{r}\right) \tag{1.29}$$

where f is the frequency of the radiation and M_c is called the *chirp mass* of the system defined by

$$M_c = \frac{(m_1 m_2)^{\frac{3}{5}}}{(m_1 + m_2)^{\frac{1}{5}}}. \tag{1.30}$$

This is the instantaneous value for h at a given frequency, however by using special filtering techniques the effective signal to noise ratio can be enhanced [10]. There is also information to be obtained from the time evolution of the signal, which is described by

$$\frac{d \ln f}{dt} = 0.126 \left(\frac{M_c}{M_\odot}\right)^{\frac{5}{3}} \left(\frac{f}{100\,\mathrm{Hz}}\right)^{\frac{8}{3}} \mathrm{s}^{-1} \tag{1.31}$$

It is apparent from Eqn.(1.29) and Eqn.(1.31) that if the strain amplitude can be measured as a function of frequency, and the rate of change of frequency deduced during the chirp event, then M_c can be eliminated to provide a value for r, the

distance to the binary system. Binary systems that change their frequency during an observation are thus standard candles in gravitational wave astronomy, since their distance can be determined from their intensity. If measurements of distance to binary systems can be associated with red-shift measurements using optical astronomy, then the Hubble constant could be determined to a high level of accuracy [11].

At present there are three known binary system *precursors*[8] whose orbital decay times are less than the age of the universe. The predicted event rate is one every 10^5 years in our own galaxy. To obtain a detected event rate of one every year, gravitational wave observatories would have to be able to see events out to a radius of 100 Mpc - likely to be possible only with interferometers fitted with signal recycling. Two independent exciting recent theoretical surveys [12, 13] suggest that there may exist a high-birthrate class of neutron-star binaries that form with closer separation of the companion stars than the Hulse-Taylor type systems. These binaries will decay on a much shorter timescale and the event rate could be as high as one hundred per year. The physics that will be revealed by coalescing binary systems depends on the types of the companion stars. In the case of two neutron stars, the coalescence will involve vast numbers of nucleons accelerating toward the speed of light. The driving mechanism is the self-gravity of the binary system and the gravitational waves produced will be characteristic of the nuclear processes taking place during the coalescence. If two black holes coalesce, the radiation emitted may well carry information about relativistic gravitational processes which could not ever be discovered in any other way. Similarly for a black hole and neutron star coalescence, where very little is known about the dynamics of such an event.

1.4.3 Gravitational Collapse and Supernovae

The prospect of detecting supernovae formed the basic motivation for starting development on resonant-bar detectors 30 years ago. Today they still represent one of the potentially most powerful sources, but like so many of the other mechanisms

[8] binary systems containing two neutron stars with orbital decay time less than the Hubble time

so far described, little is known about the dynamics of the explosions, particularly how asymmetric they may be. Supernova explosions are separated into two main classes; type I and type II. A type I supernova is thought to be associated with a binary system containing a white dwarf star that has accreted too much mass from its companion to remain stable. The resulting explosion blows the white dwarf star to pieces, and it is possible, but be no means certain, that the stellar core will collapse to form a neutron star. A type II supernova occurs when a massive star no longer has enough internal pressure to balance its own self-gravity resulting in a gravitational collapse that forms a neutron star or black hole. The remnant stars are left rotating by the explosion and in the case of neutron stars, these are of course pulsars.

The new result for the mean spatial pulsar velocity is promising because it provokes the question: how can the pulsars be born with such high initial velocities (several hundred $\mathrm{kpc\,s^{-1}}$)? The answer might lie in strong asymmetries intrinsic to the stellar collapse mechanisms that produce them, which would make supernovae very favourable gravitational wave source candidates. In general, for a burst event where the source loses energy E_{GW} through gravitational radiation emission, the strain amplitude can be expressed [4] as

$$h \approx 3 \times 10^{-20} \left(\frac{E_{GW}}{M_{\odot}c^2}\right)^{1/2} \left(\frac{1\,\mathrm{kHz}}{f}\right)^{\frac{1}{2}} \left(\frac{10\,\mathrm{Mpc}}{r}\right). \tag{1.32}$$

where f is the characteristic frequency of the burst of radiation and the formula has again been normalised, this time to a distance scale of 10 Mpc which is approximately the distance to the centre of the Virgo Cluster. Estimates of E_{GW} for supernovae range dramatically in value but in order for events to be detectable by the first generation of long baseline interferometers ($h \sim 10^{-22}/\sqrt{\mathrm{Hz}}$ at 100 Hz) the condition

$$E_{GW} \gtrsim 7 \times 10^{32}\mathrm{J} \times \left(\frac{10\,\mathrm{kpc}}{r}\right)^2 \tag{1.33}$$

should be satisfied. Occurrence rates for supernovae are thought to be about one of each type every fifty years in our galaxy[9]. In the region out to the Virgo cluster there

[9]this represents a catchment sphere of radius $\approx$ 15 kpc and takes into consideration the fact that only a fraction of supernovae are actually observable due to the opacity of the galactic plane

will be several of each type each year. Beyond the Virgo cluster, the occurrence rate will increase roughly as the volume of space (r^3). That is not to say that optical astronomy would detect this rate of events, since supernovae that are electromagnetically quiet, or hidden deep in dense clouds, are included in the above figures. In view of condition (1.33) and existing models for stellar collapse, event rates ranging from one per year to many per year have been suggested. If a gravitational wave burst from a supernova explosion was accompanied by an optical observation, then the relative time of arrival of the signals would test the velocity of gravitational radiation to high precision. Such a coincidence observation would form an important and unique test of gravitation theory.

An interesting variety of gravitational collapse is when a massive star collapses to form a black hole. In this scenario it is thought possible to have an energy conversion efficiency to gravitational radiation of up to 10% [4]. In other words, the ratio ϵ of energy emitted from the collapse through gravitational waves E_{GW} and the total available energy of the star Mc^2 is $\epsilon = 0.1$. The strain amplitude in terms of ϵ can be written

$$h \approx 10^{-18} \left(\frac{\epsilon}{0.01}\right)^{\frac{1}{2}} \left(\frac{M}{M_\odot}\right) \left(\frac{10\,\mathrm{kpc}}{r}\right) \tag{1.34}$$

where the expression has been normalised to the more modest value of $\epsilon = 0.01$. Even this lies in the upper range of values and if the collapse is axisymmetric, then it is more likely for ϵ to take values in the range 10^{-3} or less. Nevertheless such sources are of interest for the first generation of laser interferometic detectors, and particularly for the advanced designs like that of GEO 600 where signal recycling will allow for sensitivity optimisation at selective characteristic frequencies.

Even if a stellar collapse happened to be totally spherically symmetric it is thought to produce an unstable neutron star that undergoes convective boiling for the first fraction of a second of its life. In this process, super-energetic nucleons from the centre of the star are forced to the surface where they cool by neutrino emmision before being swept back again toward the centre. It has been estimated [14] that about ten cycles of gravitational radiation may be produced by this process at a frequency of about 100 Hz. The strain amplitude will be such as to be just

detectable, but only for sources in the local group of galaxies.

1.4.4 Low Frequency Sources

Most of the astrophysical events so far described are either burst sources (like coalescing binary systems and supernovae) or are high-frequency emitters (such as fast rotating pulsars). The emphasis on these has been deliberate since they form the most likely detectable candidates for the first generation of laser interferometer detectors and for existing bar detectors. However there are various sources characterised by lower gravitational radiation frequencies, say less that 1 Hz, that would not be detectable from ground based observatories (where the low frequency seismic noise becomes too high). Such sources would be observable from a space-based interferometer and there is a proposal submitted to the European Space Agency called LISA[10] which will take the form of an interferometer formed between satellites with arm length 5×10^6 km. The satellites (six of them in total) will form an equilateral triangle with two satellites at each vertex and the entire system will follow the earth in its orbit around the sun (but lagging the earth by about 20°) forming a plane inclined at 60° to the ecliptic. The strain amplitude sensitivity of LISA will be primarily limited at low frequencies by spurious accelerations of components and at high frequencies by photon counting statistics or *shot noise* in the laser light. The noise budget should allow strain sensitivities for continuous sources of around 10^{-21} to 10^{-23} over the frequency range 10^{-4} Hz to 10^{-1} Hz with optimal sensitivity roughly lying in the middle of this range.

The technology involved in the project is highly advanced with many research groups tackling various experimental challanges. For example, one problem is the tiny light power captured by the far spacecraft. If 1 W of laser power is used with a divergence of 4×10^{-6} rad then the radius of the beam after travelling 5×10^6 km is around 20 km! The capture area of the far spacecraft has radius about 0.2 m and so the fraction of 1 W in this cross-section is only $0.4^2/(2 \times 10^4)$. This amounts to at most a few hundred pico-Watts detected at the far spacecraft. Clearly, the far

[10] Laser Interferometer Space Antenna

spacecraft cannot contain just a simple mirror (for the reflected light power arriving back at the first spacecraft would be effectively zero) but rather it must sense the phase of the incoming light and return a laser beam of its own. This action can be thought of in terms of an *active mirror* which amplifies the incoming light and sends back a beam that is *phase-locked* to it. Further details regarding the LISA project can be found in [15]. Some of the sources it hopes to detect are now briefly outlined.

Binary Star Systems

The gravitational radiation emitted by a binary system is only detectable from ground during the last few moments before the coalesence, when the signals sweep through the sensitivity band of ground based instruments. However LISA could observe such systems over a long integration time (in rather the same fashion as a ground based detector could integrate signals from a pulsar). Binary star systems of interest may contain neutron stars, black holes or white dwarfs orbiting about each other at frequencies of 10^{-4} Hz to 10^{-1} Hz. The recent theoretical studies of binary evolution [12, 13] suggests that there should exist a dense population of binary systems (prototyped by the Hulse-Taylor system PSR1913+16) that have initial periods as short as an hour. The rate of change of the orbital frequency f of such a system can be calculated using Eqn.(1.31). If this equation is used with parameters typical of the new population of binaries, it turns out that spin-down times in the order of a few thousand years could be expected for some systems. This amounts to an orbital period decay of some 10^{-2} s per year, which is easily discernable by LISA[11].

Black hole binaries in their steady state are also of interest to LISA. Since black holes lose less mass when they are created it is expected that there is less chance of their creation disrupting a binary system and so there may be as many black hole/neutron star binaries as there are neutron star/neutron star binaries [16].

The evolution of close binaries is thought to end most commonly with the creation of two low mass white dwarf stars. LISA will be able to clarify the evolutionary

[11] compare this value with the Hulse-Taylor system which decays at a rate of 7.2×10^{-5} s per year

model by observing such systems. An interesting class of white dwarf binary system is the Interacting White Dwarf Binary (IWDB). These are binaries where a low mass degenerate helium star is transferring mass to a more massive compact star. There are four prototype systems having periods in the order of 1000 s which makes them good source candidates for LISA.

Extragalactic Sources

The primary sources of importance outside our galaxy almost all involve black holes. Binary systems and events such as merger, formation or interactions with other objects involving supermassive black holes are all of interest. Some galactic models suggest the existence of supermassive black holes at the centre of the galaxies. There is evidence both from ground based telescopes and the Hubble space telescope [17] that there exists a massive black hole near the centre of the dwarf elliptical galaxy M32. If this is true, it could be the prototype for many galaxies. Mergers between a black hole or other compact object, and a supermassive black hole, is believed to produce large quantities of gravitational waves. When a body of mass m spirals into a massive black hole of mass M it can be shown [5] that the time to final coalescence is inversely proportional to m/M. This means that less massive bodies merging with a black hole will stay in orbit around it for longer (and the frequency on average will be lower) and will send out a longer temporal sample of radiation. The problem for ground-based observations is that for the inspiral rates to be above the low-frequency sensitivity barrier, a peak value of $m/M \approx 1/300$ is implied. LISA with its low frequency sensitivity, should be able to detect signals from systems with $m/M < 10^7$ thus covering a far greater sample of black hole events from which to study relativistic gravity.

Primordial Gravitational Radiation

In addition to compact body sources there may exist a *stochastic background* of gravitational radiation generated by processes going on in the early universe. The frequencies of radiation associated with such a background could scale over 22 orders

of magnitude. There are several options for sources.

Most interestingly, there is the background due to the big bang. The strain amplitudes present today are difficult to predict because the radiation has to be tracked through the early epochs of the universe. There might also be contributions from phase transitions in the early universe and from cosmic strings if they existed in the early universe. Details concerning primordial sources can be found in [5, 18, 19, 20, 21, 22].

1.4.5 Conclusion

The previous sections have described some of the most traditional sources for the gravitational wave community to explore. These have been related to more recent theoretical and experimental developments from astronomers, not necessarily involved in the field. The emergence of LISA as a space-borne observatory has been discussed and in passing it should be emphasized that LISA is not in competition with terrestrial detectors but rather will provide data in a frequency band complementary to the ground-based instruments.

Chapter 2

Gravitational Wave Detectors

2.1 Introduction

For many years after the publication of general relativity there were conflicting views upon whether gravitational radiation really existed. Doubts existed over whether it could really carry energy away from a body, or impart energy to matter in its path. The theoretical surveys of [23, 24, 25] and more importantly, the observations from the Hulse-Taylor binary, have totally cast these doubts aside. However it is true that the interaction of gravitational waves with matter is very weak. The problem is that spacetime is a medium of extremely high *stiffness*, characterised by a huge impedance term c^3/G. It follows that gravitational waves propagating in this medium encounter neglible *extra* impedance in propagating through matter. This is unfortunate, since any possible invention to detect directly the waves must surely rely on some degree of interaction between the waves and the apparatus. Consequently, successful detectors have to maximise this interaction for the duration of the waves, and must be designed accordingly.

This chapter contains an overview of the types of detector already in use, and those being planned for the future. In section 2.2 resonant-bar detectors are briefly discussed and in section 2.3 laser interferometers are described. Some of the sources of noise that affect a laser interferometer are introduced via subsections of section 2.3. To obtain numerical examples of these noise limits in terms of interferometer sensi-

tivity, some of the properties of the German-British GEO 600 detector will be used. The chapter ends with a more detailed description of the GEO 600 detector in section 2.4 including a brief review of some advanced interferometric techniques such as power and signal recycling.

2.2 Resonant-Bar Detectors

The performance and complexity of resonant-bar detectors has advanced considerably since Weber's first designs. Using the simplest description, a resonant-bar detector is a large mass usually made of some sort of metal, suspended from a seismic isolation system to protect it from ground motion. When a gravitational wave passes through the bar it induces a strain in it. The strain momentarily alters the proper length of the bar however this in itself cannot be measured (since any transducer placed, say, at the end of the bar to measure the motion will itself move due the wave) but the *ringing* that persists in the bar after the initial strain can in principle be detected (since any similarly placed transducer now remains static compared with the bar). This subtlety associated with the detection process is sometimes referred to as the bar having *memory*. Since the process involves exciting the self-resonance of the bar, the system is primarily sensitive to gravitational radiation with Fourier components at the bar's self-resonant frequency (and perhaps harmonics). Consequently, resonant-bar systems are often referred to as *narrow-band detectors*.

2.2.1 Design Aspects of Bar Detectors

In view of the source strengths presented in the last chapter it is necessary for a bar detector to be able to measure length changes of order 10^{-20} m over millisecond timescales to be astrophysically useful. This is roughly 1/1 000 000 th the diameter of an atomic nucleus, and about 1/1 00 000 000 000 th the diameter of an atom! Clearly, the slightest random motion of the atoms of the bar due to their kT thermal noise modes will far exceed this required displacement sensitivity. To reduce the thermal noise the bar is cooled to a few degrees above absolute zero. Even then, the thermal vibration causes displacements around 1000 times larger than those caused by grav-

itational waves. The solution to this seemingly insurmountable problem relies on another detection subtlety associated with the resonance of the bar. The thermal noise can give rise to displacements which can only change over the timescale of the ring-down time τ of the bar[1]. If τ is large then in a given small time interval (comparable with one period of a typical gravitational wave) the vibrational amplitude change caused by the thermal noise *can* be less than that caused by the wave. The condition is that the measurement has to be performed in a small time interval compared with τ. The larger is τ the greater signal to noise for a given measurement interval there will be. This can be summarised

$$E_{noise} = kT\frac{\tau_m}{\tau} \tag{2.1}$$

where E_{noise} is the thermal noise energy, kT is the energy in an atomic thermal mode and τ_m is the measurement integration time. The demand for a high ring-down time is often expressed as the system requiring a *high Q-factor*. To obtain a system with a high Q the bar is suspended in an evacuated chamber so that the effect of air pressure is absent. The suspension system itself has to be of high quality, so that energy from the bar is not dissipated to it, thus reducing the Q. To obtain quantum-limited sensitivity in a bar at 4.2 K[2] for gravitational wave periods of 1 ms, Eqn.(2.1) can be used with E_{noise} set to $2\pi\hbar f$ to show that $\tau \approx 10^5$ s. The first bar detectors used aluminium with $\tau \approx 100$ s. Other materials such as niobium, silicon and some aluminium alloys have much higher Q values. Sapphire has an extremely high Q ($\approx 10^9$) but measured in bars so small that the resonant frequencies are typically tens of kHz. Materials like sapphire and silicon which have very pure crystal structures cannot easily be made into the large bars that are required for bar detectors.

As well as the design considerations of the bar itself, there are also those for the transducer. The transducer is the component that ultimately provides the output electrical signal corresponding to the minute displacements described above. It is evident from Eqn.(2.1) that another way to minimise the level of thermal noise

[1] the time it takes the amplitude of bar vibrations to decay to $1/e$ their initial value

[2] this is the temperature of a bar cooled using liquid helium

present in the measurement process is to have a very small measurement integration time τ_m. However this implies a large measurement bandwidth, and thus the white noise associated with the transducer becomes problematic. In practice there is a balance to be reached between measurement integration time and the achievable sensor noise.

When bar detectors were first developed, no transducers were available to measure displacement amplitudes anything like as small as 10^{-20} m. Over the years, transducer technology has evolved, with piezo-electric devices being replaced with more advanced sensors. One type of modern sensor uses an electrical capacitor or inductor whose value is modulated by the motion of the bar. An electrical signal of very small magnitude is generated and sent to an ultra-low noise amplifier called a SQUID[3].

As mentioned above, a problem associated with all forms of transducer is their intrinsic white noise, characterised by a constant value of noise power per unit bandwidth. Available transducers are not able to detect the small vibrations of the bar induced by gravitational waves. The motion of the bar must be amplified by some mechanical means, and the solution is to develop the bar as a coupled oscillator by the attachment of a very small additional resonator. When the bar is excited, some energy is transferred to the smaller oscillator which may take the physical form of a diaphragm, flap or whip. The transducer then senses this higher frequency motion which has greater amplitude. Such techniques have provided optimal measurement integration times of around 0.1 s for resonant-bar antennae.

Another source of noise associated with the measurement process is *back-action noise.* This is produced due to the input current noise of the amplifier that comes after the transducer in the measurement system. Basically, this noise can be thought of as a signal that appears across the transducer, causing a subsequent force noise that acts on the antenna. The resulting excitation of the bar is another noise source that the transducer will detect. Back-action evasion techniques have been studied and implemented on bar detectors. Details of these, along with further information

[3]Superconducting QUantum-Interface Device

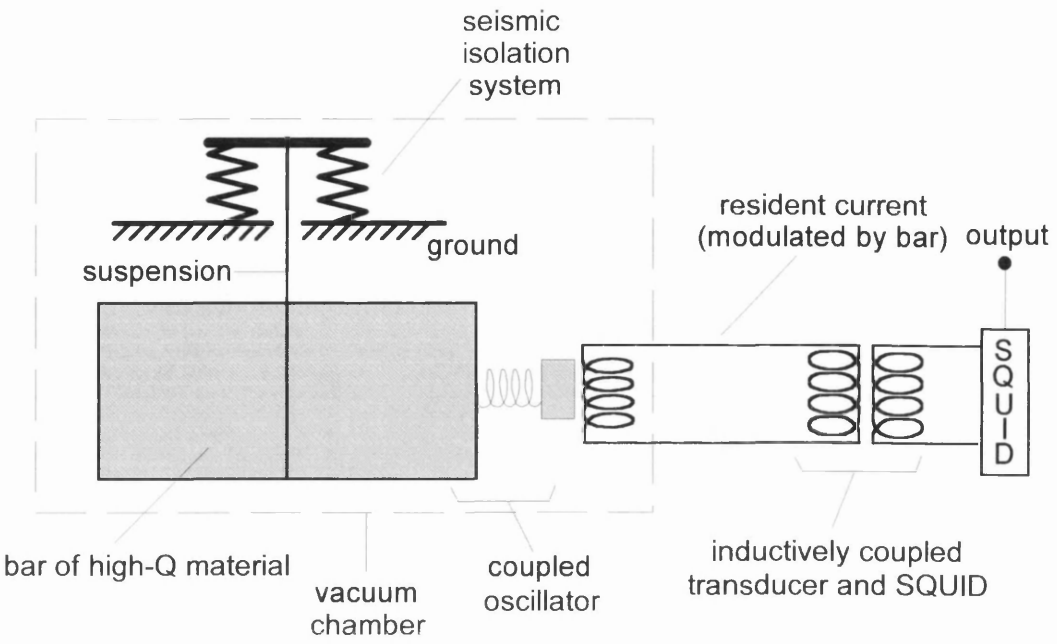

Figure 2.1: *Schematic diagram of the resonant-bar detector using a inductively coupled transducer and a SQUID amplifier.*

and references regarding other aspects of resonant-bar detector design, can be found in [26]. A schematic diagram of a possible configuration of resonant-bar antenna is shown in Fig.2.1.

2.2.2 Sensitivity of Resonant-Bar Detectors

When a gravitational wave interacts with a bar detector it usually excites the first longitudinal mode of the detector, the frequency of which is given by $f_0 = v/2L$ where v is the velocity of sound in the bar and L is the bar's length. The transducer can be considered to transform a given displacement on the bar's end wall δx into an electrical signal V. In practice there is the coupled oscillator action to take account of, but the transducer can still be regarded as obeying a transfer function of the form $V = k\delta x$ for some constant k. It can be shown [4] that the strain amplitude sensitivity h_b for a burst of gravitational waves of optimal direction and polarisation can be written

$$h_b = \left(\frac{kT\tau_b}{2\pi f_0 MQL^2} \right)^{\frac{1}{2}} \tag{2.2}$$

where k is the Boltzmann constant ($k = 1.38 \times 10^{-23}\mathrm{J/K}$), τ_b is the duration of the burst, L is the length of the bar, M is the mass of the bar and Q is the quality factor of the bar. For a bar with $M = 1000\,\mathrm{kg}$, $L = 3\,\mathrm{m}$, $Q = 10^5$, $f_0 = 1\,\mathrm{kHz}$ cooled to 4 K and measurement sample time of 0.1 s, Eqn.(2.2) amounts to a strain sensitivity of around $10^{-18}/\sqrt{\mathrm{Hz}}$. This number emphasises the challenges that bar detector designers face in reaching useful sensitivities. Groups at the University of Rome and at Stanford have developed cryostats that will enable bars to be cooled to $\sim 50\,\mathrm{mK}$ allowing a strain sensitivity of $10^{-19}/\sqrt{\mathrm{Hz}}$ to be reached. It is hoped that sensitivities approaching $10^{-20}/\sqrt{\mathrm{Hz}}$ will be possible with improved SQUID devices.

An exciting development in bar detector technology has been the design and study of a spherical bar system which would contain a number of resonant spheres, all having different resonant frequencies, forming a sort of 'xylophone' detector of gravitational waves. Such an array would help reconstruct detected waveforms better than a single bar could. Each sphere would have a much greater mass than the bars currently in existence. A 15 tonne sphere can have approximately the same resonant frequency as a 1 tonne bar, and will thus have 15 times the energy cross-section for gravitational radiation. The surface area of such a sphere is only a factor 2 to 3 more than the bar, and so there is only a relatively modest increase in the dimensions of the cryostat required. Perhaps the major advantage of the resonant sphere detector is that it has five modes of resonance, each aligned with one polarisation of the metric tensor [27] making it the most efficient resonant mass detector of gravitational radiation. It is estimated [28] that such a system may reach strain sensitivities in the order of $10^{-22}/\sqrt{\mathrm{Hz}}$ or better. There is a growing international collaboration to construct and develop such spherical mass detectors. A popular design for the precise shape of the masses is the truncated icosahedron[4] [29]. The Universities of Rome and Leyden are interested in developing a massive 3 m diameter copper alloy sphere. They plan to cool the mass to only 10 mK, using the experience of the low temperature physics groups at Leyden.

Resonant-bar detectors still have a role to play in the worldwide gravitational

[4] this provides the TIGA acronym representing Truncated Icosahedron Gravitational wave Antenna.

wave detector network, part of the reason being their geographical locations. In a coincidence experiment where data from, say, two detectors is correlated, it turns out that the correlated stochastic source sensitivity falls off as a function of the ratio of gravitional radiation wavelength and detector separation [30]. It may therefore be advantageous to have correlated observation sessions between an interferometer and a nearby bar detector, since almost all of the planned long-baseline interferometers are separated by large distances compared with the wavelengths of gravitational radiation on millisecond timescales. The exception is the American LIGO[5] project which has the scope for multiple laser interferometer detectors at one site.

2.3 Laser Interferometers

The idea of using laser interferometry to detect gravitational waves was first described by Weber and Forward [31]. The basic scheme is illustrated in Fig 2.2 and can be regarded as a Michelson interferometer with two perpendicular arms. A *relative* or *differential* fluctuation δL in the arm lengths will result in a phase shift $\delta\phi$ between the recombining beams at P given by

$$\delta\phi = \frac{2\pi}{\lambda}\delta L \tag{2.3}$$

where λ is the wavelength of the light. A photodiode placed at P will register the phase change as a fluctuation of intensity. For a given δL it can be seen from Eqn.(2.3) that smaller λ will give rise to larger $\delta\phi$ and hence greater sensitivity. Of the two most common lasers used, Nd:YAG types ($\lambda = 1064\,\mathrm{nm}$) are more stable and capable of delivering higher powers than argon ion lasers ($\lambda = 514.5\,\mathrm{nm}$), however all prototype detectors with good sensitivity are driven by argon ion lasers, largely because they were developed around this type of laser over many years. In view of the wavelength consideration (and indeed for ease of aligning optics) it would be ideal to have a green laser but with the stability and power of an infra-red system. Much research has been done with *non-linear crystals* with a view to *frequency doubling* Nd:YAG lasers to produce a stable $\lambda = 532\,\mathrm{nm}$ source [32, 33].

[5] Laser Interferometer Gravitational wave Observatory.

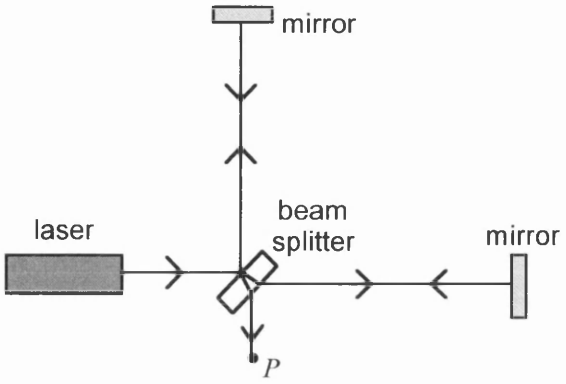

Figure 2.2: *Simple diagram of a Michelson interferometer.*

In view of typical astrophysical source strengths (see chapter 1) interferometers really need to have strain sensitivities in the order of $10^{-22}/\sqrt{\text{Hz}}$ from a few tens of Hz to several hundred Hz. This figure will be kept in mind throughout the next few sections when considering the various noise sources that have to be overcome.

Now, for a prototype laser interferometer to progress to a working detector, it must be more sensitive to arm length changes caused by gravitational waves than any other influence, at least in a given measurement integration time. To achieve this, all the components in the interferometer are shielded from ground motion using seismic isolation systems. Most components are suspended as pendulums, even as double pendulums, to provide a very sharp mechanical filter for low frequency vibration. The mirrors are of the highest quality with respect to absorptance and scatter loss (see chapter 4) and are directly coated onto test masses. The test mass material must be of very high Q so that thermally excited vibrational modes are channelled into as narrow-band a frequency range as possible. The arms must be of suitable length to ensure optimal interaction time with the gravitational wave (see section 2.3.1). The laser used must be highly stabilised in order that its intensity noise, beam geometry noise (chapter 5) and frequency fluctuations do not degrade the sensitivity. Finally the entire apparatus must be enclosed in a huge vacuum system to suppress acoustic noise and allow a clean path for the laser light. These demands define a set of experimental challenges which has kept research teams busy for many years. The laser interferometer as it looks for gravitational wave experiments is shown in Fig 2.3.

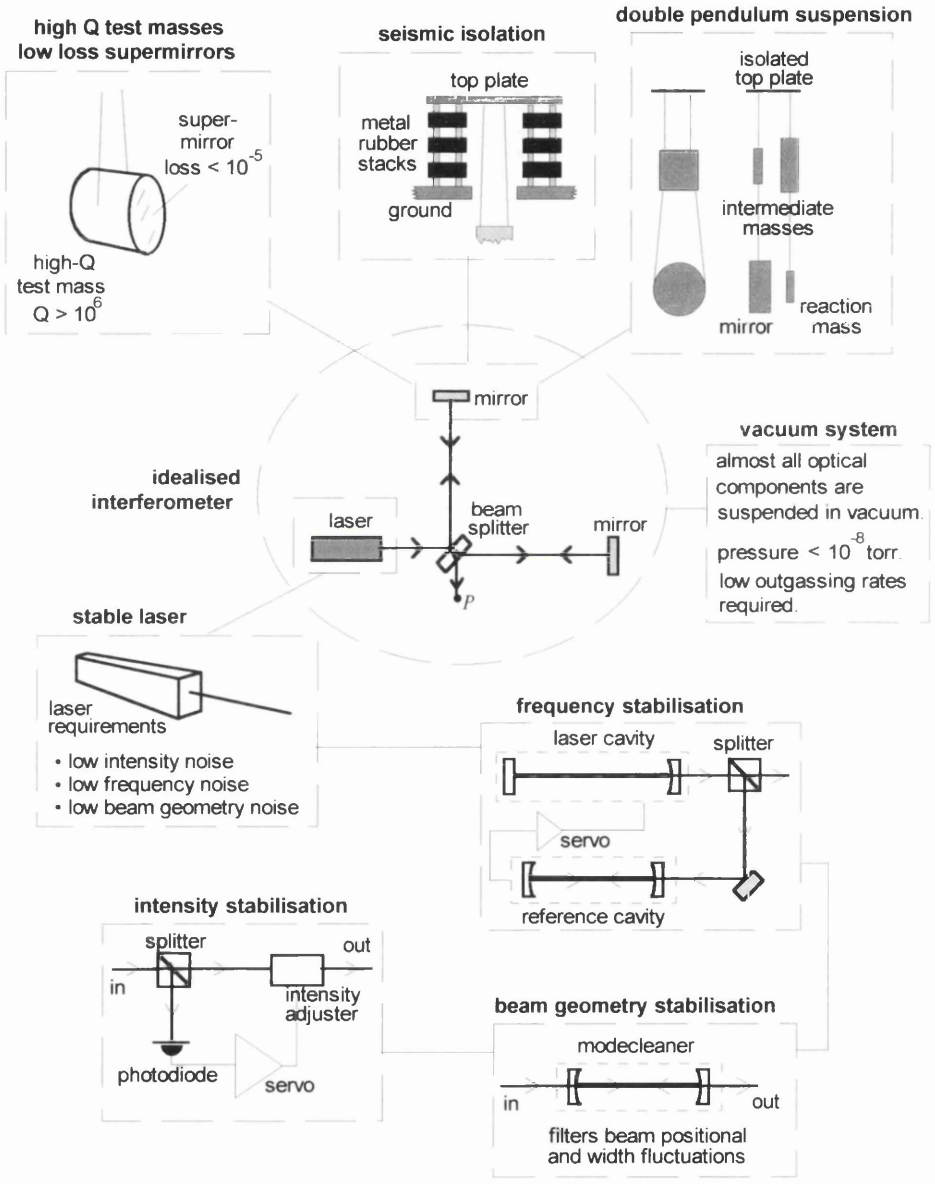

Figure 2.3: *The simplified interferometer with its many hidden complexities revealed.*

2.3.1 Interferometer Basics

By referring back to Fig 1.1 and visualising the 'L' shape of an interferometer superposed onto the test ring, it can be seen how appropriate it is to sense the length of one arm with that of a perpendicular arm. To investigate the interaction more closely consider a periodic gravitational wave signal of frequency f_g and amplitude h_0. In view of Eqn.(1.23) the effect on a length L can be expressed

$$\frac{\delta L}{L} = \frac{h_0}{2} \sin(\omega_g t) \tag{2.4}$$

where $\omega_g = 2\pi f_g$. Using Eqn.(2.3) an expression for the phase $\Delta\phi(\tau)$ acquired by light traversing the distance L in a transit time τ can be written as

$$\Delta\phi(\tau) = \frac{2\pi}{\lambda}\frac{1}{\tau}\int_0^\tau L\frac{h_0}{2}\sin(\omega_g t)\,dt \tag{2.5}$$

where the displacement has been integrated and normalised over τ. After performing the integration and some simplification, Eqn.(2.5) becomes

$$\Delta\phi(\tau) = \frac{c}{\lambda}\frac{h_0}{2}T_g\left[1-\cos(2\pi\frac{\tau}{T_g})\right] \tag{2.6}$$

where the gravitational wave frequency ω_g has been replaced by the period $T_g = 2\pi/\omega_g$. A gravitational wave of suitable direction and polarisation causes exactly the opposite phase change in the other arm and there is actually a $2\Delta\phi$ phase shift between the recombining beams. Eqn.(2.6) carries most of the information required to design a suitable interferometer. It is instructive to consider at what times $\Delta\phi(\tau)$ passes through maxima, and at what times it is zero. Eqn.(2.6) can be used to show that

$$\Delta\phi_{max} \Rightarrow \tau = \frac{T_g}{2}, \frac{3T_g}{2}, \ldots \tag{2.7}$$

$$\Delta\phi(\tau) = 0 \Rightarrow \tau = 0, T_g, 2T_g, \ldots \tag{2.8}$$

These conditions are due to the effect of the phase change on the light reversing sign after half a period of the gravitational wave (consider Fig 1.1). The optimum situation is when light spends a time $T_g/2$ in the interferometer. It follows that if a detector is to be optimised for signals at 1 kHz then the light must travel for 5×10^{-4} s corresponding to a optical path length of 150 km. If the light were to

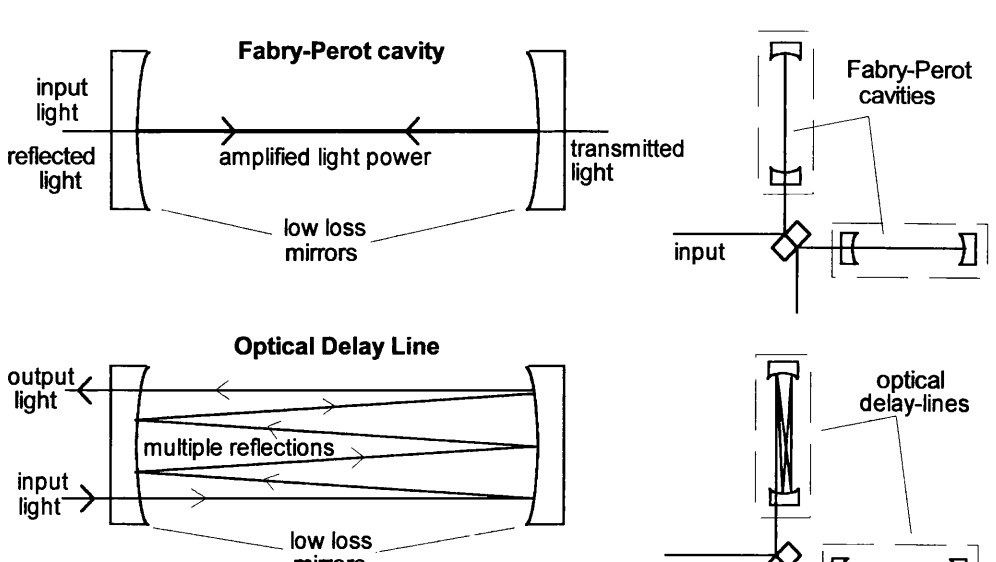

Figure 2.4: *Methods for storing the light in the arms of the interferometer to optimise the interaction time with a gravitational wave.*

undergo just one return trip in the arm, this would imply an arm length of 75 km - clearly impractical. Two methods of delaying the light within a much shorter distance have been employed. These are the *optical delay-line* and the *Fabry-Perot cavity* shown in Fig 2.4.

The optical delay-line is the scheme chosen for use in the GEO 600 detector and will be discussed in more detail in section 2.4. The Fabry-Perot cavity was first considered in the context of gravitational wave research by R. Drever. The effective arm length L in the presence of a delay-line is Nl where N is the number of beams and l is the physical length of the system. However in the case of a Fabry-Perot, the concept of effective arm length is better replaced by the *storage time* of the light in the cavity. By choosing Fabry-Perot cavity mirrors with suitable power reflectance and transmittance coefficients it is possible to arrange a storage time that is comparable with half the period of the gravitational wave signals as shown above to be the optimal case. The properties of Fabry-Perot cavities will be described in detail in chapter 3. However, even although the GEO 600 detector uses delay-lines in the arms, the role of the Fabry-Perot cavity is still important when considering

power and signal recycling schemes, as will become evident in section 2.4.

Regardless of the specific design of the interferometer, the recombining beams can be expressed via the amplitude terms E_1 and $E_2 e^{i\phi}$ where ϕ is the phase difference between the interfering beams and where $E_1 = E_2$ for a perfectly symmetric system. The light power at the photodiode $P(\phi)$ is given by

$$P(\phi) = \frac{P_0}{2}(1 + \cos\phi). \tag{2.9}$$

By taking differentials Eqn.(2.9) becomes

$$\Delta P = \frac{-P_0}{2} \sin\phi \, \Delta\phi \tag{2.10}$$

where ϕ can be regarded as a static phase difference set by the optimal operating point of the interferometer and $\Delta\phi$ is a fluctuation in phase caused for example by a gravitational wave. It can be seen from Eqn.(2.10) that for a given $\Delta\phi$ the maximum ΔP corresponds to $\phi = \pi/2$ (an interferometer locked half-way up an output fringe). In this case the output power is

$$P = \frac{P_0}{2}(1 + \cos(\frac{\pi}{2} + \Delta\phi)) \tag{2.11}$$

and the deviation in power due to a fluctuating phase is

$$\Delta P = -\frac{P_0}{2}\Delta\phi. \tag{2.12}$$

From Eqn.(2.12) and Eqn.(2.6) the maximum gravitational wave signal can be seen to be

$$\Delta P_g = \frac{2\pi P_0 c h_0}{\lambda \omega_g} \tag{2.13}$$

where the gravitational wave angular frequency has been used here. As will be indicated in the next section, although operating an interferometer half way up a fringe gives the best output signal size, it does not provide the optimum signal to noise ratio.

2.3.2 Fundamental Noise Sources

A fundamental noise source is one which sets a sensitivity limit for a *given configuration of apparatus* that cannot be lowered by *technical improvements* to the system.

This definition is worded carefully, since *in principle* it is always possible to lower fundamental noise barriers but *in practice*, it may not be possible to do so. The following descriptions might help clarify this distinction.

Shot Noise

Whenever photons are incident at a photodiode, the detection process is subject to a Poisson statistical counting error called *shot noise*. If n photons arrive in a time τ, then the error is proportional to $\sqrt{n}$. This stems from the relation $\delta Q = \sqrt{kQ/\Delta t}$ which expresses the noise δQ in a measured quantity Q due to the error in counting individual quanta (k) of the measure Q over an integration time Δt. In the case of an electric current, $k = e$ (the charge on an electron) and in the case of light power $k = 2\pi\hbar f$ (the energy of a photon of frequency f). In terms of measuring the steady state light power ($\Delta\phi = 0$) at the output of an interferometer, Eqn.(2.11) gives

$$\delta P = \sqrt{\frac{2\pi\hbar c P_0(1+\cos\phi)\Delta f}{\lambda}} \tag{2.14}$$

where $\hbar$ is the reduced Planck's constant (1.055×10^{-34} Js) and the measurement integration time has been replaced by the equivalent bandwidth ($\tau = 1/2\Delta f$). By dividing Eqn.(2.10) by Eqn.(2.14) the signal to noise ratio for the interferometer output can be derived. This contains a ($\sqrt{1-\cos\phi}$) factor showing that the greatest signal to noise ratio is obtained with $\phi = \pi$; that is, when the interferometer is locked to a null fringe. In practice this is how such systems are usually operated and modulation techniques are used to keep the interferometer locked in this state. For now though, the value $\phi = \pi/2$ shall be retained. The limiting sensitivity occurs when the shot noise δP becomes comparable with the maximum interferometer output signal ΔP_g given by Eqn.(2.13). By setting these equal Eqn.(2.14) and Eqn.(2.13) lead to a minimum strain sensitivity h_{min} given by

$$h_{min}^2 = \frac{\hbar\lambda\omega_g^2\Delta f}{2\pi\xi P_0 c} \tag{2.15}$$

where P_0 has been replaced by ξP_0 where ξ is the quantum efficiency of the photodetector and gives the fraction of P_0 actually detected. The value of ξ ranges from

50% to near 100% depending on the photodiode, and is strongly dependent on wavelength. It usually peaks in the visible spectrum where the light quanta and typical photodetector band-gaps are well matched. Eqn.(2.15) shows that the minimum detectable strain amplitude varies inversely as the square root of the laser power. So although shot noise is regarded as a fundamental limit, its effect can be reduced by using higher light powers. However laser capabilities have limitations too, and so experimentally it will not be possible to lower the shot noise limit indefinitely. As an example of the shot noise limit, consider a simple Michelson interferometer being powered by a 5 W Nd:YAG laser ($\lambda = 1064\,\mathrm{nm}$). The shot noise limit amounts to a strain sensitivity of $\sim 8 \times 10^{-23}/\sqrt{\mathrm{Hz}}$ at 100 Hz, which is just sufficient for the target sensitivities of the first generation of interferometric detectors. As will be discussed in section 2.4 this shot noise limit will be achieved in the GEO 600 detector by the use of power recycling, which allows the laser light to accumulate in the interferometer system. For increasing light power, the signal rises as the power P but the shot noise given by Eqn.(2.14) rises as $\sqrt{P}$ and therefore there is an overall advantage in having greater light powers.

Heisenberg Uncertainty Limit

There is a fundamental limit on how accurately the distance between two independent test masses can be measured set by the Heisenberg uncertainty relation

$$\Delta x \Delta p \geq \hbar \tag{2.16}$$

where Δx and Δp is the change in position and momentum of the test masses respectively. Each mass M undergoes a nominal displacement Δx in a given measurement time τ. By considering the effective force that acts on each mass it is possible to deduce a displacement noise for the *relative* positions of the masses [34]. This limit can be expressed in terms of the minimum gravitational wave strain amplitude h_{min} by

$$h_{min}^2 = \frac{2\hbar}{ML^2\pi^2 f^2}\Delta f \tag{2.17}$$

where L is the physical arm length of the interferometer (defined by two independent suspended components), $\hbar$ is the reduced Planck constant and τ has been expressed

in terms of the measurement bandwidth $\tau = 1/(2\Delta f)$. The very different frequency characteristics of shot noise and Heisenberg uncertainty noise can be seen from comparing Eqn.(2.17) with Eqn.(2.15). The Heisenberg limit is more of a problem for low frequency signals. Although a fundamental limit, it can be suppressed by using very heavy masses, but this is again limited by experimental considerations. As an example, the test masses in the GEO 600 detector weigh 16 kg and the arm length is 600 m, thus the limit imposed by the Heisenberg uncertainty relation is $\sim 2.6 \times 10^{-23}/\sqrt{\text{Hz}}$ at 100 Hz. To get this figure, Eqn.(2.17) is modified by a further factor of 2 because of the number of independent components defining the length of each GEO 600 arm (see Fig 2.6). At lower frequencies, the Heisenberg limit increases, but the magnitude of other effects, especially seismic noise, will dominate.

2.3.3 Technical Noise Sources

Of the various sources of technical noise in a laser interferometer those associated with thermal excitations of the test masses seem the most likely to limit the sensitivity. Laser noise sources have largely been defeated using advanced servo systems providing ultra-high stability intensity and frequency performance, even for noisy argon ion lasers. Nevertheless it is instructive to consider, if only briefly, the effects that technical noise sources can have on interferometer sensitivity.

Seismic Noise

An unavoidable source of noise for all terrestrial detectors is the motion of the ground itself. For a relatively quiet site this motion can be expressed through the empirical relation

$$\delta x = \frac{10^{-7}}{f^2}\,\text{m}/\sqrt{\text{Hz}}. \tag{2.18}$$

In terms of strain sensitivity, the right hand side of Eqn.(2.18) would be divided by the effective length of the detector arm to give the resulting limit as a function of frequency. For the GEO 600 detector, the seismic noise represents a strain sensitivity limit of $\sim 10^{-14}/\sqrt{\text{Hz}}$ at 100 Hz. To obtain a strain sensitivity of $10^{-22}/\sqrt{\text{Hz}}$ there must be a seismic isolation system affording a suppression of over 10^8 at 100 Hz. Al-

though this sounds like a huge suppression factor, it can be achieved with carefully designed suspended test masses hanging from a top plate supported on a multi-layer metal/rubber isolation stack. With such a design, a factor of $\sim 1/f^2$ suppression is gained for each suspension stage after its resonant frequency and a factor of $\sim 1/f$ for each stage in the metal/rubber stack after the stack resonances, which can be kept down to a few Hz. If such resonances are kept low, then a considerable factor of suppression is achievable even at a few tens of Hz [35].

Laser Frequency Noise

If the laser light undergoes a frequency deviation Δf from its nominal value f then this couples directly into an apparent length change in each arm of the interferometer. In itself this would not affect interferometer sensitivity because only *differential changes* in arm length are noticed. It follows that frequency noise only couples into sensitivity if there is a mismatch in the lengths of the arms. If one arm has length x and the other length y then $\Delta f/f = \Delta x/x$ and $\Delta f/f = \Delta y/y$. If the mismatch between the arms is $\Delta L = y - x$ then the strain amplitude limit is obtained by considering $(\Delta x - \Delta y)/L$ where L is the nominal arm length. The limit is

$$h_{min} = \frac{\Delta L}{L}\frac{\Delta f}{f}. \tag{2.19}$$

To obtain a strain sensitivity of $10^{-22}/\sqrt{\text{Hz}}$ with the arms matched to around 0.1%, the resulting frequency stability has to be $\Delta f/f \approx 10^{-19}/\sqrt{\text{Hz}}$. For an interferometer powered by a Nd:YAG laser ($f = 2.8 \times 10^{14}$ Hz) this amounts to a frequency stability of $2.8 \times 10^{-5}\,\text{Hz}/\sqrt{\text{Hz}}$ which can be achieved using high gain servo systems.

Laser Power Fluctuations

Power fluctuations couple into detector sensitivity due to a mismatch between the arm lengths. If the interferometer is not locked securely to the bottom of a fringe, due to a relative arm length offset of ΔL, then power fluctuations ΔP couple through to interferometer sensitivity to give a limit

$$h_{min} = \frac{\Delta L}{L}\frac{\Delta P}{P} \tag{2.20}$$

where P is the laser power and L is the arm length. Servo systems are available to keep $\Delta L/L$ down to the order of $10^{-14}/\sqrt{\text{Hz}}$. For strain sensitivities in the order of $10^{-22}/\sqrt{\text{Hz}}$ to be realised, demands on the level of laser power noise are placed at $\Delta P/P = 10^{-8}/\sqrt{\text{Hz}}$. This level of performance can be achieved with relatively straightforward intensity stabilisation systems [36].

Laser Beam Geometry Fluctuations

It can be shown that both positional fluctuations and beam diameter variations couple into the output signal of an interferometer and thus limit its strain sensitivity. A primary coupling mechanism originates through a misalignment of the beam splitter. If the misalignment from a perfectly symmetric position is α then lateral beam jitter δx couples to displacement noise in the arms. This limits the strain sensitivity to

$$h_{min} = \frac{2\alpha}{L}\delta x \tag{2.21}$$

where L is the nominal length of the arms. From experience gained by operating prototypes, it is known that the beam splitter can be controlled to keep the misalignment down to 10^{-7}. To obtain a strain sensitivity of $10^{-22}/\sqrt{\text{Hz}}$ the level of positional fluctuations must not exceed $\sim 3 \times 10^{-13}\,\text{m}/\sqrt{\text{Hz}}$ for $L = 600\,\text{m}$. There may be passive suppression factors afforded by power recycling cavities in the interferometer, however suppression of many orders of magnitude is required to reduce this noise adequately. The problem of beam splitter misalignment, and other coupling mechanisms for beam geometry noise, will be considered in chapter 7. Schemes for reducing beam geometry noise include *single mode optical fibres* and *resonant modecleaners*. A prototype resonant modecleaner will be described in chapter 9.

Thermal Noise in the Test Masses

At any temperature above absolute zero there will exist random thermal motion of the molecules in a material due to their kT vibrational modes. In the case of the mirror masses suspended in an interferometer, this thermal excitation produces a set of orthogonal vibrational modes of the mass. If the beam is small compared

with the diameter of the mirror then the absolute displacement of the mirror surface where the beam lands couples to the optical path length change in a simple manner. If however the beam is large compared with the mirror diameter, then it is possible that the ripples across the surface of the mirror created by a given drum mode will cancel out when integrated over the whole beam. Thus the coupling mechanisms are not straightforward. A detailed analysis can be found in [37]. Here it suffices to show the dependence on the various variables using the simplified formula

$$h_{min} \sim \sqrt{\alpha \frac{kT}{\pi^3 L^2 M_{eff} Q_n f_n^2 f}} \tag{2.22}$$

where L is the arm length of the interferometer, M_{eff} is the effective mass of the component for a given macro mode of vibration ($M_{eff} \approx M/3$ for the first longitudinal vibrational mode), Q_n is the quality factor of mode n and f_n is the frequency of that mode. The dependency on $1/\sqrt{f}$ in Eqn.(2.22) is an approximation that applies when $f << f_n$, which is reasonable given that measured mode frequencies for masses typical of long baseline interferometers begin at around 10 kHz. The constant α contains a factor to reflect the number of important independent components in the interferometer arm (two test mirrors and a beam splitter in GEO 600) and also includes a factor that takes account of the integrated noise contributions from various mode orders, mentioned above. The masses in the GEO 600 interferometer are made of fused-silica and are 25 cm diameter by 15 cm thick. The beam splitter is 25 cm diameter by 7 cm thick. With these values the resulting limit for strain sensitivity can be written as [38]

$$h_{min} \approx 10^{-22} \left(\frac{600\,\mathrm{m}}{L}\right) \left(\frac{100\,\mathrm{Hz}}{f}\right)^{\frac{1}{2}} \left(\frac{5 \times 10^6}{Q_n}\right)^{\frac{1}{2}} \tag{2.23}$$

where the thermal noise in the beam splitter as well as the interferometer masses has been considered in the evaluation of Eqn.(2.23), and is normalised to the value 5×10^6 for all modes. For the GEO 600 detector this amounts to a strain sensitivity limit of $10^{-22}/\sqrt{\mathrm{Hz}}$ at 100 Hz. This equates to the target sensitivity of the interferometer given all the possible noise sources, and clearly constitutes a major factor in obtaining good sensitivity. However there is a further thermal noise consideration; that of the suspension assembly itself, and how this affects the sensitivity.

Thermal Noise of the Suspension System

Thermally excited motion of the suspension wires can produce a severe limit on the achievable displacement sensitivity of an interferometer. Traditionally, mechanical losses in materials used for test mass suspensions were thought to be proportional to frequency. However recent research [39] has suggested that such losses are largely frequency independent over the regime of interest for laser interferometers. This has led to lower levels of thermal noise than previously expected from the suspension system. The strain sensitivity can be evaluated [38] as

$$h_{min} \approx 10^{-23} \left(\frac{600\,\mathrm{m}}{L}\right) \left(\frac{f_{pend}}{1\,\mathrm{Hz}}\right) \left(\frac{100\,\mathrm{Hz}}{f}\right)^{\frac{5}{2}} \left(\frac{16\,\mathrm{kg}}{M}\right)^{\frac{1}{2}} \left(\frac{10^7}{Q}\right)^{\frac{1}{2}} \tag{2.24}$$

where Q is the quality factor of the suspension system, f_{pend} is the pendulum frequency of the suspended mass, L is the interferometer arm length and f is the detection frequency. Contributions from the beam splitter and test mass suspensions have been included in the limit given by Eqn.(2.24). Thus the value $1.9 \times 10^{-23}/\sqrt{\mathrm{Hz}}$ represents the strain sensitivity limit for GEO 600 at 100 Hz due to the thermal noise of the test mass suspensions and beam splitter suspension. By considering Eqn.(2.24) it is clear that to reduce the thermal noise, it is necessary to make the Q value as high as possible. Consequently much research is being devoted to devising ways of maximising the quality factors of suspension systems, for example by developing a complete fused-silica suspension with no mechanical joints.

2.4 The GEO 600 Gravitational Wave Detector

There are currently four large scale laser interferometer projects underway around the world. The American LIGO team are constructing two 4 km arm length detectors, one situated in Washington State and the other based in Louisiana. The French-Italian collaboration VIRGO are building a 3 km detector in Italy. In Japan there is a project underway called TAMA 300 to build a 300 m baseline detector. Finally, the GEO 600 project is a collaboration between the groups at the University of Glasgow, University of Wales, Hannover University and the Max Planck Institute

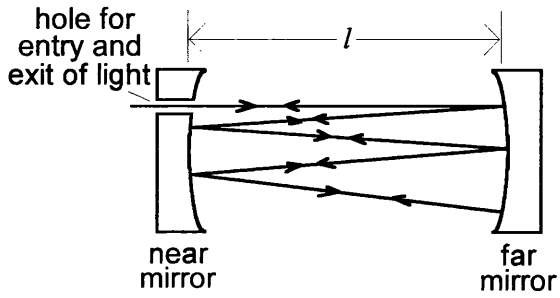

Figure 2.5: *An optical delay line.*

for Quantum Optics in Garching and Hannover. The GEO 600 detector is a delay-line interferometer with an effective arm length of 1200 m (physical arm length of 600 m). The instrument will employ advanced interferometric techniques, such as power and signal recycling.

2.4.1 Optical Delay-Line

Delay-lines were first discussed in the early 1960 s by Herriot, Kogelnik and Kompfner [40] and later proposed for use in gravitational wave detectors by Rainer Weiss at MIT [41]. The 30 m prototype detector at MPQ in Garching uses delay-lines and research related to that system has provided much useful experience of their use in interferometers generally. In its simplest form a delay line essentially traps light by causing it to undergo multiple bounces between two mirrors. In the case of the delay-line shown in Fig 2.5 the effective arm length is simply $L = Nl$ where l is the actual arm length and N is the number of beams in the arm. For the x- and y-axes as defined in Fig 2.5, the coordinates of the subsequent n^{th} spot (x_n, y_n) are given by [42]

$$(x_n, y_n) = (x_0 \sin[n\Theta + \alpha], y_0 \sin[n\Theta + \beta]) \tag{2.25}$$

where (x_0, y_0) are the coordinates of the initial spot and Θ is related to the mirror radius of curvatures R_1 and R_2 by

$$\Theta = \arccos\left(\sqrt{1 - \frac{l}{R_1}}\sqrt{1 - \frac{l}{R_2}}\right). \tag{2.26}$$

The angles α and β are defined by the position and angle the input beam makes with the optic axis. For example, the input conditions $x_0 = y_0$, $\alpha = \pi/2, \beta = 0$ give

rise to forms for x_n and y_n that define the equation of a circle for the spots.

The light is usually introduced and extracted from the system via a hole in one of the mirrors. For the initial (0^{th}) and final (N^{th}) beams to overlap at this hole, the condition $x_0 = x_N$, $y_0 = y_N$ must be satisfied, giving rise to $N\Theta = m2\pi$ where $m = 1, 2....$ The delay line behaves as a mirror to input light satisfying the above condition. Light rays reflect from the system just as if they were reflecting from the back surface of the near mirror, albeit with a time delay.

A problem associated with multi-beam delay-lines is the amount of scattered light produced by the mirrors. This is particularly important in delay-lines having a large number of beams, for then the separation of the mirrors must be made comparable to their radius of curvature, forming a cavity geometry that is very near *confocal.* The confocal cavity is known for its extreme mode degeneracy and scattered light can produce high order laser modes which find resonances in the cavity. The amount of scattered light amplitude that finds its way into the main beam can be modulated by mirror motions, and the result is a noise source that can severely limit sensitivity.

Bearing in mind this scattered light problem, the delay-line design for GEO 600 consists of only four passes of the laser light in each arm ($N = 4$). This configuration is sufficiently simple to permit the use of individual mirrors for each laser reflection and the resulting arm design is the *folded delay-line* configuration shown in Fig 2.6. The problem of the parasitic cavity is thus avoided by not having two delay-line mirrors that face one another. A more comprehensive account of the properties of delay-lines in interferometric gravitational wave detectors can be found in the contribution by Walter Winkler in [26].

2.4.2 Advanced Interferometer Techniques

To achieve the best shot noise limited performance an interferometer is operated so that there is a null fringe at its output. This implies that a great deal of laser light is directed back out of the interferometer input towards the laser. The scheme that prevents this light from being wasted is called power recycling.

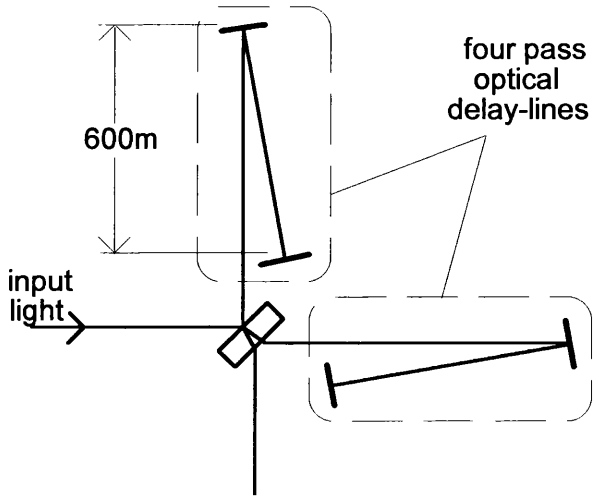

Figure 2.6: *Simplified diagram of the GEO 600 interferometer showing the folded delay-line design.*

Power Recycling

The technique of power recycling increases the circulating power in the interferometer system thus improving the shot noise limited performance of the instrument. The important components of power recycling are shown in Fig 2.7. It works by having a mirror at the input to the interferometer which directs the light travelling to the laser back into the system. The presence of this mirror forms two Fabry-Perot cavities with the mirror at the end of each arm of the interferometer as shown in Fig 2.7. The power recycling factor is defined by the properties of this cavity. Details regarding the power handling properties of Fabry-Perot cavities will be explored in chapter 3; however for now, the result

$$P_{BS} = \frac{1}{1 - \sqrt{R_{dl} R_{PR}}} P_{in} \tag{2.27}$$

will be used, where P_{BS} is the power accumulated inside the system (at the input to the beam splitter), P_{in} is the power available to the system (just before the power recycling mirror), R_{dl} is the overall reflectance of the delay-line ($R_{dl} = R^3$ where R is the nominal reflectance of the GEO 600 delay-line mirrors) and R_{PR} is the power reflectance of the power recycling mirror itself. Eqn.(2.27) applies to

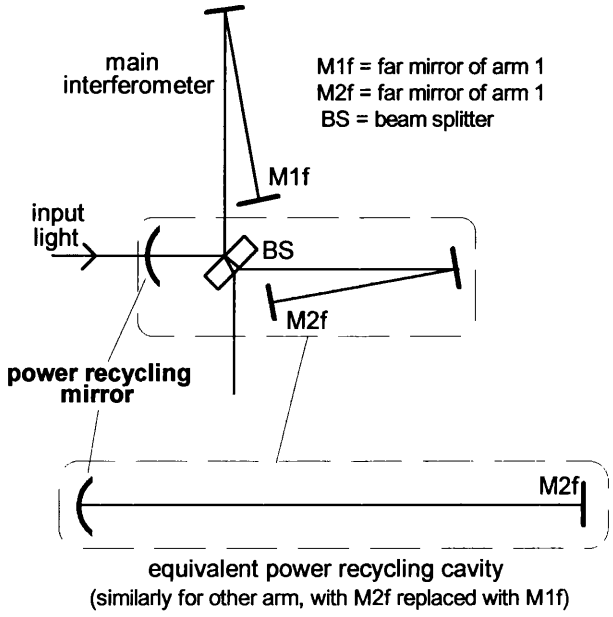

Figure 2.7: *Simplified diagram of the GEO 600 interferometer showing the power recycling sheme.*

the ideal situation of an interferometer with 100 % *constrast*[6]. Using estimates of the losses of the delay line mirrors and a typical value of a few hundred parts per million transmittance for the power recycling mirror, the power recycling factor for GEO 600 in the first instance is obtained to be around 2000. Thus to achieve, say 10 kW, at the beam splitter, the laser power would have to be 5 W just before the power recycling mirror. A convenient normalised shot noise limited integrated strain sensitivity for GEO 600 can be written [38]

$$h = 7 \times 10^{-24} \left(\frac{P_{BS}}{10\,\mathrm{kW}}\right)^{-\frac{1}{2}} \left(\frac{\Delta f_{PR}}{100\,\mathrm{Hz}}\right)^{\frac{3}{2}} \left(\frac{\lambda}{1064\,\mathrm{nm}}\right)^{\frac{1}{2}} \tag{2.28}$$

It can be seen from Eqn.(2.28) that in terms of the strain amplitude spectral density the shot noise is proportional to the bandwidth with power recycling Δf_{PR}. Thus the peak response of the detector (as far as the photon shot noise limit is concerned) is at very low frequency. This is unfortunate, since there are other far greater noise barriers (such as seismic noise) that make the instrument astrophysically useless at such low frequency. It would be convenient to move the peak shot noise limited

[6] the dark fringe condition is perfect resulting in all of the light being directed back to the laser.

performance to higher frequency, preferably in the middle of the detection window. This can be achieved with the use of signal recycling.

Signal Recycling

A gravitational wave passing through an interferometer can be thought of as introducing phase modulation sidebands to the laser beam inside the system. To the interferometer reference frame this modulation appears as *frequency sidebands* on either side of the laser carrier frequency. If the interferometer is operated so that a dark fringe appears at the output (as is the case for a real system employing a modulation scheme) then the carrier and sidebands get separated at the beam splitter; the carrier beam travels towards the power recycling mirror while the much weaker signal beam travels towards the output. Signal recycling was invented by Brian Meers [43] as a method of recycling this signal beam using a mirror placed at the output of the interferometer. In the GEO 600 detector, the signal recycling scheme works in rather the same way as the power recycling system. The signal recycling mirror forms a cavity with the end mirror of each arm. The signal is amplified by the resonant action of these cavities. The effect of signal recycling is to increase the effective time duration that a gravitational wave signal spends in the interferometer. The *signal recycling factor* G_S is defined as the ratio of the required storage time for optimal performance and the storage time of the carrier light in the system. The modified shot noise limited integrated strain sensitivity of the instrument with signal recycling can be written [44]

$$h_{min} = 7 \times 10^{-24} \left(\frac{P_{BS}}{10\,\mathrm{kW}}\right)^{-\frac{1}{2}} \left(\frac{\Delta f_{PR}}{100\,\mathrm{Hz}}\right)^{\frac{3}{2}} \left(\frac{\lambda}{1064\,\mathrm{nm}}\right)^{\frac{1}{2}} \frac{1}{G_S}. \tag{2.29}$$

The integrated strain sensitivity of the interferometer is improved by a factor G_S with signal recycling although the bandwidth is reduced and is given by $\Delta f_{SR} = \Delta f_{PR}/G_S$. An improvement in the strain amplitude sensitivity spectral density by a factor $\sqrt{G_S}$ is observed at the centre frequency of the signal recycling scheme. It should be realised that for a given bandwidth, the integrated strain amplitude sensitivity is actually degraded by the effect of the signal recycling, being worse than the equivalent optimal broadband instrument by a factor $\sqrt{G_S}$. Thus the decision

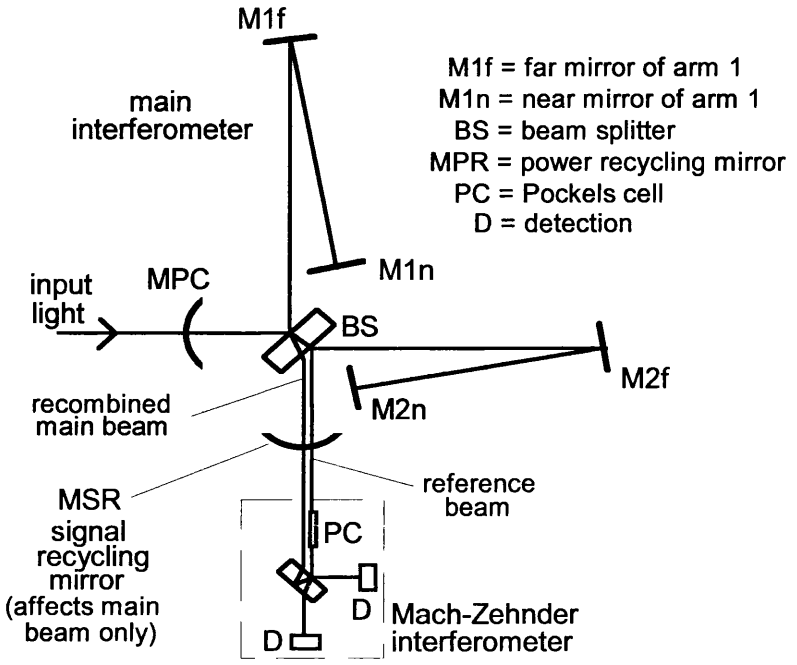

Figure 2.8: *Layout of the GEO 600 interferometer.*

to implement narrow-band signal recycling at a specific frequency (for example to search for a pulsar) compromises the ability of the interferometer to operate effectively as a broadband instrument. An illustration of the complete system layout with power and signal recycling is shown in Fig 2.8. An interferometer that is fitted with both power and signal recycling is sometimes called a *dual recycled system.* The configuration of GEO 600 in its complete state will be that of a dual recycled interferometer. A bench-top demonstration of dual recycling can be found in [45].

Signal Detection Scheme

The detection scheme is rather more complicated than just letting the recombining beams land on a photodetector. In Fig 2.8 the main output beam is mixed with a reference beam taken from a convenient stray reflection from BS. The reference beam is modulated and then the mixed signal coherently demodulated to yield the output. The method of doing this is basically a Mach-Zehnder interferometer. This scheme is often referred to as *external modulation.* One alternative to the above scheme is to phase modulate the light within the arm of the interferometer (*internal*

modulation) but this introduces a loss associated with the phase modulator and is best avoided. The signal recycling mirror (MSR) position and reflectance decides the sensitivity characteristics of the interferometer. If the reflectance of MSR is 0 then the system has broadband sensitivity with peak shot noise limited response at DC. By giving MSR a non-zero value of reflectance, signal recycling enhancement occurs over a bandwidth that gets narrower as the reflectance increases. The centre frequency of the enhancement is determined by the position of MSR.

2.4.3 Performance of GEO 600

The expected sensitivity of GEO 600 can be obtained by using the various noise formulae given earlier in this chapter and combining them with the specifications and design parameters of the GEO 600 system. The plots in Fig 2.9 show the sensitivity curves for the GEO 600 interferometer powered by a 5 W Nd:YAG laser (1064 nm) and implemented with a power recycling factor of 2000 and wideband signal recycling. The mirrors are each assumed to have loss 20 ppm and are coated onto fused-silica test masses weighing 16 kg. The quality factors associated with the mass internal modes and the pendulum suspensions are taken to be 5×10^6 and 10^7 respectively. Work has commenced at the GEO 600 site in Hannover with a projected initial on-line tests beginning late in 1998.

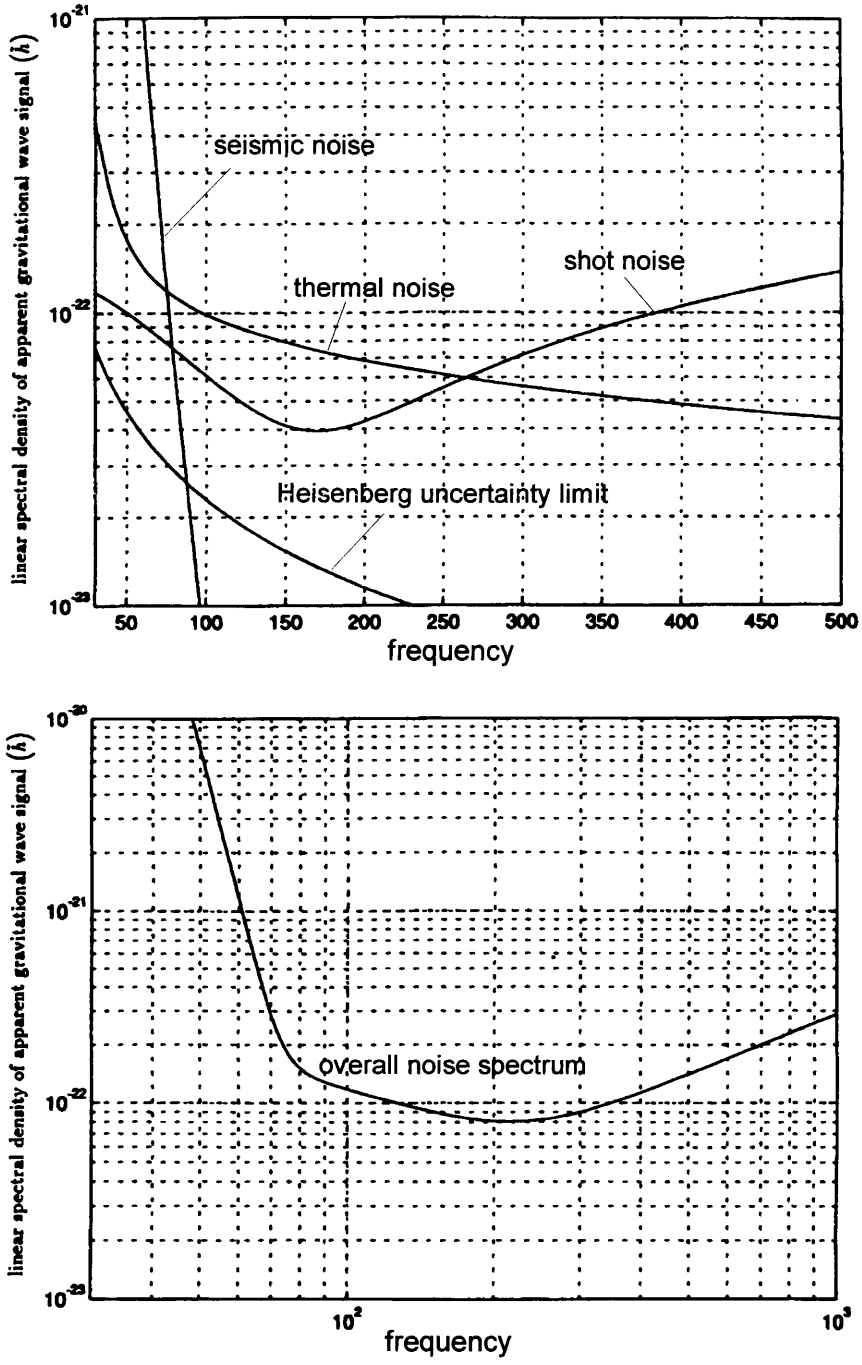

Figure 2.9: *Traces showing the projected noise budget of the GEO 600 interferometer. The top plot shows the expected limits from various sources of noise associated with the detector. The bottom plot shows the overall noise spectrum, obtained by adding in quadrature the individual noise traces. Note the differing frequency spans.*

Chapter 3

Properties of Fabry-Perot Cavities

3.1 Introduction

The Fabry-Perot optical cavity in its simple two mirror form was introduced in chapter 2. Such cavities are important in many aspects of interferometer design, and this chapter will describe some of their properties and present results that will prove valuable for the work described in later chapters. Some examples of their use have already been discussed, such as power and signal recycling schemes or the use of cavities to increase the effective arm length of an interferometer. However there are other uses for optical cavities in a laser interferometer. A cavity can be used in transmission mode as an optical filter (this will be discussed in chapters 8 and 9) or in reflection mode as a stable frequency reference, as will be outlined later in this chapter. Indeed, the laser beam itself originates in a cavity and has modes of propagation that are described in terms of the cavity geometry (this is demonstrated in chapter 5). In section 3.2 some useful properties and results pertaining to a general Fabry-Perot cavity will be presented. The use of a Fabry-Perot cavity as a frequency reference is discussed in section 3.3.

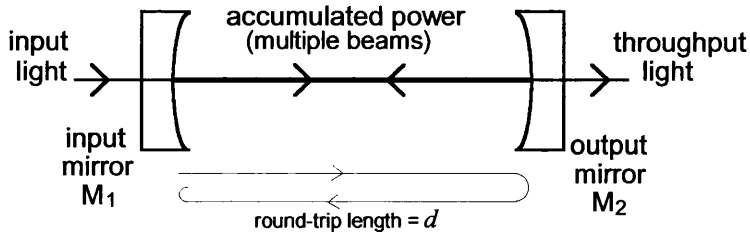

Figure 3.1: *A simple two mirror Fabry-Perot optical cavity.*

3.2 Power Handling Properties

The next few sections will introduce some important results regarding the power handling capabilities of an optical cavity. The formulae presented will be used frequently in later chapters.

3.2.1 Finesse and Storage Time

Consider the two mirror Fabry-Perot cavity of Fig 3.1. The light in the cavity is subject to a round-trip distance d. The cavity is said to be on resonance with the light inside it when an integral number of wavelengths of the light fit into d. The distance between one resonance and the next, in terms of altering the cavity length, is one wavelength of the light. In frequency space, the resonance spacing is c/d and this is called the *free spectral range* (FSR) of the cavity. Referring again to Fig 3.1, let the light field amplitude transmittance and reflectance for the mirrors M_1 and M_2 be t_1, r_1 and t_2, r_2. Light power reflectance and transmittance will be denoted by R and T, related to the amplitude coefficients by $R_i = r_i^2$, $T_i = t_i^2$. It is evident that in any round trip of the cavity the number of circulating photons n_p will drop to $(1 - R_1 R_2)n_p$. This change occurs in a time d/c giving

$$\frac{dn_p}{dt} = \frac{1 - r_1^2 r_2^2}{d/c} n_p. \tag{3.1}$$

This has solution $n_p(t) = n_p(t_0)e^{-2t/\tau_s}$ which shows an exponential decay of the photon number with time. The value τ_s is called the storage time of the cavity and is given by

$$\tau_s = \frac{2d}{c} \frac{1}{1 - r_1^2 r_2^2}. \tag{3.2}$$

By considering the above solution to Eqn.(3.1) it is apparent that τ_s gives the time for the circulating photons (or equivalently, the circulating light power) to decay by a factor $1/e^2$. The storage time can be regarded as the average lifetime of a photon in the system and this leads naturally to the use of τ_s as the quantity in a Fabry-Perot interferometer system that should be comparable with half the gravitational wave period, as discussed in section 2.3.1.

It is a straightforward extension of the theory to describe a cavity that is not a simple two mirror system but in general contains n mirrors of reflectance $r_1, ..., r_n$. The storage time can be written

$$\tau_s = \frac{2d}{c} \frac{1}{1 - \prod_{i=1}^{n} r_i^2}. \tag{3.3}$$

By expressing this decay of light power as the rate of change of energy of the system, an expression $E(t) = E(0)e^{-\omega_0 t/Q}$ can be written where ω_0 is the angular frequency of the light on resonance in the cavity. The quantity Q can be defined in words as

$$Q = 2\pi \frac{\textit{energy stored in cavity at resonance}}{\textit{energy lost during one cycle of light}} \tag{3.4}$$

or in terms of the storage time (compare with above) as

$$Q = \frac{\omega_0 \tau_s}{2} = \frac{2\pi d f_0}{c} \frac{1}{1 - \prod_{i=1}^{n} r_i^2}. \tag{3.5}$$

A *high Q* cavity is one which has very low loss for a round-trip of the light. This corresponds to reflectances near unity and in such cases the binomial expansion can be applied to the right hand side of Eqn.(3.5) to give

$$Q = \frac{\pi d}{\lambda_0} \frac{(\prod_{i=1}^{n} r_i^2)^{\frac{1}{4}}}{1 - (\prod_{i=1}^{n} r_i^2)^{\frac{1}{2}}}. \tag{3.6}$$

It is usual to express this relation as $Q = nF$ where $n = d/\lambda$ is the number of wavelengths of light in a cavity round-trip and F is called the *cavity finesse* defined by

$$F = \pi \frac{(\prod_{i=1}^{n} r_i)^{\frac{1}{2}}}{1 - (\prod_{i=1}^{n} r_i)}. \tag{3.7}$$

For the simple two mirror system of Fig 3.1 the finesse is given by

$$F = \pi \frac{(r_1 r_2)^{\frac{1}{2}}}{1 - (r_1 r_2)}. \tag{3.8}$$

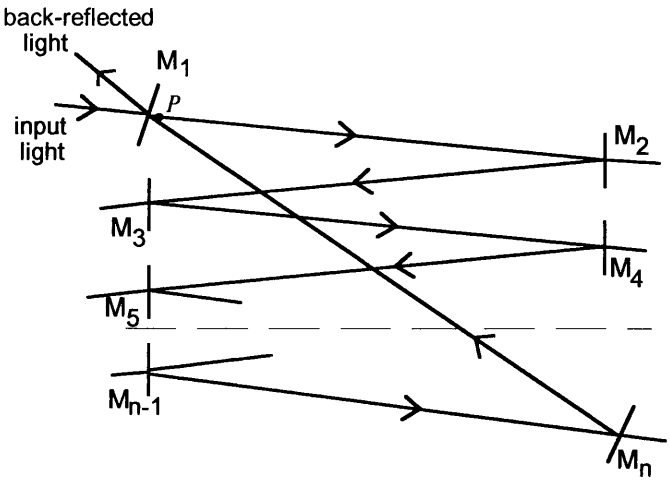

Figure 3.2: *Fabry-Perot system with mirrors* $M_1, ..., M_n$.

The expression for finesse given in Eqn.(3.8) can be written in terms of power reflectance and transmittance as

$$F = \pi \frac{(R_1 R_2)^{\frac{1}{4}}}{1 - (R_1 R_2)^{\frac{1}{2}}}. \tag{3.9}$$

It is more common to refer to a cavity as being of *high finesse* rather than *high Q*. In view of Eqn.(3.5) and Eqn.(3.7), the storage time τ_s can be written

$$\tau_s = \frac{d}{\pi c} F \tag{3.10}$$

which expresses the result that the storage time is directly proportional to the finesse of the cavity.

3.2.2 Power Throughput

In the case of Fabry-Perot cavities that are used in the arms of an interferometer, it is ultimately the reflected light that will be of use. However Fabry-Perot cavities are often used in transmission mode as well, for example to form a *resonant modecleaner* (described in chapters 8 and 9). An expression for the transmission of a Fabry-Perot cavity can be derived as follows. Consider the cavity of Fig 3.2. The light field at the point P is given by taking the incident light field E_{in} and adding up the contributions from successive round-trips of the light to give

$$E_P = E_{in} t_1 \left\{ 1 + \left(\prod_{i=1}^{n} r_i \right) e^{j\phi} + \left(\prod_{i=1}^{n} r_i \right)^2 e^{j2\phi} + ... \right\} \tag{3.11}$$

where ϕ is the phase acquired by the light during a round trip. Summing the series to infinity gives

$$\frac{E_P}{E_{in}} = t_1 \frac{1}{1 - (\prod_{i=1}^{n} r_i)\, e^{j\phi}}. \tag{3.12}$$

The power at P can be found by squaring the modulus of Eqn.(3.12) to give

$$\frac{P_P}{P_{in}} = t_1^2 \frac{1}{1 + (\prod_{i=1}^{n} r_i)^2 - 2\,(\prod_{i=1}^{n} r_i)\cos\phi} \tag{3.13}$$

which can be written as

$$\frac{P_P}{P_{in}} = t_1^2 \frac{1}{(1 - \prod_{i=1}^{n} r_i)^2 + 4\,(\prod_{i=1}^{n} r_i)\sin^2\frac{\phi}{2}}. \tag{3.14}$$

The value of power exiting any mirror when the cavity is on resonance ($\phi = 0$) can be calculated using Eqn.(3.14). If the power exiting the j^{th} mirror is required, then it is given by

$$P_j = \frac{t_1^2 \prod_{i=2}^{j} t_i^2}{(1 - \prod_{i=1}^{n} r_i)^2} P_{in} \tag{3.15}$$

where the circulating power at P has been multiplied by all the power transmittances it encounters before escaping the cavity at the j^{th} mirror. By returning to the two mirror example of Fig 2.5 the throughput power P_t is given by

$$P_t = \frac{t_1^2 t_2^2}{(1 - r_1 r_2)^2} P_{in}. \tag{3.16}$$

A mirror is usually expressed in terms of its power reflectance, transmittance and loss which are the squares of their amplitude counterparts. Using capital letters to denote power coefficients Eqn.(3.16) can be written

$$P_t = \frac{T_1 T_2}{(1 - \sqrt{R_1 R_2})^2} P_{in} \tag{3.17}$$

where for conservation of power the coefficients R, T and A (the loss coefficient) must add to unity $R + T + A = 1$. By considering Eqn.(3.14) it can be shown that the power accumulated inside the cavity is related to the incident power by the useful relation

$$P_P \simeq \frac{F}{\pi} P_{in} \tag{3.18}$$

which holds fairly accurately for cavities with finesse of a few hundred or more.

3.2.3 Visibility

Another useful quantity is the ratio of minimum to maximum *reflected* intensity from the cavity, given by taking the ratio of back-reflected light when the cavity is respectively on and off resonance. This is called the *visibility* of the cavity and is expressed in terms of reflected light powers by[1]

$$V = \frac{P_r^{max} - P_r^{min}}{P_r^{max}}. \tag{3.19}$$

The ratio of the incident light field E_0 and the amplitude leaking backwards from within the cavity on-resonance E_c is related to the visibility, as defined above, by

$$\frac{E_c}{E_0} = 1 \pm \sqrt{1 - V}. \tag{3.20}$$

The argument for deriving an expression for V in terms of mirror parameters continues along similar lines to that for throughput power, except now there is an extra term which represents the directly back-reflected component from the input mirror of the cavity. In terms of field amplitudes the back-reflected light, denoted by E_r is

$$\frac{E_r}{E_{in}} = r_1 + \frac{t_1^2}{r_1}\left\{\left(\prod_{i=1}^{n} r_i\right)e^{j(\phi-\pi)} + \left(\prod_{i=1}^{n} r_i\right)^2 e^{j(2\phi-\pi)} + ...\right\}. \tag{3.21}$$

This series can be summed to infinity to give

$$\frac{E_r}{E_{in}} = r_1 - \frac{t_1^2}{r_1}\frac{\left(\prod_{i=1}^{n} r_i\right)e^{j\phi}}{1 - \left(\prod_{i=1}^{n} r_i\right)e^{j\phi}} \tag{3.22}$$

and then mutiplied by its conjugate to yield the intensity. The important cases are when $\phi = 0$ and $\phi = \pi$ giving P_{min} and P_{max} respectively. By using Eqn.(3.19) it can be shown that

$$V = 1 - \left[\frac{r_1 - \frac{t_1^2}{r_1}\left(\frac{\prod_{i=1}^{n} r_i}{1-\prod_{i=1}^{n} r_i}\right)}{r_1 + \frac{t_1^2}{r_1}\left(\frac{\prod_{i=1}^{n} r_i}{1+\prod_{i=1}^{n} r_i}\right)}\right]^2 \tag{3.23}$$

which gives an exact value for V. A good approximation for most cavities is obtained by replacing the denominator of the bracketed term in Eqn.(3.23) by unity to give

$$V = 1 - \left[\sqrt{R_1} - \frac{T_1}{\sqrt{R_1}}\frac{\left(\prod_{i=1}^{n} R_i\right)^{\frac{1}{2}}}{1 - \left(\prod_{i=1}^{n} R_i\right)^{\frac{1}{2}}}\right]^2 \tag{3.24}$$

[1] note that this differs from the commonly used definition of visibility which is normalised to $P_r^{max} + P_r^{min}$.

where power coefficients have again been used. By multiplying this out and using the approximation for high finesse cavities that

$$F \simeq \frac{\pi}{1-(\prod_{i=1}^{n} R_i)^{\frac{1}{2}}} \tag{3.25}$$

the visibility can be written in the convenient form

$$V = \frac{T_1 F}{\pi}\left[2 - \frac{T_1 F}{\pi}\right]. \tag{3.26}$$

There are many experimental situations where the cavity finesse is known or can be measured, and so a knowledge of the transmittance of the input mirror is all that is required to determine the visibility. Eqn.(3.24) can also be used to *impedance match* the light into the cavity. Maximum power matching into the cavity occurs when $V = 1$. Solving Eqn.(3.24) and neglecting cross-terms and high order terms gives

$$T_1 = \sum_{i=1}^{n} A_i + \sum_{i=2}^{n} T_i \tag{3.27}$$

which expresses that maximum power coupling into the cavity can be achieved by choosing the transmittance of the input mirror to be the sum of the transmittances of the other mirrors, plus the sum of the losses of all the mirrors.

3.2.4 Cavity Linewidth and Filter Action

A resonant Fabry-Perot cavity acts as a low pass optical filter for practically any kind of fluctuation associated with the laser light. The linewidth of the cavity $\Delta\nu$ is determined by its free spectral range FSR and finesse F. By analogies with electronics, the linewidth of the cavity is given by determining the phase offset that causes the circulating power to drop to half its value at resonance. The cavity linewidth is then the FWHM[2] of the characteristic power against frequency curve for the cavity. Consider again the expression for the circulating light power given by Eqn.(3.14). This is used to determine the phase that satisfies $P_P(\phi) = P_P^{max}/2$. By expressing phase fluctuations from resonance ϕ as frequency fluctuations $f = c\phi/(2\pi d)$ and using the approximation $F \approx \frac{1}{1-\prod_{i=1}^{n} r_i}$ it can be shown that

$$\Delta\nu = \frac{FSR}{F}. \tag{3.28}$$

[2]Full Width at Half Maximum.

The filtering action of the cavity can be described in terms of the corner frequency of the cavity $f_c = \Delta\nu/2$ by

$$P_t = P_{max} \frac{1}{1 + \left(\frac{f}{f_c}\right)^2} \tag{3.29}$$

where P_{max} is the maximum power throughput given by the cavity when the light is on resonance and P_t is the throughput light power when the cavity is off-resonant by a small frequency offset f. These results show that higher finesse cavities provide filtering action that starts at lower frequencies. The above result could have been obtained by first considering the circulating light field *amplitude* (which will fall off as $1/f$) and then squaring to get the light power.

The action of the cavity filtering with regard to a given type of laser noise can be investigated by expressing the noise as a Fourier expansion and then considering the individual frequency components. In the light amplitude field, each Fourier component of the noise can be regarded as imposing an upper and lower sideband about the carrier frequency of the light, and these sidebands will be attenuated by $1/f$ for frequencies greater than the corner frequency of the cavity f_c. Thus, the light field emerging from the cavity will still include the sidebands imposed by the laser noise, but these sidebands will be attenuated by $\frac{1}{\sqrt{1+\left(\frac{f}{f_c}\right)^2}}$ for $f > f_c$. Thus, frequency noise and phase noise, which is present with a magnitude proportional to these sideband amplitudes, will fall off as $1/f$, however the laser power (which is obtained by squaring the light field) will have its associated noise fall off as $1/f^2$. In summary, the cavity behaves as a low pass filter with a 6 dB per octave slope for noise that is proportional to the imposed sideband amplitudes, and 12 dB per octave for power noise.

3.3 Fabry-Perot Frequency Reference

By using electronic feedback systems it is possible to stabilise a laser by endowing it with the properties of a stable Fabry-Perot cavity. A cavity used in this manner is called a *frequency discriminator.* The best method of implementing such a

stabilisation scheme is to use modulation techniques[3]. An arrangement used in common practice is the *RF reflection locking scheme.* Consider the set-up illustrated in Fig 3.3. A portion of the main laser beam, which will be linearly polarised, is split off by a partially transmitting mirror and directed through a Faraday isolator (FI). The FI acts like an optical diode, suppressing any backward travelling light from getting to the laser. Such components can afford over 40 dB of suppression when carefully set up. The light is phase modulated using an electro-optic phase modulator EOM and then passes through the polarising beam splitter PBS towards the reference cavity. The quarter-wave plate circularly polarises the light. The light field incident to the cavity can be described by a carrier plus two sidebands induced by the modulation

$$E_{in} = E_0 \left[J_0 e^{j\omega t} + J_1 e^{j(\omega t + \omega_m t)} - J_1 e^{j(\omega t - \omega_m t)} \right]. \tag{3.30}$$

The back-reflected light is made linearly polarised after passing back through the wave plate but in an orthogonal plane to the incident polarisation, so that PBS reflects the light off to the photodetector PD. The key to reflection locking is that while the directly back-reflected field component carries modulation sidebands, the light leaking backwards out of the cavity does not (unless the modulation frequency happens to match exactly the FSR of the cavity). The two superposed light fields mix at the PD and the signal can be demodulated with a local oscillator at the modulation frequency to give a suitable *error signal.* The feedback signal has a signature that is used to keep the cavity firmly locked to resonance. This is achieved by altering the length of the laser cavity using an electronic feedback system. In Fig 3.3 two paths that do this have been shown. The slow path actively changes the length of the laser cavity (thus altering the frequency of the laser) using a *piezo-electric crystal* (PZT) onto which one of the mirrors is mounted. The fast path uses another EOM, this time to alter the phase of the light in the laser cavity, which in turn alters the frequency of the laser light. By causing the laser frequency to follow

[3] the advantages of modulation schemes are well documented - here it allows the laser to lock to the cavity at the bottom of a fringe and allows signal sensing at frequencies where the laser intensity fluctuations are shot noise limited.

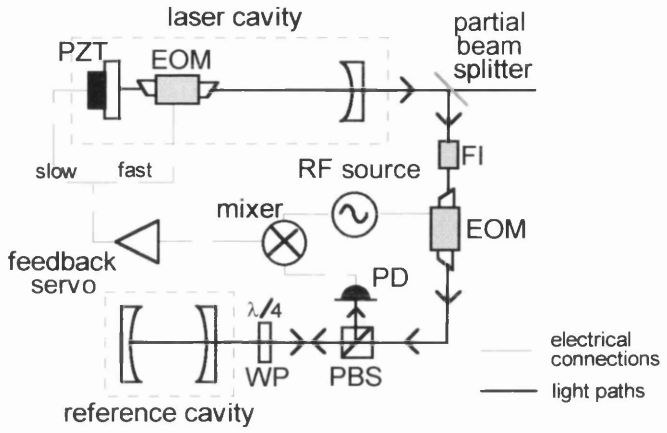

Figure 3.3: *Reflection locking scheme to stabilise a laser to a Fabry-Perot frequency discriminator.*

the characteristics of the reference cavity, the properties of the cavity (with regard to rigidity, long-term drift etc) can be imparted to the laser.

The reflected light field E_r from the cavity is of the form

$$E_r = J_0 E_c e^{j\Delta\phi} + J_0 E_0 + J_1 E_0 e^{j\omega_m t} - J_1 E_0 e^{-j\omega_m t} \tag{3.31}$$

where E_c denotes the amplitude of light leaking back from inside the cavity. The phase offset from resonance $\Delta\phi$ can be expressed in terms of frequency using $\Delta f = c\Delta\phi/(2\pi d)$. The reflected power is obtained by multiplying E_r with its conjugate. The term in the resulting expression pertinent to the demodulated signal is that at frequency ω_m. This has coefficient $-4J_0J_1E_0E_c \sin\Delta\phi$ giving

$$\frac{dP_m}{df} = \frac{4J_0J_1E_0E_c}{\Delta\nu} \tag{3.32}$$

where P_m is the light power due to signals at the modulation frequency and $\Delta\nu$ is the linewidth of the cavity. This is directly proportional to the current detected at the photodiode, the constant of proportionality being the quantum efficiency of the detector ξ. Fluctuations in photocurrent ΔI_m are thus related to fluctuations in frequency of the light Δf by

$$\Delta I_m = \frac{4\xi J_0J_1E_0E_c}{\Delta\nu}\Delta f. \tag{3.33}$$

Given the ideal case of a noiseless electronic feedback loop with unlimited gain, the best possible limit on Δf is obtained when ΔI_m becomes comparable to the

quantum shot noise of the steady state photocurrent I. I is given by

$$I = \xi(1 - V_a)E_0^2 \tag{3.34}$$

where V_a is the apparent, or measured, cavity visibility, which will differ from the theoretical value simply because a fraction of the power (that is in the sidebands) does not resonate in the cavity. In fact $V_a = MVJ_0^2$ where V is the theoretical maximum visibility and M is the fraction of input light that is actually matched into the cavity. Using the Schottky formula for noise $\delta I = \sqrt{eIB}$ the frequency stability limit can be written as

$$\Delta f = \Delta\nu\sqrt{\frac{(1 - J_0^2 MV)eB}{16\xi J_0^2 J_1^2 P_0(1 \pm \sqrt{1 - V})^2}} \tag{3.35}$$

where P_0 is the incident laser power and B is the measurement bandwidth. The $1 \pm \sqrt{1 - V}$ term comes from considering the ratio of back-reflected light amplitude when the cavity is on and off resonance (the minus sign applies when the cavity is over-coupled). A fact omitted from the derivation of Eqn.(3.35) is the cavity response function. This describes the low-pass filtering action of the cavity and can be expressed via the factor

$$\frac{1}{\sqrt{1 + \left(\frac{f_j}{f_c}\right)^2}} \tag{3.36}$$

where f_c is the corner frequency of the cavity (half the cavity linewidth) and f_j is the Fourier frequency of the j^{th} component in the expansion of Δf as a Fourier series. This filtering action degrades the performance of the cavity as frequency discriminator since it attenuates signals in the feedback loop. The stability expressed in Eqn.(3.35) is inversely proportional to the filtering term. After taking this into consideration the final expression for the shot noise limited frequency stability is (see the contribution by J. Hough et al, in [26])

$$\Delta f = 2f_c\sqrt{\frac{\hbar\omega(1 - J_0^2 MV)}{16\xi P_0}}\frac{1}{MJ_0J_1}\frac{1}{(1 \pm \sqrt{1 - V})}\sqrt{1 + \left(\frac{f_j}{f_c}\right)^2}/\sqrt{\text{Hz}}. \tag{3.37}$$

The steps leading to the above formula do not take into account the effect the modulation has on the noise associated with the detected light at the photodiode. The above derivation assumes that the shot noise formula for a constant light power

P_m leading to a constant photocurrent I_m can be used, which is not strictly correct. The modulation will also appear on the noise, producing the phenomenon of *non-stationary shot noise.* A correct analysis depends on integrating the noise over a given measurement interval. In the case of sine wave modulation/demodulation this introduces a dependence on the second order Bessel function J_2 to the noise term [46], and results in a photocurrent noise given by

$$\delta I = \sqrt{eB[1 - J_0^2 MV + 2MJ_0J_2(1 \pm \sqrt{1-V})]}. \tag{3.38}$$

The corrected expression for the frequency stability can be written as

$$\Delta f = 2f_c\sqrt{\frac{\hbar\omega[1 - J_0^2 MV + 2MJ_0J_2(1 \pm \sqrt{1-V})]}{16\xi P_0}} \times \frac{1}{MJ_0J_1}\frac{1}{(1 \pm \sqrt{1-V})}\sqrt{1 + \left(\frac{f_j}{f_c}\right)^2}/\sqrt{\text{Hz}} \tag{3.39}$$

where the symbols have their usual meanings. In practice the J_2 correction makes only a few percent difference to the frequency stability.

Chapter 4

Testing of Low Loss Optical Components

4.1 Introduction

In a laser based gravitational wave detector where precision interferometry is being performed, it is required that the random scattering of light by optical surfaces is kept to a minimum. Furthermore, if the interferometer is being driven by a high power laser then any component that has a high absorptance will heat and may exhibit *thermal lensing* [44]. In addition, absorptances associated with the beam splitter and interferometer mirrors will reduce the amount of laser power that can be accumulated in the system, and this will have a direct effect on interferometer sensitivity. To achieve optimal performance, there is a demand that all optical components in a laser interferometer are of the highest possible quality with regard to both scatter loss and absorptance loss. Consequently it is not surprising to learn that improvements in the quality of commercially available optical components over recent years (especially supermirrors[1]) have been at least partly motivated by experimental gravitational wave research.

The origin of the most commonly encountered types of loss is described briefly in section 4.2. Measurements of state-of-the-art supermirrors using a variety of tech-

[1] a mirror manufactured to have a high reflectance and very low loss at a specific wavelength.

niques are described in section 4.3. The integration of the mirror manufacturing stage and the mirror testing process (primarily for the needs of industry) has motivated the design for an automatic mirror loss meter and this is described in section 4.4.

4.2 Origin of Losses in Optical Components

Ideally, any component designed to perform some function on a laser beam should do so without wasting any laser power. However in practice, all components are intrinsically lossy in some sense, either because they scatter some of the incident light, or because they absorb it. These are two distinct processes and shall be looked at in turn.

4.2.1 Scatter Loss

When light is incident on a surface it will be scattered by an amount dependent on the surface roughness. If the root mean square surface roughness of a given material is denoted by σ then the reflectance R of the surface for light of wavelength λ, incident normally, can be written [47]

$$R = R_0 \exp\left[\frac{-(4\pi\sigma)^2}{\lambda^2}\right] + R_0 \frac{2^5\pi^4}{g^2}\left(\frac{\sigma^4}{\lambda^4}\right)\Delta\theta^2 \tag{4.1}$$

where R_0 is the reflectance of a perfectly smooth sample of the surface ($\sigma = 0$), g is the root mean square slope of the surface profile and the angle $\Delta\theta$ defines the measurement cone (with axis normal to the surface) into which light is reflected. Eqn.(4.1) can be expressed in terms of the *total diffuse reflectance* (total scatter loss) $A_{scatter}$ by considering the diffuse reflectance into a sphere rather than a cone. For a surface which exhibits very low scatter loss, the relation between surface roughness and total scatter loss becomes

$$A_{scatter} = R_0 \frac{(4\pi\sigma)^2}{\lambda^2} \tag{4.2}$$

where $A_{scatter} = R - R_0$. For supermirrors R_0 is very close to unity and Eqn.(4.2) gives a simple relationship between the scatter loss and the mirror roughness. It

can be seen from Eqn.(4.2) that for a given roughness of surface the scatter loss decreases as λ increases. For example, in going from 514.5 nm (argon ion lasers) to 1064 nm (Nd:YAG lasers) about a factor of four reduction in scatter loss is obtained.

Much effort has gone into reducing surface roughness with American companies General Optics and PMS Electro-Optics both reporting substrate roughness levels of less than 0.2 angstroms rms. With such smooth substrates, the dominating factor leading to light scattering tends to be random surface defects. In the case of supermirrors, the mirror surface profile has two components; one from the substrate and another from the multi-layer optical coating that forms the actual mirror. The *ion-beam sputtering* coating techniques now developed allow supermirrors with very low losses to be produced. For example, PMS Electro-Optics have produced mirrors coated for 514.5 nm having total loss (absorptance plus scattering) less than 5 ppm[2] and mirrors coated for 1064 nm having total loss of around 1 ppm [48]. Although these figures are for total loss, it will be shown in section 4.3.2 that the predominant contribution comes from scattering.

4.2.2 Absorptance Loss

In dealing with absorptance loss it is often necessary to distinguish between various causes. For example, a supermirror will have an absorptance associated with the thin films that form the mirror coating, and also a bulk absorptance due to the mirror substrate material. The thin film absorptance is usually of most concern in supermirror quality with multiple deposited layers of dielectrics such as titanium oxide and tantalum pentoxide giving rise to an overall absorptance that can vary greatly from one coating plant to another[3]. Depending on how the laser beam interacts with the mirror, one or both of these effects may have to be considered. For a given material the bulk absorptance for an incident light source is usually some function of the wavelength of the light. Materials with low absorptance at the key wavelengths 514.5 nm, 532 nm and 1064 nm are therefore of great interest to builders of laser gravitational wave detectors.

[2] ppm means parts per million

[3] a fuller discussion of multi-layer coatings and thin films in general can be found in [49]

Materials commonly used for mirror substrates and other optical components are virtually all forms of some sort of glass or ceramic. There are over three hundred different optical glasses commercially available with different properties. In choosing a suitable material for a given function, not only the absorptance, but the *index of refraction*, *dispersion* (rate of change of index refraction with wavelength) and thermal properties including *expansion coefficient*, *conductivity* and the rate of change of refractive index with temperature (the cause of thermal lensing) need to be considered. Popular choices include various grades of *synthetic fused silica* which can have absorptances in the order a few ppm/cm in the wavelength regime of interest for gravitational wave interferometers.

4.3 Measurement of Losses in Optical Components

There are various loss measurement techniques depending on the type of optical component under investigation and type of loss that is sought. The *cavity ring-down* method of measuring losses in supermirrors is discussed in section 4.3.1 along with results for mirror coatings from various manufacturers. A *photothermal deflection* method for measuring absorptance is described in section 4.3.2.

4.3.1 Supermirror Total Loss

In terms of coefficients of light power we can express the properties of a supermirror using the expression

$$A + T + R = 1 \tag{4.3}$$

where A, T and R are the coefficients of total power loss, transmittance and reflectance respectively. A further breakdown $A = A_{scatter} + A_{absorptance}$ could be made but is not necessary here since the measuring technique about to be described can measure only total loss.

Using Storage Time to Measure Cavity Loss

In its simplest form, the experimental configuration for measuring supermirror loss

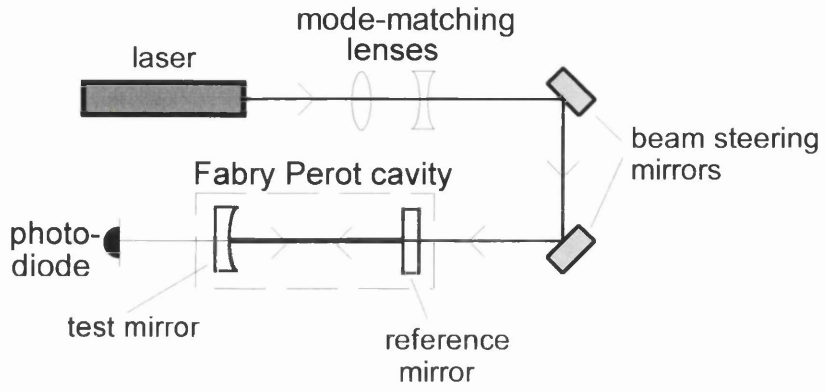

Figure 4.1: *Simple layout of the cavity loss measuring apparatus. The photodiode examines the throughput light which exhibits a characteristic decay after the cavity changes from being on resonance to off resonance.*

is shown in Fig 4.1. A laser of the correct wavelength for the mirror under test is aligned and well mode-matched into a Fabry Perot optical cavity. Ideally the cavity is made up of two mirrors one of which is the test mirror and the other is a *reference mirror* of known characteristics at the laser wavelength. Suppose initially that the light is resonating in the cavity. If this resonance condition suddenly ceases for some reason then the circulating light power in the cavity does not instantly fall to zero but rather decays exponentially at a rate determined by the loss encountered during a total cavity round-trip[4] A_{rt} where

$$A_{rt} = A_{test} + T_{test} + A_{ref} + T_{ref}. \tag{4.4}$$

By measuring the decay rate of the light power we obtain direct information about the losses of the cavity mirrors and in view of Eqn.(4.4), specifically about the test mirror (since A_{ref} and T_{ref} are known quantities). The form of the throughput light is a decaying exponential $I(t) = I(t_0)e^{-2(t-t_0)/\tau}$ where $I(t)$ is the intensity of the throughput light at time t after being switched off resonance at time t_0. The term τ is called the *cavity storage time* and is the time taken for the throughput light intensity to fall by a factor $1/e^2$. From the results of chapter 3 the storage time can

[4]total loss must represent all means by which light accumulated in the cavity is reduced during successive round trips, which must include mirror *transmittances* as well as actual losses.

be expressed in terms of the finesse F of the cavity via

$$\tau = \frac{2LF}{\pi c} \tag{4.5}$$

where in the case of a simple two mirror cavity, L is the cavity length and F is the cavity finesse given in terms of the mirror reflectances R_{test} and R_{ref} by

$$F = \pi \frac{(R_{test}R_{ref})^{\frac{1}{4}}}{1-(R_{test}R_{ref})^{\frac{1}{2}}}. \tag{4.6}$$

By using Eqn.(4.3) in Eqn.(4.6) to eliminate the mirror reflectances and then applying the binomial expansion (taking mirror transmittances and losses to be so small that cross terms or quadratic terms can be neglected) it can be shown that

$$A_{rt} = \frac{2\pi}{F}. \tag{4.7}$$

By using Eqn.(4.5) to express Eqn.(4.7) in terms of the storage time, the following experimentally useful formula is arrived at

$$A_{test} + A_{ref} = \frac{4L}{c\tau} - (T_{test} + T_{ref}) \tag{4.8}$$

which gives a method for calculating the sum of the losses of the mirrors given that their transmittances and the cavity storage time can be measured.

Principle of the Ring-Down Method

In the case where the cavity mirrors are of low loss and particularly where the output mirror of the cavity has a small transmittance, the throughput light intensity can be very small indeed. An alternative approach often preferred to the throughput light method described above, and the one used here, is to measure the reflected light from the cavity. The reflected light is a mixture of two overlapping beams. Firstly there is a component that is the light directly reflected from the input mirror having not even entered into the cavity, and secondly there is the light resonating in the cavity that leaks backwards through the input mirror. If the cavity, initially on resonance with the laser light, is forced off resonance by a sharp frequency fluctuation in the laser light, then it must be true that these two backward travelling components

of light have slightly different frequencies and so when directed at a photodiode they produce a distinctive *beat signal.* Furthermore because the component leaking backwards out of the cavity will be decaying as a function of the storage time, the beat signal will also decay at a related rate and will be characterised by a ring-down whose upper and lower envelopes can be scrutinised as follows.

Let E_{refl} and E_{leak} denote the amplitudes of the directly back-reflected beam and the beam leaking backwards from the cavity. The total amplitude of light reflected from the cavity E_{back} during a decay period beginning at $t = 0$ can be written

$$E_{back} = E_{refl} \pm E_{leak} e^{-t/\tau} \tag{4.9}$$

where τ is the cavity storage time[5]. The intensity I_{back} monitored by a photodiode placed to measure this reflected light can be expressed as the square of the amplitude

$$I_{back} = E_{refl}^2 \pm 2E_{refl}E_{leak}e^{-t/\tau} + E_{leak}^2 e^{-2t/\tau}. \tag{4.10}$$

The + and − options for Eqn.(4.10) represent the upper and lower envelopes of the ring-down pattern. Eqn.(4.10) suggests the existence of three experimentally significant possibilities, namely the three regimes where $E_{refl} \ll E_{leak}$, $E_{refl} \simeq E_{leak}$ and $E_{refl} \gg E_{leak}$. If the cavity mirror parameters are such that the first is true then the envelopes of the ring-down pattern are predominantly proportional to $e^{-2t/\tau}$ whereas if the third regime is applicable then the envelopes are mainly characterised by an $e^{-t/\tau}$ dependence. However if $E_{refl} \simeq E_{leak}$ then neither envelope decay is purely exponential. In practice therefore, it is safer to measure the decay of either the sum or difference of the ring-down envelopes which is guaranteed always to be exponential. A comparison of the transmitted decay curve and the ring-down beat signal for a given cavity is illustrated in Fig 4.2 where the $1/e$ time for the envelope difference has been labelled, and from Eqn.(4.10), can be seen to be τ. This is twice the $1/e$ time for the throughput intensity.

In summary, the measurement procedure involves obtaining a ring- down pattern for a given cavity and measuring the $1/e$ time (τ) of the *difference* between the upper and lower envelopes. Once τ is known Eqn.(4.8) is used to calculate the mirror

[5]note that the decay time constant for light amplitudes is twice that for light intensities since $intensity \propto (amplitude)^2$

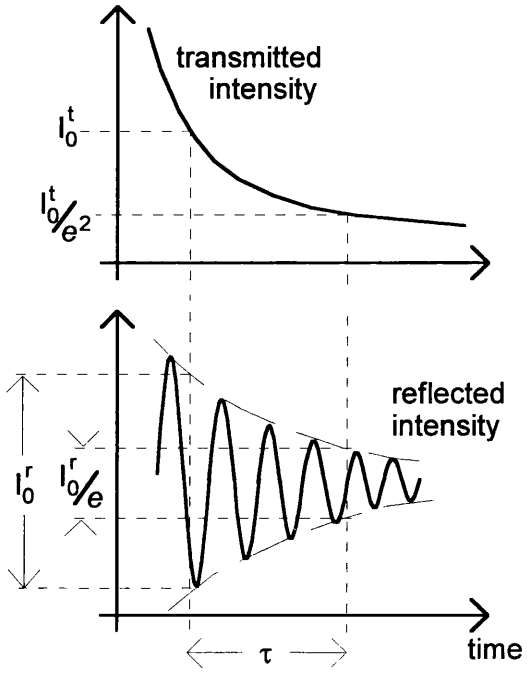

Figure 4.2: *Comparison of photodiode signals from the transmitted light and the back-reflected ring-down signal.*

losses. It is apparent from Eqn.(4.8) that the accuracy of the cavity losses will be critically dependent on good knowledge of the mirror transmittances. It follows that the transmittance of each mirror must be carefully measured in advance and this is sufficiently important to be discussed separately.

Measuring Mirror Transmittance

By looking at Eqn.(4.8) it can be seen that errors in the mirror transmittances are directly coupled to errors in the losses. This is not such a concern if neither mirror transmittance is large compared to the losses, but becomes important when the situation deviates from this ideal. A good practice is to choose mirror transmittances that are of the same order as the cavity losses. Even then, it is best that factory stated parameters are not taken literally, and the transmittance of each mirror should be experimentally measured. This was done for each mirror under test here. The light hitting a photodiode was measured with, and then without, a mirror

blocking its path and the relative intensities noted. Care must be taken to block stray room light and scattered laser light from entering the photodiode and corrupting the readings (especially for the case of the transmitted light passing through the supermirrors which may be very small indeed). In practice this was done using a series of screens and narrow band interference filters. The results obtained agreed with the quoted values from the mirror manufacturers to within a few percent in each case. In the following sections the measured values of transmittance are used in the analysis of the mirror losses.

Procedure and Experimental Configuration

If neither mirror loss is known then a single cavity is sufficient to reveal only the sum of the losses of the two mirrors, not individual mirror losses, and we may write

$$A_1 + A_2 = \frac{4L}{c\tau} - (T_1 + T_2) \tag{4.11}$$

where neither A_1 or A_2 are known and T_1 and T_2 are measured. To reveal the individual losses A_1 and A_2 we require a third mirror so that Eqn.(4.11) can be applied to all three possible two-mirror cavity permutations. This yields a system of equations of the form

$$A_1 + A_2 = k(T_1, T_2)$$
$$A_1 + A_3 = k(T_1, T_3)$$
$$A_2 + A_3 = k(T_2, T_3)$$

where A_1, A_2, A_3 are the mirror losses and T_1, T_2, T_3 are the mirror transmittances and $k(\ ,\ )$ is a function that represents the right hand side of Eqn.(4.11). Since there are as many equations as there are unknowns it is possible to calculate individual mirror losses in the absence of a well-defined reference mirror.

The apparatus used for measuring supermirror total loss is shown in detail in Fig 4.3. The laser used was a Spectra-Physics 165 argon ion type giving a few hundred milliwatts single longitudinal and transverse mode power. The laser was unstabilised and its random frequency fluctuations provided an ample mechanism

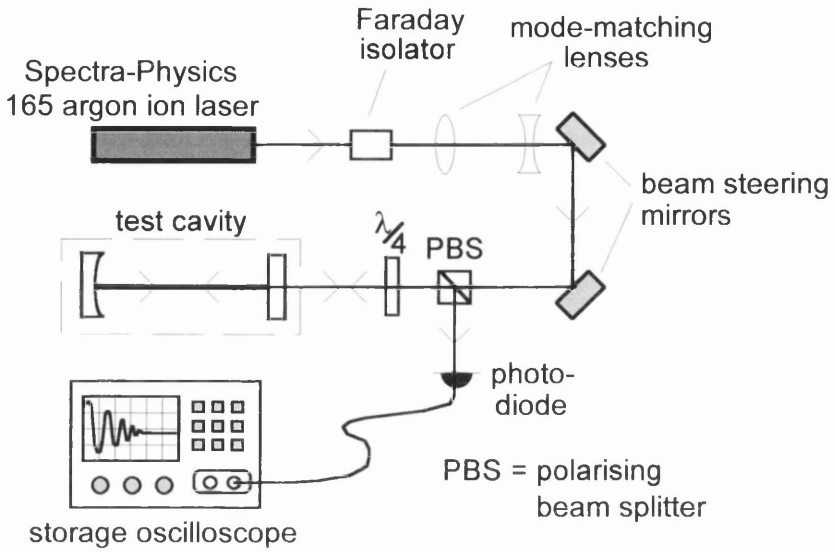

Figure 4.3: *Experimental set up for measuring supermirror losses using the ring-down method.*

for flickering the test cavity in and out of resonances. This allowed a convenient measurement practice whereby a storage oscilloscope was set to trigger automatically when the photodiode measures the start of a large ring down. For a well aligned and mode matched system, the largest ring downs are associated with the fundamental mode of the cavity and so by setting the trigger level sufficiently high, these traces could be (almost) exclusively singled out. There is a temptation to tap the optical table in order to provoke a ring down, but this is dangerous because it can move the cavity mirrors which would lead to a ring down pattern that although may look exponential, would provide the wrong time constant. An advantage of the ring down technique is that the number of beats gives a clue as to how the resonance condition was departed from. Ring down patterns with only a few beats imply that the cavity mirrors happened to move as the laser frequency altered, and in such a way as to reduce the sharpness of the change. Another potential problem is that of higher order modes flickering into resonance. Although the trigger threshold usually prevented these from producing ring downs, occasionally some got through. Many traces were examined and with experience it became possible to distinguish 'good' results from 'bad' ones.

mirror	company	transmission	radius of curv.
PMS1	PMS Ltd	570 ppm	1 m
PMS2	PMS Ltd	13 ppm	1 m
OMI1	OMITEC Ltd	240 ppm	flat
OMI2	OMITEC Ltd	6 ppm	15 m

Table 4.1: *Supermirrors used in the ring-down tests.*

Results

Measurements were made on mirrors from two manufacturers; PMS Electro-Optics based in Boulder in North America, and OMITEC Thin Films based in Devon in the UK. Both these companies have close links with gravitational wave interferometry groups and at Glasgow we have used mirrors from both companies.

PMS have established themselves as one of the most successful manufacturers of supermirrors in the world. The low loss coatings that they produce have total losses at infra-red wavelengths of only 1 ppm or less. Tests were made on a batch of PMS mirrors coated for 514.5 nm where the factory measured losses were reported to be around 5ppm.

OMITEC bought a mirror coating plant from British Aerospace (BA) after BA reduced its production of supermirror coatings in 1992. BA have produced very good quality mirrors [50] and manufactured the mirrors used in the 10 m prototype gravitational wave interferometer at Glasgow. OMITEC have since produced test coatings for 514.5 nm, but production temporarily stopped in the latter part of 1995 while they relocated their factory. The following results demonstrate their best efforts at coatings for 514.5 nm produced before their relocation.

The results that will be given involved the use of four mirrors the properties of which are summarised in Table 4.1. Individual cavity geometries need not be discussed, except to point out that the cavity lengths were always arranged to be a few centimetres only. This was to minimise the effects of scattering in air. In order to provide a suitable permutation of stable cavity geometries with convenient

mirror	total loss
PMS1	(24 ± 7) ppm
PMS2	(24 ± 7) ppm
OMI1	(18 ± 5) ppm
OMI2	(40 ± 20) ppm

Table 4.2: *Results for supermirror total loss as measured using the ring-down method.*

input transmittances etc, four mirrors and four cavities were decided upon. Each test cavity was re-aligned more than once during each measurement run to prevent random flaws on the mirror surfaces leading to inaccurate results. The mirror total losses are shown in Table 4.2. The degree of cleanliness of the air at the test lab probably accounts for the inability to measure losses as low as 5 ppm for the PMS mirrors. As soon as any supermirror is exposed in air it appears to collect tens of little dust particles that are practically impossible to remove. In the absence of an ultra-clean environment[6] the results of Table 4.2 are unlikely to be consistently bettered. An encouraging aspect of the results was the very good quality of the OMITEC mirrors, since it would be convenient to be able to deal with a local (within UK) manufacturer of high quality optics.

As mentioned previously the ring down method can reveal only the total loss of the supermirrors under test. It is instructive to try and separate out the relative components due to scattering and absorptance. This requires another experimental technique, this time to measure only absorptance, and this will be described in the next section.

4.3.2 Supermirror Absorptance Loss

The method employed here to measure mirror absorptance uses the *photo-thermal deflection method* [51] which relies on the fact that a mirror which absorbs some laser power will heat up and exhibit *thermal lensing.* The thermal lens produced can be characterised by a localised region of refractive index variation around the

[6] there are clear implications for the quality of the environment that real detector mirrors will be installed in.

beam. If a second laser beam is directed through this region it will be deflected by the lens and the amount of bending will be directly related to the level of absorption.

Principle of the Photo-Thermal Deflection Method

In the simplest set-up there is a high-power laser (sometimes called the *pump laser*) of appropriate wavelength focused down so that a very small beam lands on the sample under test (be it a mirror or other component). The sample will heat by an amount depending on its absorptance and a thermal lens will be formed. Another laser (called the *probe laser*) is aimed in such a way as to pass through the test sample at exactly the same spot as the pump beam and then to hit a split photodetector that measures its deviation. When the pump laser beam is steered very delicately, thus moving the position of the thermal lens on the test sample, the probe laser beam deflects and this deflection is measured by the photodetector. Suppose the pump beam is initially pointed so that the thermal lens region is slightly to one side of the probe beam. If it is now scanned so that the lens moves to the opposite side of the probe beam, then a very distinctive signature of signal is obtained where the probe beam moves first in one direction, and then in the opposite direction. This rather recognisable signal is one advantage in using this method. Another advantage is the rather simple model by which the technique can be calibrated. By treating the localised region of heating as a symmetric linear function of varying refractive index, the absorbed power P_{abs} is related to the peak-peak probe beam deviation α_{p-p} by the expression

$$P_{abs} = \frac{4\pi\kappa\omega_H}{\beta}\alpha_{p-p} \tag{4.12}$$

where κ is the thermal conductivity of the material, β is the rate of change of refractive index with respect to temperature and ω_H is the radius of the heating beam [52].

Procedure and Experimental Configuration

The apparatus used to measure mirror absorptance is shown in Fig 4.4. The entire experimental set-up was enclosed in a purpose-built tent which had two fans blowing filtered air into the tent from outside. This provided a positive pressure environ-

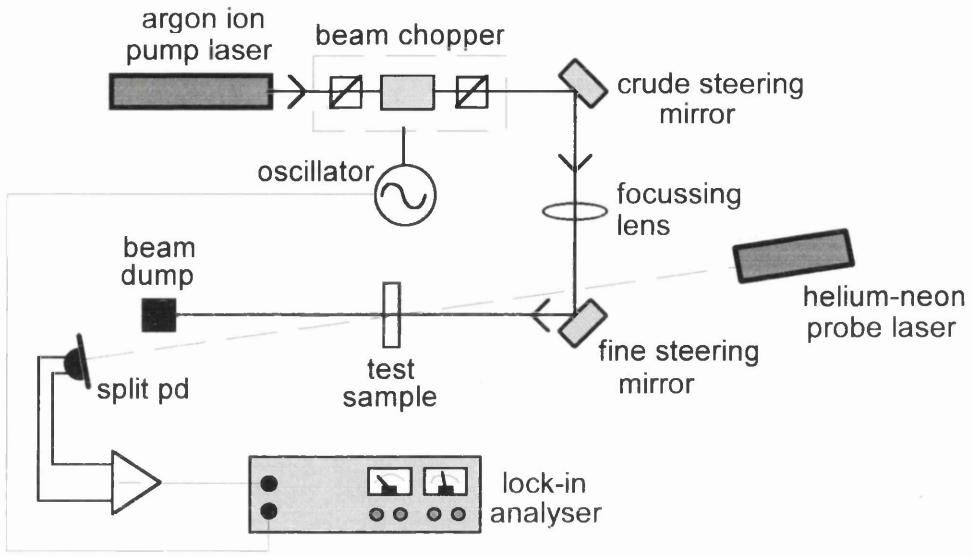

Figure 4.4: *Apparatus to measure mirror absorptance loss using the photo-thermal deflection method.*

ment which it was hoped would influence dust away from the measurement area when sections of the tent were removed to allow access to parts of the apparatus. The measurements were again performed at $\lambda = 514.5\,\mathrm{nm}$ and the laser used was a Spectra-Physics 165 argon ion laser, as for the total loss measurements. However this time the laser need not run in a single longitudinal mode, and the etalon was removed from the laser cavity, giving somewhat more power (about 1 W). The probe beam was from a Uniphase Inc. helium neon laser giving about 2 mW of light and having good pointing stability. To increase the signal to noise ratio of the measurement, the beam was modulated at a depth close to 90% by a polariser/electro-optic modulator arrangement and then a lock-in amplifier was used to provide the output signal. The lock-in amplifier gave a very good way of discriminating true signals because, as the pump beam is scanned across the position of the probe beam on the test sample, the signature of the thermal lens provides a faithful double peak separated in phase by 180°. Experimentally it was found that modulation frequencies of around 25 Hz to 40 Hz gave the best signal to noise ratio. Care must be taken to prevent scattered light entering the split photodetector as even a tiny amount of this could destroy the validity of the measurements.

mirror	absorptance
PMS1	~ 1 ppm
PMS2	~ 1 ppm
OMI1	(8 ± 2) ppm
OMI2	(15 ± 4) ppm
BA	(55 ± 14) ppm

Table 4.3: *Results of supermirror absorptance using the photo-thermal deflection method.*

Results

The results for the four mirrors labelled previously as PMS1, PMS2, OMI1 and OMI2, as well as a result for a British Aerospace supermirror, are shown in Table 4.3. It can be seen that there are substantial differences between the various mirrors and it is especially interesting to compare the first four results with the last, which is for a British Aerospace mirror that dates from 1992. Table 4.3 would suggest that the differences in quality between the OMITEC mirrors and the PMS mirrors lie primarily with the absorptance associated with the mirror coatings rather than scatter loss. Given that random defects in the supermirror coatings may account for some of this scatter loss, it seems more likely that exposure in an environment that is not clean (even for a short duration) causes an irreversible change in the scatter loss.

The absorptance measurement process described is for surface absorptance (coating absorptance in the case of a supermirror) however with a small adjustment to the apparatus, the system can also be used to measure the bulk absorptance of materials. In this case the probe and pump beam must be made to overlap over at least a few millimetres in the material. Details of bulk absorptance measurements for various grades of fused-silica at $\lambda = 514.5\,\text{nm}$ can be found in [53].

4.4 Automatic Supermirror Loss Meter

The success of the methods to measure supermirror total loss described in section 4.3 rely quite heavily on the human interface between the operator and the apparatus at each stage of the measurement process. In an industrial environment this may be inconvenient and too time consuming and the procedure would benefit from at least some degree of automation. The next two sections describe a prototype automatic loss meter being built in the lab at Glasgow.

4.4.1 Motivation for an Automatic Loss Meter

In the past, any mirror testing contract between a company and the Glasgow lab has involved the sending back and forth of carefully packaged test samples and the inevitable time delays associated with this. It would be better, especially with regard to a company like OMITEC Ltd with whom we are in contact frequently, to prepare a loss measuring device that they could install in their factory. The path to achieving this was financed by a PPARC Industrial Support Grant and involves a collaboration between OMITEC and ourselves. OMITEC primarily manufacture mirrors coated for 632.8 nm, for example for use in helium-neon laser gyroscopes. However, to be sure of the mirror qualities they are achieving they require an in-house testing unit which is relatively straightforward to use. Thus the aim of the project is to build a prototype loss meter system that OMITEC can basically duplicate. There now follows a brief outline of the design of the loss meter.

4.4.2 Conceptual Design for the Loss Meter

The loss meter will be designed primarily for use with laser-gyro mirrors coated for 632.8 nm. A simplified diagram of the loss meter is shown in Fig 4.5. The test cavity is a folded design with the middle mirror nominally fixed (maximum reflector) and the first and third mirrors interchangeable. The first mirror will be chosen from a selection of reference mirrors (having known loss) exhibiting a range of transmittances. When a third mirror (a test mirror) is supplied, a suitable reference mirror is inserted to complete the cavity. The system will use the decay curve of

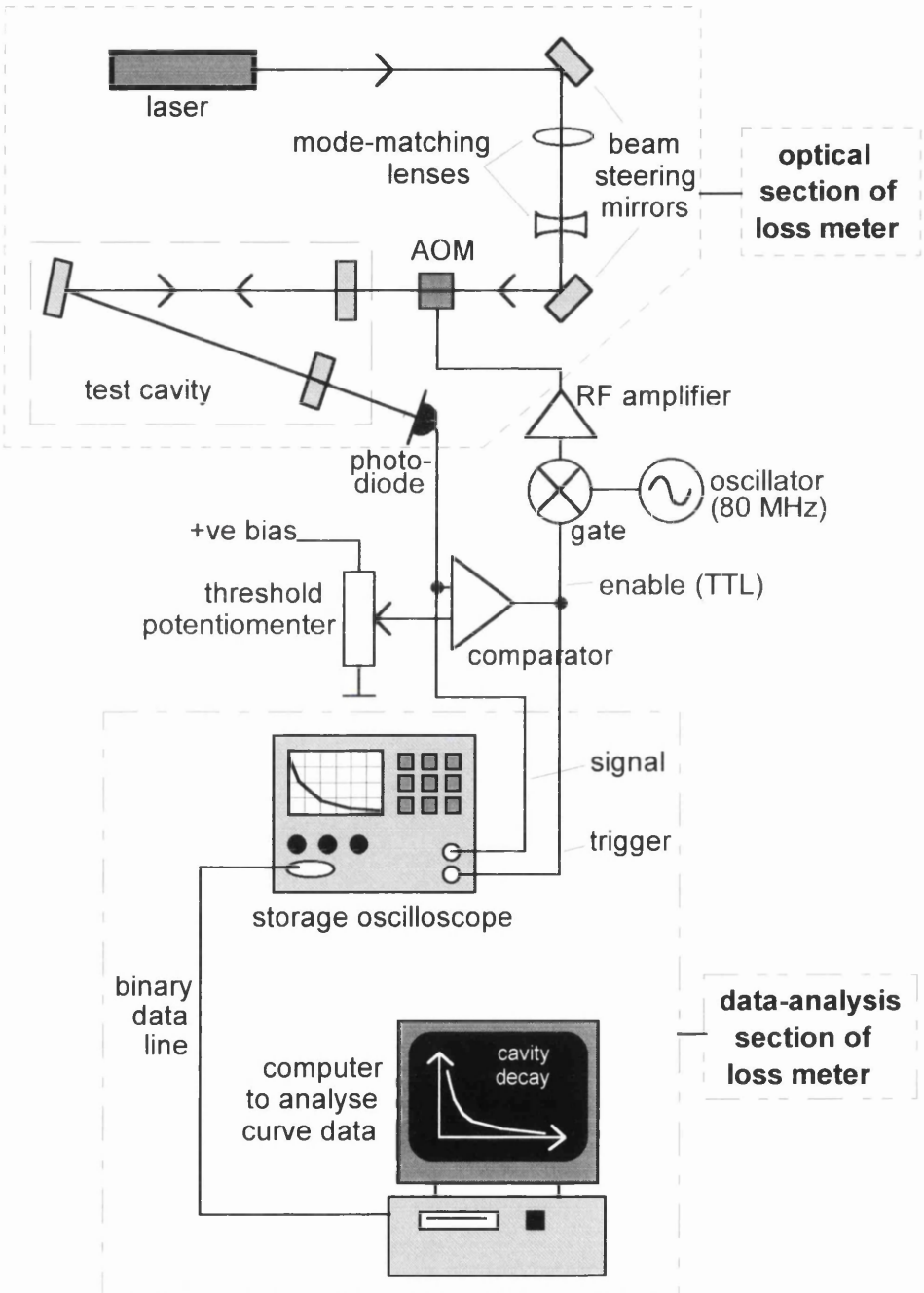

Figure 4.5: *Block diagram of the automatic loss meter being developed for use by OMITEC Thin Films Ltd.*

the throughput light to relay information about mirror loss. Helium-neon lasers are more frequency stable than argon ion lasers, and so cavity resonances happening by accident may be considerably less frequent. Therefore, to be sure that a resonance is detected and used by the system, the light to the test cavity is switched off as soon as the photodiode measures a throughput intensity greater than a preset threshold value. This ensures that the light in the cavity decays cleanly. At the same time as the light is switched off, a storage oscilloscope is triggered to record the subsequent decay of the light, and then a computer is used to down-load the trace and analyse the curve. The light is not really switched at all, but rather undergoes a rapid deflection by an acousto-optic modulator (AOM). Such a device can change state at great speed and provides a very fast cut-off of light to the test cavity. The AOM requires about 1 W of power at 80 MHz to deflect the incident beam. The RF signal is generated from a 20 MHz crystal oscillator clocked to a programmable skew buffer (CY7B 991) that steps the frequency up to 80 MHz. The 80 MHz signal is input to an RF mixer (Mini Circuits SRA-1). The comparator part of the circuit delivers a TTL logic signal which is impedance matched to the other input of the mixer. The mixer output is fed into an RF amplifier (CA 2835) which provides the required 1 W of power into the AOM. The mixer acts as a fast switch, controlling the 80 MHz signal applied to the AOM in response to state changes of the TTL level produced by the photodiode comparator circuit.

The data-analysis part of the system has software (written in Turbo C++) to read in the decay curve data to the computer over an RS 232 interface, and then subsequently to analyse its validity by fitting an exponential line to the data. The computer can then immediately calculate the total loss of the test cavity using Eqn.(4.8).

Chapter 5

Laser Beam Geometry Fluctuations

5.1 Introduction

Laser beam geometry fluctuations are variations in the position, size or shape of a laser beam. The various types of geometry noise are shown in Fig 5.1. They can either originate in the laser itself or be introduced by subsequent components in a system. For example, fluctuation in beam position could be due (at least in part) to seismically induced vibration of a beam steering mirror, while distortions of the beam phase front may be caused by irregularities in the surface curvature of some component. A useful approach in dealing with laser beam geometry noise is to model it as the fundamental transverse mode of the laser light being contaminated with higher order transverse modes. The justification for this is presented in section 5.2. The measurement processes involved in determining beam geometry noise levels can be quite complex, and they require very carefully designed instruments, some of which have been purpose built and are described in section 5.3. Results of both beam position and width fluctuations, measured using these instruments, are presented in section 5.4 and then a concluding section follows in which the results are summarised and compared for two different types of laser; argon ion and Nd:YAG.

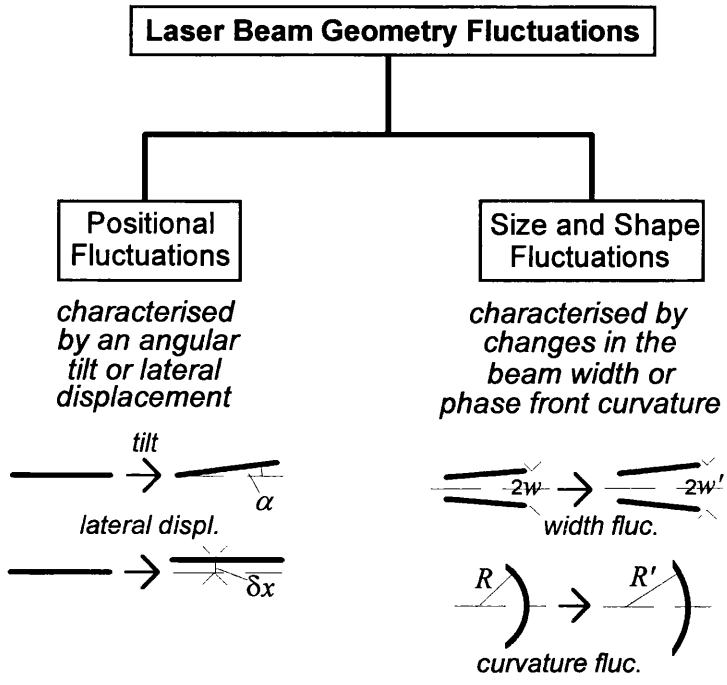

Figure 5.1: *Categorisation of varieties of beam geometry fluctuation.*

5.2 Beam Geometry Noise and Transverse Modes

A laser beam originates in an optical cavity which is filled with some lasing medium. Such a system is sometimes called an *active* cavity. A laser beam may also be fed into a *passive* cavity elsewhere in a system, for frequency stabilisation purposes for example. A condition that must be met by light circulating in such cavities is that the light field replicates itself after each round trip. Consider an optical cavity where the optic axis is made to be the z-axis in cartesian coordinates, as shown in Fig 5.2. By writing down the wave equation $(\nabla^2 - \frac{1}{c^2}\frac{\partial^2}{\partial t^2})E = 0$ for the system, and postulating a solution of the form $E = f(x,y,z)e^{j(\omega t - kz)}$ which is separable into time and spatial parts, it can be shown that for waves travelling parallel to the cavity axis (or very nearly parallel so that $\frac{\partial^2 f}{\partial z^2}$ can be neglected), f must satisfy

$$\frac{\partial^2 f}{\partial x^2} + \frac{\partial^2 f}{\partial y^2} - 2jk\frac{\partial f}{\partial z} = 0. \tag{5.1}$$

This is called the *paraxial wave equation* for the reason given above. Various solutions to Eqn.(5.1) can be sought, and the simplest will be presented first.

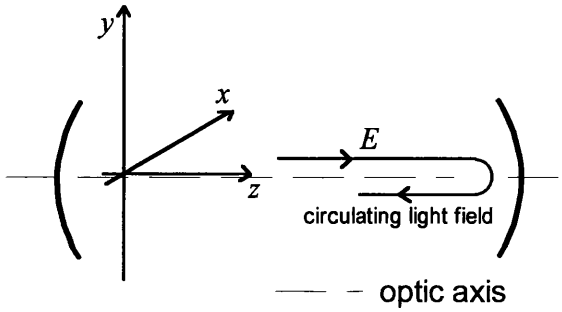

Figure 5.2: *Optical cavity with circulating light field.*

5.2.1 The Fundamental Transverse Cavity Mode

Taking f to be of the form

$$f(x,y,z) = A(z)e^{-jkr^2/2q} \tag{5.2}$$

where $r^2 = x^2 + y^2$ and q shall be defined shortly, and substituting it into Eqn.(5.1) gives

$$\left[\frac{k^2A(z)}{q^2}\frac{dq}{dz} - \frac{k^2A(z)}{q^2}\right]r^2 - \left[\frac{2jkA(z)}{q} + 2jk\frac{dA}{dz}\right] = 0 \tag{5.3}$$

where like powers of r have been collected. The bracketed terms are set to zero to satisfy Eqn.(5.3) and this yields (by integration of dq/dz and dA/dz) the results $q(z) - q(z_0) = z - z_0$ and $A(z)/A(z_0) = q(z_0)/q(z)$. Two variables R and w are now defined in terms of q by

$$\frac{1}{q} = \frac{1}{R} - j\frac{\lambda}{\pi w^2}. \tag{5.4}$$

In this form, q is called the *complex beam parameter.* The physical meaning of R and w can be deduced by substituting Eqn.(5.4) into Eqn.(5.2) to give

$$f(x,y,z) = A(z_0)\frac{q(z_0)}{q(z)}e^{-\frac{r^2}{w^2}}e^{\frac{1}{2}\frac{jkr^2}{R}} \tag{5.5}$$

where both R and w are functions of z. R can be regarded as the radius of curvature of the beam phase front, while w can be seen to be the value of r which causes the light field amplitude to diminish to $1/e$ its value at the optic axis[1] and is defined as the radius of the beam. A *beam waist* is a point where the laser beam width passes through a local minimum. At a beam waist $R = \infty$ and the complex beam

[1] recall that this is equivalent to a factor $1/e^2$ for light intensity.

parameter takes the simple form $q(z_0) = j\pi w_0^2/\lambda$. It is sensible to make the beam waist the point at which the reference values $q(z_0)$ and $A(z_0)$ apply, and from now on, the notation q_0, A_0 etc will be used to denote parameters measured at a beam waist ($z_0 = 0$). By considering the result $q(z) = q_0 + z$ and the definition of the complex beam parameter in Eqn.(5.4) it can readily be shown that

$$w(z)^2 = w_0^2 \left[1 + \left(\frac{\lambda z}{\pi w_0^2}\right)^2\right] \tag{5.6}$$

and

$$R(z) = z \left[1 + \left(\frac{\pi w_0^2}{\lambda z}\right)^2\right]. \tag{5.7}$$

The ratio of Eqn.(5.6) and Eqn.(5.7) can be simplified to

$$\frac{\lambda z}{\pi w_0^2} = \frac{\pi w^2}{\lambda R} \tag{5.8}$$

which is a useful result in Gaussian optics. In view of Eqn.(5.5), Eqn.(5.6) and Eqn.(5.7) the intensity profile and propagation of the laser beam can be illustrated as in Fig 5.3. The distance from the waist out to the point where the beam width has increased by a factor of $\sqrt{2}$ is called the *Rayleigh length* and is given by $z_R = \pi w_0^2/\lambda$. At distances beyond the Rayleigh range the beam approaches asymptotes inclined at angle $\lambda/(\pi w_0)$ to the propagation axis. The Rayleigh length is also the distance from the waist where the phase front curvature of the beam has a local minimum value given by $R = \frac{2\pi w_0^2}{\lambda}$ (R is infinite at a waist and also at $z = \infty$, and therefore must have a minimum between these values of z). In passing, it is interesting to note that the Rayleigh length is also the smallest value that the beam waist radius can adopt, thus $w_{min} = \lambda/\pi$. This can be deduced by using Eqn.(5.6) and Eqn.(5.7) to calculate the inclination of the beam asymptotes to the optic axis $\theta = \sin^{-1}(w/R)$ and then considering the diffraction limiting case of the asymptotes tending to $\pm\pi/2$. The function $A(z)$ can be written in terms of the beam waist parameters as

$$A(z) = A_0 \left[\frac{w_0^2}{w(z)^2} + j\frac{\pi w_0^2}{\lambda R}\right] \tag{5.9}$$

which, using Eqn.(5.6), can be written in polar form as

$$A(z) = A_0 \frac{w_0}{w(z)} e^{j\tan^{-1}\left(\frac{\lambda z}{\pi w_0^2}\right)}. \tag{5.10}$$

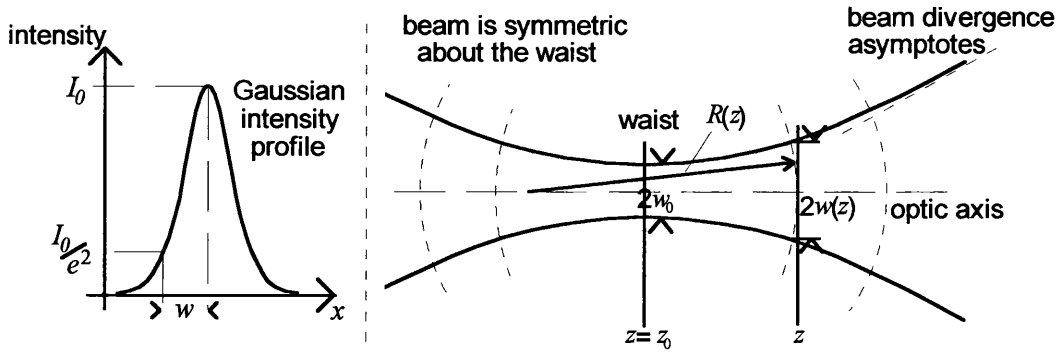

Figure 5.3: *Profile of a Gaussian laser beam. Local minima in beam radius are known as beam waists.*

The expression for f given in Eqn.(5.5) can now be written

$$f(x,y,z) = A_0 \frac{w_0}{w(z)} e^{j \tan^{-1}\left(\frac{\lambda z}{\pi w_0^2}\right)} e^{-r^2\left(\frac{1}{w(z)^2} + \frac{jk}{2R}\right)}. \tag{5.11}$$

Applying the normalisation integral $\int_{-\infty}^{+\infty} f^* f dx dy = 1$ to Eqn.(5.11) it can be shown that a normalised solution for f can be expressed as

$$f(x,y,z) = \sqrt{\frac{2}{\pi}} \frac{1}{w(z)} e^{j \tan^{-1}\left(\frac{\lambda z}{\pi w_0^2}\right)} e^{-r^2\left(\frac{1}{w(z)^2} + \frac{jk}{2R}\right)} \tag{5.12}$$

where Eqn.(5.6) has been used to simplify this result. The function described by Eqn.(5.12) is called the *fundamental transverse mode* of the optical cavity. If the cavity concerned is the laser cavity, then Eqn.(5.12) would describe the fundamental transverse mode of the laser light.

5.2.2 Higher Order Transverse Cavity Modes

The form for f given in Eqn.(5.2) is the simplest transverse mode of the cavity, with intensity profile as shown in Fig 5.3. However there are higher order modes of the light and these can be described by postulating f to be of the form

$$f(x,y,z) = A(z) g\left(\frac{x}{p(z)}\right) h\left(\frac{y}{p(z)}\right) e^{-jkr^2/2q} \tag{5.13}$$

which now gives scope for patterns of light field amplitude in the x- and y-axes which are functions of the beam propagation. A full analysis can be found in [54].

The results are important for the work of later chapters and the details will be sketched here. By substituting Eqn.(5.13) into the paraxial wave equation Eqn.(5.1) the function g is required to satisfy

$$g'' - 2jk\left[\frac{p(z)}{q} - \frac{dp}{dz}\right]xg' - \frac{jkp(z)^2}{q}\left[1 + \frac{2q}{A(z)}\frac{dA}{dq}\right]g = 0 \tag{5.14}$$

with an identical equation having to be satisfied for h. Eqn.(5.14) is very similar to the standard differential equation

$$g'' - 2\frac{x}{r(z)}g' + 2ng = 0 \tag{5.15}$$

that has the Hermite polynomials $H_n(\frac{x}{r(z)})$ defined by

$$H_n(\alpha) = (-1)^n e^{\alpha^2}\frac{d^n e^{-\alpha^2}}{d\alpha^n} \tag{5.16}$$

as its solutions. In fact, the two equations Eqn.(5.14) and Eqn.(5.15) will become identical if

$$2jk\left[\frac{p(z)}{q} - \frac{dp}{dz}\right] = \frac{2}{p} \tag{5.17}$$

$$\frac{-jkp(z)^2}{q}\left[1 + \frac{2q}{A(z)}\frac{dA}{dq}\right] = 2n. \tag{5.18}$$

These can be solved simultaneously to yield solutions for g and h which will be of Hermite polynomial form. It can be shown that $p(z) = w(z)/\sqrt{2}$ is a solution of Eqn.(5.17). By observing also that $dq^* = dq$, where q^* denotes the complex conjugate of q, Eqn.(5.18) can be expressed in the form

$$A(q) = A_0\left(\frac{q_0}{q(z)}\right)^{\frac{1}{2}}\left(\frac{q_0 q_0^*}{q_0^* q(z)}\right)^{\frac{n}{2}} \tag{5.19}$$

allowing Eqn.(5.13) to be written as

$$f(x,y,z) = A_0\left(\frac{q_0}{q(z)}\right)\left(\frac{q_0 q_0^*}{q_0^* q(z)}\right)^{(\frac{n+m}{2})} H_n\left(\frac{\sqrt{2}}{w(z)}x\right) H_m\left(\frac{\sqrt{2}}{w(z)}y\right) e^{-jkr^2/2q}. \tag{5.20}$$

As with the fundamental mode, the functions described by Eqn.(5.20) should be normalised. In the case of the Hermite polynomials this can be done using their *generating function.* This result shall be quoted here however the calculation is

done explicitly in [55]. The final normalised form for f is given by

$$f_{nm}(x,y,z) = \left(\frac{2}{\pi}\right)^{\frac{1}{2}} \left(\frac{1}{2^n n! w_0}\right)^{\frac{1}{2}} \left(\frac{1}{2^m m! w_0}\right)^{\frac{1}{2}} \frac{q_0}{q(z)} \left(\frac{q_0 q^*(z)}{q_0^* q(z)}\right)^{\left(\frac{m+n}{2}\right)} \times H_n\left(\frac{\sqrt{2}}{w(z)}x\right) H_m\left(\frac{\sqrt{2}}{w(z)}y\right) e^{-jkr^2/2q}. \quad (5.21)$$

By using the result $\frac{q_0}{q(z)} = \frac{w_0}{w(z)} e^{j\tan^{-1}(\lambda z/\pi w_0^2)}$ Eqn.(5.21) can be written

$$f_{nm}(x,y,z) = \left(\frac{2}{\pi}\right)^{\frac{1}{2}} \left(\frac{1}{2^n n!}\right)^{\frac{1}{2}} \left(\frac{1}{2^m m!}\right)^{\frac{1}{2}} \frac{1}{w(z)} e^{j(n+m+1)\tan^{-1}\left(\frac{\lambda z}{\pi w_0^2}\right)} \times H_n\left(\frac{\sqrt{2}}{w(z)}x\right) H_m\left(\frac{\sqrt{2}}{w(z)}y\right) e^{-jkr^2/2q} \quad (5.22)$$

where the notation f_{nm} emphasises that there exist multiple solutions for f separable in the x- and y-axes. The phase term $e^{j(n+m+1)\tan^{-1}(\lambda z/\pi w_0^2)}$, which can now be seen to depend on the transverse mode order through the $(n+m+1)$ factor, is often referred to as the *Guoy phase* for the mode. These solutions expressed in Eqn.(5.21) are called the *higher order transverse modes* or sometimes the *higher order radial modes* of the cavity with respect to the fundamental mode. They all have the same phase front curvature as the fundamental mode, but in general cover a greater transverse area (although the waist radius w_0 that appears in the expressions above is still that defined for the fundamental mode). The functions for the x- and y-axes can be written down explicitly. Writing $f_{nm}(x,y,z) = f_n(x,z) \times f_m(y,z)$ gives

$$f_n(x,z) = \left(\frac{2}{\pi}\right)^{\frac{1}{4}} \left(\frac{1}{2^n n! w}\right)^{\frac{1}{2}} e^{j(n+\frac{1}{2})\tan^{-1}\left(\frac{\lambda z}{\pi w_0^2}\right)} H_n\left(\frac{\sqrt{2}}{w(z)}x\right) e^{-jkx^2/2q} \quad (5.23)$$

$$f_m(y,z) = \left(\frac{2}{\pi}\right)^{\frac{1}{4}} \left(\frac{1}{2^m m! w}\right)^{\frac{1}{2}} e^{j(m+\frac{1}{2})\tan^{-1}\left(\frac{\lambda z}{\pi w_0^2}\right)} H_m\left(\frac{\sqrt{2}}{w(z)}y\right) e^{-jky^2/2q}. \quad (5.24)$$

Using Eqn.(5.16) and setting $n = m = 0$, Eqn.(5.22) can be seen to reduce to the normalised fundamental mode solution Eqn.(5.12). The first few Hermite polynomials are

$$\begin{aligned} H_0(\alpha) &= 1 \\ H_1(\alpha) &= 2\alpha \\ H_2(\alpha) &= 4\alpha^2 - 2 \\ H_3(\alpha) &= 8\alpha^3 - 12\alpha. \end{aligned}$$

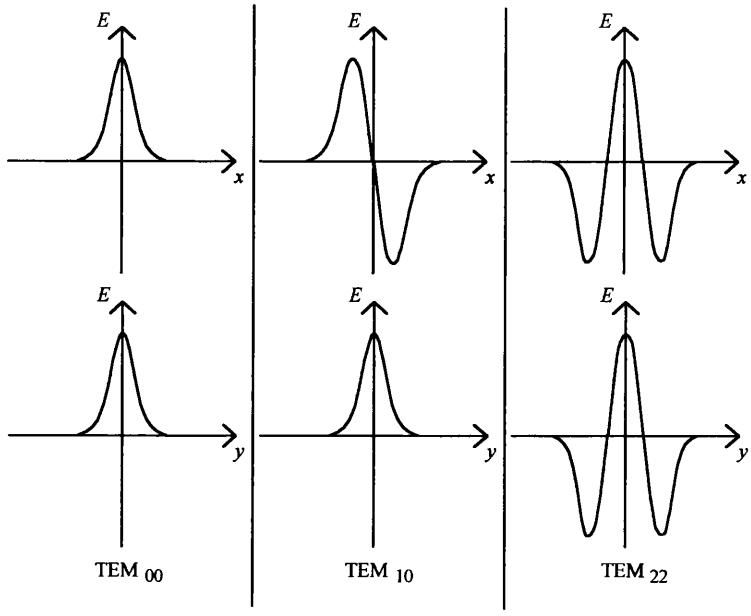

Figure 5.4: *Light field amplitude patterns for selected regions across the first three TEM_{nm} modes.*

These functions have roots along the x- and y-axes which cause nulls in the transverse light field. A transverse mode light field is represented by the symbol TEM_{nm} where TEM stands for Transverse Electric and Magnetic and the values n and m give the number of *nulls* in the field pattern along the x- and y-axes. With this notation the fundamental mode is represented as TEM_{00}. The field amplitude functions for three TEM modes are shown in Fig 5.4. Photographs of the first few TEM modes are shown in Fig 5.5 after [56]. The set of functions described by Eqn.(5.23) and Eqn.(5.24) define a *basis* for describing any light field. Given a laser beam with light amplitude field $E(x,y,z,t) = E(x,y,z)E(t)$ the spatial part $E(x,y,z)$ can be written as

$$E(x,y,z) = \sum_{n=0}^{\infty} \sum_{m=0}^{\infty} A_n f_n(x,z)\, B_m f_m(y,z) \tag{5.25}$$

Since the form for $E(x,y,z)$ is separable, the components of the laser field in the x- and y-axes can be written

$$E(x,z) = \sum_{n=0}^{\infty} A_n f_n(x,z) \tag{5.26}$$

$$E(y,z) = \sum_{m=0}^{\infty} B_m f_m(y,z) \tag{5.27}$$

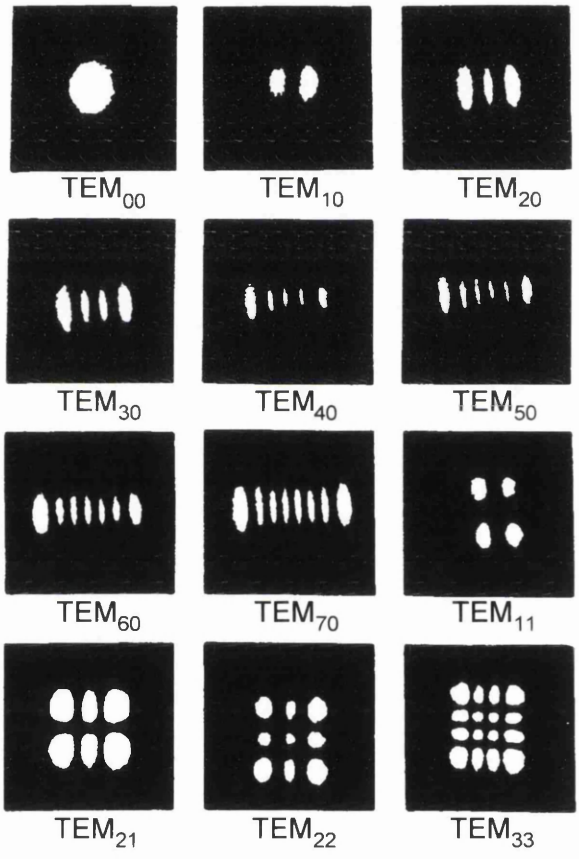

Figure 5.5: *Photographs of the first few TEM laser cavity modes.*

for some A_n and B_n given by

$$A_p = \int_{-\infty}^{+\infty} E(x,z) f_p{}^*(x,z) dx \tag{5.28}$$

$$B_p = \int_{-\infty}^{+\infty} E(y,z) f_p{}^*(y,z) dy. \tag{5.29}$$

These equation have been arrived at using the orthogonality of the eigenmodes described by Eqn.(5.23) and Eqn.(5.24) which can be stated via the expression

$$\int_{-\infty}^{+\infty} f_p(x,z) f_q^*(x,z) dx = \delta_{pq} \tag{5.30}$$

where δ_{pq} denotes the Kronecker delta symbol. It is worth noting that the Hermite polynomial functions described above do not form a unique set of eigenmodes for expressing a general light field. Rather, they prove a convenient choice in a rectangular coordinate system. If the radial coordinates r and θ had been used instead of x and y then the differential equations would have had solutions given by *Laguerre-Gaussian functions.* A normalised set of Laguerre-Gaussian functions can be found in [54]. The functions have the form

$$f(r,\theta) = \sqrt{\frac{2p!}{(1+\delta_{0m})(m+p)!\pi}}\, e^{j(2p+m+1)\tan^{-1}\left(\frac{\lambda z}{\pi w_0^2}\right)} \left(\frac{\sqrt{2}r}{w}\right)^m \times L_p^m\left(2\frac{r^2}{w^2}\right) e^{-jkr^2/2q} e^{im\theta} \tag{5.31}$$

where r is the radial coordinate ($r^2 = x^2 + y^2$), θ is the azimuthal coordiate $\theta = \tan^{-1}(y/x)$, p and m are the radial and azimuthal mode numbers[2]. The δ_{0m} is inserted for normalisation purposes and takes the value zero except for when $m = 0$ whereupon $\delta_{00} = 1$. As with the Hermite-Gaussian functions, the solutions are separable into r and θ dependent parts. The term L_p^m represents the Laguerre polynomials defined as the solutions of the differential equation

$$x\frac{d^2 L_p^m}{dx^2} + (l+1-x)\frac{dL_p^m}{dx} + pL_p^m = 0. \tag{5.32}$$

[2]these have similar interpretation as n and m in the Hermite-Gaussian functions but now, p is the number of nulls in the intensity pattern as one travels radially out from the centre of the beam, and m is the number of nulls in a 360° circular scan of the beam.

The first three Laguerre polynomials are

$$\begin{aligned} L_0^m(x) &= 1, \\ L_1^m(x) &= m+1-x, \\ L_2^m(x) &= \frac{1}{2}(m+1)(m+2) - (m+2)x + \frac{1}{2}x^2. \end{aligned}$$

The Laguerre-Gaussian functions are useful when dealing with fluctuations in the laser beam geometry that possess a cylindrical symmetry, such as fluctuations in beam width and curvature. In this case the azimuthal mode number can be set to zero and the functions take a particularly simple form. The rectangular modes described by the Hermite-Gaussian functions are often seen in gas lasers which have rectangular symmetry imposed by the Brewster windows mounted on the plasma tube. They are also convenient when dealing with beam perturbations that can be dealt with in two orthogonal components, such as lateral beam displacements and beam tilts. Mathematically, the rectangular modes can be converted to cylindrical modes using a set of transformation equations [57]. Experimentally, the conversion can be achieved with a system of cylindrical lenses placed in the beam path.

As already mentioned, it can be shown that small fluctuations in beam position, width and phase front curvature can be expressed by adjusting the weightings of the coefficients given by Eqn.(5.28) and Eqn.(5.29). This is an extremely important result and will now be considered in more detail.

5.2.3 Modelling Beam Geometry Noise as Transverse Modes

In the last section it was demonstrated that any light field could be expressed as a linear combination of the cavity eigenmodes given by Eqn.(5.23) and Eqn.(5.24). It follows that if a beam containing initially only the fundamental mode were to, say, move sideways by an amount δx or change width by an amount δw then the new light field in each case should still be expressable in terms of the cavity eigenmodes. Thus beam geometry fluctuations in general can be thought of as changes in the relative amounts of higher order TEM modes present in the beam.

Lateral Beam Movement

Consider again the fundamental laser mode given by Eqn.(5.12). If the laser beam moves off-axis by an amount δr then the new laser field can be written

$$E_{displ}(x,z) = \left(\frac{2}{\pi}\right)^{\frac{1}{4}} e^{\frac{j}{2}\tan^{-1}(\frac{\lambda z}{\pi w_0^2})} e^{-jk(x+\delta x)^2/2R} e^{-(x+\delta x)^2/w^2} \tag{5.33}$$

$$E_{displ}(y,z) = \left(\frac{2}{\pi}\right)^{\frac{1}{4}} e^{\frac{j}{2}\tan^{-1}(\frac{\lambda z}{\pi w_0^2})} e^{-jk(y+\delta y)^2/2R} e^{-(y+\delta y)^2/w^2} \tag{5.34}$$

where $E_{displ}(x,z)$ and $E_{displ}(y,z)$ denote the new light fields along the x- and y-axes due to the lateral displacement components δx and δy. The two equations are identical and it will suffice to consider only Eqn.(5.33). If δx is small compared with the beam radius w and tiny compared with the phase front curvature R, then Eqn.(5.33) can be approximated as

$$E_{displ}(x,z) = \left(\frac{2}{\pi}\right)^{\frac{1}{4}} e^{\frac{j}{2}\tan^{-1}(\frac{\lambda z}{\pi w_0^2})} e^{-jkx^2/2R} e^{-x^2/w^2} \left(1 - 2\frac{x\delta x}{w^2}[1 + j\frac{\pi w^2}{\lambda R}]\right) \tag{5.35}$$

where terms of order δx^2 have been neglected. The term in square brackets can be expressed in polar form using Eqn.(5.6) and allows Eqn.(5.35) to be written

$$E_{displ}(x,z) = \left(\frac{2}{\pi}\right)^{\frac{1}{4}} e^{\frac{j}{2}\tan^{-1}(\frac{\lambda z}{\pi w_0^2})} e^{-jkx^2/2R} e^{-x^2/w^2} \left(1 - 2\frac{x\delta x}{ww_0} e^{j\tan^{-1}(\frac{\lambda z}{\pi w_0^2})}\right). \tag{5.36}$$

From Eqn.(5.23) it is apparent that Eqn.(5.36) can be likened to the fundamental mode plus a contribution of first order mode

$$E_{displ}(x,z) = f_0(x,z) + \frac{\delta x}{w_0} f_1(x,z). \tag{5.37}$$

The above argument applies to any point along the beam propagation. The Guoy phase terms make no appearance in the final coupling coefficient. This is to be expected, since a lateral displacement must affect the entire beam by the same amount. The above expression must therefore agree with that obtained at a waist ($z = 0$), where the Guoy phase is zero for all modes.

The lateral perturbation to the beam has caused the TEM_{00} mode to be contaminated by a contribution of TEM_{10} mode. There will be a similar result for $E_{displ}(y,z)$ except that it will be an amount of TEM_{01} mode that is involved. The

above simple analysis is a convenient way to express the coupling mechanism using the Hermite-Gaussian functions. A more exact treatment requires the use of the Fourier integrals given in Eqn.(5.28) and Eqn.(5.29). The method can be illustrated for the case of a lateral displacement as follows.

The argument shall deal with the component of a lateral beam jitter in the x-axis. An identical argument for the y-component can of course be made. The light amplitude field after an initially fundamental mode undergoes a lateral displacement δx was given in Eqn.(5.33). Assuming an amplitude coefficient A_0 for the fundamental mode, this can be re-stated here as

$$E_{displ}(x,z) = A_0 \left(\frac{2}{\pi}\right)^{\frac{1}{4}} e^{\frac{j}{2}\tan^{-1}\left(\frac{\lambda z}{\pi w_0^2}\right)} e^{-jk(x+\delta x)^2/2R} e^{-(x+\delta x)^2/w^2} \tag{5.38}$$

Using Eqn.(5.28) it is possible to write down an expression for the relative contributions of higher order modes weighted to the fundamental mode as

$$\frac{A_n}{A_0} = \left(\frac{1}{\pi}\right)^{\frac{1}{2}} \frac{1}{(2^n n!)^{\frac{1}{2}}} e^{-jn\tan^{-1}\left(\frac{\lambda z}{\pi w_0^2}\right)} e^{-\delta x^2/w^2} e^{-jk\delta x^2/2R} \times \int_{-\infty}^{+\infty} e^{-(1+j\frac{kw^2}{2R})X\delta X} e^{-X^2} H_n(X) dX \tag{5.39}$$

where A_n is the amplitude coefficient of the TEM_{n0} mode and $X = \sqrt{2}x/w$. By considering the definition of the n^{th} Hermite polynomial, given in Eqn.(5.16), the above expression can be written

$$\frac{A_n}{A_0} = \frac{(-1)^n}{(2^n n!\pi)^{\frac{1}{2}}} e^{-jn\tan^{-1}\left(\frac{\lambda z}{\pi w_0^2}\right)} e^{-\delta x^2/w^2} e^{-jk\delta x^2/2R} \times \int_{-\infty}^{+\infty} e^{-(1+jkw^2/2R)X\delta X} \frac{d^n}{dX^n} e^{-X^2} dX. \tag{5.40}$$

This can be integrated by n applications of integration by parts whereupon Eqn.(5.40) becomes

$$\frac{A_n}{A_0} = \frac{1}{(2^n n!\pi)^{\frac{1}{2}}} e^{-jn\tan^{-1}\left(\frac{\lambda z}{\pi w_0^2}\right)} A^n (\delta X)^n \int_{-\infty}^{+\infty} e^{(-AX\delta X - X^2)} dX. \tag{5.41}$$

where $A = 1 + j\frac{\pi w^2}{\lambda R}$. The integral in Eqn.(5.41) can be evaluated to be $\sqrt{\pi} e^{(A\delta X)^2/4}$. Higher order contributions in δX will be present for each mode due to the exponential terms, and these will be neglected here. Doing this gives

$$\frac{A_n}{A_0} = \frac{1}{(2^n n!)^{\frac{1}{2}}} e^{-jn\tan^{-1}\left(\frac{\lambda z}{\pi w_0^2}\right)} A^n (\delta X)^n. \tag{5.42}$$

By expressing A in complex polar form, and with the help of Eqn.(5.6), a final expression for A_n/A_0 can be written

$$\frac{A_n}{A_0} = \frac{1}{\sqrt{n!}} \frac{(\delta x)^n}{w_0^n}. \tag{5.43}$$

Eqn.(5.43) shows that a lateral beam jitter can be modelled as contributions of all TEM_{nm} modes but with coupling coefficients that decrease in size with higher mode order. The strongest coupling is to the first order mode and for small positional fluctuations, it is usually sufficient to consider only this mode.

Angular Beam Tilt

The effect of a beam tilt on the higher order mode coupling can be demonstrated through a simple argument provided that the beam is assumed to rotate about a waist. The Guoy phase is zero at a waist and the analysis becomes straightforward. If a beam described by a fundamental cavity mode undergoes an angular tilt α then the resulting change in the mode picture couples through a phase term. If the angular tilt is about a waist, then the path change increment Δs caused by the tilt in the x-direction is simply $\Delta s = x \sin\alpha$ where x is measured from the beam axis. This leads to a phase increment $\Delta\phi(x) = \frac{2\pi}{\lambda} x \sin\alpha$. For small tilts this can be written $\Delta\phi(x) = \frac{2\pi}{\lambda} x\alpha$. The modified light field $E_{tilt}(x,z)$ can be written

$$E_{tilt}(x,z) = f_0(x,z) e^{j2\pi x\alpha/\lambda}. \tag{5.44}$$

If α is small the exponential can be expanded and Eqn.(5.44) can be written

$$E_{tilt}(x,z) = f_0(x,z) + \frac{\pi w_0 \alpha}{\lambda} e^{j\frac{\pi}{2}} f_1(x,z) \tag{5.45}$$

where $f_1(x,z)$ is the function describing the TEM_{10} mode. Notice that the coupling constant has an extra 90° phase term in it. Eqn.(5.45) gives the appropriate field distribution at any value of z for a beam, initially containing only the TEM_{00} mode, which is then tilted about its waist. The fact that the TEM_{10} has a greater Guoy phase than the fundamental mode does not matter here, since these phase terms are zero at a waist. This argument breaks down for the more general case where the beam tilts by an amount α about an arbitrary distance z from the waist. In

this case the effect can be traced back to the waist position where the beam can be considered to have undergone a superposition of lateral displacement $z\alpha$ and tilt α. The resulting light field will still be expressable as the fundamental mode contaminated mainly with the TEM_{10} mode, however there will be two coupling terms, one in phase (see lateral displacement case) and one phase shifted 90° as above.

Beam Width Fluctuation

It is convenient to consider a beam width fluctuation at the waist position where the Guoy phase terms can be disregarded. If the TEM_{00} laser mode undergoes a fluctuation in beam width δw at its waist, then the new light fields along the x- and y-axes can be expressed as

$$E_{\delta w}(x,z) = \left(\frac{2}{\pi}\right)^{\frac{1}{4}} \left(\frac{1}{w(z)+\delta w}\right)^{\frac{1}{2}} e^{-jkx^2/2R}\, e^{-x^2/(w+\delta w)^2} \tag{5.46}$$

$$E_{\delta w}(y,z) = \left(\frac{2}{\pi}\right)^{\frac{1}{4}} \left(\frac{1}{w(z)+\delta w}\right)^{\frac{1}{2}} e^{-jky^2/2R}\, e^{-y^2/(w+\delta w)^2}. \tag{5.47}$$

It is sufficient to consider only Eqn.(5.46) since Eqn.(5.47) is identical. By applying binomial expansions to Eqn.(5.46) (since δw is small) it is possible to express $E_{\delta w}(x,z)$ in the form

$$E_{\delta w}(x,z) = \left(\frac{2}{\pi}\right)^{\frac{1}{4}} \frac{1}{w^{1/2}} e^{-jkx^2/2R}\, e^{-x^2/w^2}$$
$$+\frac{\delta w}{w}\left(\frac{2}{\pi}\right)^{\frac{1}{4}} \frac{1}{w^{1/2}} \left[\frac{2x^2}{w^2} - \frac{1}{2}\right] e^{-jkx^2/2R}\, e^{-x^2/w^2}. \tag{5.48}$$

By comparing the second term with the TEM_{20} mode given by Eqn.(5.23) it can be seen that Eqn.(5.48) is really just the fundamental mode added to some second order mode. Since the calculation is being performed at a waist, w terms should really be denoted w_0. Eqn.(5.48) can be simplified to

$$f_{\delta w}(x,w) = f_0(x,z) + \frac{1}{\sqrt{2}}\frac{\delta w}{w_0} f_2(x,z). \tag{5.49}$$

where the coupling coefficient represents a contribution of TEM_{20} mode that is in phase with the fundamental mode. For a beam width fluctuation that takes place at some point along the beam axis other than the waist, the situation becomes more

complicated. In the cavity mode picture, such a process cannot happen without considering the beam waist location to have changed. Thus such an effect has to be traced back to the waist which can in general be considered to have undergone a displacement along the beam axis combined with a fluctuation in width.

Phase Front Curvature Fluctuation

All the beam geometry fluctuations so far discussed have had a natural interpretation as perturbations to the beam waist of one sort or another. A difficulty regarding variation of the radius of curvature of the beam phase front R is that R becomes infinite at a beam waist. Having said this, suppose that the calculation *is* referenced to what happens at the beam waist. If the curvature changes from ∞ to, say, R, at the waist position, then clearly the equivalent situation is that of the beam waist having undergone a displacement along the optic axis. Using Eqn.(5.6) and Eqn.(5.7) it is apparent that the resulting expressions for R and w at the reference point can be expressed as

$$R(\delta z) \approx \frac{1}{\delta z}\left(\frac{\pi w_0^2}{\lambda}\right)^2 \tag{5.50}$$

and

$$w(\delta z) \approx w_0 \tag{5.51}$$

where δz is the displacement of the waist, assumed here to be small enough that the approximations of Eqn.(5.50) and Eqn.(5.51) can be made. To examine the effect on the mode structure it is convenient this time to work in cylindrical coordinates. The geometry fluctuation is symmetric about the optic axis and the azimuthal part of the Laguerre-Gaussian functions can be neglected ($m = 0$). Since the perturbation is being considered near a waist, the Guoy phases can be neglected and the expression for the initial beam containing only the fundamental mode can be written

$$E(r) = \left(\frac{1}{\pi}\right)^{\frac{1}{2}} e^{-r^2/w_0^2}. \tag{5.52}$$

After the perturbation takes place, the beam radius has a finite value of R and Eqn.(5.52) becomes

$$E_R(r) = \left(\frac{1}{\pi}\right)^{\frac{1}{2}} e^{-r^2/w_0^2}\, e^{-jkr^2/2R} \tag{5.53}$$

where the value of R from Eqn.(5.50) can be substituted and the exponential expanded to give

$$E_R(r) = \left(\frac{1}{\pi}\right)^{\frac{1}{2}} e^{-r^2/w_0^2} \left[1 - 2\frac{r^2}{w_0^2}\left(\frac{\lambda\delta z}{2\pi w_0^2}\right)\right] \tag{5.54}$$

where Eqn.(5.54) has been written in this way to emphasise the similarity with the Laguerre-Gaussian function of order $p = 1$. The new light beam can be expressed as an amount of the original fundamental mode added to some first order mode

$$E_R(r) = f_0(r) - j\left(\frac{\lambda\delta z}{2\pi w_0^2}\right) f_1(r) \tag{5.55}$$

where δz is related to the beam curvature using Eqn.(5.50). This formula is essentially that obtained for an axial displacement of the waist of the fundamental cavity mode, for example due to poor mode matching into an optical cavity [58]. However its purpose here is to serve as the coupling description for a beam curvature fluctuation at a waist. If the argument is generalised to points on the optic axis away from the waist, then the treatment relies on the use of Fourier integrals. As the waist position is deviated from, first the approximations in Eqn.(5.51) and Eqn.(5.50) fail, and then the Guoy phases become non-negligible. An argument neglecting the Guoy phases can be made, where now the phase front curvature changes from R to $R + \delta R$. The exponential term involving R in Eqn.(5.53) now becomes $e^{-j\frac{k}{2R}(1-\delta R/R)}$ and when the resulting exponential is expanded, the coupling coefficient in Eqn.(5.55) now has δz replaced with z, the (small) distance from the waist where the curvature is changing, and is modified by a factor $\delta R/R$ to give

$$E_{\delta R}(r) = f_0(r) - j\left(\frac{\delta R}{R}\frac{\lambda z}{2\pi w^2}\right) f_1(r). \tag{5.56}$$

The effect of conservation of the beam width at the reference point on the optic axis requires the beam waist *size* to change in the general case as well as its position. This effect is not considered above. It is straightforward to write down the relationship between the curvature, beam waist position and beam waist radius fluctuation using the laws of Gaussian optics given in Eqn.(5.6) and Eqn.(5.7). The argument for beam width fluctuation can be used to take account of the waist size variation. In the general case the coupling coefficient would consist of a term in phase with the original fundamental mode plus a term out of phase by 90° as above. In this respect,

the general case for a fluctuation in the radius of curvature of the beam phase front is similar to the general case for describing a beam tilt.

5.3 Instruments for Measuring Beam Geometry Fluctuations

A sound knowledge of the typical levels of noise associated with various lasers is an essential basis for determining the sensitivity limits that such noise will impose. To measure the level of beam geometry fluctuations of a given type, the measurement process consists of a careful series of measurements, each conceived to exclude the possibility that other noise sources are dominating the one of interest. Instruments to measure fluctuations in beam position and pulsations in beam width will now be described.

5.3.1 Beam Jitter Meter

The simplest way to measure beam positional fluctuations is to use a split photodetector. The beam is positioned on the detector so that equal light powers fall on each sector[3]. The signals from each sector are then subtracted to provide the output signal. This method affords a first order insensitivity to laser power fluctuations, provided that the beam does not deviate from its initial position throughout the course of a measurement. Normally the output from the photodetector would be spectrum analysed and this involves the taking of averages using an analyser. In the frequency domain of interest (tens to thousands Hz) this could involve a total measurement time of many tens of seconds. During this time, the very low frequency component of the beam positional noise (which will be referred to as *beam drift*) can, and usually does, cause the beam to deviate sufficiently from its optimal position on the detector, so as to couple power fluctuation noise into the measurement. The result is that the noise spectrum obtained may not be due only to beam positional noise in the frequency range of interest (which will be called *beam jitter*) but may

[3]the temptation to say 'centered' has been avoided since this would only be true if the beam had a perfectly circular power distribution.

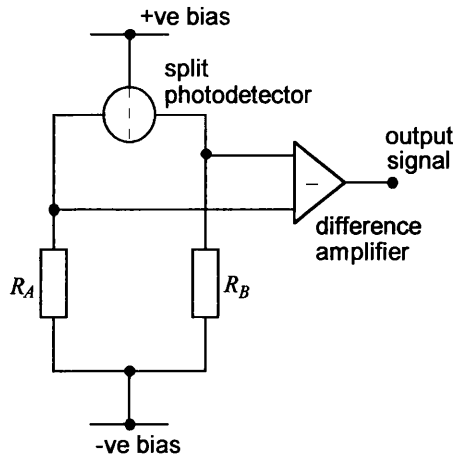

Figure 5.6: *Simple schematic of a split photodetector.*

be due in part to the laser power noise. There are various ways to overcome this problem. Consider Fig 5.6 which shows a simple version of a beam jitter measuring system. The aim is to keep equal light powers on each half of the photodetector so that $V_A - V_B = 0$. One option is to maintain this condition by physically navigating the beam. This can be done using a feedback system driving beam steering mirrors for example. Another option, and the approach taken here, is to correct for deviations electronically. The electronic scheme has the advantage that it will be insensitive to acoustic noise which would certainly not be the case for systems using active mirrors to steer the beam. The electronic feedback method is shown in Fig 5.7. The resistors R_A and R_B, now variable, are controlled to keep the voltages V_A and V_B equal to zero, and thus maintain the condition $V_A - V_B = 0$. This can be written in terms of the currents I_A and I_B in each side of the circuit as

$$I_A R_A - I_B R_B = 0 \tag{5.57}$$

A fluctuation of light power $P \rightarrow \beta P$ (β close to 1) at the photodetector causes a fluctuation in the currents I_A and I_B producing the new values βI_A and βI_B. Considering Eqn.(5.57) this can be seen to make no difference to the subtraction signal, which is still zero. However a beam jitter signal which causes a differential change in the currents I_A and I_B *will* couple through to the output *provided* that the servo circuits are not fast enough to correct for this. This insensitivity to intensity noise is a result of the *passive* properties of the system - made possible using *active*

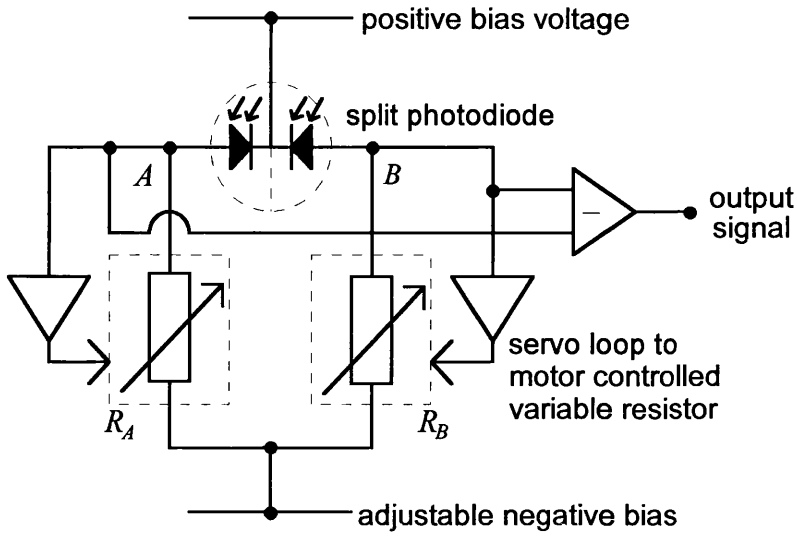

Figure 5.7: *Electronic feedback system used to correct for beam drift.*

feedback over timescales comparable with the beam drift. Therefore in practice the servo circuits controlling the resistors V_A and V_B must have bandwidths such that their action rolls off before the frequency domain of the jitter begins. A requirement of the feedback system is that the servo inputs at A and B draw a very small current compared with the average current fluctuation produced by a typical intensity variation. If this is not the case, then deviations from a totally symmetric system will couple in power noise since Eqn.(5.57) will no longer hold.

A further condition that the resistors must meet is that they are very linear with respect to their controlling voltage *and* with respect to changes in current through them. The first type of linearity is met be choosing an appropriate servo design, while the second basically imposes a requirement on the intrinsic *dynamic resistance* of the components used. Experimental work carried out with standard split photodetectors using fixed load resistors has shown that an intensity suppression of about 50 dB is possible at any instant by carefully adjusting the beam position. If this is taken as a specification for the automatic system, then a limit is set on the linearity of the load resistors. If the values of V_A and V_B (initially zero) become δV_A and δV_B as the result of a power fluctuation, then 50 dB suppression requires roughly that $1 - \delta V_A/\delta V_B < 0.3\%$. In terms of the DC and dynamic resistance of

each side, this can be written

$$1 - \left(\frac{R_A^{dyn}}{R_A^{DC}}\right) \div \left(\frac{R_B^{dyn}}{R_B^{DC}}\right) < 0.3\% \tag{5.58}$$

Circuits using FETs were found not to satisfy the above criteria adequately, due to their lack of linearity both with regard to input voltage range, and to intrinsic dynamic resistance. Even linearised FETs proved unsuitable, mainly through the difficulties in producing a system that worked over a convenient range of laser power. The most linear type of voltage controlled resistance is a motor contolled potentiometer, and in view of the low bandwidth required of the system, two of these proved to be a very satisfactory solution. The motors fitted into the MCR devices[4] are precision quality high speed ($\sim$ 6000 rpm) components. A gear system converts the speed down to about 60 rpm to turn the potentiometer shafts. The potentiometers (which are used in variable resistor mode here) are of sealed plastic design, having far greater resolution than carbon or wire-wound varieties, and having no end-stops. The complete circuit is shown in Fig 5.8. Calibration is achieved by moving the photodetector by a known amount, usually in the order of $\frac{1}{100}$th mm, and monitoring the DC response of the system.

5.3.2 Beam Width Fluctuation Meter

Pulsations in laser beam width can be detected by monitoring the relative intensities at the centre and edge of the beam. This can be done using an annular photodiode system, shown in its simplest form in Fig 5.9. The coupling of intensity noise is minimised by requiring that equal light powers fall on the central and outer part of the photodetector. This is difficult to achieve because it requires fine tuning of the width of the beam, which is possible with an adjustable lens, but is better avoided. A better approach is to achieve the intensity noise reduction using electronics to vary the load resistors. Consequently, the MCR system described above was used again here, but with a different photodiode head suitable for beam width fluctuation sensing. In this situation, the MCR system corrects for any long timescale effects that would lead to a deviation from the ideal $V_A - V_B = 0$ condition, including slow

[4] from now on, MCR will denote the term Motor Controlled Resistor.

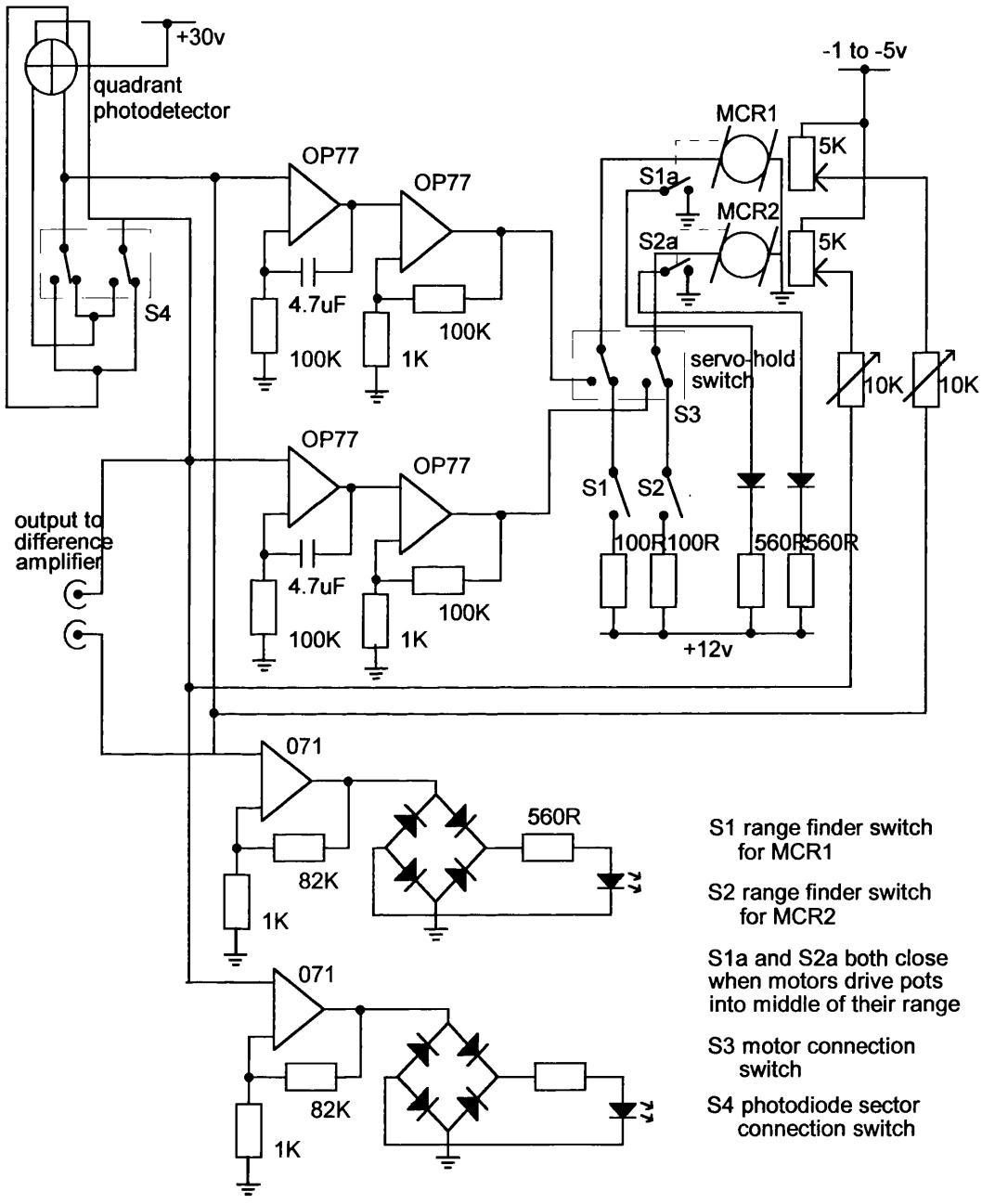

Figure 5.8: *Circuit diagram for the MCR beam jitter measuring system.*

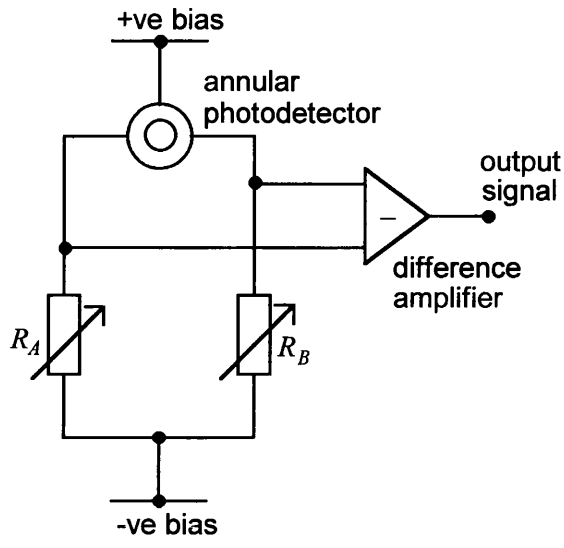

Figure 5.9: *Simple schematic of a beam width fluctuation meter.*

beam drift and beam width variation. The result is a measurement process where the primary sensitivity to beam width fluctuation is improved; however care has to be taken in the interpretation of any measurements, for the following reason.

In the jitter meter, the coupling of beam width fluctuations is a very small effect, due to the symmetry of the coupling between each half (or quadrant) of the photodetector. However in the case of measuring beam width fluctuations, it is not clear that beam jitter will not couple significantly into the measurement. Calculations aimed at integrating the gaussian beam profile over the photodiode surface can be performed, but variations in intensity across the beam, or in the sensitivity of the photodetector across its surface, can make such theoretical predictions unreliable. Consequently, coupling of beam jitter noise, as well as intensity noise, is something that is best checked experimentally. It is certainly true that deviations from a perfectly radially symmetric beam position on the annular photodetector will cause coupling factors for beam position noise. Thus as well as relying on the electronics to create the optimum operating conditions, it is also necessary to centre the beam on the annular photodetector with good accuracy.

A schematic of the apparatus is shown in Fig 5.10. The annular photodetector is actually a module containing two photodetectors and a beam splitter. The splitter

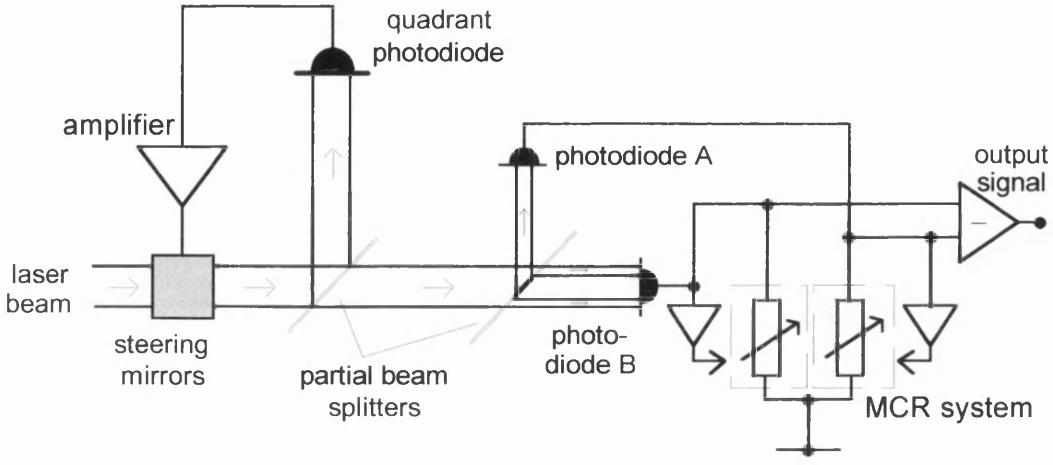

Figure 5.10: *Diagram of the beam width fluctuation measuring system.*

is mainly transparent except for a small mirror coated on its centre. When a beam is incident at 45° to the splitter, a circular portion of the beam is reflected off to one photodiode while the outer edge of the beam is throughput to the other photodiode. In this way, the action of an annular photodiode is duplicated while there is the added advantage of easy initial alignment using the symmetry of the stray reflections from the photodiode surfaces. Calibration of the system relied on changing the beam width by a known amount using a lens, and measuring the change in DC output of the system. This has to be done carefully, because the insertion of a lens inevitably refracts the beam and will produce a DC signal from the system that is not due to the beam width change. The refraction problem, and that of maintaining a central beam spot in general, was solved using an active beam steering module. This took the form of two galvanometer movements with small mirrors mounted on their shafts. Both x- and y-direction of the beam can be controlled using these, by locking a sample of the beam to the centre of a quadrant photodiode at the same distance from the beam splitter. It could then be assured that even if the input beam was tilted, the mirrors would steer the beam so that after the galvanometer module the beam direction was unaltered.

5.4 Beam Geometry Fluctuations of Nd:YAG and Argon Ion Lasers

The instruments described above were used to measure beam geometry fluctuations for two types of laser commonly used in gravitational wave interferometer research. These were a small Nd:YAG monolithic ring laser from the Laser Zentrum in Hannover (providing about 300 mW single longitudinal and transverse mode power at 1064 nm) and two argon ion lasers; a Spectra-Physics 165 and a Spectra-Physics 171 (supplying about 1-4 W single mode power at 514.5 nm). The former type is of importance for injection locked high power Nd:YAG systems [59, 60, 61] which are being considered for use in the German-British GEO 600 and French-Italian VIRGO projects, while the latter type is similar to the laser used in the 10 m prototype detector at Glasgow and those previously planned for the American LIGO project[5].

5.4.1 Nd:YAG Laser Beam Geometry Noise

Generally speaking, Nd:YAG lasers are more stable than their gas laser counterparts. They have no violent gaseous lasing medium and demand less cooling water due to their better efficiency. The laser under test here was supplied by the Laser Zentrum in Hannover and is a 300 mW monolithic slab ring laser. The lasing action in the slab is excited by a separate laser diode operating at a wavelength of about 812 nm where the absorptance of the slab is high. The slab forms a laser cavity via internal reflections from its walls, as shown in Fig 5.11. Measurements of beam jitter for this laser were made over various frequency spans and these will now be discussed.

Nd:YAG Laser Beam Jitter Noise

The beam jitter associated with the Nd:YAG laser was measured using the split photodetector connected to the MCR system. The photodetector was positioned at a point on the optical bench 1.5 m from the laser. The beam width w at this point was 1.5 mm and this is usually taken into account by expressing the jitter level via

[5]the LIGO team took the decision in late 1995 to use Nd:YAG rather than argon ion lasers.

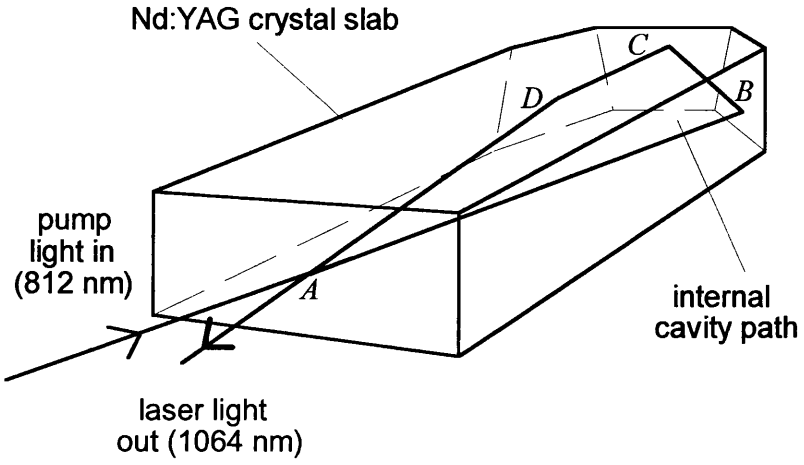

Figure 5.11: *Diagram of the monolithic slab Nd:YAG ring laser crystal. The laser cavity is formed within the interior walls of the crystal via total internal reflection at A, B, C and D. The actual width of the crystal is only about 1 cm.*

the normalised value $\delta x/w$ where δx is the rms beam jitter in the x-direction at a given Fourier frequency in the noise spectrum. Measurements for the y-direction were also taken but were found to be of a similar magnitude and so only those for the x-direction will be presented. The trace in Fig 5.12 shows the beam jitter noise in the frequency domain from DC to 100 Hz. The peak at 75 Hz is an artificially applied intensity peak imposed by a modulating the power of the diode pump laser. In order to verify that the background level in Fig 5.12 is actually due to beam jitter noise, it is necessary to check that intensity noise is being suppressed to an even lower background level by the MCR system. This check is performed by basically grounding one half of the split photodiode, thus significantly raising the sensitivity of the system to intensity noise. The relative levels of the intensity peak and background are noted and then the system is switched back to the subtraction mode, and the relative levels noted again. If the background level is seen to change by less than the intensity peak, then the background cannot be due purely to intensity noise. This is the justification for judging the background level in Fig 5.12 to be produced by beam jitter. The traces in Fig 5.13 show where the background noise level would be expected to fall in the event of it being pure intensity noise. The background level of the subtracted signal is clearly seen to be limited by a noise

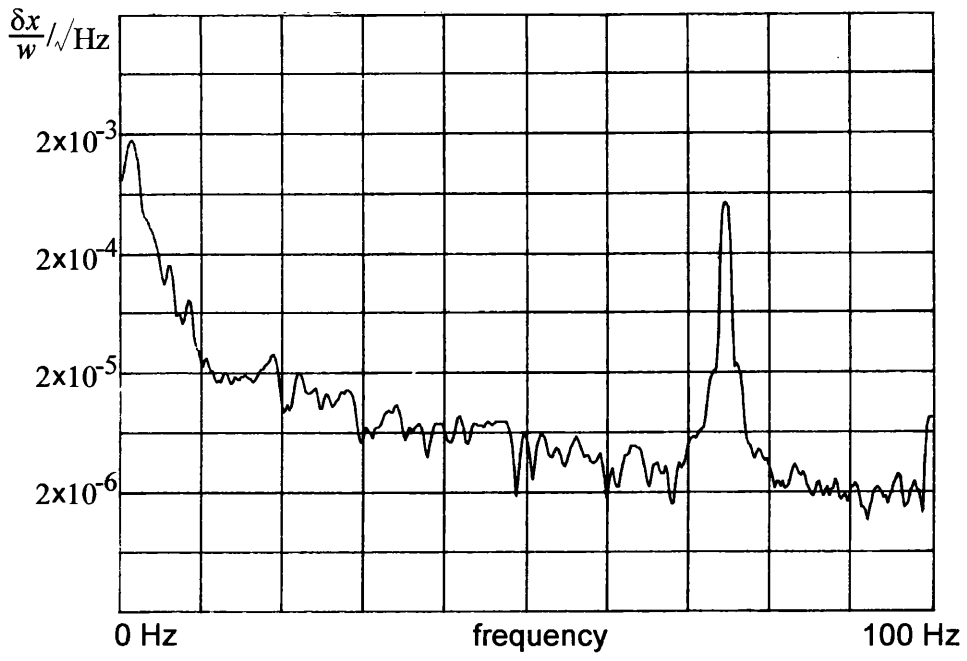

Figure 5.12: *Beam jitter spectrum for the Nd:YAG laser over a 100 Hz frequency span.*

source other than intensity noise. Measurements of shot noise were also made to ensure that these do not limit the reduction of the intensity noise level.

Nd:YAG Laser Beam Width Pulsation

The beam width pulsation levels were measured using the dual photodetector module placed in front of the galvanometer unit and connected to the MCR system. The measurements were again made at a point 1.5 m from the laser output where the beam width was 1.5 mm. The dependence of the rms beam width fluctuation level δw on the beam width w, at a given measuring point, is removed by normalising it to the width, providing the measure $\delta w/w$. The traces in Fig 5.14 shows a beam width fluctuation spectrum for the Nd:YAG laser over the frequency range from DC to 100 Hz. The peaks at 34 Hz and 73 Hz are artificially applied beam jitter and intensity signals respectively. By conducting a similar procedure to that for the beam jitter background, the validity of the background level in Fig 5.14 as something other than intensity noise and beam jitter can be established. Here it was found that the

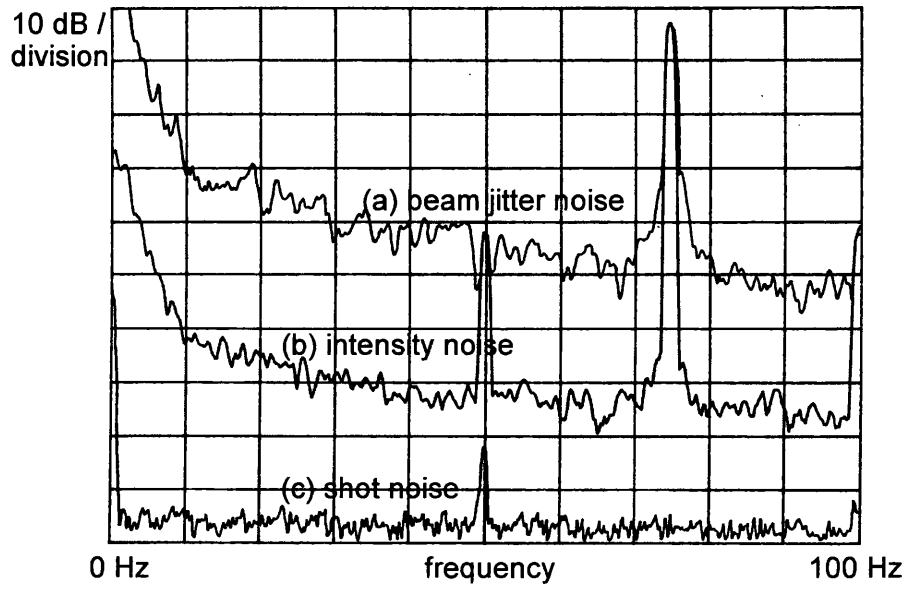

Figure 5.13: *Position of background level (a) as actually measured, (b) if it was due purely to intensity noise and (c) due to shot noise.*

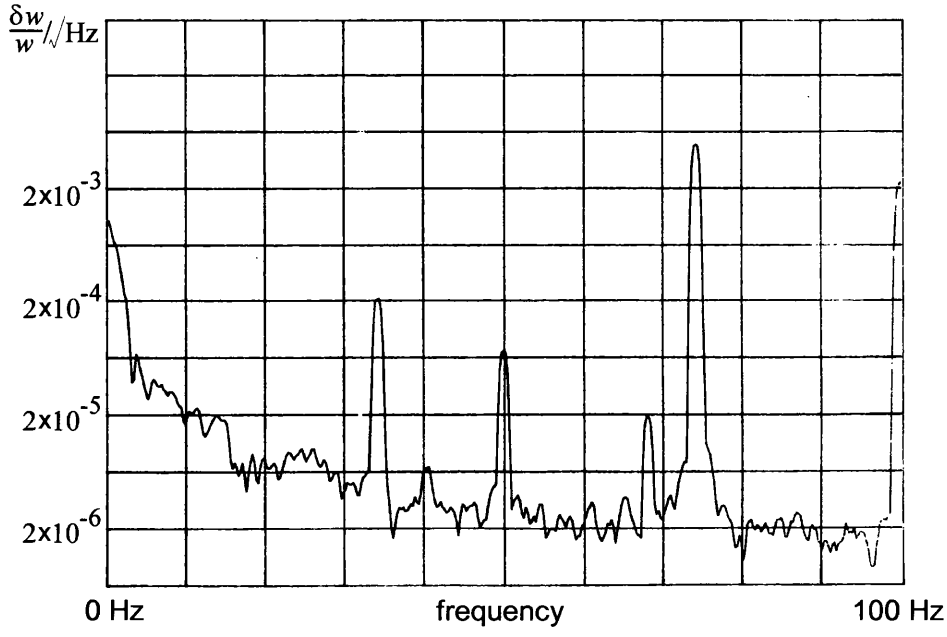

Figure 5.14: *Beam width fluctuation noise for the Nd:YAG laser over a 100 Hz frequency span.*

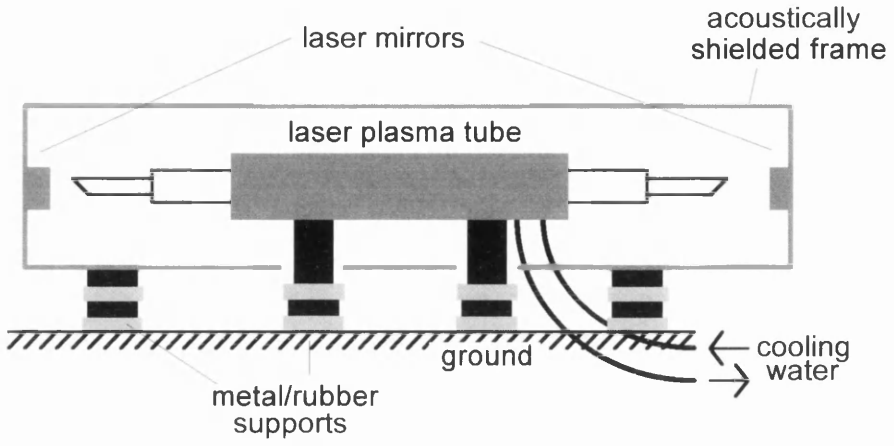

Figure 5.15: *Illustration of an external laser resonator used to isolate the laser mirrors from the vibrations of the plasma tube induced by the flow of cooling water.*

sensitivity was limited by beam pulsation noise.

5.4.2 Argon Ion Laser Beam Geometry Noise

Argon ion lasers are subject to relatively large levels of most varieties of laser noise, mainly because of their poor energy efficiency. It would not be unusual to apply 200-300 v across an argon ion plasma tube giving rise to a current of up to 50 A, only to produce a few Watts of light. Most of the energy is wasted as heat in the plasma tube, and this has to be dissipated using a constant supply of cooling water, often flowing under pressures up to 70 psi. The effect of the cooling water is physically to rattle the entire laser tube and much of the laser noise (including beam geometry noise) arises due to this simple, but unavoidable, coupling mechanism. Some degree of suppression is obtained by mounting the laser mirrors on a separate acoustically protected frame called an *external resonator* as shown in Fig 5.15. However even with this measure taken, the levels of beam geometry noise are seen to be rather high. Measurements are presented here primarily for the Spectra-Physics 165 laser tube, except for a comparison of beam jitter level between this laser and the larger Spectra-Physics 171 laser.

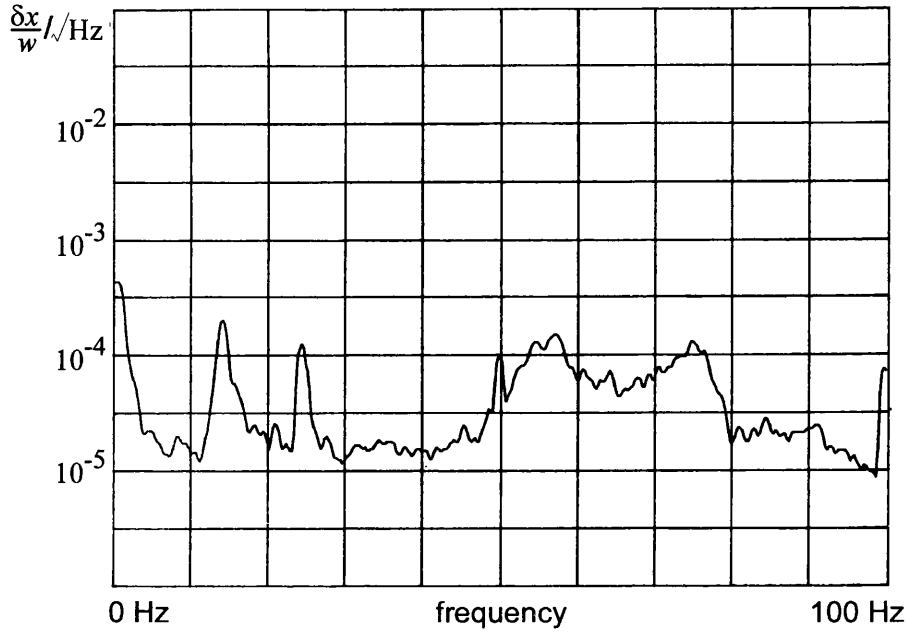

Figure 5.16: *Beam jitter spectrum for the Spectra-Physics 165 argon ion laser over a 100 Hz frequency span.*

Argon Ion Laser Beam Jitter Noise

The beam jitter associated with the Spectra-Physics 165 argon ion laser was measured by the split photodetector connected to the MCR system as before. The photodetector was positioned at a point on the optical bench 1.5 m from the laser. The beam radius w at this point was 1.1 mm and this is taken into account again by expressing the jitter level in normalised fashion $\delta x/w$. The trace in Fig 5.16 shows the beam jitter noise in the frequency domain from DC to 100 Hz.

Finally, the traces in Fig 5.17 show the beam jitter spectrum for the Spectra-Physics 171 argon ion laser (providing up to 4 W single mode power and also having an external cavity). This is the type of laser used in the Glasgow 10 m prototype detector. The laser tube is relatively long ($\sim$ 1.5 m) and it requires cooling water flowing under a pressure of about 60 psi. The background level is similar to the smaller argon ion laser suggesting that the coupling mechanisms responsible for the beam jitter noise are due primarily to the vibrations induced by the cooling water. It would not be surprising to find these sorts of levels present in all high power argon

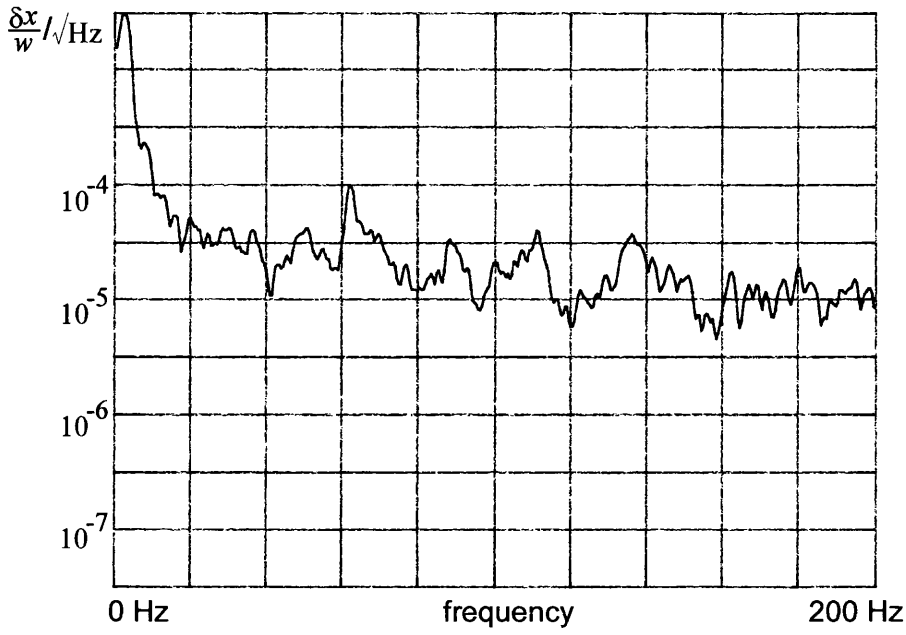

Figure 5.17: *Beam jitter spectra for the Spectra-Physics 175 argon ion laser over a 200 Hz frequency span. The background level is similar to that in Fig 4.16.*

ion lasers resonating in external cavities.

Argon Ion Laser Beam Width Pulsation

The measurements were made at a point 1.5 m from the Spectra-Physics 165 laser output where the beam width was 1.1 mm as before. The trace in Fig 5.18 shows a beam width fluctuation spectrum for the Spectra-Physics 165 argon ion laser. The sensitivity to beam jitter noise was checked by applying a beam jitter peak at 56 Hz and using this to probe the expected level of the background if it were due purely to beam jitter. To check the sensitivity of the beam width fluctuation meter to laser power fluctuations, a different approach was taken to that of applying an intensity modulation. The trace of Fig 5.18 was taken after the laser beam had passed through a commercial 'noise eater'. With the noise eater off, the laser power fluctuations were seen to increase by around 20 dB. However the beam width fluctuation spectrum was unaltered by the turning off of the noise eater as shown in Fig 5.19. This shows in a simple but direct manner that the measurement process cannot be

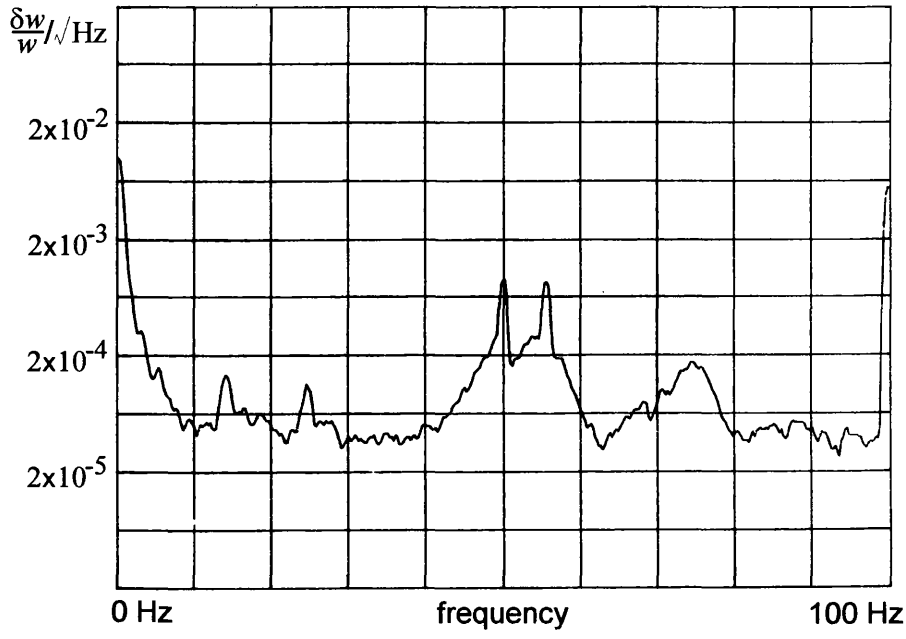

Figure 5.18: *Beam width fluctuation spectrum for the Spectra-Physics 165 argon ion laser over a 100 Hz frequency span.*

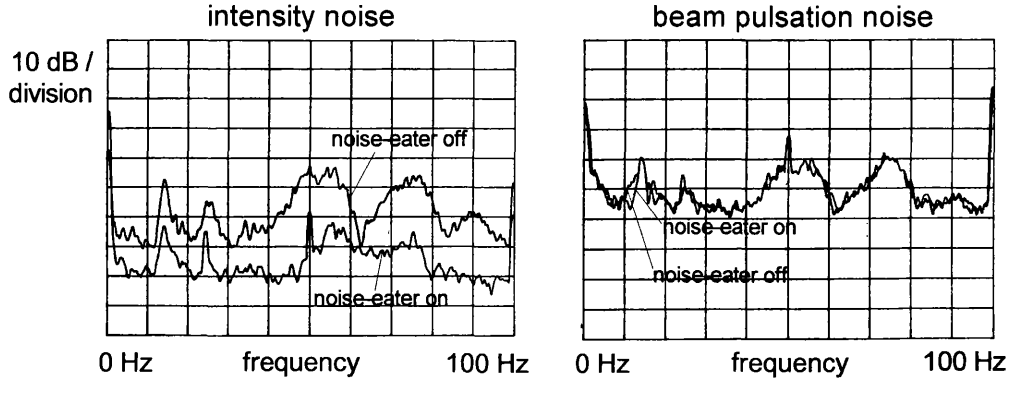

Figure 5.19: *Traces showing the effect of the noise-eater on intensity noise and on a beam pulsation spectrum.*

	Nd:YAG	argon ion
beam jitter ($/\sqrt{\text{Hz}}$)	$\sim 2 \times 10^{-6}$	$\sim 10^{-5}$
beam pulsation ($/\sqrt{\text{Hz}}$)	$\sim 10^{-6}$	$\sim 4 \times 10^{-5}$

Table 5.1: *Summary of the beam geometry noise at 100 Hz for the Nd:YAG and argon ion lasers.*

limited by intensity noise. No beam width fluctuation traces were taken for the Spectra-Physics 171 laser, but the background level is unlikely to differ greatly from that in Fig 5.18.

Now that the levels of beam jitter noise and beam width pulsation have been discussed for the two types of laser, their relative magnitudes will be compared in the following concluding section.

5.5 Comparisons and Conclusion

A number of traces have been presented in the previous section which form a valuable reference for determining the typical levels of beam geometry noise associated with different types of laser. In this section the conclusions of particular interest to gravitational wave detectors will be outlined, and a summary of the most important results will be given.

The frequency window of interest for ground based gravitational wave detectors can be regarded as a few tens of Hz to a few tens of kHz. The levels of beam geometry noise in the lasers studied all decreased with increasing frequency, and so it is sufficient to consider only the low frequency ranges where the noise is worst (up to 100-200 Hz in the traces presented here). The following summary will make reference to the average background levels recorded at 100 Hz. A review of the results shown in the graphs is given in Table 5.1. There is a clear advantage in using Nd:YAG lasers over argon ion lasers in that they are intrinsically more stable with respect to beam geometry noise. As will be investigated in more detail in chapter 6, both types of laser have noise levels that are unacceptably high for use in gravitational wave interferometers. The need for suppression systems is inevitable

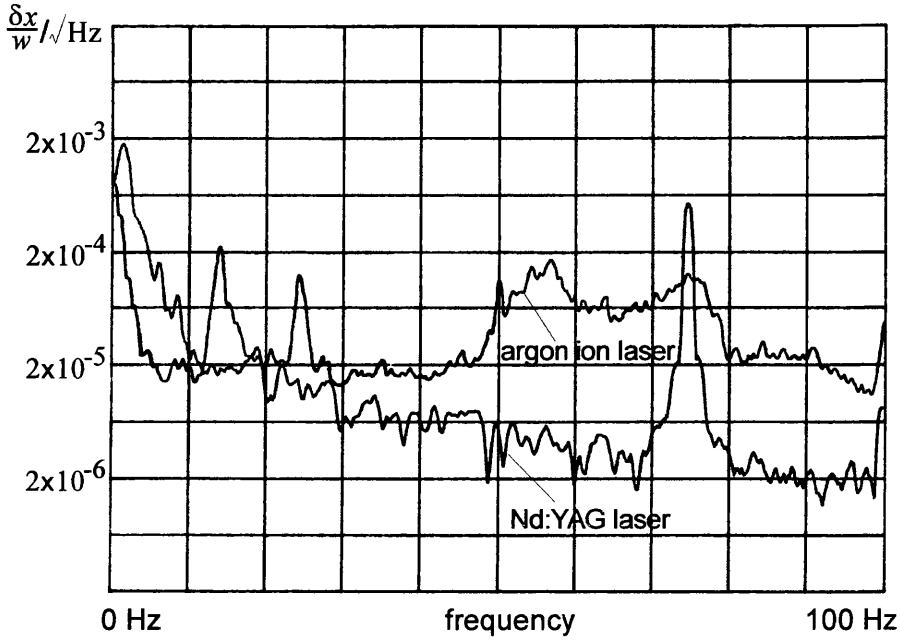

Figure 5.20: *Comparison of the beam jitter noise in the Nd:YAG ring laser and the Spectra-Physics 165 argon ion laser.*

but the demands on such a system would be less if the interferometer was powered by a Nd:YAG laser having similar, if not better, properties to the model under test here. The graphs in Fig 5.20 and Fig 5.21 show comparisons between the levels of beam jitter noise and beam width pulsation noise for the two types of laser.

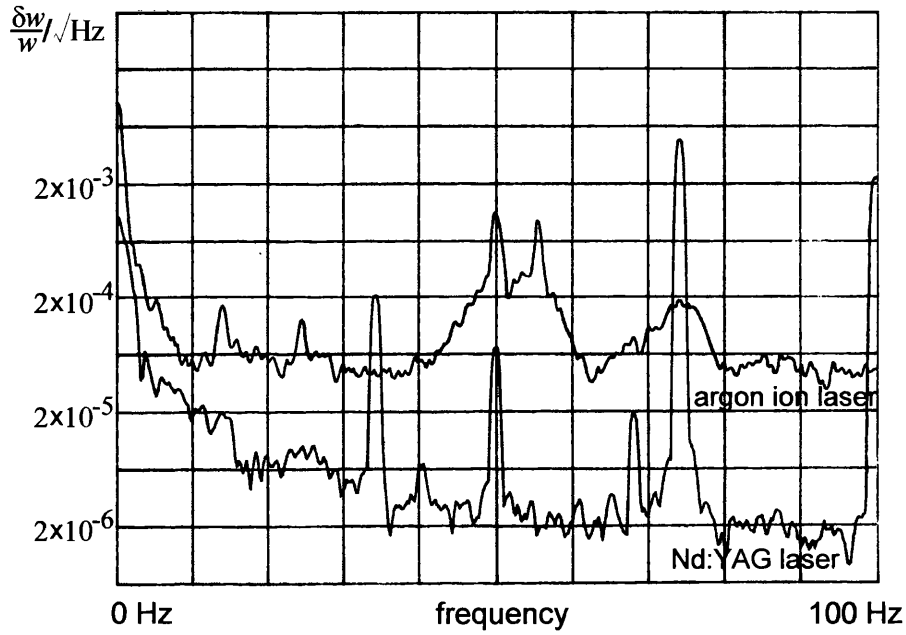

Figure 5.21: *Comparison of the beam width pulsation noise in the Nd:YAG ring laser and the Spectra-Physics 165 argon ion laser.*

Chapter 6

Study of Beam Geometry Noise of a Nd:YAG Laser

6.1 Introduction

The Nd:YAG monolithic ring laser has already been introduced in chapter 5. In this chapter the same Nd:YAG laser will form the subject of two separate studies, both provoked by problems encountered when building an intensity servo for the laser. The purpose of the intensity servo, at least in the first instance, was to suppress the well-known intensity noise peak at high frequency caused by internal *relaxation oscillations* in the lasing medium [54]. This study had shown the existence of apparent frequency noise at the relaxation oscillation frequency [62] and it was decided to investigate the level of beam jitter that may exist at this frequency also. In the longer term, the intensity servo was designed with an aim of providing a broader band reduction of noise. After working with the broadband system it became apparent that limitations to the performance of the servo at low frequencies were being reached that were not due to photon shot noise. This posed questions about the level of beam geometry noise present that may couple into the broadband servo.

The question regarding whether beam geometry noise (particularly beam jitter) was present at, and perhaps produced by, the relaxation oscillation in a Nd:YAG

laser is interesting in its own right, and measurements concerned with this will be presented in section 6.2. The broadband intensity servo study is discussed in section 6.3.

6.2 Beam Jitter at the Relaxation Oscillation Frequency of a Nd:YAG Laser

The relaxation oscillation (RO) of a Nd:YAG laser has been traditionally regarded as producing a peak in intensity noise seen at a frequency around a few tens of kHz to a few hundreds of kHz, with a linewidth of a few kHz to tens of kHz (depending on the properties of the laser cavity). It is produced in solid state lasers where perturbations in the pumping rate (in this case due to noise in the laser diode) produce a dynamic imbalance between the inverted state and photon populations. The result is a self-supporting oscillation in cavity photon number producing a subsequent modulation of output power.

The view was taken here that no attempt to explain the limitations of an intensity servo designed to reduce noise at the RO frequency would be complete without considering the possible coupling of beam geometry noise, and whether the relaxation oscillations do in fact generate a peak in the geometry noise spectrum. If beam jitter was present then it may produce a small signal at the photodetector of the servo loop, which of course should register only intensity changes. This signal may arise from poor choice of beam positioning on the photodetector. For example, if the beam is just larger than the photodiode active area, then local intensity variations across its area may couple beam jitter into intensity noise. Alternatively, if the beam is made far smaller than the photodiode, then variations in response over the active area of the photodiode could provide a coupling mechanism. Another important consideration is that of multiple reflections in the glass front of the photodiode providing variations in throughput light power as a function of the incident beam position and direction. A further possible coupling mechanism, that is more difficult to quantify, is the effect of laser speckle at the photodetector: if the beam is static then the presence of such a speckle pattern should not matter, however if

the beam is varying in position, the speckle pattern may change, coupling in noise at unpredictable frequencies.

All the above effects could produce a varying intensity signal at the photodiode which would couple into the feedback path and may limit servo performance. The simplest and most direct check is then to measure the beam jitter present at the RO frequency. This presented a challenge because the technique of measurement would have to be able to identify what might conceivably be a minute level of beam jitter noise at a frequency where there is already a significant amount of intensity noise.

6.2.1 Measurement Procedure

The measurement process entailed applying a laser power fluctuation at a given frequency by modulating the current to the pump diode. By using the MCR split photodiode system (see chapter 5) and comparing the normal subtraction signal with the signal produced by grounding one half of the split photodetector, it is possible to compare the relative contributions of beam jitter and intensity noise associated with a given peak or background level. Here, it is the relative change in magnitude of the applied intensity peak compared with the RO peak that is of interest. If they change by the same amount when switching between the two modes of the MCR system then they are both most likely to be intensity noise. However if the RO peak changes by a different amount than the intensity peak, then the measurement process is sensitive to an additional noise associated with the RO peak, which in the case of a split photodiode would almost certainly be beam jitter noise.

There is an implicit assumption here that the applied intensity peaks do not themselves modulate the position or width of the beam which, given the nature of the modulation technique, is probably a fair assumption. Given this uncertainty, however small, it is safer to regard the results presented for beam jitter levels at the RO frequency as upper limits.

In practice, two artificial peaks were applied to either side of the RO peak each a few kHz from it. This was done to ensure that the measuring apparatus did not show an appreciable change in performance over the frequency difference between the applied peak and the relaxation oscillation peak due to un-intentional filtering

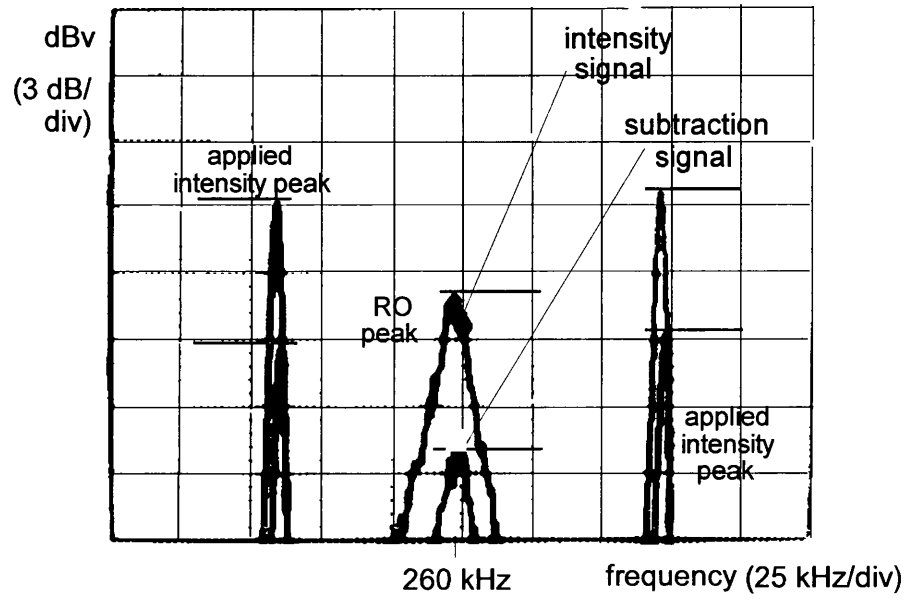

Figure 6.1: *Graph showing the signal from the MCR system before (top trace) and after the subtraction mode is switched on.*

within the electronics.

6.2.2 Results

All the traces were obtained by taking 1000 averages with a high-frequency spectrum analyser. The graph in Fig 6.1 shows two spectra superposed on the same picture. The top trace is the signal from the MCR system with one half of the split photodetector grounded and the lower trace shows the subtraction signal. By scrutinising the amount by which each peak has been reduced it can be seen that the two intensity peaks have been reduced by exactly the same amount (which is reassuring) but the RO peak has been reduced by about 1 dB more. This is such a small difference that it would only become interesting if it were to be seen again and again. In practice many traces were recorded, with a statistical slant towards a repetition of Fig 6.1 with differences in some cases approaching a little over 1 dB. However, many traces showed no significant difference and as mentioned before, the best that can be done is to set an upper limit on the beam geometry noise level at the RO frequency. The system was calibrated at DC by moving the photodetector

by a measurable amount and noting the peak to peak signal produced at the input to the analyser. A high-frequency sinusoidal signal was then run through the system starting effectively at the photodetector and monitored on the analyser. This was to check for any deviation of the calibration at the RO frequency from that at DC, imposed by filtering effects in the cables or electronics.

A peak in the subtracted signal trace can be regarded as being due to a contribution of beam jitter noise V_j and laser power noise V_P. The height of a peak in dBv is then given by

$$peak_{dB} = 20\log_{10}(V_j + V_P). \tag{6.1}$$

If the discrepancy in the reduction seen in the RO peak is due purely to beam jitter noise, then a 1 dB change (which was about the largest measured) amounts to

$$V_j = 0.11 \times (V_j + V_P) \tag{6.2}$$

obtained by using the reduction of the applied peaks as a reference for the level of intensity suppression, and then solving $1\,\mathrm{dB} = 20\log_{10}(V_j + V_P) - 20\log_{10} V_P$. The quantity $(V_j + V_P)$ can be measured directly from the spectrum analyser trace in Fig 6.1 providing an explicit value for V_j. Using the system calibration, an upper limit for the rms beam jitter can be obtained and is found to be

$$\begin{aligned} \delta x &= 10^{-11}\mathrm{m}/\sqrt{\mathrm{Hz}} \\ \frac{\delta x}{w} &= 5 \times 10^{-9}/\sqrt{\mathrm{Hz}} \end{aligned}$$

where the latter value has been normalised for the beam radius w which was measured to be 2 mm.

In an attempt to improve the sensitivity of the measurement technique still further, the suppression of the intensity noise was now optimised manually, rather than being left completely to the MCR unit. This was achieved by monitoring in real time, and trying to minimise, the height of an applied intensity peak while very carefully scanning the position of the laser spot on the split photodetector. After careful adjustment, reduction of intensity noise such as that shown in Fig 6.2 was possible. The measurements were then repeated with this new improved performance, and a typical trace is shown in Fig 6.3. The intensity peaks are now reduced by notably

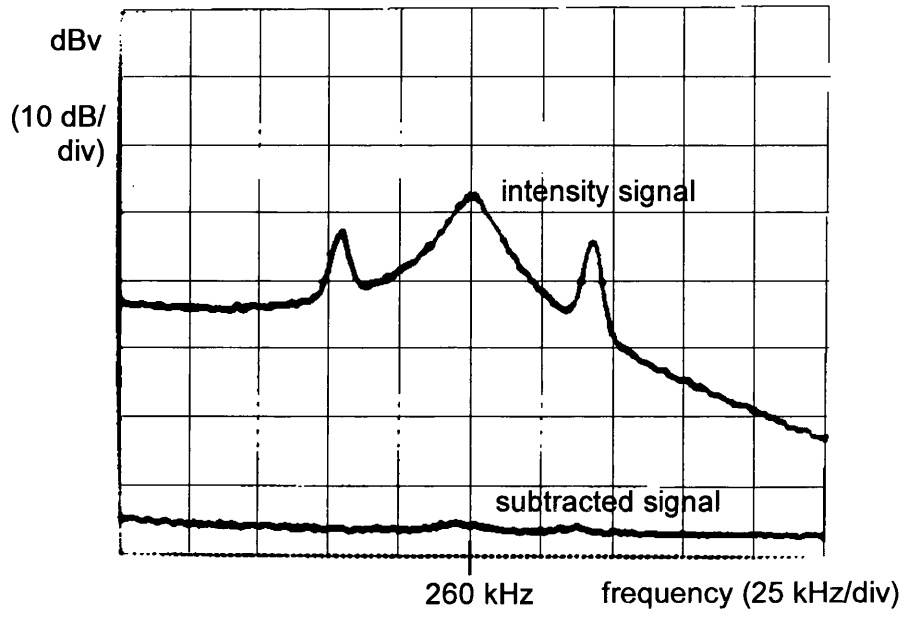

Figure 6.2: *Typical level of intensity noise suppression achievable using the MCR system with initial fine manual adjustment.*

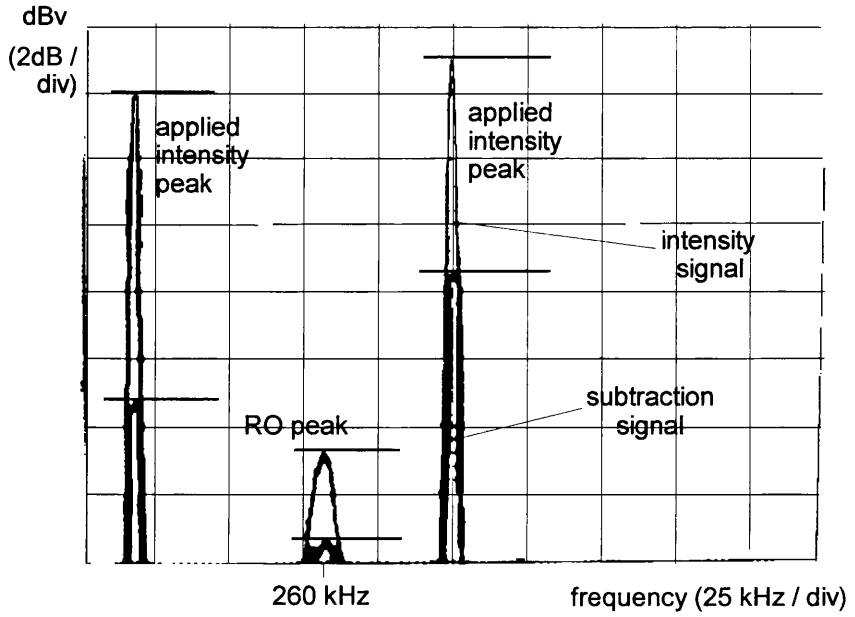

Figure 6.3: *Graph showing the signal from the MCR system before and after the subtraction mode is switched on, with manually optimised reduction of the applied intensity peaks.*

different amounts, however this difference is small, given that the system is providing over 40 dB suppression for each intensity peak. The difference between the reduction in height of the applied peaks and the RO peak is about 5 dB in Fig 6.3, which is typical of many traces taken. Using this as an upper limit gives after calibration

$$\frac{\delta x}{w} = 1.9 \times 10^{-9}/\sqrt{\text{Hz}} \tag{6.3}$$

which is a tighter limit than before.

6.2.3 Conclusion

Care must be taken in interpreting the figures given above for the following reason. The peaks in Fig 6.3 are getting very close to the noise floor, especially those in the subtracted signal trace. When investigating a peak of this size it has to be remembered that it can never really disappear since it will always add to the existing noise. Thus it may be the case that the RO peak would sink to a lower level if the signal to noise ratio of the measurement process was greater. As a final check, a series of measurements was taken where the intensity servo, designed to reduce the RO peak, was switched on and then off and the traces from the MCR system in subtraction mode were recorded. This series of measurements appeared to suggest that, on average, the applied intensity peaks were reduced by the same amount as the RO peak. This implies that the level of beam jitter at the RO frequency is very small, if not zero. In any event the values of beam jitter given above still represent an upper limit to the beam jitter noise associated with the relaxation oscillation of the laser.

6.3 Coupling of Beam Geometry Noise into a Broadband Intensity Servo

The intensity servo initially designed to reduce the noise at the RO frequency was eventually generalised to provide a broadband reduction of laser intensity noise. The performance of the servo was again seen to be limited by some effect other than shot noise or electronic noise. For example, an applied intensity peak would be reduced by

30 dB but the neighbourhood background level would be reduced by only 20 dB even though fundamental noise barriers were around 10 dB lower. To ascertain whether or not the effect of beam geometry fluctuations was a factor in this degradation of servo performance, the beam was fed through a single mode optical fibre designed to suppress beam geometry noise. The results, which took a particularly unpredictable path, are presented below.

6.3.1 Measurement Procedure

The laser beam was fed through a single mode optical fibre before being used as a reference for the intensity servo feedback loop as illustrated in Fig 6.4. Several measurements were made, both of beam jitter noise and intensity servo performance in an attempt to investigate the differences between signals present before and after the fibre. The fibre was mounted on an adjustable translation stage to allow fine control of its relative orientation and position with respect to the input beam. The light was coupled in by a +40 D lens and coupled out with a +25 D lens. An interesting but rather annoying phenomenon was that of interference effects within the fibre. If the fibre bent, even by a small amount, then the optical path length inside it changed and a large intensity fluctuation was observed on the output light. It was possible in practice to change the fractional throughput power from 20% to 65% just by flexing the fibre slightly. To reduce the effects of air currents and acoustic noise imposing intensity noise on the output light from the fibre, the entire arrangement including the translation mount was housed in an acoustically shielded box.

6.3.2 Results

The fibre was found to reduce the level of beam jitter noise by a measureable amount as shown in Fig 6.5 although the overall level of reduction can be seen to vary greatly over different parts of the frequency domain. The most obvious experiment to perform after installing the fibre was simply to switch on the intensity servo and note any improvement in its perfomance. This was checked and the amount

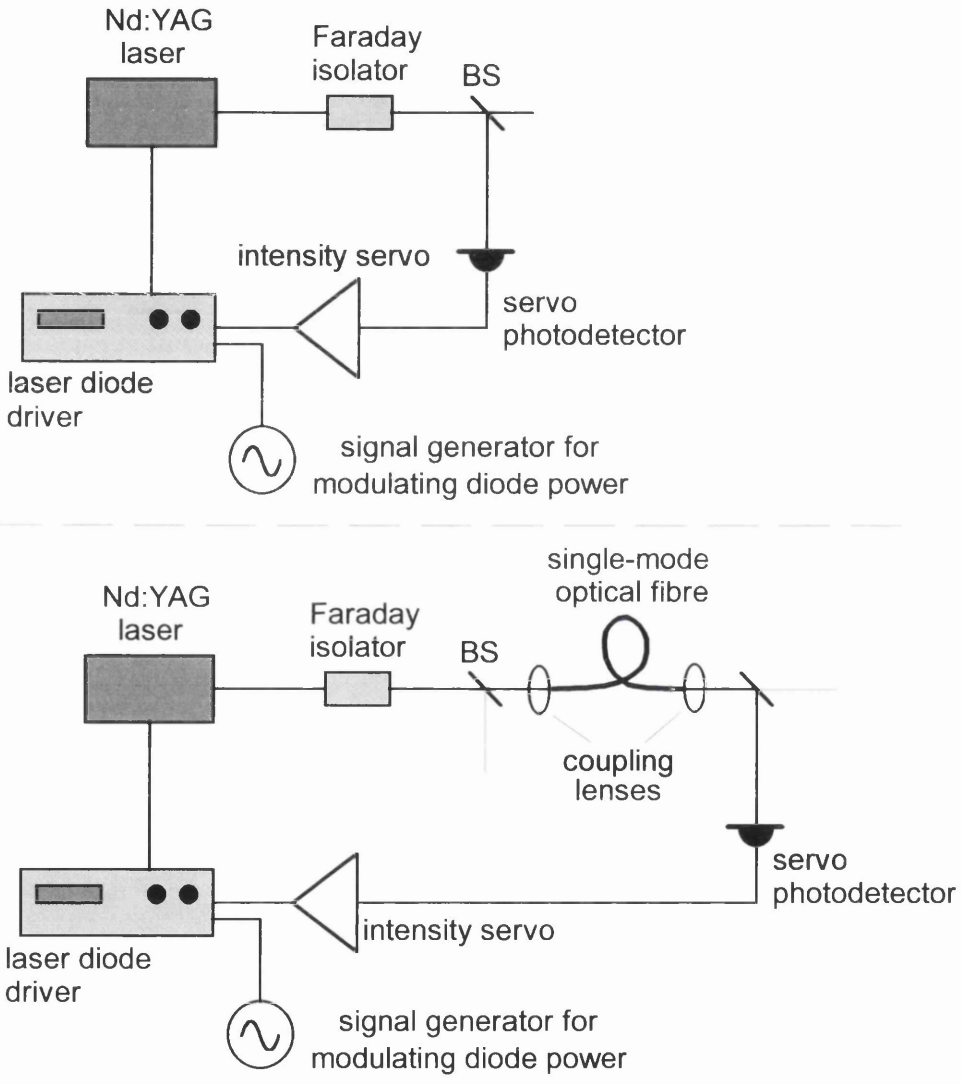

Figure 6.4: *Schematic of the broadband intensity servo before and after the installation of a single mode optical fibre.*

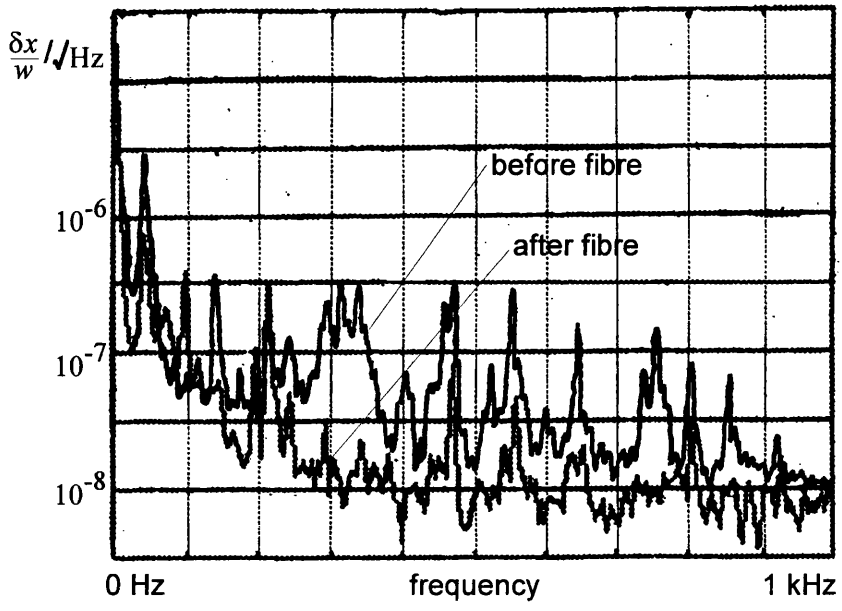

Figure 6.5: *Traces showing the level of beam jitter noise of the Nd:YAG laser in a 1 kHz span before and after the single mode optical fibre.*

of reduction of the background intensity noise level was seen to improve, finally providing the level of suppression expected in view of the photon shot noise barrier.

On a seemingly unrelated matter, subsequent measurements on the performance of the intensity servo (with the fibre now removed) were seen to be affected by large excursions of the laser power at low frequency. A well known cause of this in many types of laser is instability in the laser cavity induced by light directly back-reflected into the laser. This poor *optical isolation*, as it is often called, is usually dealt with using one or more Faraday isolators but these are sensitive to alignment and require careful setting up to achieve optimal reduction of back-reflected power reaching the laser. In an attempt to reduce the low frequency power drifts, the Faraday isolator, of which there was only one here, was realigned to optimise the level of isolation. This not only had the effect of reducing the low frequency power fluctuations, but more surprisingly, it also led to an improvement in the performance of the intensity noise servo, yielding a similar level of performance to that observed after the fibre had been installed. This suggested the possibility that poor isolation could cause

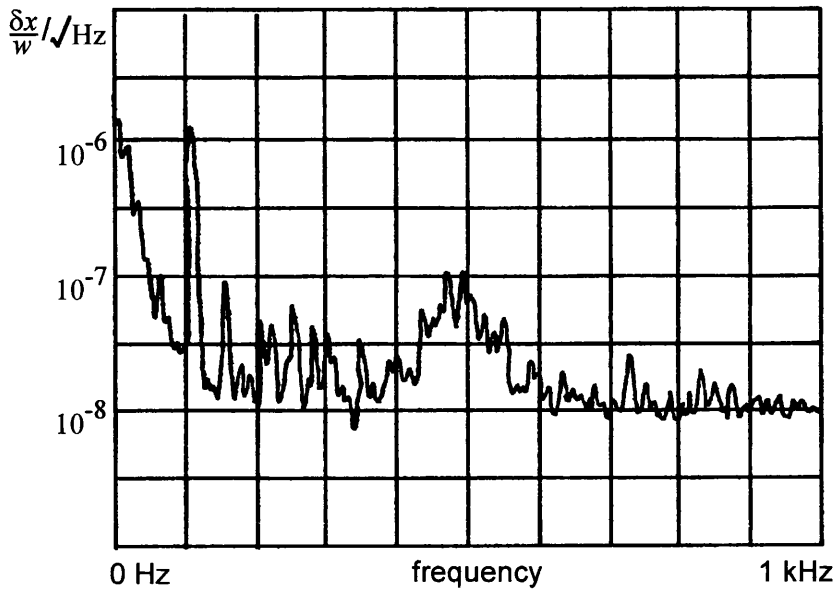

Figure 6.6: *Beam jitter level of the Nd:YAG laser in a 1 kHz span taken after the improvements in optical isolation were made.*

an increase in beam geometry noise, and so the level of beam jitter noise was again measured, this time with the improved isolation state. A trace showing the new beam jitter level is shown in Fig 6.6.

6.3.3 Conclusion

It would appear that the performance of the intensity servo was being limited, at least in part, by the beam geometry noise associated with the laser. The beam geometry noise level was partly caused by the poor isolation in the system, which is an informative result in itself. This can be seen by comparing the level of beam jitter measured after the isolation had been improved with the level measured before. This is shown for completeness in Fig 6.7. A fuller analysis of the design and properties of the broadband intensity servo can be found in [63].

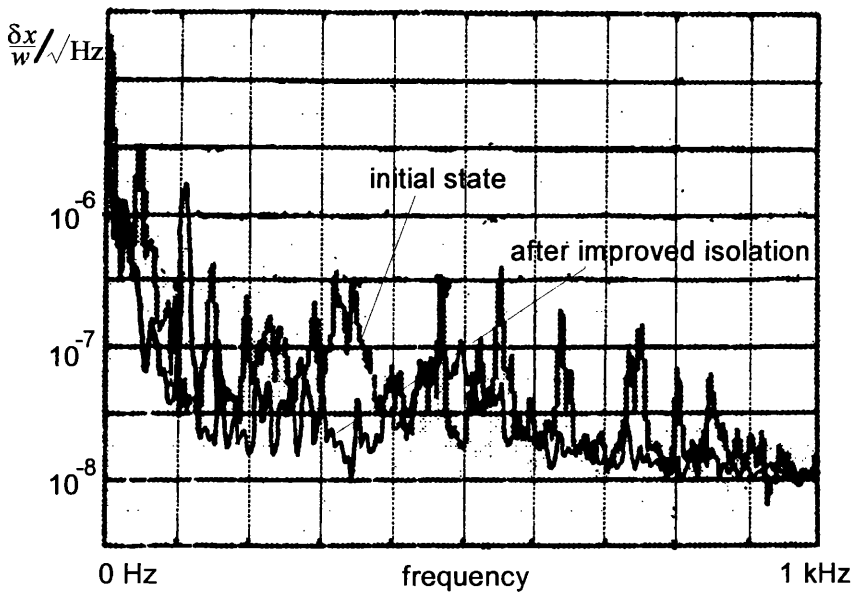

Figure 6.7: *Comparison of beam jitter levels associated with the Nd:YAG laser over a 1 kHz span before and after the improvement in isolation was made.*

Chapter 7

Beam Geometry Noise Coupling Mechanisms in Laser Interferometers

7.1 Introduction

There are various ways that beam geometry noise can couple into the displacement sensitivity of a laser interferometer. One example, already mentioned in chapter 2 is that of a tilt of the main interferometer beam splitter and this will be discussed in section 7.2. Possible asymmetries in the interferometer arms that could couple in pulsations in beam width are discussed in section 7.3. The problem of scattered light as a coupling mechanism is covered in section 7.4. Concluding remarks regarding the implications for long baseline interferometric gravitational wave detectors are presented in section 7.5.

7.2 Coupling of Beam Jitter

Consider the simple Michelson interferometer shown in Fig 7.1. Suppose that the beam splitter BS is aligned so that the angle it makes with each arm is exactly 45°. In this scenario, the symmetry of the system safeguards the sensitivity of the

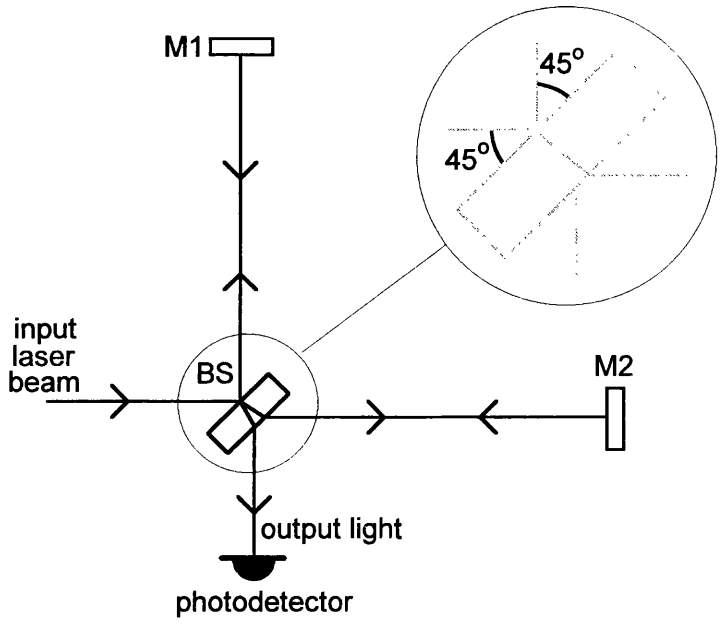

Figure 7.1: *Michelson interferometer with a perfectly aligned beam splitter.*

interferometer from being affected by lateral beam jitter. However if the beam splitter is misaligned from this ideal position, then a horizontal lateral beam movement at the interferometer input (just before the beam splitter) will couple directly to an effective differential displacement fluctuation. Furthermore, if the beam lateral motion is present over the detection frequency band (say 10 Hz to a few kHz) then the noise that this couples in will seriously affect the astrophysical usefulness of the instrument.

A misalignment of the beam splitter is shown in Fig 7.2. The misalignment itself does not affect the performance of the interferometer other than to reduce the contrast of the interfered light. The misalignment causes the interfering wavefronts to be tilted with respect to each other but the effect is static for a given misalignment. However if the beam exhibits a fluctuation in lateral position then the interfering wavefronts move with respect to one another. Considering the geometry of Fig 7.3, the differential displacement signal δx_s produced by the lateral beam fluctuation can be seen to be given by

$$\delta x_s = 4\alpha\delta x_J \tag{7.1}$$

where α is the misalignment of the beam splitter from the perfect 45° symmetry and

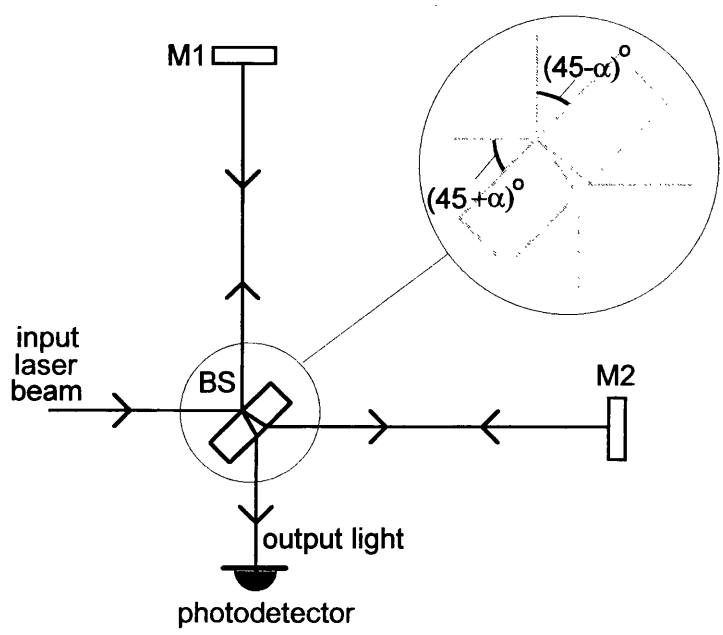

Figure 7.2: *Michelson interferometer with a misaligned beam splitter.*

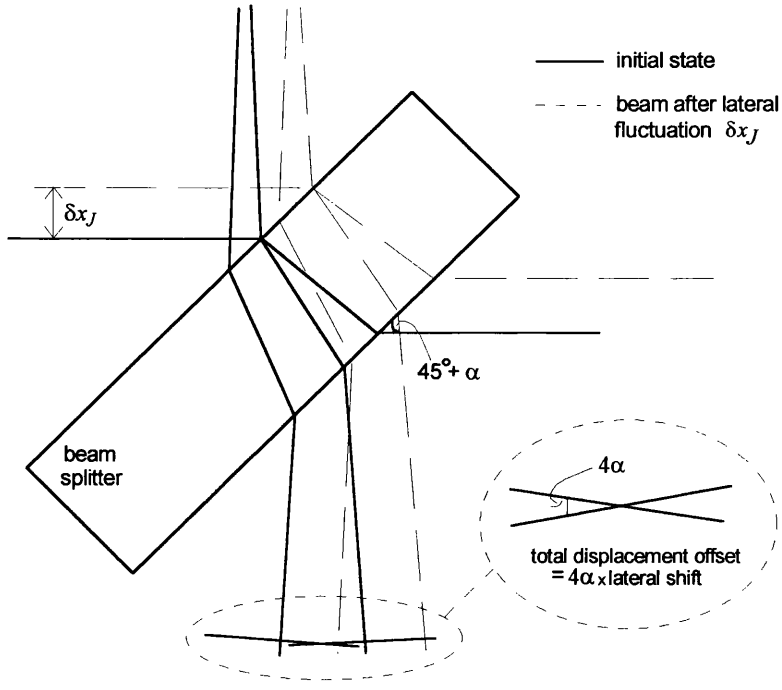

Figure 7.3: *In the case of a misaligned beam splitter, the recombining phase fronts are tilted with respect to each other. Lateral beam motions at the interferometer input then couple into the interferometer output signal.*

δx_J is the lateral beam jitter level measured at the interferometer input. This simple but important formula allows the level of beam jitter associated with typical lasers (see chapter 5) to set an upper limit to the amount of displacement noise produced in an interferometer. The measurements of beam jitter presented in chapter 5 were made 1.5 m from the lasers and contain contributions from lateral beam motion and tilt of the beam, perhaps about the laser cavity waist. If the beam splitter in Fig 7.1 happened to be situated 1.5 m from the laser, then the typical level of beam jitter measured in chapter 5 would be the value to substitute into Eqn.(7.1) in order to determine the resulting sensitivity limit.

The results of chapter 5 showed the level of normalised beam jitter for a Nd:YAG laser at 100 Hz to be $\delta x_J/w = 2 \times 10^{-6}/\sqrt{\text{Hz}}$. Given that $w \approx 1$ cm at the beam splitter in GEO 600, this corresponds to a beam jitter level of $\delta x_J = 2 \times 10^{-8} \text{m}/\sqrt{\text{Hz}}$. Experience with prototype interferometers has shown that it is possible to maintain the alignment of the beam splitter to around 1 part in 10^7 so taking $\alpha = 10^{-7}$ seems reasonable. These values can be substituted into Eqn.(7.1) to produce the displacement sensitivity limit

$$\delta x_s = 8 \times 10^{-15} \text{ m}/\sqrt{\text{Hz}} \text{ at } 100 \text{ Hz}. \tag{7.2}$$

This represents a serious limit on interferometer sensitivity and makes it clear that such noise will have to be suppressed at some stage in the system before the beam splitter.

7.3 Coupling of Beam Width Pulsation

Any mechanism that breaks the symmetry of the beam paths in each arm of the interferometer could in principle affect the sensitivity. The problem of beam jitter producing displacement noise due to a misaligned beam splitter has an analogous couterpart for beam width pulsation, except that it is thermal lensing effects in the beam splitter, rather than tilt, that is the important consideration. In addition, the mirrors in each arm may not have identical curvatures, and this is another potentially problematic asymmetry. A change in beam width will cause a subsequent change in

interaction with these effects in each arm and the end result is a recombined pair of beam wavefronts whose curvature and width differ with respect to one another. The important frequency regime is the detection window for gravitational waves, and the beam width fluctations for typical lasers measured in this window will lead to a tolerance for arm asymmetries, whatever their nature.

The most important consideration for the recombined beams is that their phase fronts do not fluctuate with respect to one another. In particular, the values of their Guoy phase measured at a specific point (namely, the detection point) must not fluctuate relative to one another. The beam propagation laws for Gaussian optics along with the $ABCD$-law (given in appendix A) can be used to chart the Guoy phase properties of the beam as it propagates from the beam splitter of a simple Michelson interferometer, up and down one arm, and eventually to the recombination point. The expression for Guoy phase G at the recombination point must be referenced to the input beam and the calculation is best done using a computer program. The Guoy phase calculation has been performed for the GEO 600 interferometer with an input beam waist of radius w_0 located at the beam splitter. By examining the effect on G induced by variations in the input beam waist radius w_0, it is possible to deduce a relationship between the degree of beam pumping in the laser and the resulting fluctuations in Guoy phase of the light returning from each arm to the recombination point.

Now if the arms are perfectly matched, then the differential displacement noise is zero for a width pulsation. However if there is an asymmetry, which will be represented here by a mismatch in the radii of curvature of the end mirrors $\delta R/R$ then the differential displacement sensitivity limit δx_s corresponding to the GEO 600 parameters given above can be written as

$$\delta x_s \simeq 10^{-6} \frac{\delta R}{R} \frac{\delta w_0}{w_0}. \tag{7.3}$$

From chapter 5, the typical level of beam width fluctation noise measured at 100 Hz for the Nd:YAG laser was $\delta w/w \simeq 10^{-6}/\sqrt{\text{Hz}}$. By substituting this value for $\delta w/w$ into Eqn.(7.3) a simple relationship between δx_s and $\delta R/R$ can be written as

$$\delta x_s = 10^{-12} \frac{\delta R}{R} \tag{7.4}$$

From past experience with mirror manufacturers contracted to produce supermirrors of large radius of curvature, it would not seem unreasonable to assume a curvature error of 1 part in 100. In this case the displacement noise limit becomes

$$\delta x_s = 10^{-14}\ \mathrm{m}/\sqrt{\mathrm{Hz}}\ \text{at}\ 100\,\mathrm{Hz} \tag{7.5}$$

which is an even higher limit than that imposed by the coupling of beam jitter. Consequently, it would appear that beam width pulsation has to be suppressed by many orders of magnitude.

7.4 The Problem of Scattered Light

In chapter 4 the causes of scattering from optical components were examined, and the general trend of improvement in manufacturing techniques was noted by comparing the losses of present day supermirrors to those available a few years ago. Given the relatively small amount of scattered light expected to be produced, it is only in the arms of the interferometer where the effects are likely to pose a problem to the displacement sensitivity.

Scattered light in the interferometer may seem to be rather removed from the notion of beam geometry noise, but in fact the two are very much related and the nature of the relationship is best discussed in the TEM mode picture introduced in chapter 5. An idea of the problem can be presented by considering first that the sensitivity of the interferometer might be degraded if the light in the arms gets partially channelled into higher order transverse modes by some mechanism, yet to be defined. In terms of a phasor representation, this can be thought of as the fundamental mode phasor being added to by small phasors representing the higher order modes. The worst possible effect on the phase of the light at the photodetector is when these extra modes are 90° out of phase with the fundamental mode. In this case the effective displacement noise δx_s produced in one arm of the interferometer can be written

$$\delta x_s = \frac{\lambda}{2\pi} \tan^{-1}\left(\frac{A_h}{A_0}\right) \simeq \frac{\lambda}{2\pi}\frac{A_h}{A_0} \tag{7.6}$$

where A_h is the total amplitude of higher order modes added in quadrature to the

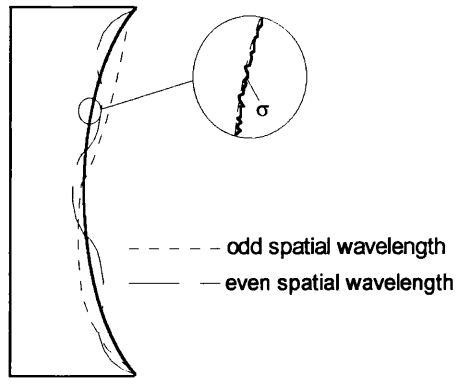

Figure 7.4: *Surface imperfections that can contribute to the scattering of an incident laser beam.*

amplitude of fundamental mode A_0. The approximation in Eqn.(7.6) can be made since the relative magnitudes of the higher order mode amplitudes being considered are generally small. The important issue regarding scattered light is to what extent it can produce a fluctuation in the amplitudes of these higher order modes that will generate an apparent *differential* displacement signal via Eqn.(7.6). Probably the worst scenario would be for one arm to undergo a modulation of the mode amplitudes while the other arm undergoes the same modulation, but of opposite sign. Such a situation is perhaps unrealistic, but will certainly provide an upper limit to the magnitude of any coupling mechanism.

It has been demonstrated [64] that scattering associated with the mirrors or beam splitter in an interferometer can be thought of as channeling light power out of the fundamental mode and into higher order transverse modes. In general, any surface with which the beam interacts can have two types of irregularity associated with it, as shown in Fig 7.4. These are the *microscopic surface roughness* denoted by the rms deviation σ from a locally flat surface, and the *surface irregularity* usually expressed via a Fourier series of ripples each having a characteristic *spatial wavelength* λ_s. In terms of these parameters, the relative amplitude of TEM_{n0} with respect to the fundamental mode, that a scattering from a mirror surface will produce can be

written [65]

$$\frac{A_n}{A_0} = \frac{-j}{(n!2^n)^{\frac{1}{2}}} \left[\frac{4\pi\sqrt{2}\sigma}{\lambda} \cos(n\pi/2) \left(\frac{\sqrt{2}\pi w_0}{\lambda_s} \right)^n e^{\frac{-\pi^2 w_0^2}{2\lambda_s^2}} \right]. \tag{7.7}$$

The form of Eqn.(7.7) given here allows for only even order mode amplitudes and thus any coupling mechanism introduced should ideally possess axial symmetry. By substituting this into Eqn.(7.6) it is possible to model the equivalent displacement noise that this amount of scattering equates to. Of course, it does not yet set a limit to the sensitivity of the interferometer, because the scattered light is so far a static effect common to both arms, and serves merely to degrade the contrast of the interference fringes of the recombined light. The amplitudes represented by Eqn.(7.7) would have to fluctuate in order to produce a displacement noise and furthermore this fluctuation would have to be different in each arm to create a differential displacement noise that would ultimately limit gravitational wave sensitivity. The role of beam geometry noise can now be introduced as one potential modulation mechanism. It has been shown in chapter 5 that various types of beam geometry noise lead to the contamination of the TEM_{00} mode with higher order TEM modes. In the presence of scattered light, the effect of beam geometry noise will be to modulate the amplitudes of higher order modes already present in the light. As usual, this will couple into detector sensitvity through mismatches between each arm of the interferometer. It is however difficult to quantify the limit imposed by the combination of scattered light and beam geometry noise, because the precise coupling mechanisms are not well known. For example, it is not well documented exactly how the scattering level at a mirror will change if the incident beam fluctuates in position or pulsates in width.

As a crude estimate, let us consider the case of a beam width fluctuation, where the total scattering from a mirror varies linearly with the width of the beam. The modulation imposed on the amount of light scattered out of the fundamental mode is then simply $\frac{\delta w}{w}\frac{A_h}{A_0}$ and assuming the worst case where both arms undergo opposite effects, the resulting differential displacement noise is given using Eqn.(7.6) and Eqn.(7.7) to be

$$\delta x_s = 2\frac{\delta w}{w}\sigma \tag{7.8}$$

where the contribution from the harmonic deformation has been neglected completely, and the contribution from only the strongest coupled mode (TEM_{20}) has been considered. Typical rms roughness levels achievable with current mirror manufacturing techniques were given in chapter 4. Here the value of 1 angstrom will be used, together with the normalised beam width level at 100 Hz for the Nd:YAG laser presented in chapter 5 (about $10^{-6}/\sqrt{\text{Hz}}$) to give a sensitivity limit of

$$\delta x_s = 2 \times 10^{-16}\,\text{m}/\sqrt{\text{Hz}} \text{ at } 100\,\text{Hz}. \tag{7.9}$$

It has to be remembered that this limit is arrived at in the absence of any suppression whatsoever of beam geometry noise. Compared with the coupling mechansims of section 7.2 and 7.3 it represents the least serious limit to sensitivity and a more detailed investigation is unlikely to generate an answer that is orders of magnitude different. Consequently, suppression schemes designed to safeguard detector performance against the previous coupling effects should also be sufficient to suppress the effects of beam geometry noise coupling with scattered light.

7.5 Conclusion

The emphasis in this chapter has been to present a set of simple arguments describing how the effects of beam geometry noise could couple into the differential displacement sensitivity of an interferometer. Sections 7.2, 7.3 and 7.4 have all provided numbers which are important to the design of long baseline gravitational wave interferometers. The first generation of such instruments have projected strain sensitivities of around $10^{-22}/\sqrt{\text{Hz}}$ at 100 Hz. It is clear that the limits derived in the previous sections imply that this sensitivity cannot be realised without considerable suppression of beam geometry fluctuations. A summary of the suppression factors required to (just and no more) achieve a strain sensitivity goal of $10^{-22}/\sqrt{\text{Hz}}$ for the GEO 600 detector is given in Table 7.1. These numbers are obtained by likening the values of differential displacement noise δx_s seen in the previous sections to the equivalent signal produced by a gravitational wave of strain amplitude h ($h = \delta x_s/1200$). It should be remembered that the figures shown in Table 7.1 represent the worst limits imposed on interferometer sensitivity, in the absence of any

mechanism	displacement noise at 100 Hz	suppression
beam splitter misalignment	$8 \times 10^{-15}\,\mathrm{m}/\sqrt{\mathrm{Hz}}$	6.7×10^{4}
mirror curvature mismatch	$10^{-14}\,\mathrm{m}/\sqrt{\mathrm{Hz}}$	8.3×10^{4}
light scattering	$2 \times 10^{-16}\,\mathrm{m}/\sqrt{\mathrm{Hz}}$	1.7×10^{3}

Table 7.1: *Summary of the displacement noise at 100 Hz induced in an interferometer by various couplings of beam geometry noise and the level of suppression required to achieve the desired sensitivity of the first generation of detectors.*

other suppression mechanisms. In practice there will be a degree of passive suppression of beam geometry noise afforded by the power recycling cavities and, if present, the Fabry-Perot arm cavities of an interferometer[1]. However such factors will be regarded here merely as providing extra reductions, obtained over and above those afforded by the suppression system we deliberately design. Thus the figures of Table 7.1 alone will dictate the specifications of our beam geometry noise suppression system.

The required suppression factors, particularly those for the beam splitter misalignment and mirror curvature mismatch, can be seen to be significant. The use of a single mode optical fibre to reduce beam geometry fluctuations was described in chapter 6 but the power handling anomalies associated with such fibres, some of which were outlined in that chapter, preclude them from serious consideration for the long baseline interferometers. The favoured suppression device in all of the planned large detectors is a Fabry-Perot cavity used as an optical filter. A system like this is called a *modecleaner* because it works by making use of the fact that beam geometry noise can be modelled as contaminations of high order TEM modes in the fundamental mode. A modecleaner suppresses these high order modes. The next chapter will present the theory behind such a system and then chapter 9 will describe in some detail a modecleaner scheme developed in the laboratory at Glasgow.

[1] details regarding the actions of a Fabry-Perot cavity with regard to suppressing beam geometry noise are presented in chapter 8

Chapter 8

Fundamentals of Modecleaner Design

8.1 Introduction

A modecleaner is a Fabry-Perot optical cavity placed between the laser and the interferometer and designed to operate in transmission mode. The cavity must therefore have a high throughput so that as little as possible of the laser light is lost. The cavity is made to resonate in its fundamental mode using a locking scheme such as that described in section 3.3. As discussed in chapter 5, beam geometry fluctuations can be regarded as the fundamental mode being contaminated with varying amounts of higher order TEM modes. The action of a modecleaner (locked to the TEM_{00} mode) will be to suppress these higher order modes *provided* that they resonate in the cavity at different frequencies from the fundamental mode. Therefore, in order to assess just how much suppression the modecleaner will impose on a given TEM mode, the frequency offset between the mode and the fundamental must be calculated.

The calculation of TEM mode frequencies and the resulting expression for the suppression factors are presented in section 8.2. The required suppression factors are one aspect of the modecleaner design, but there are other issues that need to be considered also, and some of these are outlined in section 8.3. General conclusions

are drawn in section 8.4 including how the suppression factors calculated in chapter 7 dictate the specifications of a working modecleaner system for the German-British GEO 600 project.

8.2 Fabry-Perot Cavity as a Modecleaner

The use of a Fabry-Perot cavity as a transverse mode selector was first shown in detail at the Max Planck Institute for Quantum Optics [66]. For a general cavity such as that shown in Fig 3.2, the calculation of transverse mode frequencies is actually rather difficult. The factor that causes this difficulty is the Guoy phase term $\tan^{-1}(\pi w^2/\lambda R)$ (see chapter 5) and in particular, how this quantity accumulates as the beam propagates round the cavity. The calculation can be done for a general two mirror cavity as will be demonstrated here. A more elaborate cavity can be analysed in a simple manner only if it can be reduced to a two-mirror cavity, and this can be done only for cavities that possess certain symmetry. It is worth keeping this in mind when designing a modecleaner system.

8.2.1 Transverse Mode Frequencies

A general two mirror cavity is shown in Fig 8.1. The mirrors have radii of curvature[1] R_1 and R_2 and the distance between them is L. Following an argument after [54], the frequency for the TEM_{nm} mode can be derived by writing down the phase condition for resonance in the cavity. For the cavity in Fig 8.1 the phase offset $\delta\phi$ acquired in a single traverse of the cavity can be written as

$$\delta\phi = \frac{2\pi}{\lambda}L - (n+m+1)[\tan^{-1}(\frac{\pi w_1^2}{\lambda R_1}) - \tan^{-1}(\frac{\pi w_2^2}{\lambda R_2})] \tag{8.1}$$

where the two Guoy phases are measured at each mirror. For resonance the phase offset $\delta\phi$ must be an integral number of π and this is usually expressed via the condition $\delta\phi = (q+1)\pi$ where q is the *longitudinal mode number*. To obtain the

[1] in previous chapters these symbols have been used for mirror power reflectances and thus to avoid confusion, the results of this chapter will retain mirror amplitude coefficients denoted by lower case characters.

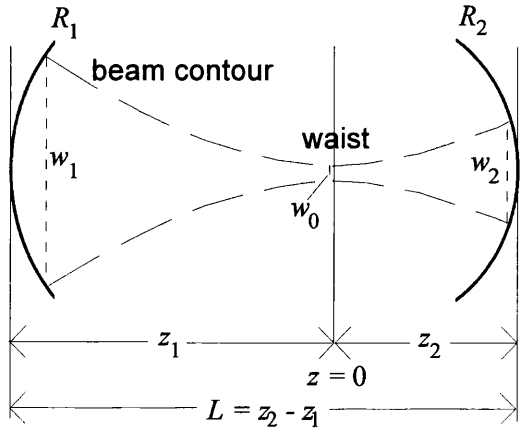

Figure 8.1: *A general two mirror cavity with waist w_0 at some point between the mirrors.*

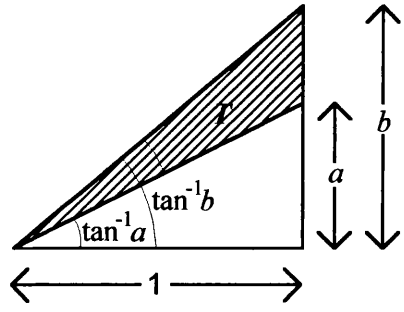

Figure 8.2: *Triangle construction to allow manipulation of the Guoy phases.*

frequencies from Eqn.(8.1) two further steps are necessary. Firstly, the beam widths w_1 and w_2 are expressed in terms of the waist size w_0 and the distances z_1 and z_2 using Eqn.(5.6). Secondly, the difference in the arctans featured in Eqn.(8.1) is simplified by expressing it as an arccos term. This is achieved using the formula

$$\tan^{-1} a - \tan^{-1} b = \cos^{-1}\left(\frac{1+ab}{\sqrt{(1+a^2)(1+b^2)}}\right) \tag{8.2}$$

which can be derived by considering the cosine rule applied to the triangular section T in the right-angled triangle set-up of Fig 8.2. After some fairly lengthy algebraic manipulation the phase condition can be written in terms of the cavity geometry as

$$(q+1)\pi = \frac{2\pi}{\lambda}L - (n+m+1)\cos^{-1}\left(\sqrt{1-\frac{L}{R_1}}\sqrt{1-\frac{L}{R_2}}\right). \tag{8.3}$$

By multiplying by c and expressing c/λ as the resonant frequency for a mode in the cavity, the frequency for the TEM_{nm} mode can be written

$$f_{nm} = \left[(q+1) + \frac{1}{\pi}(n+m+1)\cos^{-1}\left(\sqrt{1-\frac{L}{R_1}}\sqrt{1-\frac{L}{R_2}}\right)\right]\frac{c}{2L}. \tag{8.4}$$

The notation TEM_{nmq} is often used to denote a given mode since the longitudinal mode number is also required to uniquely specify a given laser mode. This notation will not be used here where only the transverse modes are of interest. Eqn.(8.4) can be used to determine the frequency difference between successive TEM modes. The difference in frequency between the TEM_{nm} mode and the $\mathrm{TEM}_{n+1,m}$ mode is given by

$$f_{nm} - f_{n+1,m} = \frac{c}{2\pi L}\cos^{-1}\left(\sqrt{1-\frac{L}{R_1}}\sqrt{1-\frac{L}{R_2}}\right). \tag{8.5}$$

This is an important relation as it defines the amount by which each TEM_{nm} mode is off resonance in a cavity that is locked to resonate the fundamental mode. By considering Eqn.(8.5) it can be deduced that some cavity geometries would not make good modecleaners. By setting $R_1 = R_2 = L$ (a particular geometry known as the *confocal* arrangement) the frequency difference between successive modes is c/L which is half the free spectral range, or longitudinal mode spacing, of the cavity. Thus if all the even modes TEM_{00}, TEM_{20} etc are resonant, it follows that all the odd modes TEM_{10}, TEM_{30} etc will be optimally suppressed, or anti-resonant. This multiple mode resonance or *degeneracy* is something that has to be avoided in a modecleaner. Exactly how the suppression factors are arrived at is demonstrated next.

8.2.2 Transverse Mode Suppression Factors

It was shown in chapter 3 that the power throughput of a two mirror Fabry-Perot cavity can be expressed as

$$\frac{I_{thro'}}{I_{in}} = \frac{t_1^2 t_2^2}{(1-r_1 r_2)^2}\frac{1}{1+4\frac{r_1 r_2}{(1-r_1 r_2)^2}\sin^2\phi/2} \tag{8.6}$$

where t_1, t_2 and r_1, r_2 are the amplitude transmittances and reflectances of the mirrors and ϕ is the phase acquired by the light during a round trip. Since beam

geometry fluctuations are modelled by amounts of high order mode *amplitude* rather than *intensity*, it is the amplitude throughput that is of more interest here, given by

$$\frac{E_{thro'}}{E_{in}} = \frac{t_1 t_2}{(1 - r_1 r_2)} \frac{1}{\sqrt{1 + 4\frac{r_1 r_2}{(1-r_1 r_2)^2} \sin^2 \phi/2}} \tag{8.7}$$

By using Eqn.(8.3) to calculate the phase offset between the TEM_{00} mode and an arbitrary TEM_{nm} mode, it is possible to rewrite Eqn.(8.7) in terms of the cavity geometry

$$\frac{E_{nm}}{E_{in}} = \frac{t_1 t_2}{(1 - r_1 r_2)} \frac{1}{\left[1 + 4\frac{r_1 r_2}{(1-r_1 r_2)^2} \sin^2 \left\{(n+m)\cos^{-1}\left(\sqrt{1 - \frac{L}{R_1}}\sqrt{1 - \frac{L}{R_2}}\right)\right\}\right]^{\frac{1}{2}}} \tag{8.8}$$

where E_{nm} is the amplitude of the TEM_{nm} mode transmitted through the cavity. By writing out Eqn.(8.8) for the TEM_{00} mode and then taking the ratio of E_{nm}/E_{in} and E_{00}/E_{in} the amplitude of TEM_{nm} relative to the fundamental mode can be written as

$$\frac{E_{nm}}{E_{00}} = \frac{1}{\left[1 + 4\frac{r_1 r_2}{(1-r_1 r_2)^2} \sin^2 \left\{(n+m)\cos^{-1}\left(\sqrt{1 - \frac{L}{R_1}}\sqrt{1 - \frac{L}{R_2}}\right)\right\}\right]^{\frac{1}{2}}}. \tag{8.9}$$

The term in the denominator of Eqn.(8.9) is what shall be defined here as the *suppression factor* of the TEM_{nm} mode relative to a resonant TEM_{00} mode. Substituting the expression for cavity finesse given by Eqn.(3.8) into Eqn.(8.9) allows the suppression factor to be written as

$$S_{nm} = \left[1 + \frac{4F^2}{\pi^2} \sin^2 \left\{(n+m)\cos^{-1}\left(\sqrt{1 - \frac{L}{R_1}}\sqrt{1 - \frac{L}{R_2}}\right)\right\}\right]^{\frac{1}{2}}. \tag{8.10}$$

The suppression factor for a given cavity geometry and finesse can be determined using Eqn.(8.10). Almost everthing relevant to the cavity design of a modecleaner is contained in this equation. In view of Eqn.(8.10) the suppression afforded to high order modes by a Fabry-Perot cavity is often considered to vary directly as the cavity finesse, since the 1 can be neglected for large suppression factors. Thus, the suppression factor ranges from 1 (no suppression at all) to a maximum of $\sim 2F/\pi$ for modes completely anti-resonant in the cavity. By considering a symmetric cavity ($R_1 = R_2 = R$) it is possible to simplify Eqn.(8.10), so that for a given cavity

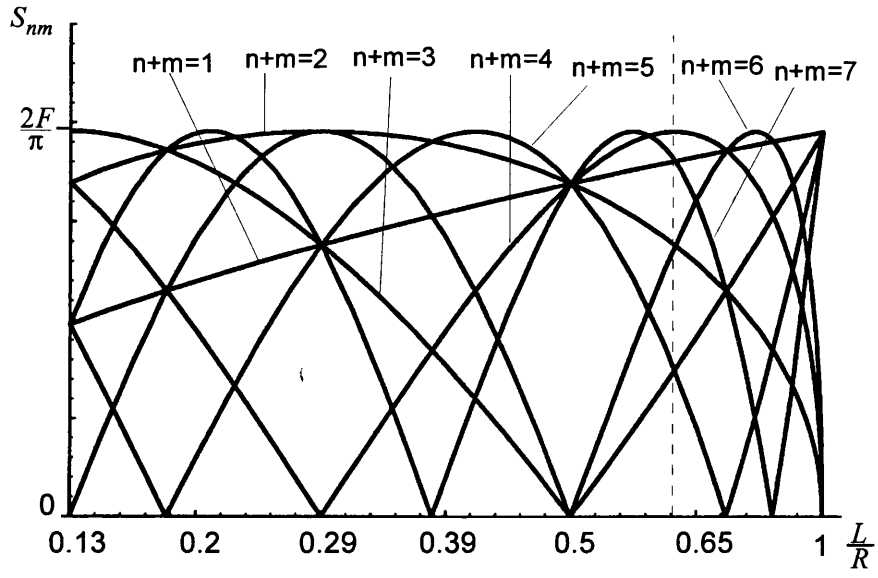

Figure 8.3: *Graph of supression factors against the ratio of mirror separation and curvature for the first few high order transverse modes.*

finesse, only one variable (L/R) determines the suppression factor of the modes. It is then instructive to plot the suppression factor S_{nm} for such a symmetric cavity as a function of L/R, at least for the first few TEM_{nm} modes to which beam geometry fluctuations couple most strongly. Adapting Eqn.(8.10) to deal with a symmetric cavity, and taking the suppression to be sufficiently large so that the 1 can be neglected, leads to

$$S_{nm} = \frac{2F}{\pi} \sin\left\{(n+m)\cos^{-1}\left(1-\frac{L}{R}\right)\right\}. \tag{8.11}$$

A graph of S_{nm} against L/R for the first few modes is shown in Fig 8.3. A value of $L/R \simeq 0.6$ (denoted by the faint vertical line in Fig 8.3) gives good suppression of the first few modes. With this geometry, the TEM_{10} and TEM_{20} modes (to which beam jitter and width pulsation respectively are most strongly associated) are suppressed by about 95 % and 75 % of the maximum possible suppression factor available.

8.3 Other Design Aspects

Given the results of the last section it would appear that the best modecleaner cavity is one having geometry $L/R = 0.6$ and as high finesse as possible. However there

are other factors regarding the performance of a modecleaner that the suppression factor analysis does not take into account. Some of the most important of these will now be dealt with.

8.3.1 Passive Filtering Action

One aspect of the modecleaner suppression factors that has not been emphasised is that they do not depend explicitly on the length of the cavity, only on the ratio of length and mirror curvature(s). It is possible to build a cavity 1 m long that has the same modecleaning action as one 100 m long. It might seem unecessary to build a long cavity when a short one would do just as well, however there are advantages associated with a long cavity, one of which is its lower free spectral range (FSR) and consequently, its smaller linewidth. The passive filtering action of an optical cavity can be useful in filtering all sorts of laser noise including beam geometry fluctuations, frequency noise and variations in the laser power. The filtering action begins to take real effect after the corner frequency of the cavity f_c, which is half the cavity linewidth ($\Delta\nu/2$). As an example, a two mirror cavity having a finesse of 1000 and a length of 15 m has $FSR = 10\,\mathrm{MHz}$ and linewidth $\Delta\nu = 10\,\mathrm{kHz}$. Any laser power noise above 5 kHz will be subject to a $1/f^2$ filtering action afforded by the cavity. Laser noise, such as frequency noise, which can be modelled by perturbations to the light field *amplitude* will be suppressed by $1/f$ above the corner frequency. If the cavity in the above example was only 1.5 m long then the filtering action would not come into effect until 50 kHz which is much less useful, being outside the detection frequency window.

8.3.2 Mirror Power Handling

A longer cavity will have proportionately larger laser spot sizes on the cavity mirrors. This could be an advantage in high finesse cavities where the mirror absorptance could pose a problem. The power accumulated in a high finesse Fabry-Perot cavity P_{accum} is given by

$$P_{accum} = \frac{F}{\pi} P_{in} \tag{8.12}$$

where P_{in} is the incident power. This equation was first introduced in chapter 2. To safeguard the cavity mirrors from thermal damage, it is best to limit the absorbed power to 50 mW for a beam of radius $\sim$ 1 mm. In view of the results of chapter 3, a conservative estimate of the absorptance at each mirror can be given as 10 ppm. This sets a limit of 5 kW to the intra-cavity power which in turn defines an upper limit to the finesse for a given input laser power. If the input laser power is around 10 W say, then the finesse must not exceed about 1500. This produces upper limits on the suppression factors available and affects the specifications of the cavity as a modecleaner.

8.3.3 Passing Modulation Frequencies

In a complicated interferometer where there are many electronic feedback systems keeping various cavities on resonance, it may be desirable to modulate the light before a modecleaner for use in a scheme that the beam encounters after the modecleaner. If there is even the possibility of this being desirable, then the modecleaner must have a FSR that matches the modulation frequency. It becomes quite difficult to build modulation schemes that operate at frequencies much above 30 MHz and so it would be beneficial to have a modecleaner with FSR less than this. This sets a lower limit to the optical round trip path length of 10 m. In the case of a two mirror modecleaner this would imply a physical length of no less than 5 m. The emphasis on optical path length here stems from the next factor, which tends to favour the use of cavity designs that are not of the familiar two mirror type.

8.3.4 Laser Isolation

A system such as a modecleaner, in which the laser beam is aligned to propagate through, has a danger of reflecting some light directly back into the laser cavity itself. This is undesirable, as the second study of chapter 6 demonstrated. As far as the modecleaning system is concerned, the problem of isolating the laser from back-reflected light can be lessened by designing the modecleaner to be a *ring cavity*. If this approach is taken, it should be possible to have all back reflected laser beams

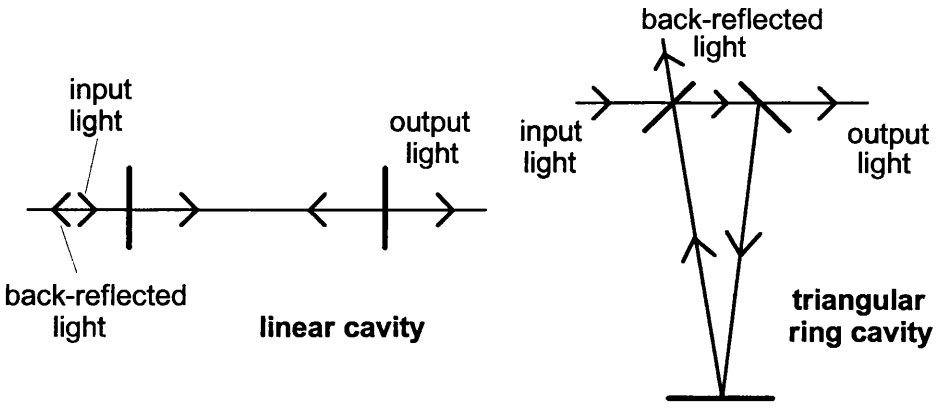

Figure 8.4: *Modecleaner designs which are bad (the linear cavity) and good (the ring cavity) for isolation purposes.*

misaligned with the main input beam as shown in Fig 8.4. A more complicated cavity need not be more complicated to analyse than its two mirror counterpart discussed so far, but it has to be designed with some symmetry in mind. An example of a four mirror system that is implicitly as simple to analyse as a two mirror cavity will be introduced in chapter 9 when the Glasgow prototype modecleaner is discussed.

8.4 Conclusion

The theory behind a Fabry-Perot cavity used in transmission mode as an optical modecleaner has been presented. An expression for the suppression factor of the TEM_{nm} mode when the cavity is securely locked to the fundamental TEM_{00} mode has been derived (Eqn.(8.10)). A upper bound for the finesse has been obtained as ~ 1500 limited by an estimate[2] of the absorptance of the supermirrors used to build the cavity. With the optimal cavity geometry (a symmetric cavity with $L/R = 0.6$) these numbers provide suppression factors

$$S_{10} = 876$$

$$S_{20} = 573$$

[2] 10 ppm is probably an overestimate if the currently available best mirror coatings are used.

for the first and second transverse modes. The required suppression factors for long baseline interferometers can be recalled from chapter 7 to be considerably higher than those given above. A suppression of up to $\sim 10^5$ was thought necessary, in the absence of any other filtering mechanism. If the suppression factors above are squared, then the necessary level of suppression would be achieved, and this indicates that two modecleaners placed in series will have to be employed for a long baseline interferometer. This is indeed the basis of the scheme proposed for the GEO 600 detector and more will be said of this in the conclusions of chapter 10.

Chapter 9

Experimental Development of a Modecleaner

9.1 Introduction

The previous chapters have demonstrated the need for a modecleaner system that will suppress beam geometry noise by several orders of magnitude. In chapter 8 it was pointed out that this can be achieved using two modecleaning cavities arranged in series, so that the beam geometry fluctuations are reduced by the product of the suppression factors for each cavity alone. Each cavity is best designed with the provision to transmit modulation frequency sidebands, requiring an optical path length of around 10 m or more.

The modecleaner cavity developed at Glasgow acts as a prototype for the kind of system planned for use in the GEO 600 detector. The mirrors in the cavity are all fully suspended and the entire intra-cavity optical path is contained in a vacuum. The optical path length is increased by the use of a folded ring cavity design, in this case a bow-tie shaped cavity. This allows a relatively small physical space to be occupied and ensures good optical isolation properties and suitable free spectral range for the transmission of modulation frequencies. The system was developed in two main phases.

Associated with the first phase was the physical construction of the system and

the initial version of the injection optics table. In this first configuration, the modecleaner cavity formed the frequency discriminator to which the laser was locked. The initial system is described in section 9.2.

The final modecleaner system uses the same laser, except that it is now pre-stabilised to a small rigid reference cavity, and then one of the modecleaner mirrors is actively controlled to change the length of the cavity in response to any remaining frequency fluctuations of the laser light. In this way the modecleaner can be kept on resonance to the pre-stabilised light. This final scheme is described in detail in section 9.3. Conclusions and possible improvements that could be made to the system are discussed in section 9.4.

9.2 Initital Development

In September 1993 the 10 m prototype gravitational wave detector was completely dismantled and the laboratory renovated. This was to make way for a new system incorporating various improvements, such as new mirror suspension designs, and also to accommodate further experiments, one of which was the development of a modecleaner. The pre-September 1993 detector occupied two arms in a complete square of metal vacuum tubing and the entire system was mounted in a metal framework which made contact with the floor at only four places around the room. A description of the 10 m prototype system before the renovation of the laboratory can be found in [67]. As various improvements in sensitivity were made over the years, the structural resonances of the framework became apparent as a major factor in limiting the performance of the interferometer, even though the framework was built for seismic isolation purposes in the first place. Consequently, a major part of the renovation was to remove it completely. The before and after views of the lab are shown in the floor plans of Fig 9.1. The two unused sides of the square were removed and provided six spare pieces of vacuum tubing of around 3 m and 4 m in length. The modecleaner was constructed using a piece of this spare tubing mounted between two small vacuum tanks each 70 cm in diameter. The position of the modecleaner system relative to the detector permits the option of later integrating it into the

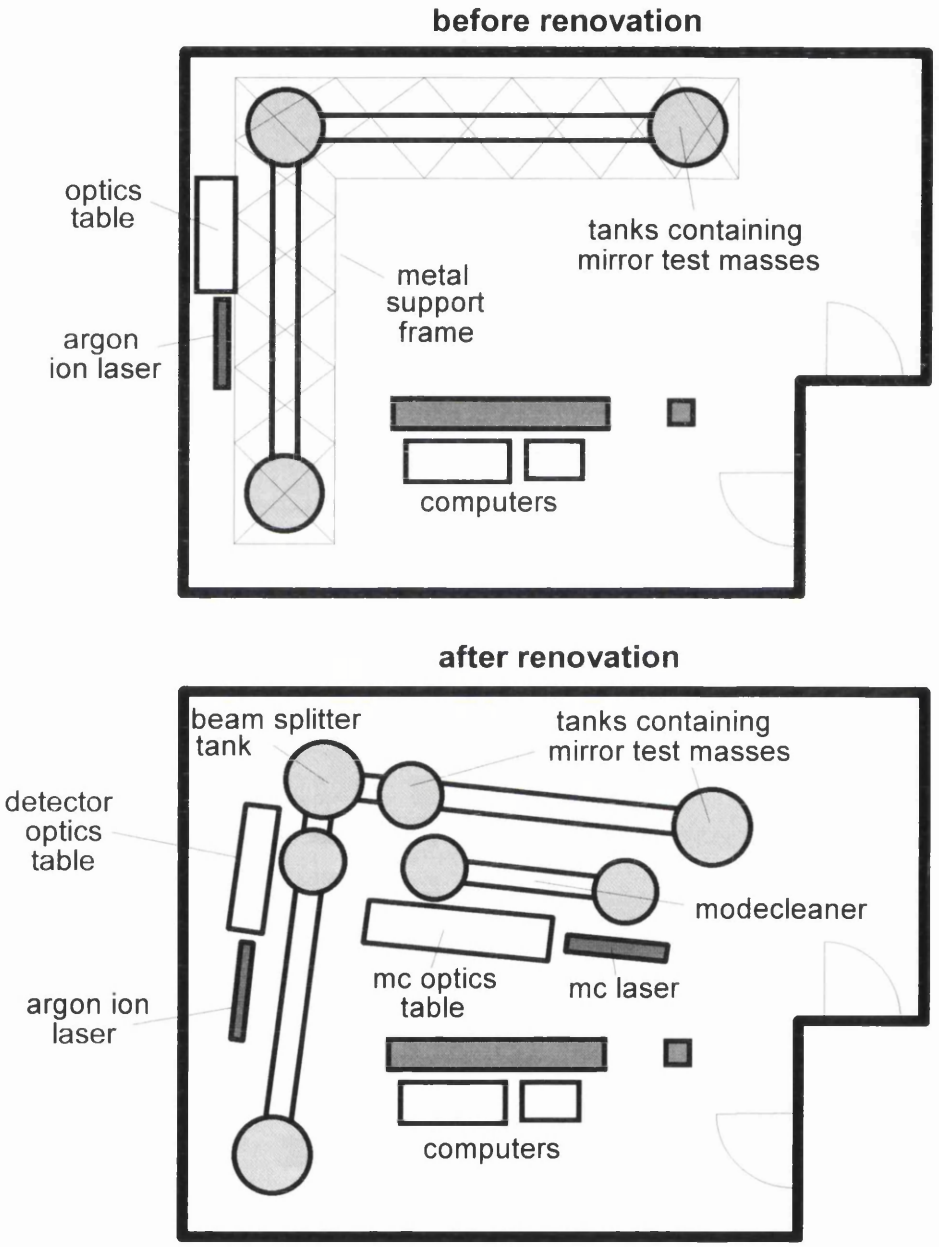

Figure 9.1: *The layout of the detector lab before and after its renovation.*

manufacturer	radius of curvature	transmittance
British Aerospace	15 m	maximum reflector
British Aerospace	15 m	maximum reflector
British Aerospace	flat	0.5 %
British Aerospace	flat	0.5 %

Table 9.1: *High quality mirrors of convenient transmittance and/or curvature for use in the prototype modecleaner.*

main prototype detector, as a 'plug-in' replacement for the existing injection optics scheme which currently uses an optical fibre to suppress beam geometry noise.

9.2.1 Modecleaner Specifications

The physical length of the modecleaner cavity was determined by the available lengths of spare vacuum pipe freed when the detector was rebuilt. A 4 m pipe was chosen which, along with the space inside the end tanks, provided a mirror-to-mirror separation of about 4.5 m. The aim was to design a system having comparable properties to the modecleaners required for the GEO 600 interferometer. There were four suitable mirrors already available in the laboratory in Glasgow as shown in Table 9.1. Two 15 m radius of curvature mirrors separated by a length of 9 m would provide a suitable cavity geometry[1] (convenient given that the physical separation of the mirrors is exactly half 9 m). Unfortunately the 15 m mirrors were designed as maximum reflectors and would not provide a suitable finesse on their own. However the flat mirrors in Table 9.1 would make good input and output coupling mirrors in view of their transmittances, giving a finesse in the order of 1000. The solution was therefore adopted of constructing a bow-tie cavity where the flat mirrors form the input and output couplers but where the curved mirrors are still encountered every 9 m. The four mirror system and the equivalent two mirror cavity are shown in Fig 9.2. The equivalence of the four mirror arrangment and the simple two mirror arrangement is important because it allows all the results developed in chapter 8

[1] recall from Chapter 8 that $L/R = 0.6$ gives good suppression of the first few high order modes.

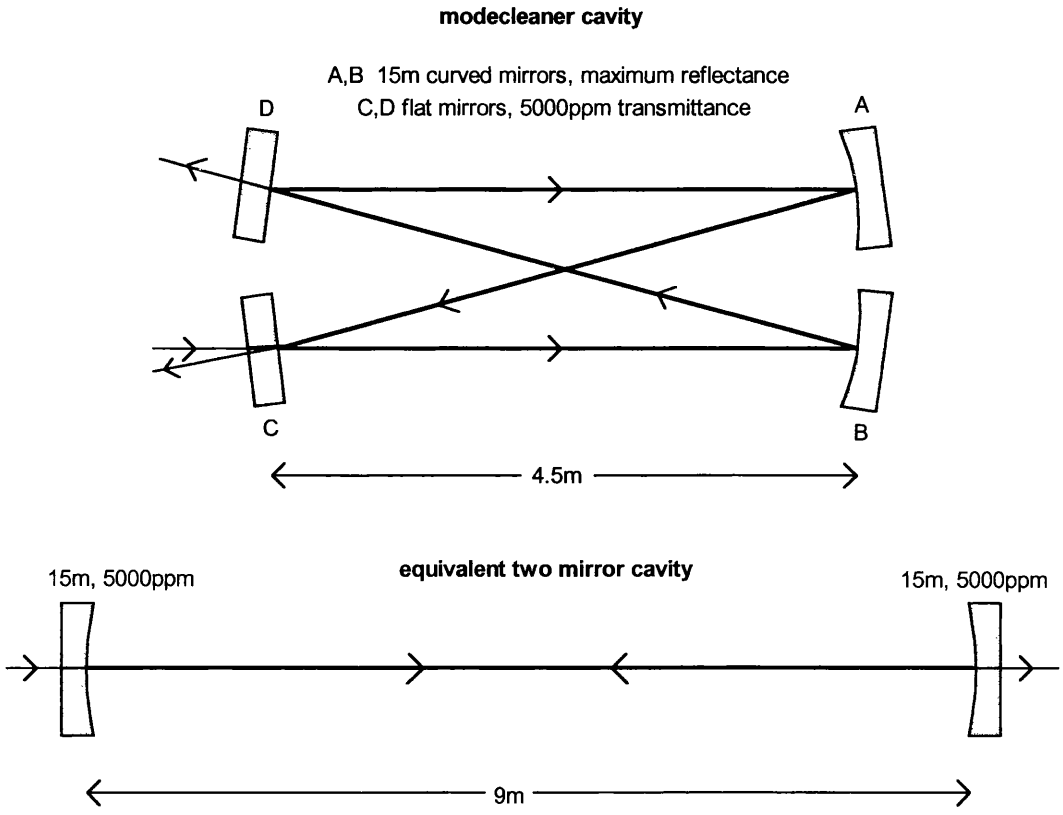

Figure 9.2: *The four mirror modecleaner cavity and its equivalent two mirror counterpart as far as mode structure is concerned.*

optical path length	18 m
free spectral range	16.67 MHz
finesse	627
linewidth	26.6 kHz
TEM_{00} throughput	96 %
TEM_{10} suppression	356
TEM_{20} suppression	320
visibility	100 %

Table 9.2: *Theoretical specifications of the modecleaner assuming that the mirrors have no loss and all the incident laser light is perfectly mode matched into the cavity.*

to be applied. The specifications in Table 9.2 are based on cavity geometry and theoretical calculations, assuming for the moment that the cavity mirrors are lossless. The theoretical throughput is very high, as will always be the case for a cavity which is well impedance matched and mode matched to the incoming light (see chapter 3). In practice it can prove difficult to realise such a high throughput efficiency and more will be said of this in the section on performance.

9.2.2 General Aspects of Design

The optics of the modecleaner system can be regarded as including the laser, the injection optics and the components of the modecleaner cavity itself. The various parts of the system will be described in the same order as the light meets them, and so the laser is introduced first.

Laser

The laser used throughout the modecleaner development was a Spectra-Physics 170 argon ion tube driven by a Model 270 power supply unit. The laser and the power supply pass bank that regulates the plasma current are cooled by circulating water flowing under a pressure of about 65 psi. The laser has a prism back reflector allowing the selection of various lasing wavelengths (514.5 nm being selected here).

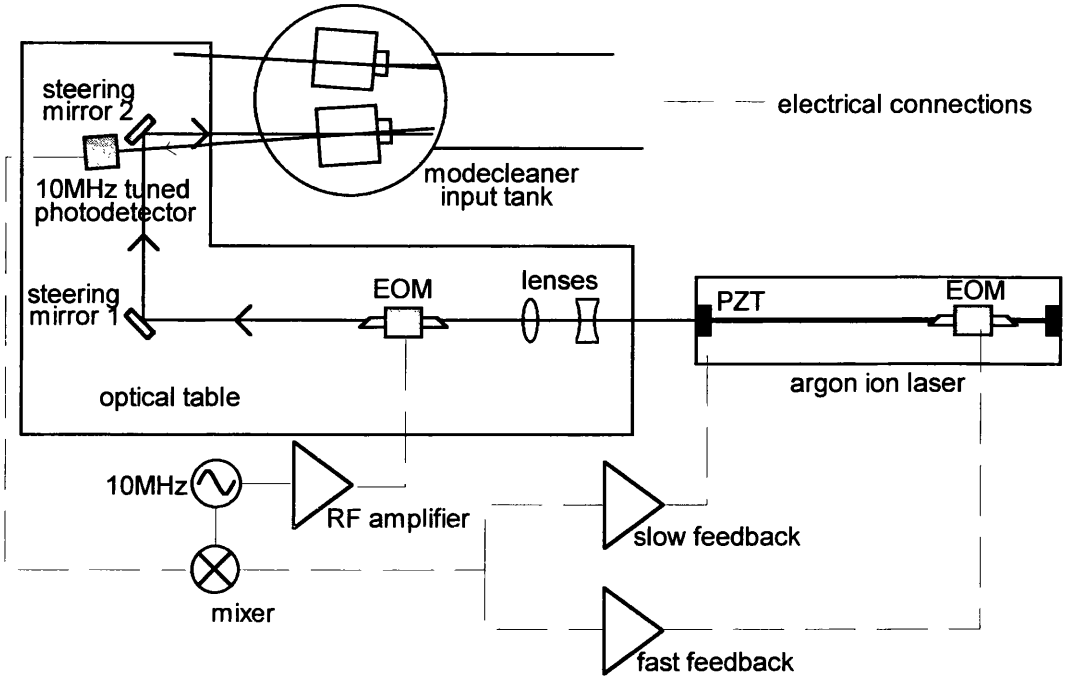

Figure 9.3: *The optical layout from the laser up to the modecleaner input.*

The front output coupling mirror has transmittance 4 % and radius of curvature 10 m. The emerging beam is diverged by the flat side of the output coupler and the phase front radius of curvature at the beginning of the optical system is actually 6.7 m. The laser resonator is mounted separately from the plasma tube as shown in Fig 5.15. The length of the resonator cavity is 2.4 m. To allow the laser to be frequency stabilised, the output coupling mirror is mounted on a multi-stack piezo-electric transducer (PZT) and a PM25 electro-optic phase modulator (EOM) is fitted into the laser resonator. These components allow control of the effective resonator length, and hence the frequency of the light, over a broad bandwidth.

Injection Optics

The components that formed the injection optics for the intitial development phase were all mounted on a large aluminium optics table resting on four pillars with rubber layers to provide some degree of isolation from ground noise. The optical scheme was quite simple, consisting only of a Faraday isolator, another PM25 EOM, mode

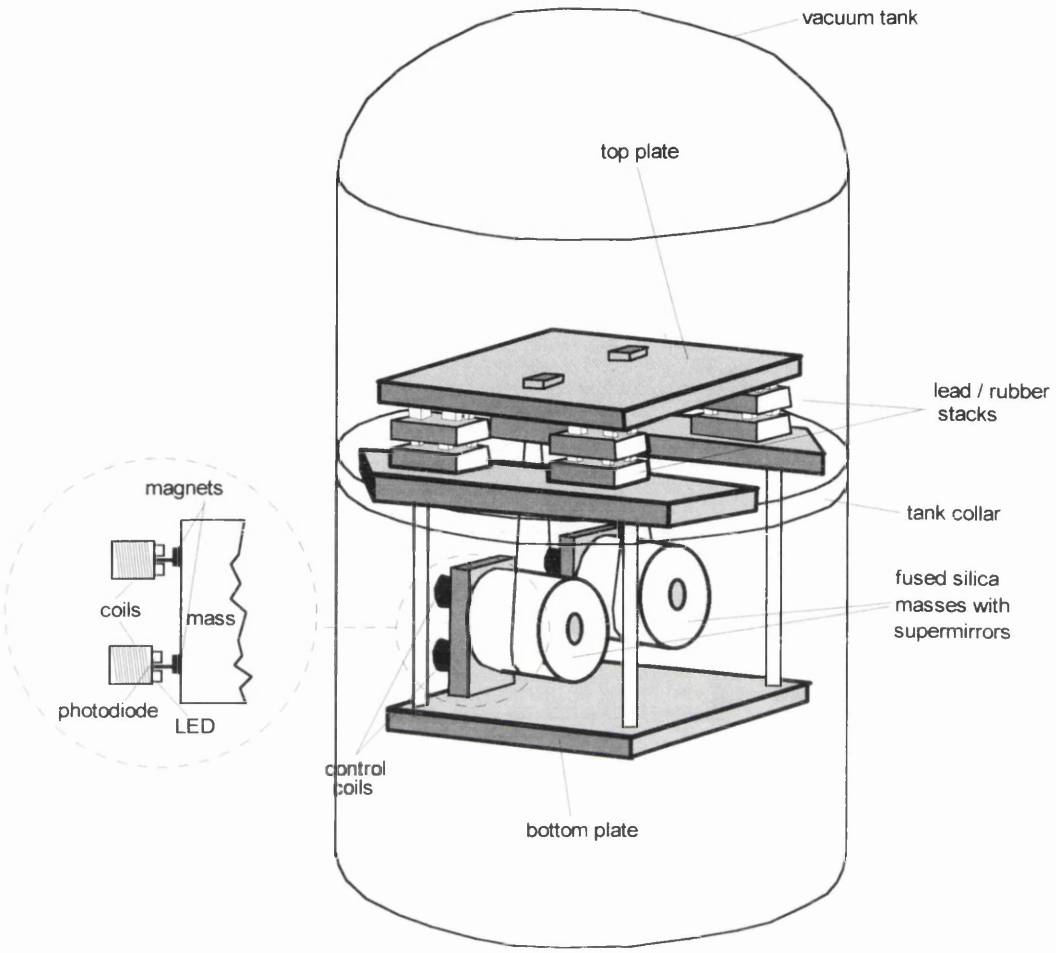

Figure 9.4: *The suspension assembly for the initial modecleaner development.*

matching lenses and beam steering mirrors. The EOM was used to modulate the phase of the light at 10 MHz. An RF reflection locking scheme for the modecleaner kept the light resonant in the modecleaner cavity by altering the frequency of the laser. A schematic of the optical layout including a block diagram of the laser feedback system is shown in Fig 9.3.

Modecleaner Cavity

The light enters and exits the modecleaner through a 20 cm port hole on the left most tank as illustrated in Fig 9.3. The port hole is made of untreated glass, having no special optical quality or anti-reflection coatings. Measurements made on the

port hole showed it to have a loss of around 10 % for a throughput laser beam. All future values of light power throughput for the modecleaner as a whole will have this loss already taken into account, bearing in mind that the light is subjected to it twice. For the purposes of measurement and testing, such a loss does not really matter, but for actual use with an interferometer the system would of course have to be modified.

The modecleaner vacuum system contains the four cavity mirrors. There are two in each tank, suspended side by side. The mirrors were manufactured by British Aerospace and are coated onto 2.5 cm diameter fused silica substrates. In the initial development phase, the substrates were optically contacted to fused silica masses which were then suspended in a single pendulum system as shown in Fig 9.4. The bottom basket contains two coil holder assemblies, one for each mass. These each contain four shadow sensor damping units which locally control motions of the mass using feedback to coils which interact with four magnets attached to the mass. These local control systems will be discussed in more detail in the next section. The masses were suspended from a top plate which rests on a multi-layer stack. The stack contains blocks of lead separated by small RTV pieces. Such a stack system provides a substantial degree of mechanical isolation from ground motion. The entire suspension assembly fits into the collar of the vacuum tank and electrical connections are made via 19-way vacuum feedthroughs mounted to flanges on the side of the vacuum tanks. Each of the two vacuum tanks contain essentially identical assemblies except that the pair of flat mirrors are mounted on masses of diameter 9 cm while the curved mirrors are attached to masses of diameter 13 cm, dictated by the availability of fused silica masses in the laboratory at Glasgow.

9.2.3 Technical Design

The technical aspects of the initial design will be taken to cover vacuum system details and electronic circuitry associated with the system. The electronics can be further divided into two categories pertaining to the modecleaner mass local damping controls and the locking of the argon ion laser to the modecleaner cavity. The vacuum system, which did not alter from the intitial development through to the

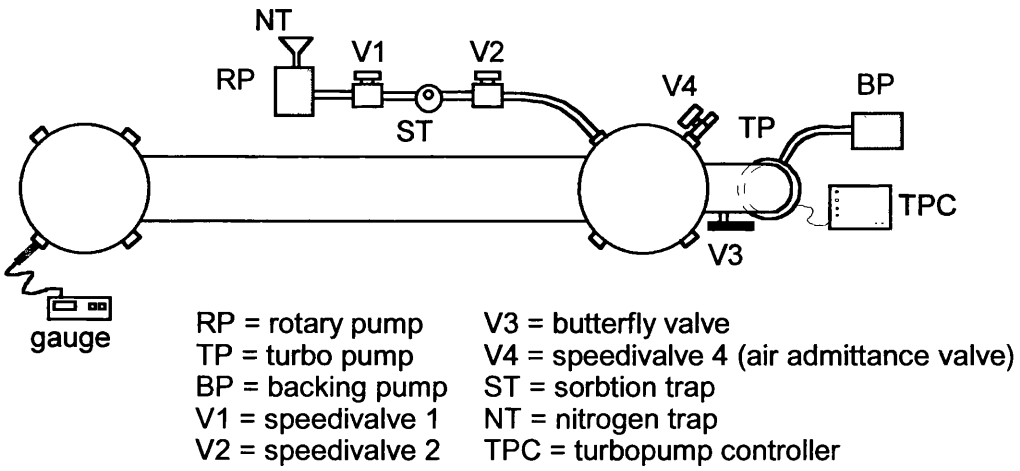

Figure 9.5: *The vacuum system for the modecleaner cavity.*

final development, will be introduced first.

Vacuum System

The total volume of the modecleaner vacuum system is around $10\,\mathrm{m}^3$. A turbo pump backed by a rotary pump is used to keep the system at a pressure of around 10^{-5} torr. To bring the system down to a pressure suitable for the turbo pump to commence working, another pump called a roughing pump is first used. This is just a simple rotary pump and will take perhaps ten to twenty minutes to bring the system from atmospheric pressure to about 10^{-2} torr whereupon the compression ratio of the turbo pump allows it to take over. The complete arrangement is shown in Fig 9.5. After the initial construction of the vacuum system the entire structure was wrapped in heating tape and baked for several days whilst being pumped with the turbo pump. This was done in an effort to remove water from inside the system. A helium leak tester was used to investigate any major imperfections in the system. By allowing helium gas to reside inside the sealed vacuum system, any cracks or poor seals become evident as they emit small amounts of the helium gas. Although the turbo pump is relatively quiet, most measurements on the modecleaner performance were performed with it turned off, unless otherwise stated.

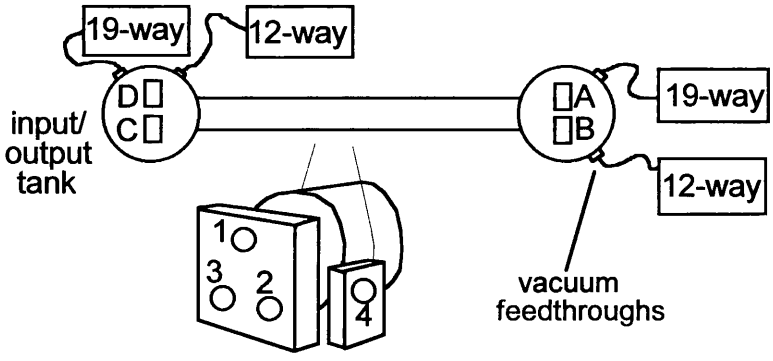

Figure 9.6: *Feedthrough connections for the local control damping circuits.*

Local Control Electronic Circuits

As shown in Fig 9.4 each mirror in the modecleaner is attached to a mass which is suspended on a single loop of wire from a seismically isolated aluminium top plate. In this form the pendulum has rather a high Q and will swing for several hours if disturbed. Even with the seismic isolation, there will still be some ground motion to excite the pendulum resonance and so some sort of damping must be employed. Passive damping would be an option, for example using Eddy current plates, but here it is also necessary to tilt and rotate the masses so that the beam can be aligned in the cavity[2].

An electronic system is used whereby the damping and control are combined into the functions of a multi-channel circuit. Each channel controls one of the coils on a given mass. Since there are four masses, each having four magnets with which to interact, it follows that there must be sixteen channels in total. The necessary connections that have to be made to the system are shown in Fig 9.6. Each circuit derives its signal from a shadow sensor which measures the position of a small flag attached to a magnet on the mass. The signal is processed by the circuit shown in Fig 9.7 and then applied with negative feedback to a coil situated beside the magnet. In this way, the position of the flag, and hence the mass, is stabilised. For each suspended mass, four magnets placed as shown in Fig 9.6 are sufficient to

[2]it is desirable to be able to do this without having to constantly bring the system back to atmospheric pressure and open the tanks.

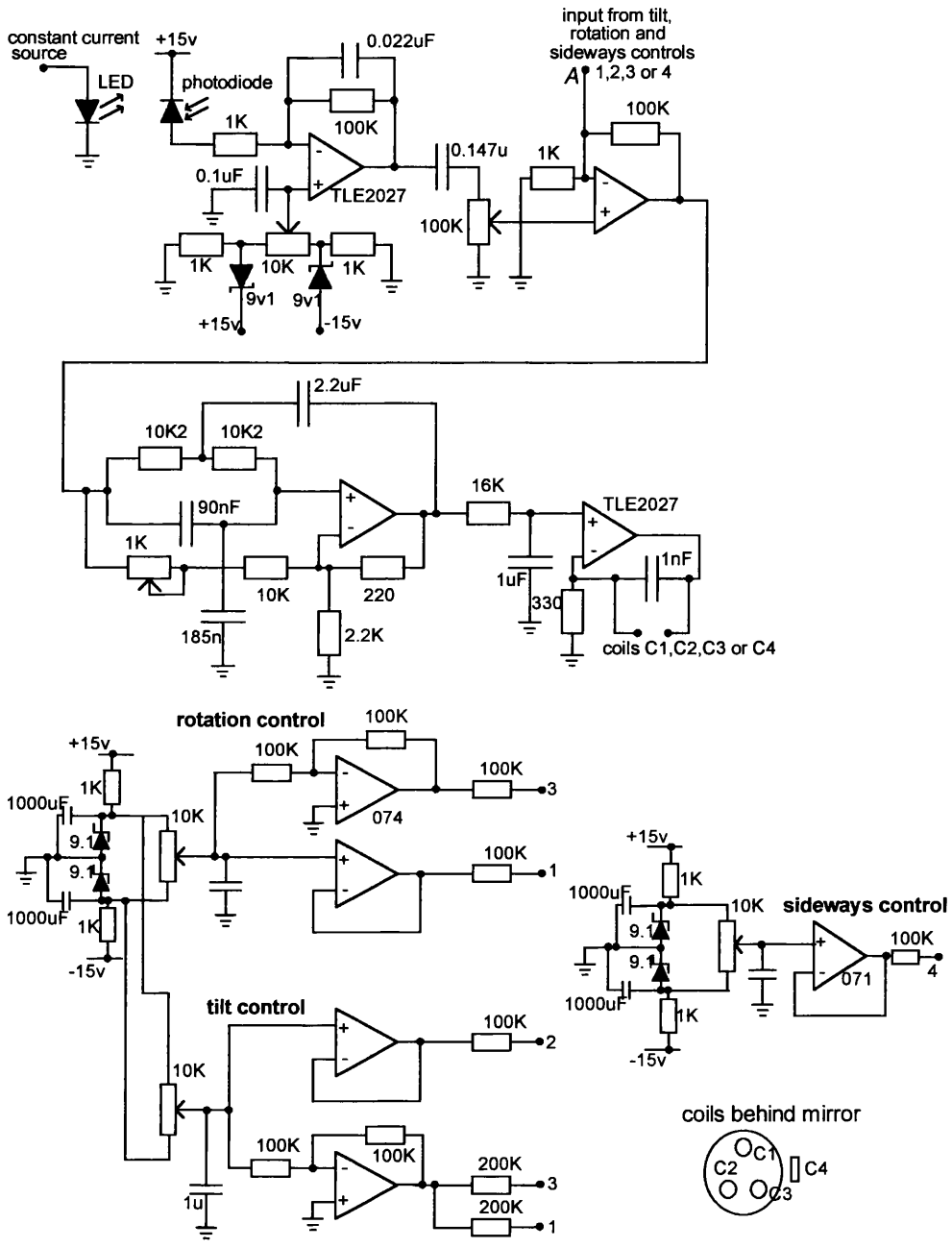

Figure 9.7: *The local control damping circuit diagram. There are four channels, one for each coil on a mass. Then there are four identical circuits for each of the four masses making sixteen channels in all.*

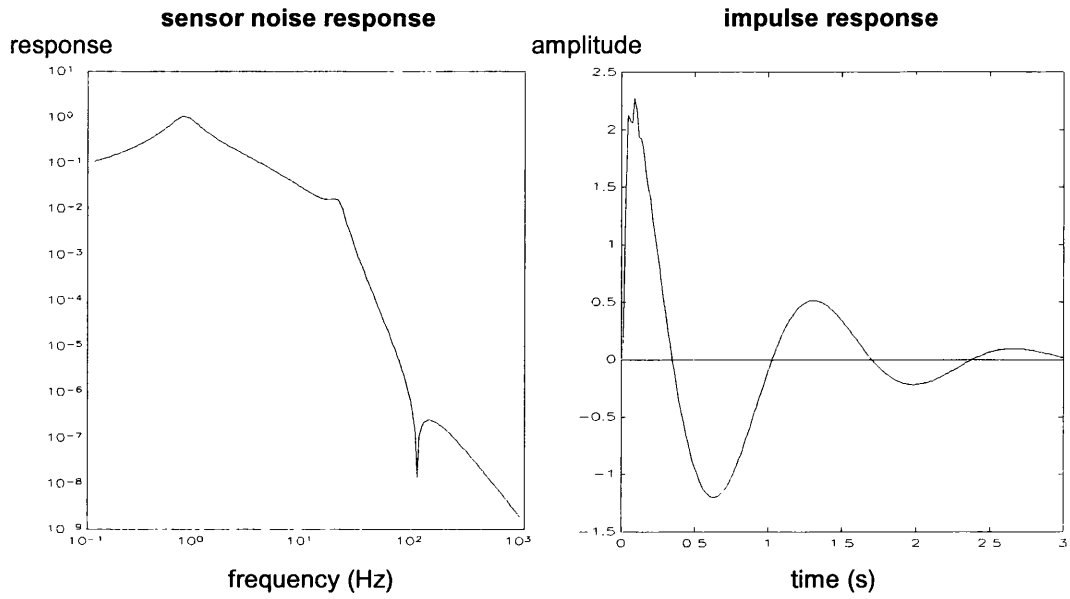

Figure 9.8: *The closed loop sensor noise frequency response and impulse response of the local control damping circuits.*

control all degrees of freedom of motion.

Each channel has an initial current to voltage converter which translates light changes at the photodiode to a varying voltage signal. This signal is then amplified and passed through a high pass filter with corner frequency 15 Hz to produce some phase lead at low frequency. The next stage has an input A where the control signals from the tilt and rotation circuits are applied. A further stage is included, first suggested for use in such contexts by Roland Schilling at MPQ, called a Scultéty filter. This has a notch in its gain bode plot, followed by a steep decrease in gain, is used to filter out noise at high frequency. Such a filter provides a far sharper attenuation of gain than a simple low pass RC filter would provide, without incurring severe phase penalty over the servo bandwidth. The net effect of the control system is to produce a closed loop response to photodiode signals as shown in Fig 9.8. Also shown in Fig 9.8 is the predicted impulse response, modelled using a standard simple pendulum for the suspension system. By applying controllable DC signals to point A of the circuit in Fig 9.7 it is possible using electronic algebra circuitry, as shown at the bottom of Fig 9.7, to rotate and tilt the mass. This enables the laser

beam reflected from each mass to be moved in both horizontal and vertical directions.

Laser Feedback System

The feedback circuit was designed to achieve a reasonably firm lock of the laser to the modecleaner cavity. In this phase of development, little attention was paid to optimisation of the feedback loop with respect to phase or gain margins, other than the requirement that the modecleaner should lock with good stability over a long period of time to allow measurements to be made. In this sense the servo loop is not really a laser frequency stabilisation scheme as such, but rather just a means of locking the laser cavity to the modecleaner cavity to allow preliminary throughput properties of the modecleaner to be assessed. The circuit designed to achieve this locking is shown in Fig 9.9. The top part of the circuit shows the 10 MHz photodiode, mixer and overall gain stage with a DC offset control. The bottom part contains the slow and fast feedback paths controlling respectively the PZT and phase modulator in the laser resonator.

9.2.4 Performance

The performance of the modecleaner after its initial development stage was evaluated via two measured properties. These were the laser *power throughput* and the *spatial filtering* of the input beam.

Power Throughput

The throughput of the modecleaner was rather disappointing being typically 65 %. Part of the reason for this was that the input beam was found to be quite elliptical having a ratio of widths in the x- and y-directions of about 2/3. This was eventually discovered to be caused mainly by bad alignment of the laser resonator with respect to the argon ion plasma tube. The consequence for the modecleaner was that not all the fundamental mode power could be matched into the cavity. There is also a small amount of light power channelled into the phase modulation sidebands by the 10 MHz EOM. In the modecleaner cavity frame, these phase sidebands can be

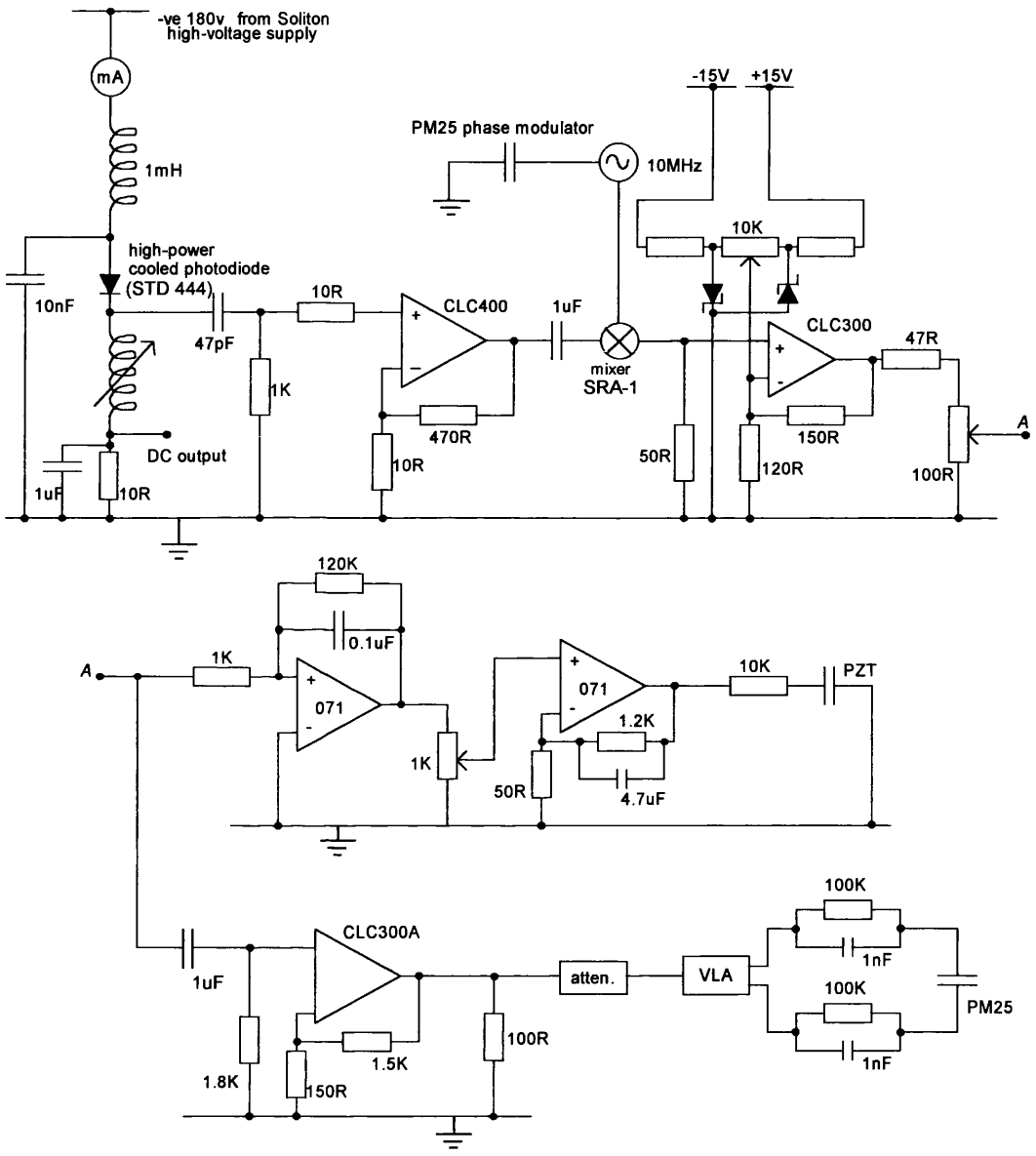

Figure 9.9: *Circuit diagram of the control system to lock the laser to the modecleaner cavity.*

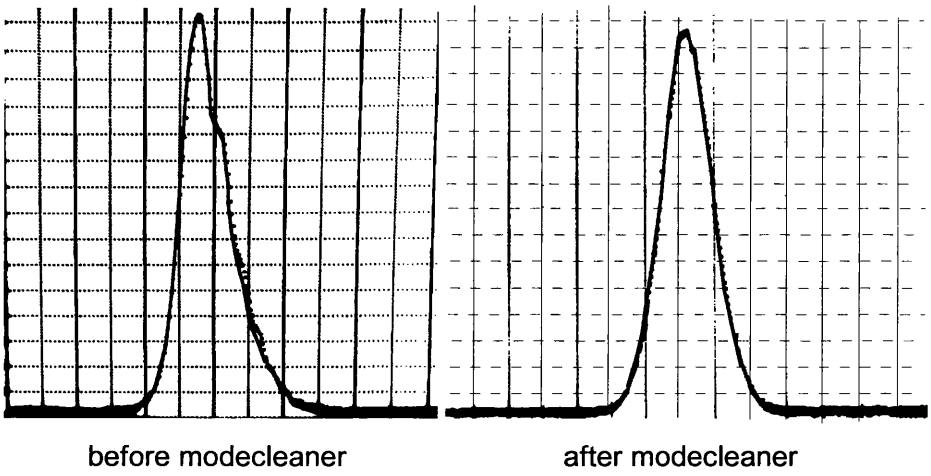

Figure 9.10: *Laser beam profiles of a distorted input beam before the modecleaner and the corresponding output beam examined after the modecleaner.*

regarded as frequency sidebands which will not resonate in the modecleaner cavity. Both these effects contributed to a cavity visibility which could not be improved much beyond 90 %, suggesting that only about 90 % of the input light power was being successfully coupled into the cavity. To explain the throughput of only 65 % it must follow that 25 % of the light is wasted in the cavity through losses in the mirrors. This would imply a total round trip loss of over 1500 ppm or around 375 ppm per mirror. This rather high loss is indicative of the need to protect the mirrors from the atmosphere of the lab, unless clean room standards are adhered to. Such standards were not feasible here, and the mirrors often spent many days exposed to the lab air, as developments and changes were made to the system.

Spatial Filtering Action

The output of the modecleaner should be a very pure Gaussian beam even if the input beam is distorted. Deviations of the input beam from a Gaussian intensity profile will manifest themselves as fluctuations of the light power transmitted through the modecleaner. The pictures in Fig 9.10 show a distorted input Gaussian beam profile and the corresponding output beam when the modecleaner is locked to the fundamental mode of the laser. The beam maps were obtained using a scanning slit

beam profiler. The spatial filtering toward the Gaussian form is evident.

In view of the above throughput value, working methods were altered for the second phase of development in the hope that if the mirrors were cleaned and the system pumped down promptly enough, the level of contamination would be reduced. Various other aspects of the system were altered or improved during the second phase of development and these will now be described.

9.3 Complete Development

A major aim in the final development of the modecleaner system was to bring the design to a state closer to the likely implementation in the GEO 600 interferometer. The laser is no longer locked to the modecleaner cavity but is locked to a rigid reference cavity. The modecleaner cavity is then actively controlled to stay on resonance with the pre-stabilised light. In the descriptions that follow, the laser stabilisation scheme and the modecleaner locking system will be referred to as the *first* and *second* loops respectively. As well as this major change to the locking topology, other aspects of the design were altered. Modifications to the modecleaner mass suspension systems were made and two of the modecleaner mirrors were changed to attempt to reduce the losses experienced by the light inside the cavity.

9.3.1 Modified Optics and Feedback Design

The new optical layout accommodates the reference cavity and associated optics and is shown in Fig 9.11. The beam splitter BS1 splits off about 2 % of the laser light off to the reference cavity optics chain. This chain consists of an EOM, Faraday isolator, mode-matching lenses, wave-plate and the reference cavity itself. The reference cavity went through various stages of design. The first approach was to use a fused-silica tube with mirror mounts glued to the inside. However this was found to be susceptible to flexing and was physically too large to be placed in any vacuum tank available in the laboratory. The cavity, not being under vacuum, was very sensitive to acoustic noise. In fact, the removal of this sensitivity to acoustic noise

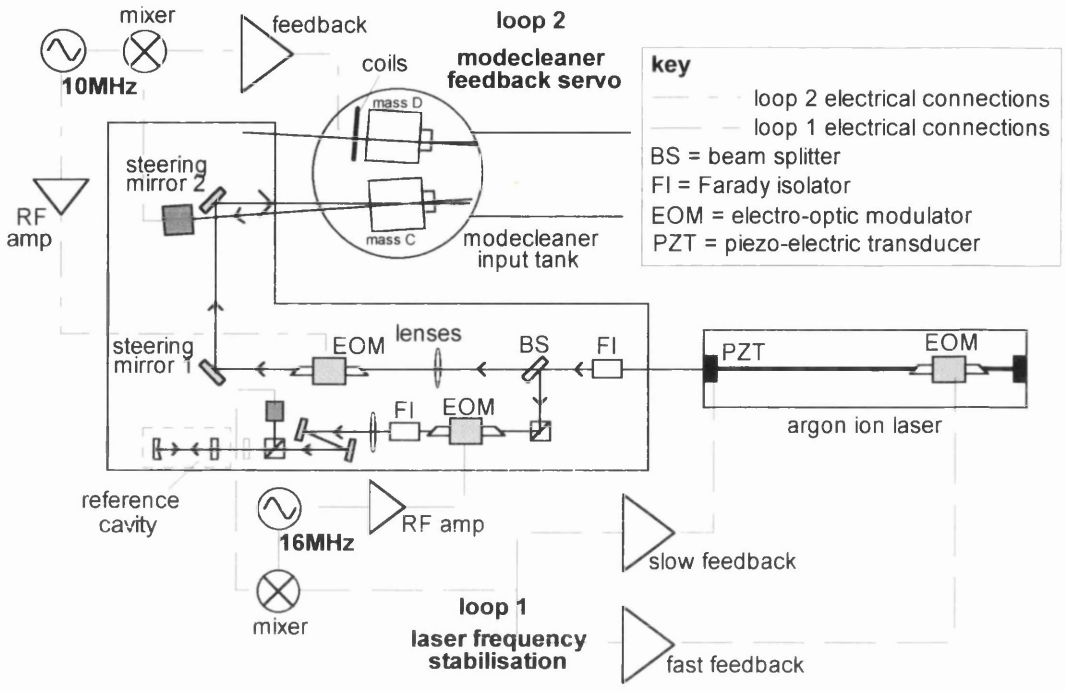

Figure 9.11: *The new optical layout showing a simplified version of the locking topology.*

by moving toward a system that could be placed under vacuum proved a critical step in achieving a working system. The cavity was eventually constructed from a solid aluminium block about 25 cm long and 15 cm diameter. A hole drilled down the centre lets the light through and the mirrors were glued directly to the ends. A flat 2000 ppm transmitter and a 1 m radius of curvature 600 ppm transmitter were used as the input and output coupling mirrors respectively, giving a theoretical finesse of about 770. One mirror, the 600 ppm transmitter, was mounted on three P25 PZT rings which provide a method of tuning the cavity length. The reference cavity is shown in Fig 9.12. Although aluminium is a bad choice as far as thermal drift is concerned, it was the best solution available at the time, and provided a cavity compact enough to be contained in a vacuum tank. The resulting isolation from acoustic noise provided a huge reduction in frequency noise in the first loop and was easily the most important improvement made in the reference cavity design. Ideally the cavity would be constructed from zerodur which has practically zero thermal expansion coefficient. The modulation frequency for the first loop is 16 MHz and an

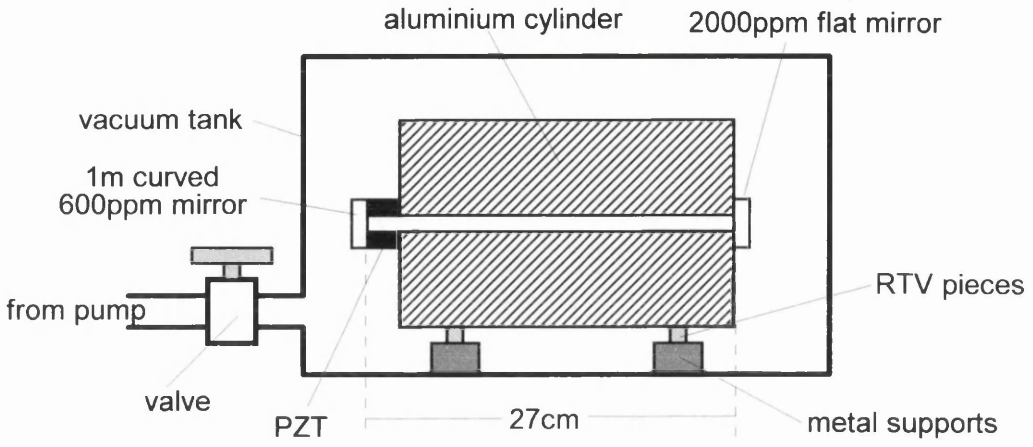

Figure 9.12: *An illustration of the design of the reference cavity.*

RF-reflection locking scheme is used to provide a suitable error signal for feedback to the PZT and Pockels cell in the laser cavity. The system works in much the same way as the previous scheme where the laser was locked to the modecleaner, but the electronic circuitry is different. These differences take account of the very much increased linewidth of the reference cavity. More importantly, the differences show a more careful approach to the feedback design, where the greatest possible gain over a broad frequency band (up to ~1 MHz) is required. If a good level of frequency stability is not achieved, then it will be difficult for the second loop to control the modecleaner to lock to the light. The complete circuit is shown in Fig 9.13 (excluding power supply circuits and decoupling details). A Colpitts crystal oscillator provides a 16 MHz signal which can drive 1V across an impedance of 50 Ω. This feeds into a 2W RF power amplifier which drives a tank circuit involving a PM25 EOM as the capacitor. Voltage magnification creates about 200 V across the modulator which is enough to produce 15 % phase modulation sidebands on the light. A tiny coil derives a local oscillator signal which is then combined with fringes from the RF photodiode of the reflection lock scheme by a SRA-1 low level mixer. The mixer feeds into two parallel feedback paths. The low frequency path drives the laser PZT and the high frequency path controls the intra-cavity EOM. The gains of the two paths cross over typically at a few kHz although this is adjustable using the slow gain control. The fast feedback path uses a CLC101 high frequency op-amp to drive the 50 Ω input

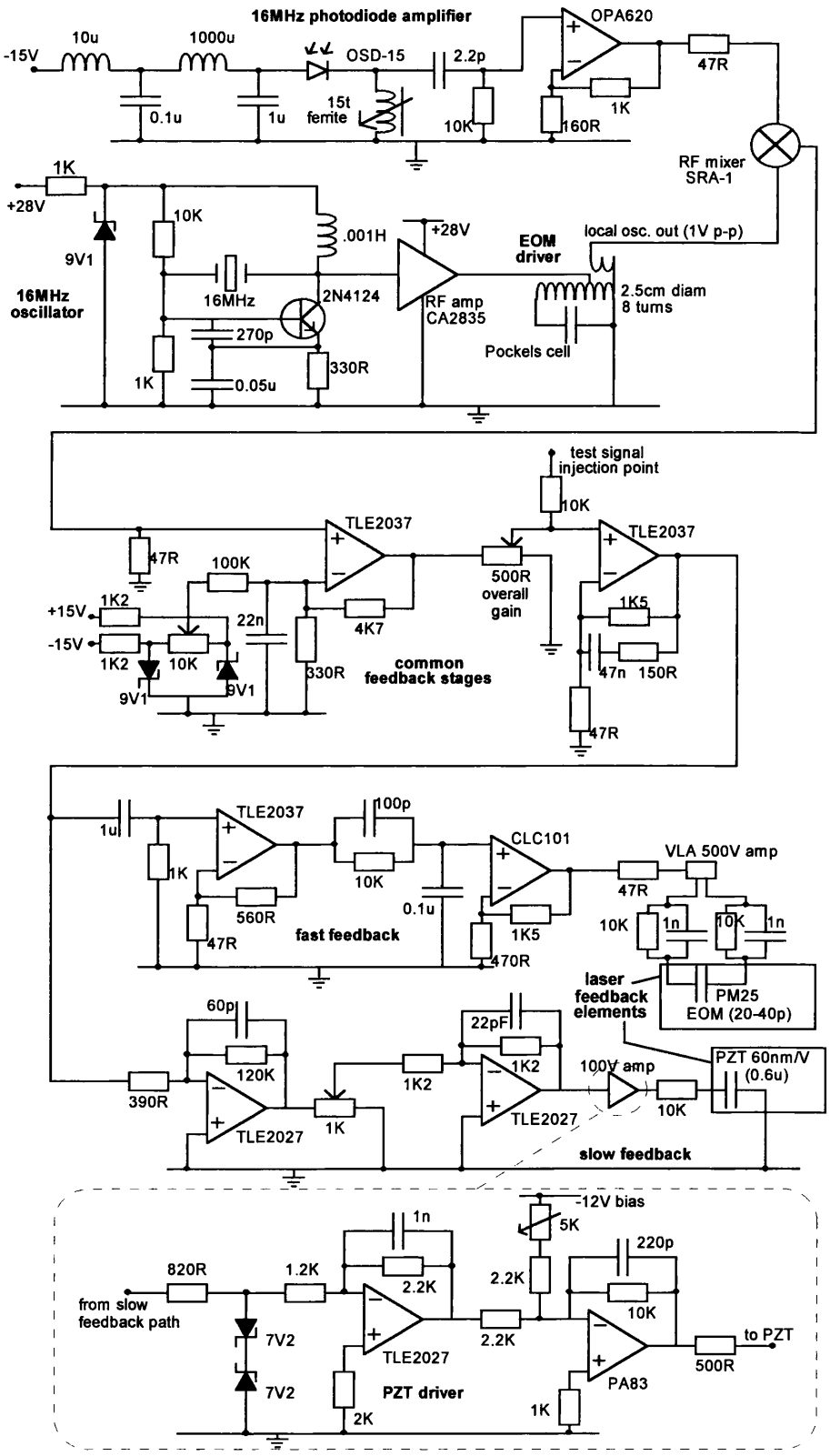

Figure 9.13: *Circuit diagram for the frequency stabilisation loop.*

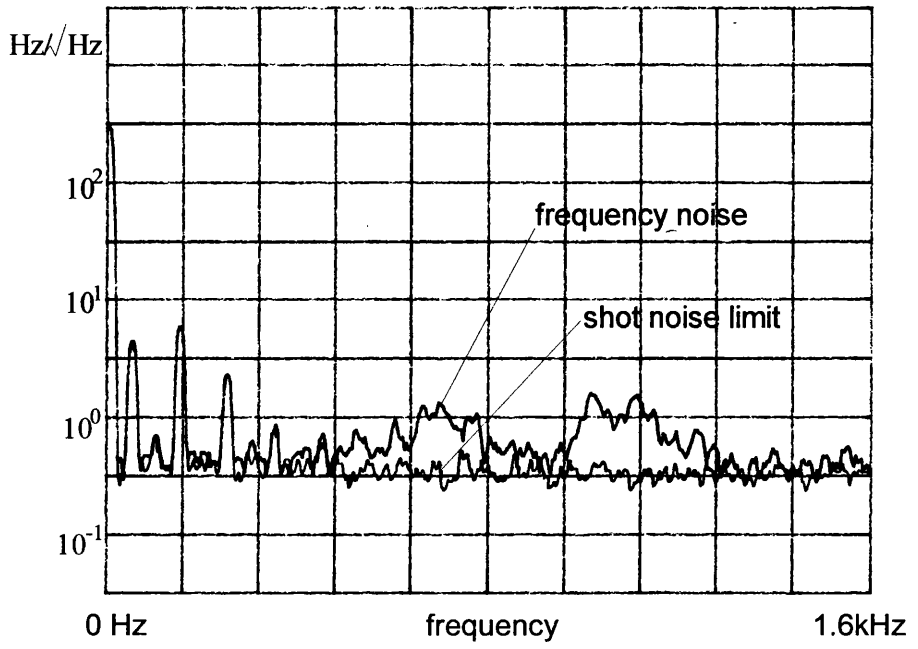

Figure 9.14: *Laser frequency noise as measured at the error point of the stabilisation loop.*

impedance of a commercial video linear amplifier (VLA). The VLA then drives the Pockels cell, another PM25, directly. The trace shown in Fig 9.14 shows the level of frequency noise as measured at the error point of the first loop. Shot noise is also shown for the equivalent level of signal produced by a constant light at the RF photodiode.

The second loop also uses an RF reflection locking scheme this time using 10 MHz modulation. The important parts of the circuit are shown in Fig 9.15. The back-reflected light from the modecleaner is used to develop an error signal which is filtered and amplified and sent back to the back three coils used to control mass D of the modecleaner (mass D contains the output coupling mirror). By pushing evenly on the mass, the cavity length can be controlled to stay on resonance with the light. The pushing has to be done carefully so that the mass is not tilted when the feedback signal is applied. Adjustable variable resistors on each of the three coil driver inputs allow some degree of equalisation to be achieved. Clearly, the better stabilised is the light in the first place, the less are the demands on the second loop.

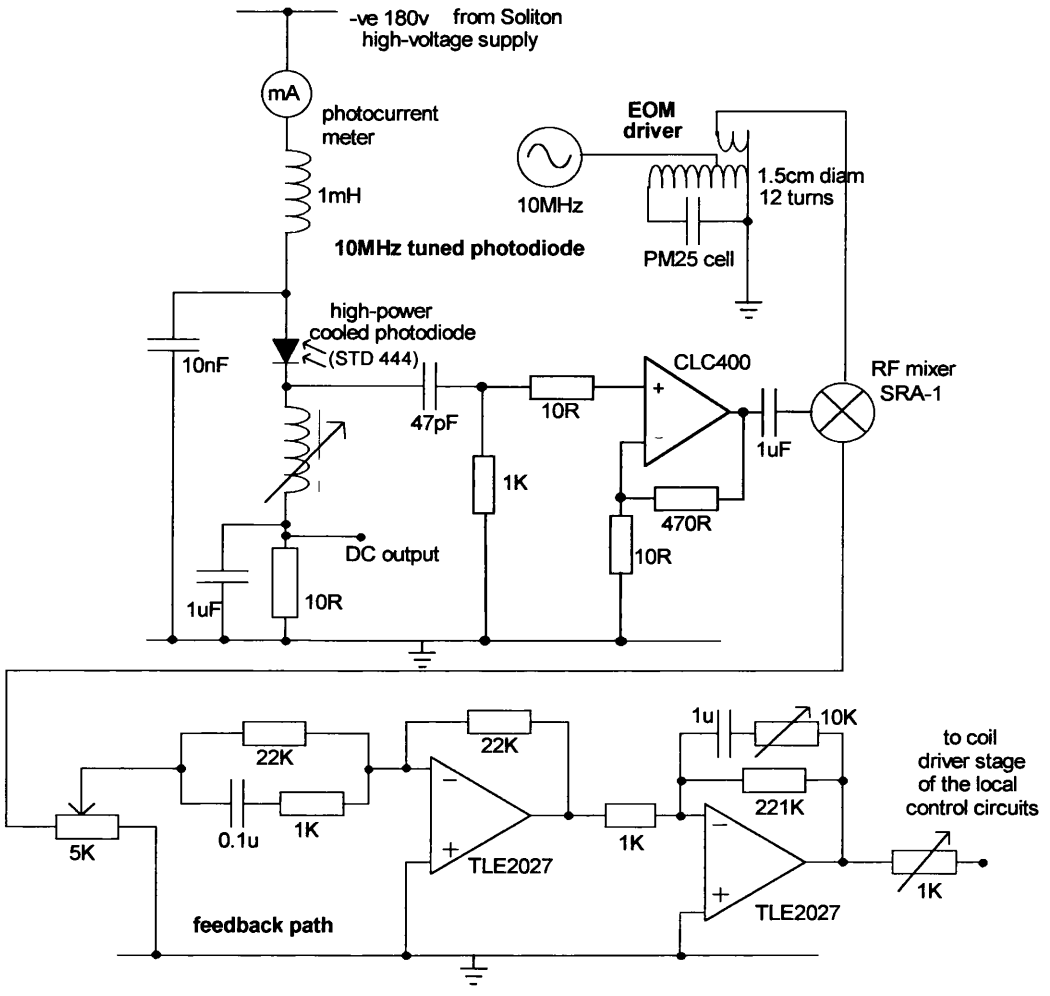

Figure 9.15: *Circuit diagram for the modecleaner locking loop.*

This reiterates the need for a laser stabilisation first loop with high gain.

In an effort to reduce the modecleaner cavity losses, two of the older mirrors (the British Aerospace 15 m curved mirrors) were removed from their masses and replaced with specimens of identical parameters (and age) which had been kept in their packaging except when brought out for loss tests. Each mirror was attached to its mass using two tiny dabs of superglue. Another aspect of the system that was modified was the mode-matching to the modecleaner cavity. A knowledge of the laser mirror parameters and resonator length should give the necessary data to predict the beam properties at any further place along the optical path, taking into consideration lenses and other components which may alter the beam shape or phase front curvature. However, access to a beam profiler demonstrated that predicted values of beam width were manifestly inaccurate when compared with measured values. Even with the laser well-aligned with intra-cavity beam adjusted for optimal plasma tube transit, and all its optical parts cleaned, these deviations from an ideal Gaussian propagation still persisted and as a result, further mode-matching was perfomed experimentally rather than relying upon the solutions provided by calculation, or Gaussian optics software packages.

9.3.2 Modified Technical Design

The modecleaner vacuum system design remained unchanged in the final configuration with the reference cavity being pumped down from a separate pump. The original suspension design exhibited a large vibrational motion which was caused by a basket resonance as shown in Fig 9.16. The vertical bars supporting the bottom plate to which the coils are mounted were replaced with thicker versions, but no longer directly connected to the tank. Rather, the entire assembly now rests on RTV pieces so that the coils themselves are somewhat isolated from ground noise. The new assembly has a much lower structural resonance around a few Hz but this does not prove problematic in the feedback systems. The residual motion of the masses with respect to their control coils when the local control circuitry is switched on can be measured by monitoring the signals being sensed at the shadow sensors. It is instructive to do this because it can identify potential problems such as a mass

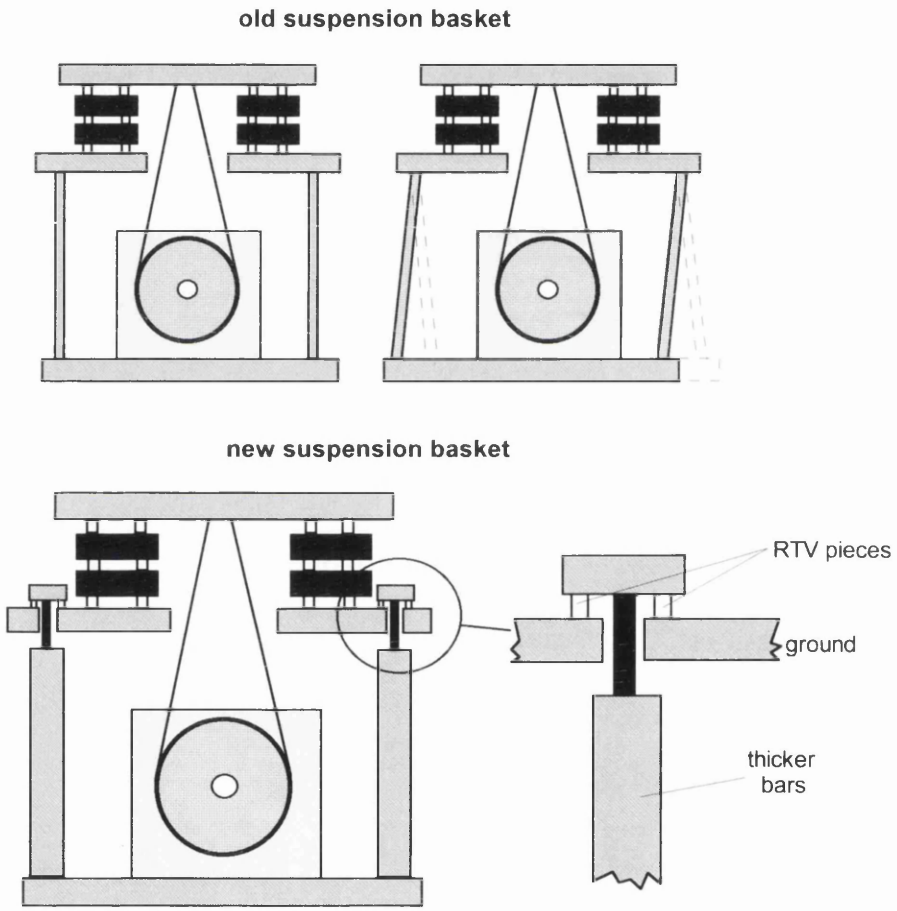

Figure 9.16: *Diagram showing the shortcomings of the old suspension system and the replacement design.*

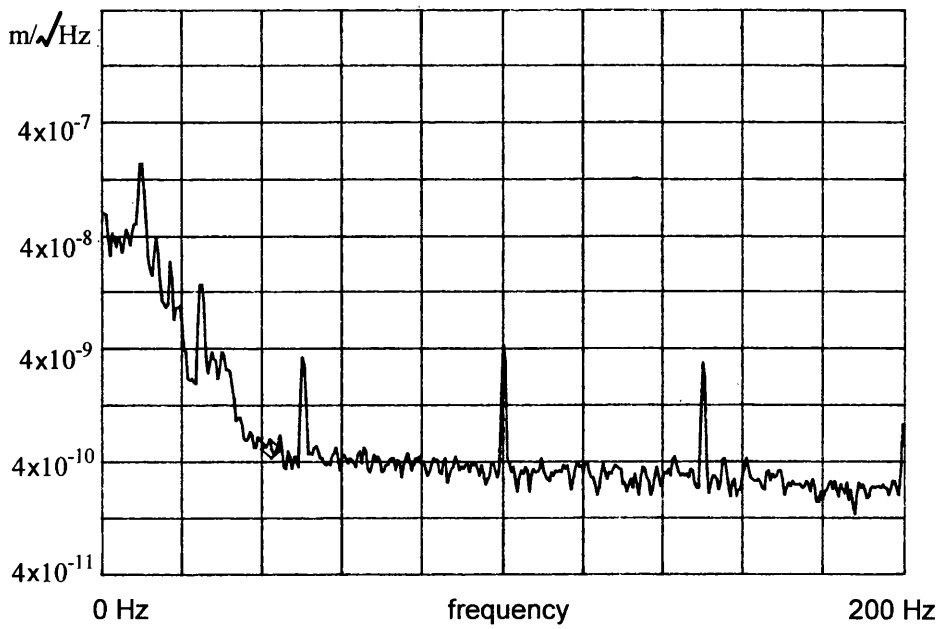

Figure 9.17: *Residual motion of the output mass in the modecleaner, as measured by sensing the motion of the flag at the top coil.*

scraping a coil. Fig 9.17 shows a typical trace of residual motion for the output mass of the modecleaner. It is most likely the case that the background level in Fig 9.17 is predominantly absolute motion of the coil rather than of the flag attached to the mass, since the pendulum is subject to a much greater degree of seismic isolation than the coil. The measurement was made at the output of the first amplifier after the photodiode in the local control path.

9.3.3 Performance

The performance of the modecleaner was investigated in much greater detail in its modified state. Measurements of laser power *throughput*, *finesse*, *passive filtering action*, *spatial filtering*, *long term stability* and *beam jitter reduction* were made and these will now be described in turn.

Power Throughput

The power throughput of the modecleaner, even with two of the mirrors replaced,

was still not very good given the theoretical throughput of 96 %. A maintainable value of 70 % could be achieved although this must be adjusted for the effects of modulation and mode matching before a proper comparison with the theoretical value can be made. A fairly steady 90 % visibility was monitored implying that 90 % of the incident light power is matched into the cavity. If only 70 % gets transmitted then 20 % is being lost in the cavity, which again implies a round trip loss of over 1000 ppm. It was certainly observed that the beam spots on the mirrors appeared visually very bright. Given brand new mirrors and more stringent operational procedures[3] a higher throughput would undoubtedly be achieved.

Finesse

The finesse of the cavity was evaluated using the ring-down measurement process described in chapter 4. The finesse of the cavity was measured to be around 550 using this technique. This is consistent with a cavity round trip loss of 1400 ppm, again suggesting that the mirrors are not as good as they should be, and need replacing before the best performance can be obtained from the system.

Passive Filtering Action

The modecleaner cavity should act as a low-pass optical filter with corner frequency given by half the cavity linewidth. In view of the above measurement of finesse, the linewidth of the cavity is in the region of 30 kHz giving a corner frequency of 15 kHz. Laser power noise above this Fourier frequency should be subject to an attenuation characterised by a 12 dB per octave slope. An experimental demonstration of this is shown in shown in Fig 9.18 which illustrates four superposed intensity noise traces measured at the output of the modecleaner. The traces show how an intensity peak applied before the modecleaner with constant amplitude, but increasing frequency, will be suppressed according to the low pass filtering action of the cavity.

[3] ideally the mirrors should be thoroughly cleaned immediately prior to system pump down.

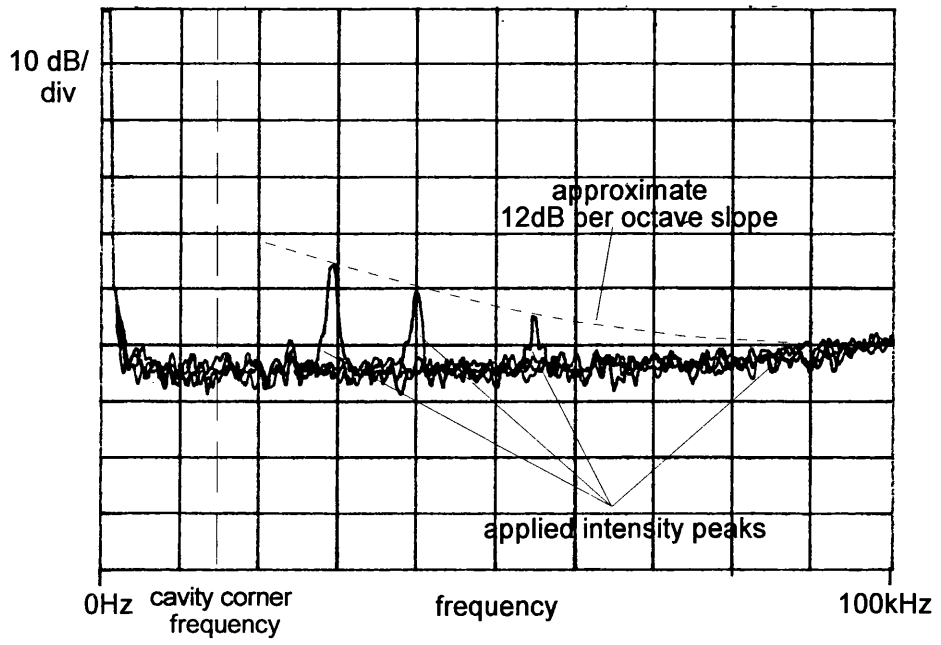

Figure 9.18: *Traces showing how an applied intensity noise peak is subject to a 12 dB per octave attenuation after the cavity corner frequency.*

Spatial Filtering Action

The modecleaner cavity should resonate in a perfect fundamental cavity mode limited only by imperfections in the mirrors. Even if the input beam has poor spatial characteristics, the beam output from the modecleaner should have a very accurate Gaussian intensity profile. The intensity profile of the beam can be investigated with a scanning slit beam profiler. The traces in Fig 9.19 show the results of such an investigation. The discrepancy near the peak of the throughput beam horizontal profile is most probably due to a double reflection in the glass port hole that the output beam must pass through. In principle it should be possible to add the reflected beam profile to the throughput profile and obtain the input beam profile. The traces in Fig 9.19 are all scaled so that the peaks are all approximately the same height, but of course the reflected beam is of much lower power than the input or throughput beams, and this must be kept in mind when comparing the traces.

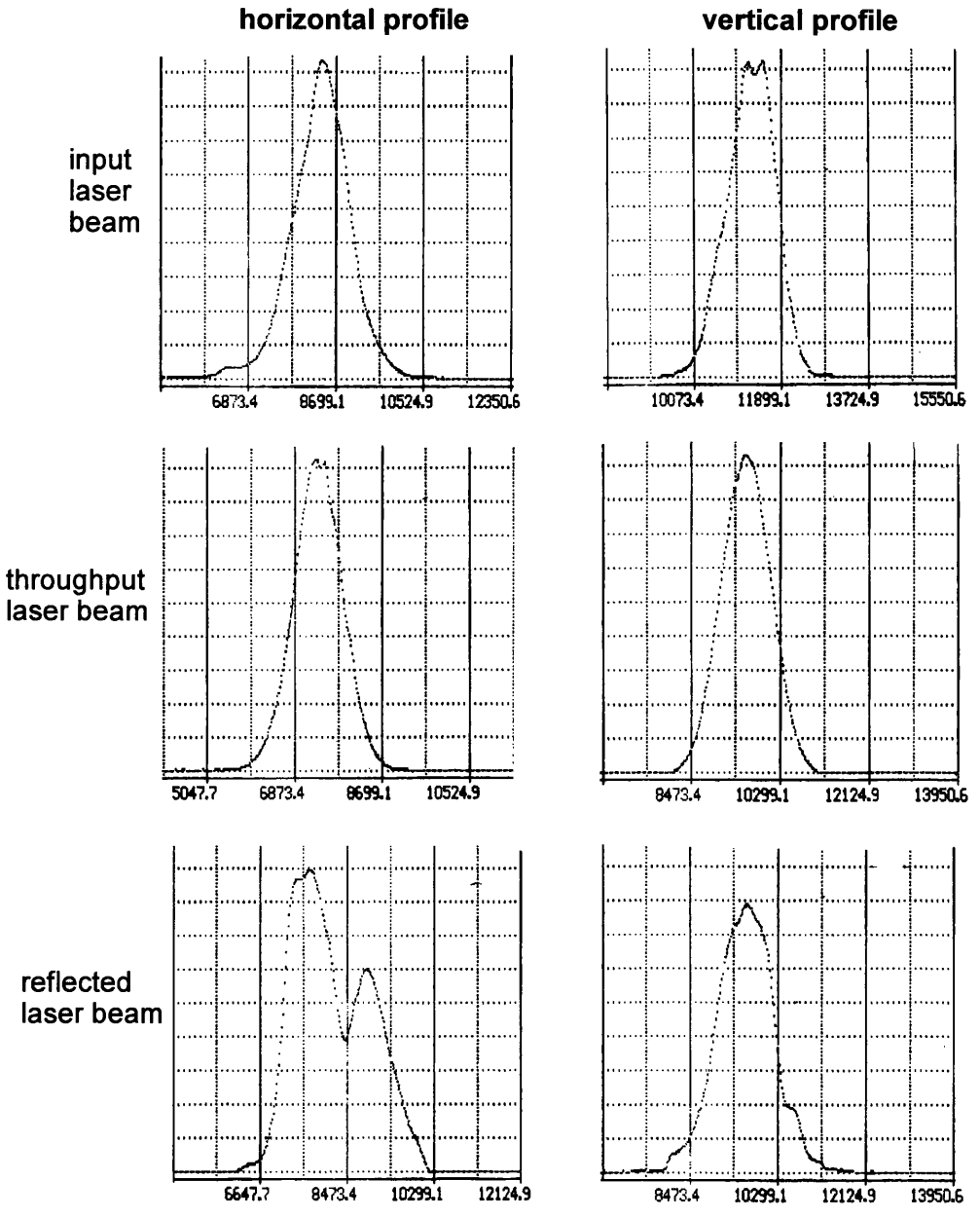

Figure 9.19: *Horizontal and vertical beam intensity profiles measured with a scanning slit beam profiler. The top traces show the state of the input beam. The middle traces show the throughput beam when the modecleaner is locked. The bottom traces illustrate the condition of the reflected beam.*

Long Term Stability

If the modecleaner is to perform as part of a detector which is required to run for long periods of time then it is important that the cavity alignment does not drift significantly over this period. Automatic alignment schemes [68],[69] can correct for small deviations but these have limited range. Mechanical settling in the suspension parts and thermal drift in the local control electronics could both lead to changes in the relative mirror positions and this would slowly misalign the cavity, reducing the visibility and proving detrimental to the throughput. Such long term stability is difficult to predict, and so an experiment was performed to investigate how the visibility of the modecleaner would change over a period of several weeks. The system was locked up and optimally aligned so that the visibility was around 90 %. The entire system was then left undisturbed for two months, after which time the visibility was re-examined and was found to have dropped to 20 %. The system was not on-line throughout this period, but the test shows that the average alignment drift over this time is reasonably small, and stays within the range of an easily measurable fringe depth, which may be considered to be anything greater than 10 %.

Long term tests with the system locked up and the laser at full power have only been performed over a few hours; whereupon the lock stability is satisfactory. The modecleaner cavity will stay in lock through general room acoustic noise, doors slamming etc. The most common reason for it falling out of lock is the failure of the first loop, because of a mode-jump in the laser for example.

Beam Jitter Reduction

The beam geometry noise reduction is the most important aspect of the system performance, being the noise that the modecleaner is primarily designed to attenuate. The performance of the modecleaner as a suppressor of beam geometry fluctuations was investigated by studying its ability to suppress beam jitter noise. Measurements of beam jitter over a 200 Hz frequency span were taken before and after the modecleaner when the input beam was subjected to artificially applied jitter noise. The jitter noise was injected first using a refracting glass slab about 5 mm thick. The slab

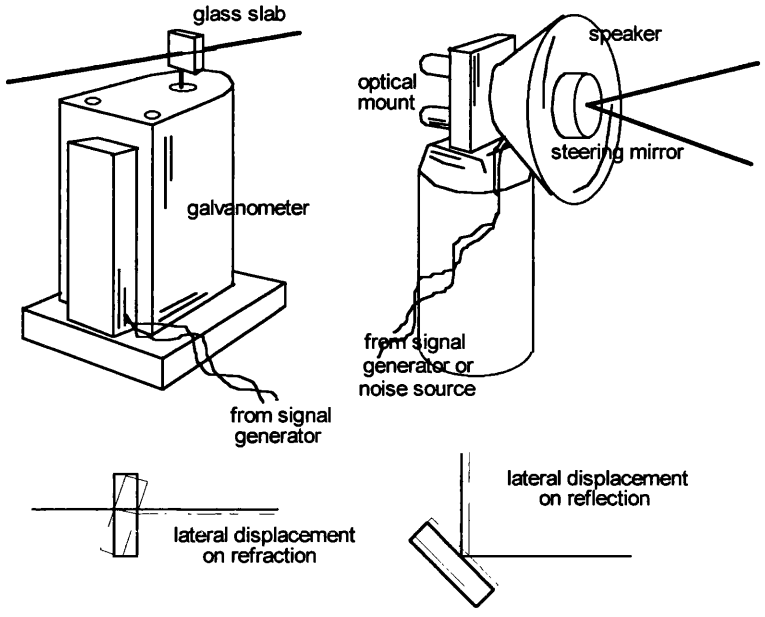

Figure 9.20: *Methods to introduce an artificial beam jitter to the laser beam.*

was mounted to the shaft of a galvanometer movement which was powered from a variable frequency signal generator as shown in Fig 9.10. The oscillation of the slab produced a periodic refraction which fluctuated the lateral position of the through-put beam. Unfortunately the slab was not anti-reflection coated and its varying reflectivity when tilted caused a small intenstiy variation in addition to the beam jitter. To avoid introducing intensity noise, an alternative method was employed whereby one of the steering mirrors to the modecleaner was mounted on a small loudspeaker cone also shown in Fig 9.20. The loudspeaker was driven from a signal generator or a white noise generator, producing a lateral fluctuation to the reflected beam, but this time with no associated intensity variation. The results that follow all had artifical jitter noise introduced using the mirror mounted on the speaker cone. The beam jitter level was measured using a quadrant photodiode connected and oriented as a split photodiode sensitive to beam jitter in the horiziontal direction. The photodiode was mounted on a micrometer translation stage which allowed fine adjustment ($\sim$ 0.01 mm) of the beam position on the photodiode and proved useful in calibrating the measurement system. The photodiode was connected to the motor controlled resistor unit described in chapter 5. This device corrects for

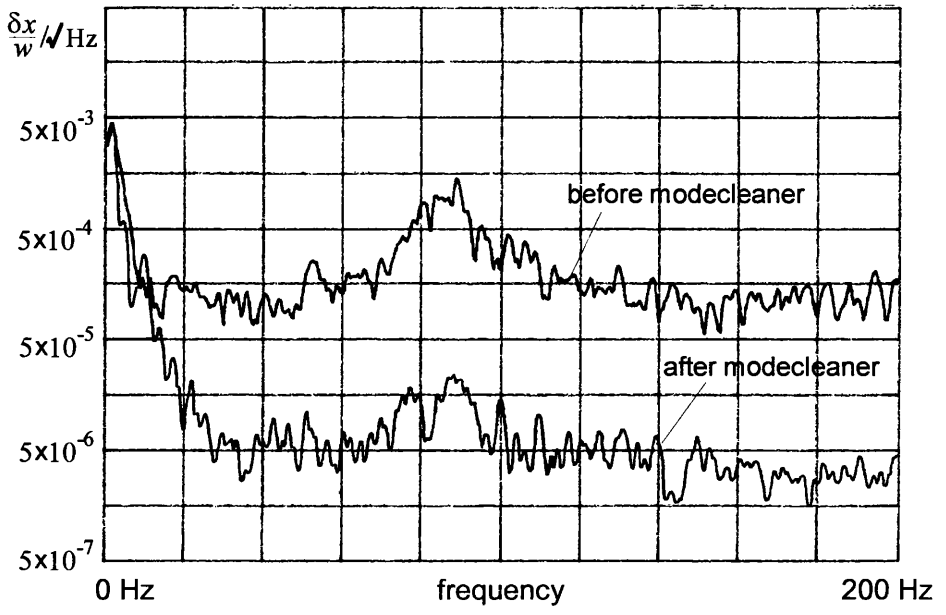

Figure 9.21: *Beam jitter levels measured at the input and output of the modecleaner over a 200 Hz span. The measurements were made with a white noise lateral beam positional fluctuation applied to the input light.*

imbalances between the currents in each half of the split photodiode caused by slow drifts of the beam during a measurement. In its absence, the measurement process quickly becomes dominated by intensity noise in the laser light.

A first impression of the beam positional fluctuation reduction afforded by the modecleaner is given by Fig 9.21. This shows two beam jitter traces, one taken before the modecleaner and the other measured at the output of the modecleaner. The measurements at the output of the modecleaner were made $\sim$ 1 m from the output mass, the beam being guided by a single beam splitter onto the photodiode surface. The laser beam was subjected to a white noise positional fluctuation at the input to the modecleaner generated by applying a 50 mV rms white noise signal to the loudspeaker cone onto which is mounted the beam steering mirror. As can be seen from Fig 9.21 the level of beam jitter noise is reduced by up to 40 dB in places. Given the measured finesse of the modecleaner cavity and using the results of chapter 8, the level of suppression for the TEM_{00} mode (to which beam jitter noise is most strongly related) should be around $\sim$ 350 or $\sim$ 51 dB. A possible

reason for the lack of the full 51 dB suppression in Fig 9.21 is that the lower trace is being limited by the background jitter noise level at the modecleaner output, due to the residual motion of the steering beam splitter and indeed the photodiode itself. Another explanation is that the measurement procedure is being dominated by intensity noise at the modecleaner output. This is not inconceivable given that the action of the modecleaner is basically to convert beam geometry noise in the input light to intensity noise in the output light. The demands placed on a measuring instrument with regards to intensity noise insensitivity become rather high at the modecleaner output.

Another series of measurements was performed this time with a sinusoidal signal of frequency 125 Hz applied to the loudspeaker cone in place of the white noise. This introduced a more well defined reference jitter peak with which to probe the performance of the system. The traces obtained from the beam jitter meter for the laser beam at the input and output of the modecleaner are shown in Fig 9.22. Again, it can be seen that the reduction in the applied peak, and in the level of the background generally, in not as much as expected.

Possibly the most effective method of finding out whether or not the measured traces at the modecleaner output are being limited by intensity noise is to actively intensity stabilise the output light, and repeat the measurements on the stabilised light. It was decided that an electro-optic phase modulator[4] would not be the best choice for such an intensity stabilisation scheme, because of its tendancy to introduce beam jitter noise onto the light. Instead, a system using an acousto-optic modulator (AOM) was constructed and this is illustrated in Fig 9.23. The AOM used was an ISOMET 40 MHz crystal, powered by a commercial 40 MHz driver capable of supplying a maximum power of 1 W into the crystal. The action of the AOM is to diffract the incident laser beam into secondary beams at Bragg's angle to the incident beam. The amount of power channelled out of the undeflected beam depends on the level of RF signal applied to the AOM. By modulating the RF signal amplitude to the crystal, the intensity of the undeflected light can be varied. As shown in

[4] an EOM used with a polarising beam splitter is a popular way to modulate the intensity of a laser beam.

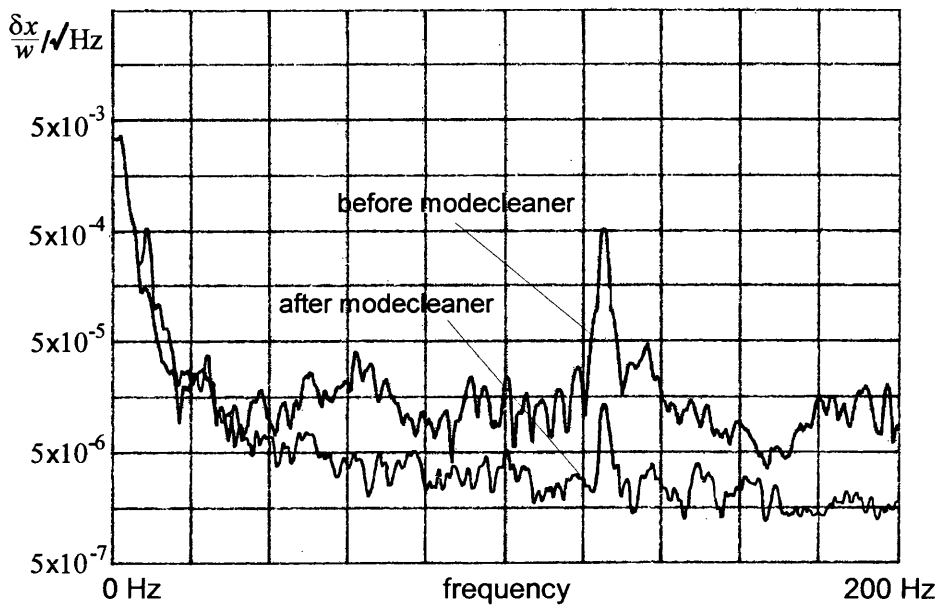

Figure 9.22: *Beam jitter levels measured at the input and output of the modecleaner over a 200 Hz span. The measurements were made with an artificial lateral beam positional fluctuation at 125 Hz applied to the input light.*

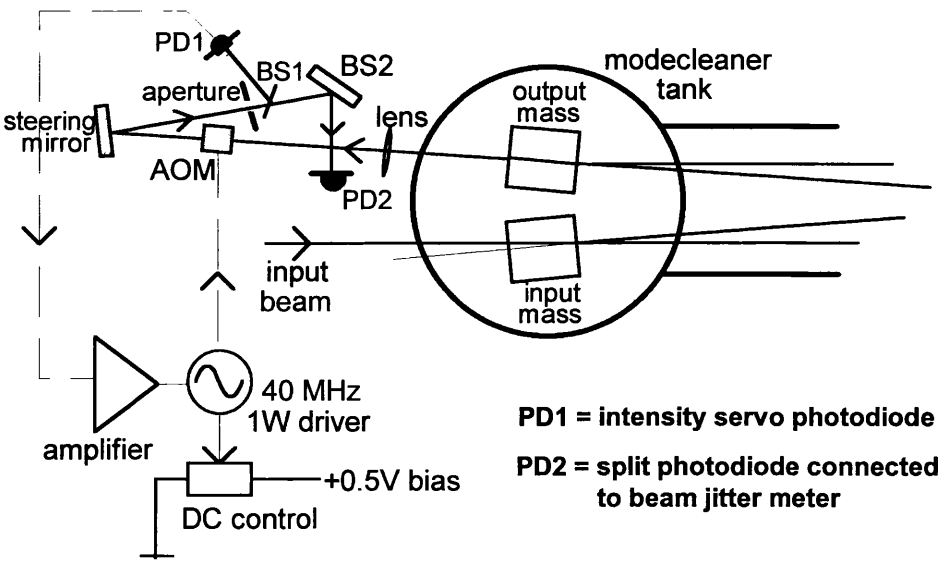

Figure 9.23: *Intensity stabilisation scheme for the light output from the modecleaner.*

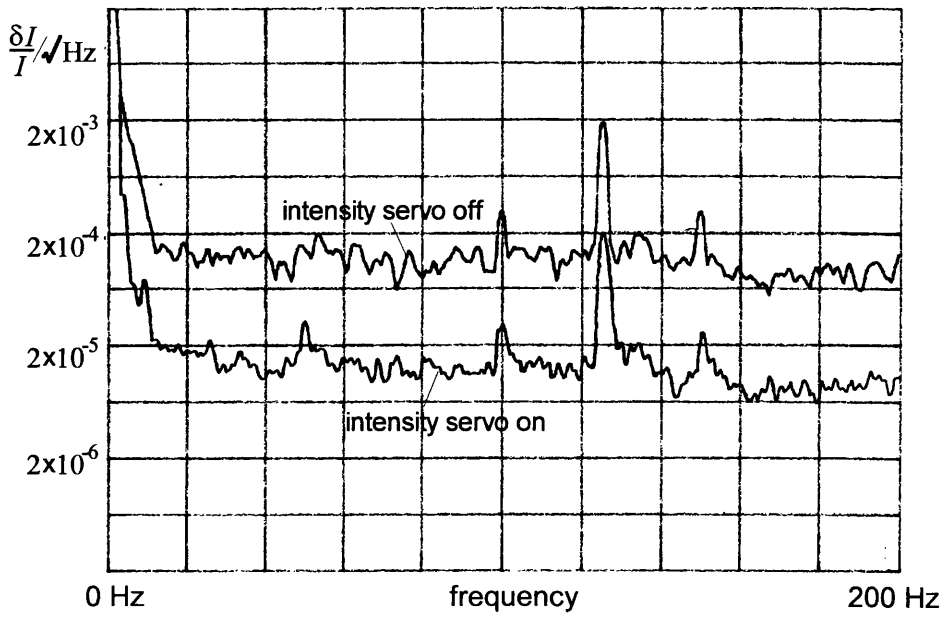

Figure 9.24: *Intensity noise levels measured at the output of the modecleaner over a 200 Hz span with the intensity servo switched on and off.*

Fig 9.23, a small reference beam was extracted from the main modecleaner output beam by a glass slide beam splitter BS1 and directed towards photodiode PD1. The signal from this photodiode was amplified and applied with negative feedback to a low level mixer (Mini Circuits Lab SRA-1) which controlled the RF drive to the AOM. A DC control allowed the static operating point of the intensity servo to be varied. By adjusting the input to the mixer from 0 to 0.5 V it was possible to channel up to 40 % of the incident power into the diffracted beams. The system afforded 20 dB suppression of intensity noise over the frequency range of interest, which was adequate for this purpose. It should be pointed out that careful construction of such a system can provide far greater intensity noise suppression over a bandwidth limited only by the time delays incurred because of the finite velocity of sound in the AOM crystal [70].

The traces in Fig 9.24 show the intensity noise spectra at the output of the modecleaner with the AOM intensity servo switched off and on. These intensity traces were measured using an external photodiode situated in place of the split photodiode PD2 in Fig 9.23. The signal at 125 Hz is the artificially applied jitter

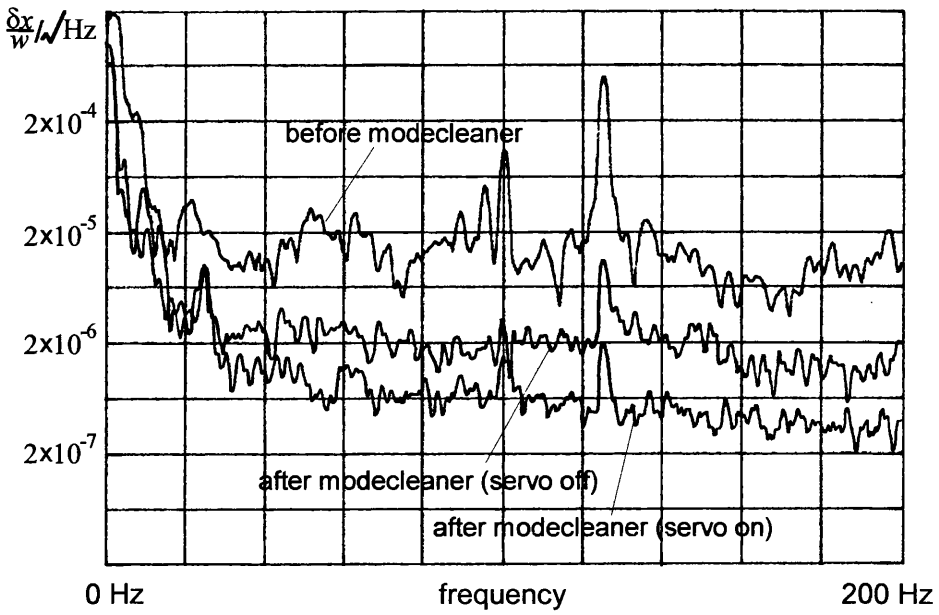

Figure 9.25: *Beam jitter levels measured at the input and output of the modecleaner over a 200 Hz span. The measurements were made with an artificial lateral beam positional fluctuation at 125 Hz applied to the input light. The two output levels correspond to the intensity servo being switched on and off.*

peak manifesting itself as intensity noise in the throughput light. The traces in Fig 9.25 show the levels measured by the beam jitter meter on the modecleaner input beam, and then on the output light with the AOM intensity servo switched off and on. It can now be seen that the beam jitter levels measured previously were in fact being limited by intensity noise. By increasing the gain of the intensity servo from the situation corresponding to Fig 9.25, it was possible to reduce the background further, but not the peak at 125 Hz suggesting that this now represents mostly beam jitter. By comparing the top and bottom traces in Fig 9.25 the suppression of the beam jitter peak at 125 Hz can be measured to be $\sim$ 48dB which is getting comparable with the expected value of $\sim$ 51dB. Closer inspections become rather meaningless, since the photodiode calibration is subject to a error in the region of $\sim$ 25 % resulting in an error of $\sim$ 2.5dB in the suppression factor. The jitter level in Fig 9.25 is not reduced by the full 20 dB suppression that the intensity noise is subject to. If it was, then it would still be unclear that the lowest level in Fig 9.25

was due to beam jitter rather than intensity noise, and there would be a temptation to increase the gain of the intensity servo. The fact that the beam jitter meter appears not to be limited by intensity noise when the AOM servo is switched on gives confidence about the calibration of the jitter meter along the vertical axis of Fig 9.25. At 100 Hz the normalised beam jitter level is $\sim 6 \times 10^{-7}/\sqrt{\text{Hz}}$ falling to a level of $\sim 3.5 \times 10^{-7}/\sqrt{\text{Hz}}$ at 200 Hz.

9.4 Conclusion

The purpose of constructing prototype apparatus is as much to gain experience in tackling the potential problems met in the construction and development phases, as it is in testing the results and ensuring that the required performance goals are met. In both these respects the Glasgow modecleaner system has been a successful development, with most of the measured aspects of the system meeting desired specifications. The major exception is the power throughput obtainable using the present mirrors. Although the modecleaner with 70 % throughput is still more efficient than the single mode optical fibre currently used in the Glasgow 10 m prototype detector[5], the efficiency could be made far better with a change of mirrors. This is one improvement that will possibly be made in the future, particularly if the scheme is eventually integrated into the 10 m detector to replace the fibre.

In the final development stage, the reliability of the output light was determined primarily by the first loop laser stabilisation servo. If this loop was operating at its best, then the modecleaner would practically never fall out of lock on its own. The system would lock for up to two hours before thermal drift in the aluminium reference cavity caused the first loop to fail. With a better choice of material, such as fused silica, or optimally, zerodur, this problem would be overcome. The acquisition of lock, which can often be difficult in suspended mass servo systems, did not prove to be problematic here. After the first loop was operating well, the modecleaner would lock onto a fringe within a second or two.

The beam jitter reduction of the system as described towards the end of section

[5] this achieves at best 60 % power throughput with extremely delicate alignment.

9.3 is encouraging. The background level of beam jitter in the bottom trace of Fig 9.25 corresponds to a residual motion of around $10^{-9}\mathrm{m}/\sqrt{\mathrm{Hz}}$ associated with the beam at the point of measurement. It is interesting to compare this with the ground noise at the optical table where the modecleaner measurements were made. Using an accelerometer, the level of ground noise was measured to be $\sim 5 \times 10^{-10}\,\mathrm{m}/\sqrt{\mathrm{Hz}}$ at 100 Hz. The construction and subsequent alignment of the AOM intensity servo resulted in there being two beam steering mirrors guiding the modecleaner output beam to the split photodetector, both of which will be subject to the above level of seismic noise. In view of this, it is perhaps unsurprising that the background level in Fig 9.25 is not lower, since this level is of the same order as the positional noise that the steering mirrors will impose on the beam. Ideally, the split photodetector should be suspended, preferably in vacuum, and the modecleaner output allowed to fall on it without being steered by any components directly contacted to the ground.

The Glasgow modecleaner development has provided useful experience and results which can be used in the construction of the GEO 600 detector and its associated modecleaner scheme and more will be said of this in the final chapter. For now, suffice to say that the necessary beam geometry noise suppression should be achievable, although double suspension systems will be used throughout to reduce the residual motion of the suspended masses. Good mirror handling procedures are essential to keep the losses of the mirror coatings down; certainly it would be desirable to maintain the loss of each mirror in the sub-100 ppm region. How this is achieved is yet to be decided, but will almost certainly involve the use of temporary clean tents which are set up around the vacuum tanks containing the suspended mirrors, as the components inside are worked with.

Chapter 10

Conclusion

10.1 Review

The development of successful laser interferometer gravitational wave detectors depends on having available the finest quality optical components, controlling them with carefully designed feedback systems involving a mixture of mechanical and electronic techniques and ensuring that many noise barriers are overcome.

Chapter 1 introduced the typical strain amplitudes that many popular astrophysical sources are expected to produce. In chapter 2 the properties of bar detectors and laser interferometers were discussed and the sensitivity and bandwidth requirements from chapter 1 were seen to favour laser interferometers. Laser based systems have the potential to achieve very high broadband strain sensitivities, and, with the technique of signal recycling, can provide enhanced narrow band performance. The quality of mirrors involved in these advanced detector designs needs to very high, and chapter 4 presented results of the losses of currently available supermirrors, showing that mirror coatings are available today with only a fraction of the losses of those available a few years ago. In chapter 5 laser beam geometry fluctuations were introduced as an important source of laser noise. Instruments designed to measure beam positional fluctuations and beam width variation were described and results for argon ion and Nd:YAG lasers were presented. Chapter 6 illustrated two situations where beam geometry noise was considered potentially problematic

in Nd:YAG laser servo systems. This led to measurements of beam jitter at the relaxation oscillation frequency of a Nd:YAG laser, and to a study of beam geometry noise as a limiting factor in the performance of a laser intensity servo. The justification for considering beam geometry noise as a serious problem for detector sensitivity was emphasised in chapter 7 where some coupling mechanisms were introduced. The strengths of these coupling mechanisms make it clear that a large suppression of beam geometry noise is essential before laser interferometers can reach their target sensitivity. Chapter 8 described the resonant modecleaner as a system for suppressing beam geometry noise while chapter 9 explained the design of the prototype resonant modecleaner built in the lab at Glasgow. The performance of the modecleaner was discussed in some detail.

The important consideration now is how the modecleaner scheme for GEO 600 should be implemented, and what specifications are required of it in view of the results of the previous chapters. These important conclusions form the subject of the next section.

10.2 Modecleaner Scheme for GEO 600

After the investigation in chapter 7 of some primary coupling mechanisms between beam geometry noise and interferometer sensitivity, the necessary suppression factors required were seen to be of order 10^5. This is too large for a single modecleaner to achieve, and two modecleaners in series are required, each having properties similar to the Glasgow modecleaner. Before introducing the specifications of the modecleaner scheme for GEO 600, it is first helpful to illustrate its location relative to the rest of the interferometer system.

The proposed GEO 600 optical layout is shown in Fig 10.1. The diagram illustrates the layout of vacuum tanks and pipes in the central station enclosure of the interferometer. The inboard tanks contain the 'end' mirrors of each arm which are suspended above the path of the beam entering each arm. The 'far' mirrors are suspended in their own tanks which reside in smaller enclosures 600 m from the central tank. The two modecleaners are shown in greater detail in Fig 10.2. They have

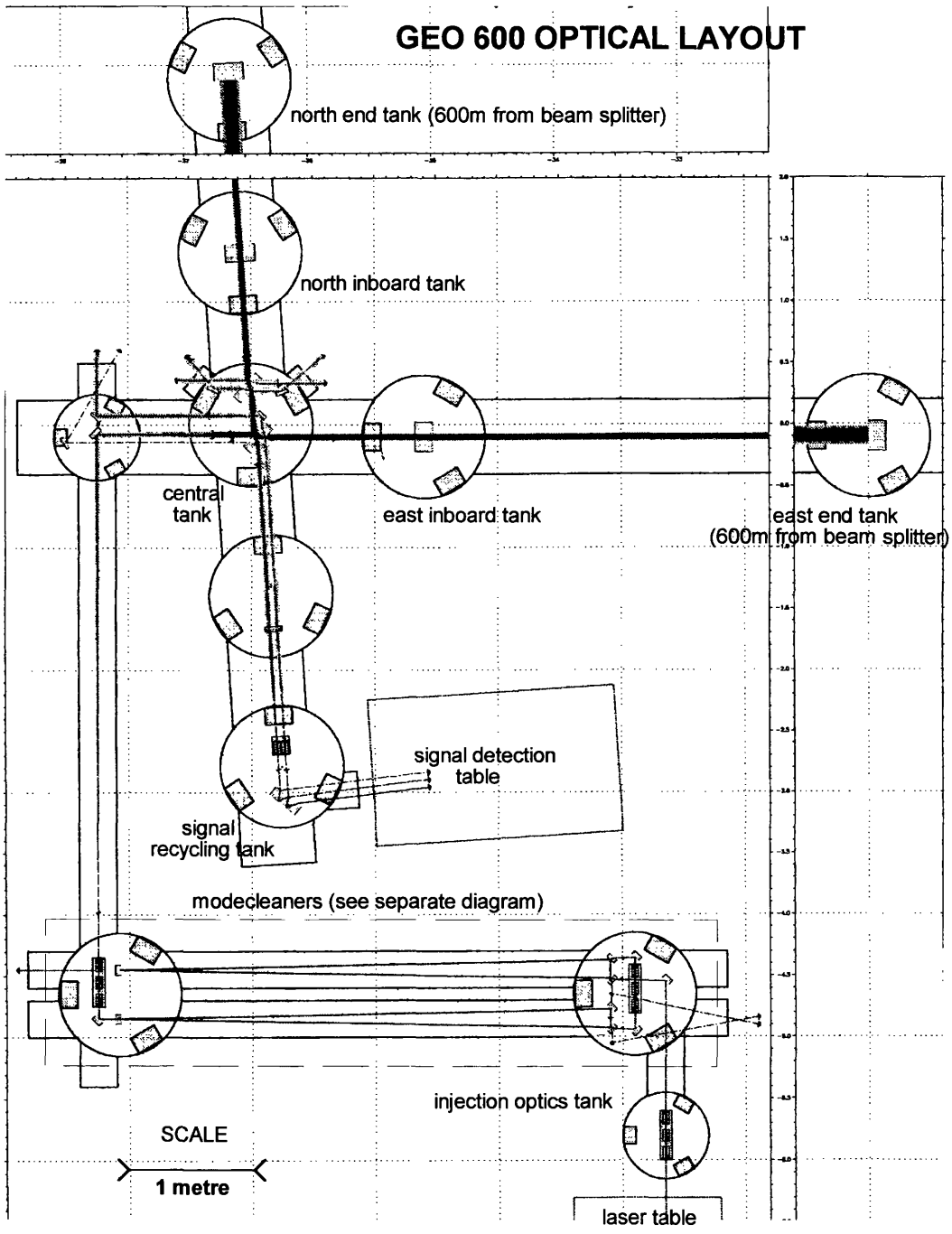

Figure 10.1: *The optical layout of the GEO 600 interferometer. The diagram is taken from an AUTOCAD technical drawing produced by Roland Schilling at MPQ in Garching. The beam enters from the laser table (bottom right) and passes through the triangular modecleaners before heading for the main interferometer.*

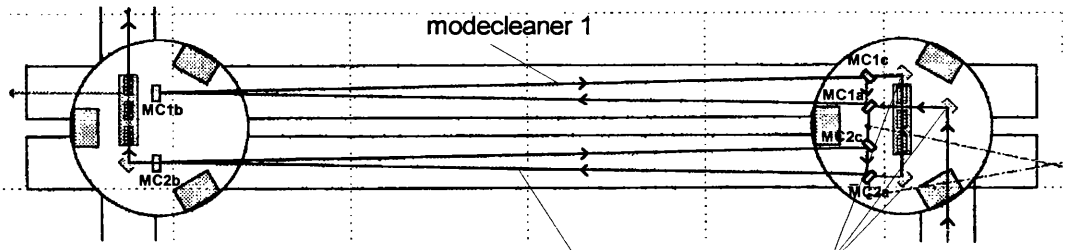

mirror	transmittance	curvature
MC1a	1500ppm	flat
MC1b	max reflectance	6.7m
MC1c	1500ppm	flat
MC2a	1500ppm	flat
MC2b	1500ppm	6.7m
MC2c	max reflectance	flat

Figure 10.2: *The modecleaner scheme for GEO 600. The laser beam encounters two triangular cavities, placed in series.*

very similar properties, each having cavity finesse $\sim$ 2100 and optical path length of about 8 m. Each cavity is based on a triangular ring with two closely spaced flat mirrors ($\sim$ 0.1 m apart) and a further ($\sim$ 4 m distant) curved mirror of radius of curvature 6.7 m. This cavity geometry can be modelled as a simple plane-curved cavity with $L/R = 0.6$, where L is the cavity length and R is the radius of curvature of the curved mirror. This geometry provides a similar level of suppression to the optimal curved-curved cavity with $L/R = 0.6$ described in section 8.2.2, and should give suppression factors of order 10^3 for the TEM_{10} and TEM_{20} modes. The choice of a ring cavity reduces the demands on laser isolation. All the mirrors will be suspended as double pendulums. Also suspended as double pendulums are the various beam steering mirrors, phase modulators and Faraday isolators. Particular care has to be taken not to compromise the performance of the modecleaner scheme by introducing beam geometry noise via components suspended after the modecleaners. The locking topology will most likely be similar to that of the Glasgow modecleaner system in its final stage. The laser will be stabilised to a rigid reference cavity and then each modecleaner will be locked to the pre-stabilised light. There is an option of using one of the modecleaners to provide a degree of frequency stabilisation, but there are many other possible scenarios, and it will have to be decided, perhaps experimentally, which will provide the most suitable configuration in practice.

10.3 Closing Remarks

It looks likely that gravitational waves will be detected by laser interferometric detectors around the year 2000 or soon after. By then there should be four operational laser based detectors forming a ground based network that will be able to investigate coincidence signals, exclude false alarms and make better the analysis of accepted signals. The achievement of this situation has only been possible given the perseverance and dedication of many researchers over the past twenty years, in both the laser interferometer and resonant bar groups. Together they have designed detectors, conquered many different noise barriers, solved problems through calculation and experiment and brought about the general acceptance of gravitational wave astronomy as an exciting astrophysical goal as well as an innovative technical achievement. This thesis has presented some of these technical challenges and the experimental solutions developed to meet them. The work presented is important not only in its own right but as part of the team effort in Glasgow, and with our colleagues in Germany, to complete our contribution to the worldwide network of gravitational wave observatories - GEO 600.

Appendix A

Eigenmodes of a General Cavity Geometry

A Gaussian laser beam is characterised at each point along its propagation by two quantities. These are the radius of curvature of the beam phase front R and the radius of the beam w. Together they define the *complex beam parameter* q to be

$$\frac{1}{q} = \frac{1}{R} - \frac{\lambda}{\pi w^2}. \tag{A.1}$$

In chapter 5 (section 5.2.1) the propagation of the beam was seen to be described very conveniently using q. The equation

$$q_2 = q_1 + d \tag{A.2}$$

gives the relationship between the complex beam parameters at two points along the propagation axis separated by a distance d. By solving real and imaginary parts, relationships for w_2 and R_2 in terms of w_1 and R_1 can be derived. Eqn.(A.2) is a special case of a more general relationship called the $ABCD$-law. This can be expressed as

$$q_2 = \frac{Aq_1 + B}{Cq_1 + D} \tag{A.3}$$

where A, B, C and D are the entries of the *ray transfer matrix* that describes the optical system between the points where q_1 and q_2 are measured. Some common optical systems and their associated ray transfer matrices are shown in Table A.1.

optical system	ray transfer matrix
length 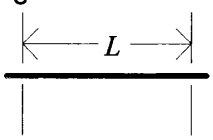	$\begin{bmatrix} 1 & L \\ 0 & 1 \end{bmatrix}$
thin lens 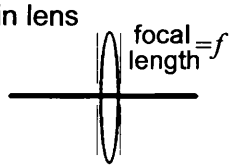	$\begin{bmatrix} 1 & 0 \\ -1/f & 1 \end{bmatrix}$
lens system 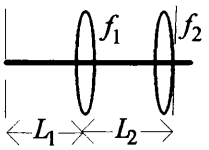	$\begin{bmatrix} 1-\frac{L_2}{f_1} & L_1+L_2-\frac{L_1L_2}{f_1} \\ -\frac{1}{f_1}-\frac{1}{f_2}+\frac{L_2}{f_1f_2} & 1-\frac{L_1}{f_1}-\frac{L_2}{f_2}-\frac{L_1}{f_2}+\frac{L_1L_2}{f_1f_2} \end{bmatrix}$
block 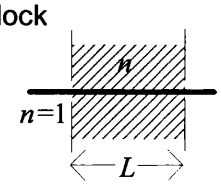	$\begin{bmatrix} 1 & \frac{L}{n} \\ 0 & 1 \end{bmatrix}$

Table A.1: *Some common optical systems and their corresponding ray transfer matrices.*

An optical cavity can be characterised using a ray transfer matrix to describe a complete cavity round trip of the light. For a stable eigenmode to exist, the light field must replicate itself after each round trip and this requires the existence of a solution of

$$q = \frac{Aq + B}{Cq + D}. \tag{A.4}$$

By equating real and imaginary parts of Eqn.(A.4), the equations for R and w in terms of A, B, C and D can be derived as

$$R = \frac{2B}{D - A} \tag{A.5}$$

$$w^2 = \frac{\lambda}{\pi} \frac{2B}{\sqrt{4 - (A + D)^2}}. \tag{A.6}$$

By considering Eqn.(A.6) it is apparent that the beam radius is real provided that the trace of the ray transfer matrix satisfies the condition

$$-1 < \frac{1}{2}(A + D) < 1 \tag{A.7}$$

sometimes referred to as the *stability condition* for the cavity. If this condition is not satisfied then the cavity under consideration is unstable and will not support a resonant eigenmode. The properties of some common cavity geometries are shown in Table A.2. More elaborate cavities can be described using the round-trip ray transfer matrix along with Eqn.(A.5) and Eqn.(A.6), although some cavities can be generalised from those in Table A.2. For example, a general three mirror ring cavity with one curved mirror and two flat mirrors can always be described by a modification of the last structure in Table A.2.

A stability diagram for the generic two mirror cavity can be produced by plotting the factors $1 - L/R_1$ and $1 - L/R_2$ along orthogonal axes as shown in Fig A.1. These factors appear so commonly in two mirror cavity formulae that they have been called the g-factors, denoted by g_1 and g_2. In terms of cavity stability, a two mirror resonator will be stable provided

$$0 < g_1 g_2 < 1 \tag{A.8}$$

and allows the regions in Fig A.1 to be deduced.

optical cavity	waist size w_0^2	waist position
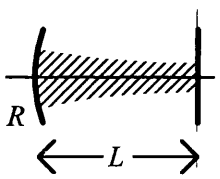	$\frac{\lambda}{\pi}\sqrt{L(R-L)}$	L
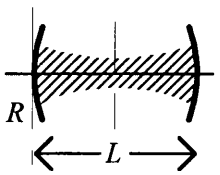	$\frac{\lambda}{2\pi}\sqrt{L(2R-L)}$	$\frac{L}{2}$
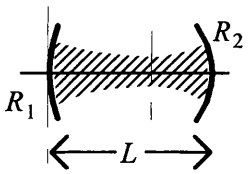	$\frac{\lambda}{\pi}\frac{\sqrt{L(R_1-L)(R_2-L)(R_1+R_2-L)}}{R_1+R_2-2L}$	$\frac{L(R_2-L)}{R_1+R_2-2L}$
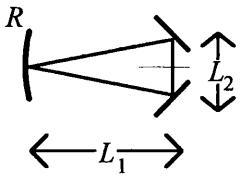 $[L_1 >> L_2]$	$\frac{\lambda}{\pi}\sqrt{(L_1+\frac{L_2}{2})(R-L_1-\frac{L_2}{2})}$	$L_1+\frac{L_2}{2}$

Table A.2: *Properties of some optical cavities. Waist positions are given in terms of the distance measured from the left hand mirror along the optic axis.*

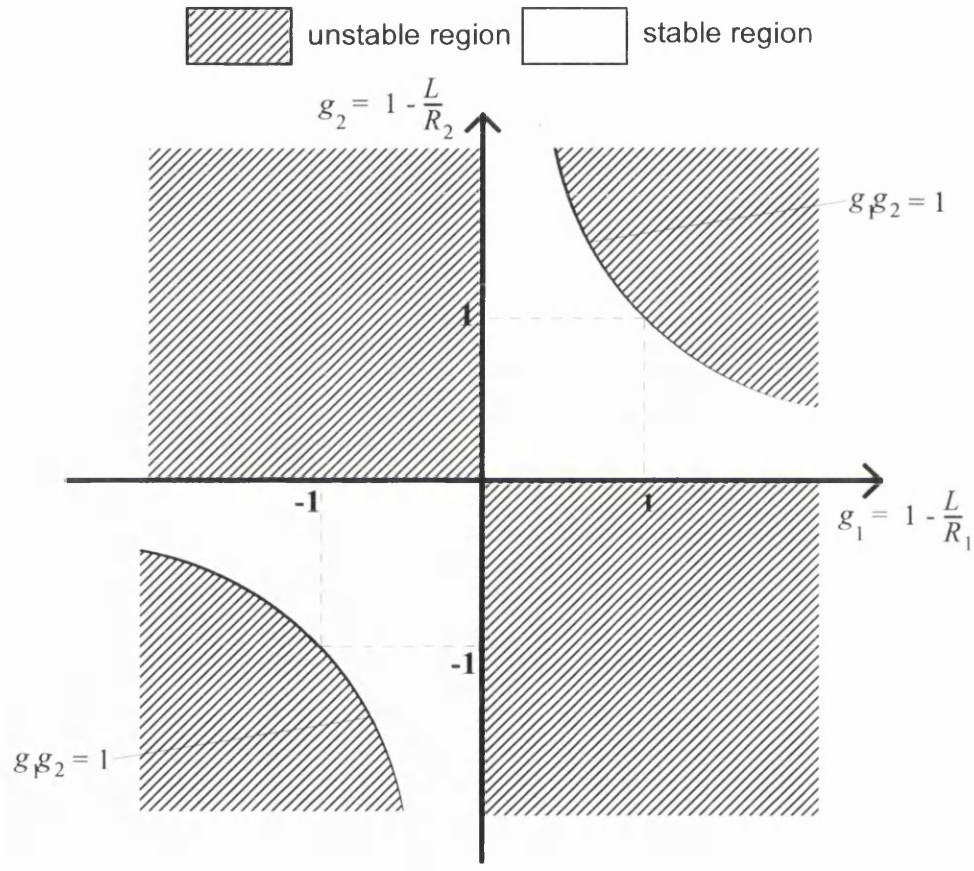

Figure A.1: *Stability diagram for a two mirror Fabry Perot cavity.*

The $ABCD$ matrix must calculated from a given point, round the cavity, and back to the given point. Then the values of R and w calculated using Eqn.(A.5) and Eqn.(A.6) will apply to this point.

Appendix B

Gaussian Optics Package for GEO 600

When designing a large interferometer such as GEO 600 it is convenient to have a record of the various beam sizes and divergences at any given location. This helps when it comes to designing the layout of the system or specifying physical dimensions of optical components. An obvious solution is to map out the path of the beam and plot the beam phase front curvature R and the beam radius w as a function of the propagation through the system. A flexible approach would be to have a computer program, rather like a spreadsheet package, which will modify the complete beam plot if any part of the system is altered. This appendix describes such a program, written in Turbo C++ for DOS. The demands on the computer hardware are low, and the program uses DOS graphics screens throughout and requires a mouse.

The basic structure contains two primary functions called by the user via various drop-down menus. One of these functions deals with geometrical considerations such as mode matching, cavity mode frequencies and beam propagation. The other function handles all aspects of laser power in the system, including throughput of cavities, losses in components and such like. Together they describe any aspect of the interferometer that the user wishes to apply them to, or a custom system can be entered in and the functions applied to it. Optical layouts fall into two categories as far as the program is concerned. The first is a simple chain of optical components,

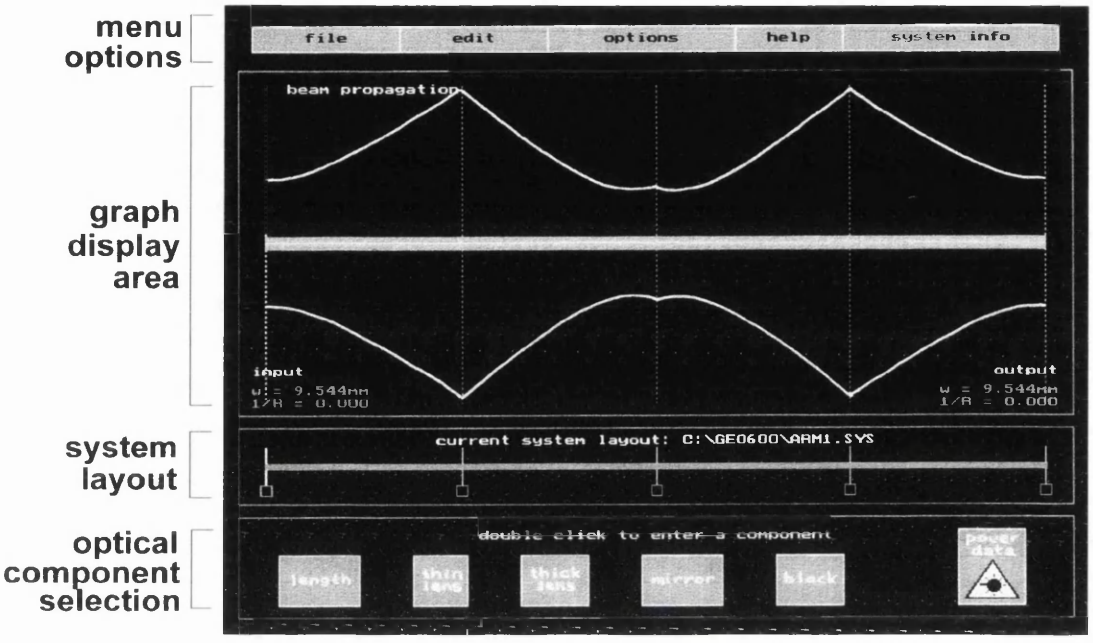

Figure B.1: *Screen showing the eigenmode of one of the GEO 600 power recycling cavitites.*

such as an injection optics chain for an interferometer or a simple mode matching solution. The other type of layout is that of a cavity round trip. Depending on which type of system the user wishes to study, the program may apply eigenmode routines to find cavity modes, or else advise if an optical system does not constitute a stable cavity.

The screen shot in Fig B.1 shows an example output from one of the geometry function routines. It is actually the fundamental eigenmode of the power recycling cavity associated with one of the arms of the GEO 600 interferometer. The various parts of the screen are described via the captions in Fig B.1. More quantitative plots can be obtained by selecting a scaled graph of beam radius or beam phase front curvature. As an example, Fig B.2 illustrates a propagation plot of the reciprocal of beam phase front radius of curvature for a laser cavity that the user has entered. In practice, use is made of the computer's mouse to read information from the graph. The program displays a data box containing the beam curvature and position in the cavity corresponding to the current mouse position. Similar graphs for beam radius, guoy phase and cavity circulating power can be selected.

Two examples of the power function routines are shown in Fig B.3. One screen shows the visibilty of one of the proposed modecleaner cavities in the GEO 600 detector. It also shows details regarding the fringe separation and free spectral range, which are useful if the cavity were to be scanned, for example to align it. The other screen shown in Fig B.3 is the light resonance curve for the same modecleaner cavity. The linewidth is shown along with power loss details for each component in the system. Although this cavity contains only lengths and mirrors, it is possible to enter blocks of various refractive indices and lenses too, if required. There are graphical interface options for entering the power reflectance, transmittance and loss values of any component. By calling screens such as those shown in Fig B.3, or selecting a power histogram, the user can obtain a list of the power loss details at each component as the beam propagates round the optical system or cavity.

The structure of the program is such that an alteration to one aspect of the GEO 600 detector will cause subsequent changes to the light in later parts of the system, just as if the alteration had been made to the real system. The user can choose to keep the alterations if desired. Entire data sets for complete modules of the interferometer are stored by the program in separate files to allow flexibility between multiple users. For example, all parameters relevant to, say, the first modecleaner are stored in a file MODECL1.SYS. If a colleague has a very different idea about the particulars of the first modecleaner, then he or she can prepare his or her own data file pertaining to it. Similarly for the injection optics, laser cavity design, other modecleaner, interferometer arms and signal recycling cavities. In a similar manner, users can enter and then store their own custom designed optical systems to disk. There is also a facility to model a Gaussian beam, given two user input beam radius values at different points along the optic axis.

In summary, the software provides a database for storing information about various parts of the GEO 600 interferometer, but particularly for determining the beam parameters at any given point. It also provides a set of optical functions and routines that can replace (often tedious) calculations on paper. The program allows optical system parameters to be entered and changed at will, while immediately conveying the consequences such changes have on the beam propagation.

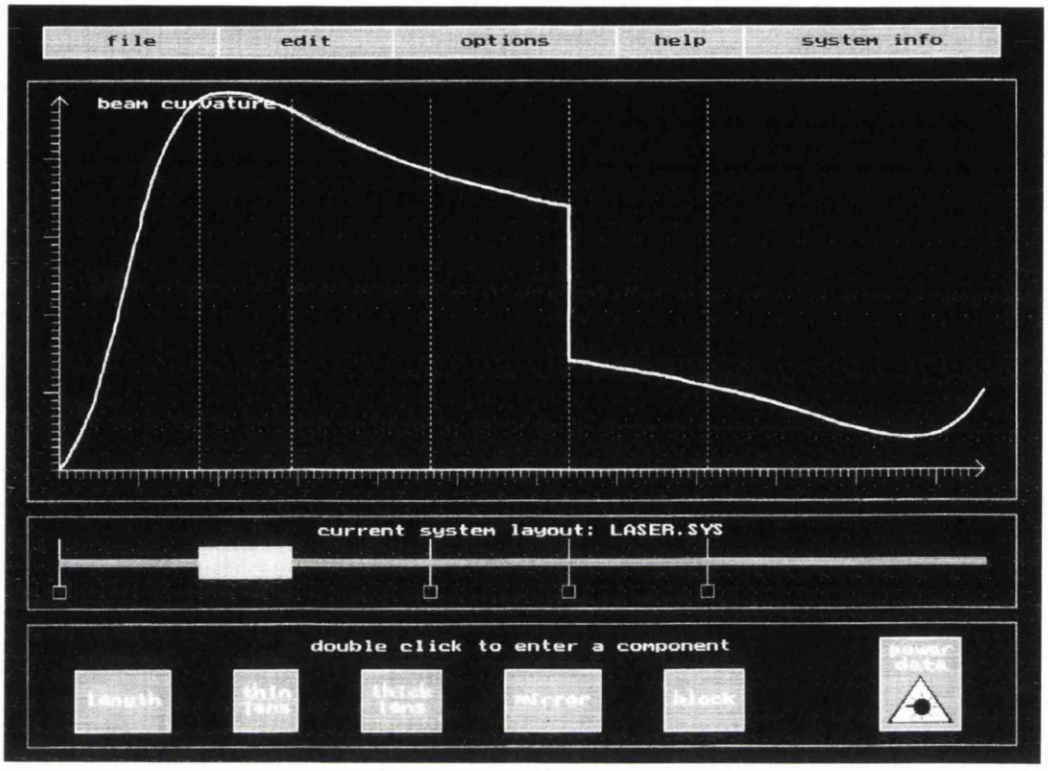

Figure B.2: *Screen showing a plot of the reciprocal phase front radius of curvature for a ring laser cavity.*

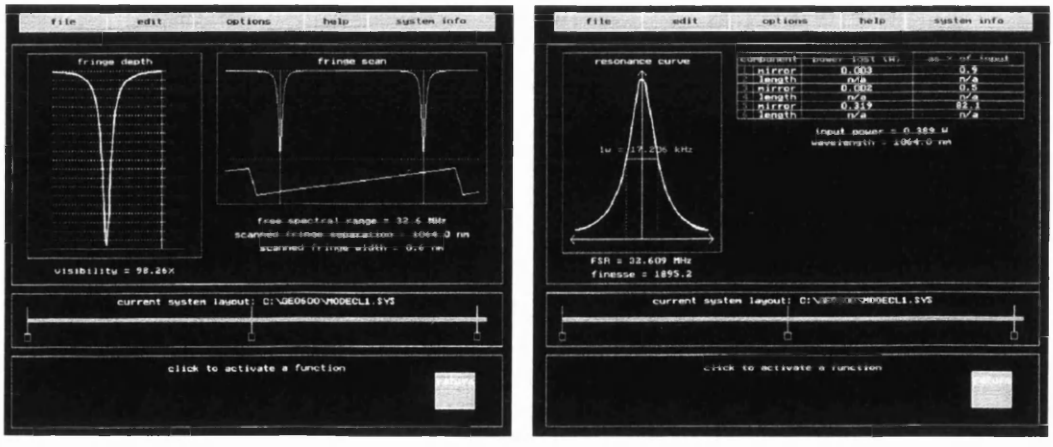

Figure B.3: *Screens showing information regarding cavity visibility and power handling details, in this case for one of the modecleaners in the GEO 600 detector.*

Bibliography

[1] A. Einstein, *Preuss. Akad. Wiss. Berlin* (1916) p.688.

[2] C.W. Kilmister, *Special Theory of Relativity, Pergamon, Oxford* (1970).

[3] B.F. Schutz, *A First Course in General Relativity, Cambridge University Press* (1985).

[4] S.W. Hawking and W. Israel, *300 Years of Gravitation, Cambridge University Press* (1987).

[5] K.S. Thorne, *Proc. of IAU Symp.165, Kluwer Academic Publishers.* (1995).

[6] A.G. Lyne and D.R. Lorimer, *Nature* **369** (1994) p.127.

[7] B.F. Schutz, *Proc. 1st Edoardo Amaldi Conf. on Grav. Waves* (1995) (in print).

[8] J.H. Taylor and J.M. Weisberg, *Astrophys. J.* **253** (1982) p.908.

[9] J.H. Taylor and J.M. Weisberg, *Astrophys. J.* **345** (1989) p.434.

[10] S.V. Dhurandhar and B.F. Schutz, *Phys. Rev. D.* **50,4** (1994) p.2390.

[11] B.F. Schutz, *Nature*, **323** (1986) p.310.

[12] A.V. Tutukov and L.R. Yungelson, *Monthly Not. RAS*, **260** (1993) p.675.

[13] H. Yamaoka et al, *J. Astron. Astrophys.* **267** (1993) p.433.

[14] A. Burrows et al, *Astrophys. J.*, **450, 2** (1995) p.830.

[15] K. Danzmann et al, MPQ report, (1993).

[16] R. Narayan et al, *Astrophys. J.* **379** (1991).

[17] T.R. Lauer et al, *Astronom. J.* **104** (1992).

[18] L.P. Grishchuk, *Soviet Physics-JETP*, **40** (1974) p.409.

[19] L.P. Grishchuk, *Class. Quant. Grav.* **10** (1993) p.2449.

[20] E. Witten, *Phys. Rev. D.* **30** (1984) p.272.

[21] A. Kosowsky and M.S. Turner, *Phys. Rev. D.* **49** (1994) p.2837.

[22] M. Sasaki, *Relativistic Cosmology*, *Universal Academic Press* (1994).

[23] F.A.E. Pirani, *Phys. Rev.* **105** (1957) p.1089.

[24] H. Bondi, *Nature*, **179** p.1072.

[25] R.A. Isaacson, *Phys. Rev.* **166** p.1263.

[26] D.G. Blair, *The Detection of Gravitational Waves*, *Cambridge University Press* (1991).

[27] J. Alberto Lobo, *sub. to Phys. Rev.* (1995).

[28] A. Abramovici et al, *Proc. 1994 Snowmass Summer Study* (in print).

[29] W.W. Johnson and S.M. Merkowitz, *Phys. Rev. Lett.* 70 (1993) p.2367.

[30] P. Astone et al, *Class. Quantum Grav.* **11** (1994) p.2093.

[31] R.L. Forward, *Appl. Opt.* **10** (1971) p.2495.

[32] S.T. Yang et al, *Opt. Lett.* **16** (1991) p.1493.

[33] V. Magni et al, *Opt. Lett.* **18** (1993) p.2111.

[34] W.A. Edelstein et al, *Jour. Phys. E.* **11** (1978) p.710.

[35] C.A. Cantley et al, *Rev. Sci. Inst.* **63** 4 (1992) p.2210.

[36] N.A. Robertson et al, *Appl. Phys. B.* **39** (1986) p.149.

[37] A. Gillespie and F. Raab, *Workshop on Thermal Noise, Caltech* (1994).

[38] J. Hough et al *GEO 600 Proposal*, (1994).

[39] A. Gillespie and F. Raab, *Phys. Lett. A.* **190** (1994) p.213.

[40] D. Herriot, *Appl. Opt.* **3** (1964) p.523.

[41] R. Weiss, *Quaterly Report, RLE, MIT* **105** (1972) p.54.

[42] J.R. Pierce, *Theory and Design of Electron Beams, Van Nostrand, New York* (1954).

[43] B.J. Meers, *Phys. Lett. A.* **142** (1989) p.465.

[44] K.A. Strain et al, *Phys. Lett. A.* **194** (1994) p.124.

[45] K.A. Strain and B.J. Meers, *Phys. Rev. Lett.* **66** (1991) p.1391.

[46] T.M. Niebauer et al, *Phys. Rev. A.* **43, 9** (1991) p.5022.

[47] H.E. Bennett and J.O. Porteus, *Journ. Opt. Soc. America* **51,2** (1961) p.123.

[48] PMS Electro-Optics, *mirror specifications communication* (1994).

[49] H.A. MacLeod, *Thin-Film Optical Filters, Adam Hilger* (1986).

[50] N.A. Robertson, *Opt. Comm.* **69, 5,6** (1989) p.345.

[51] A.C. Boccarra et al, *Opt. Lett.* **5** (1980) p.377.

[52] W. Winkler et al, *Phys. Rev. A.* **44** (1991) p.7022.

[53] K.A. Strain et al, *Opt. Comm.* **117** (1995) p.385.

[54] A.E. Siegman, *Lasers, Oxford University Press* (1986).

[55] K.D Skeldon, *internal review paper*, (1991).

[56] H. Kogelnik and T. Li, *Proc. IEEE*, **54** (1966) p.1312.

[57] F. Bayer-Helms, *Appl. Opt.* **23, 9** (1984) p.1369.

[58] D.Z. Anderson, *Appl. Opt.* **23, 17** (1984) p.2944.

[59] C.D. Nabors, *Opt. Lett.* **14** (1989) p.1159.

[60] A.D. Farinas et al, *Opt. Lett.* **19**(1994) p.114.

[61] A.D. Farinas et al, *J. Opt. Soc. Am.* **12, 2** (1995) p.328.

[62] A. Campbell et al, *Phys. Lett. A.* **170** (1992) p.363.

[63] S. Rowan et al, *Jour. Mod. Opt.* **41, 6** (1994) p.1263.

[64] J. Mizuno, *PhD thesis, MPQ Garching*, (1995).

[65] W. Winkler et al, *Appl. Opt.* **33** (1994) p.7547.

[66] A. Rudiger et al, *Optica Acta*, **28, 5** (1981) p.641.

[67] D.I. Robertson et al, *Rev. Sci. Inst.* **66, 9** (1995) p.4447.

[68] E. Morrison et al, *Appl. Opt.* **33, 22** (1994) p.5037.

[69] E. Morrison et al, *Appl. Opt.* **33, 22** (1994) p.5041.

[70] H.P. Layer, *Appl. Opt.* **18, 17** (1979) p.2947.